

ELECTROSPINNING AND AIR-CONTROLLED ELECTROSPRAYING OF  
POLYMER/PRECURSOR SOLUTIONS TO PRODUCE NANOMATERIALS FOR  
ENERGY STORAGE APPLICATIONS

A Dissertation

Presented to the Faculty of the Graduate School  
of Cornell University

In Partial Fulfillment of the Requirements for the Degree of  
Doctor of Philosophy

by

Joseph Michael Carlin Jr.

December 2019

© 2019 Joseph Michael Carlin Jr.

ELECTROSPINNING AND AIR-CONTROLLED ELECTROSPRAYING OF  
POLYMER/PRECURSOR SOLUTIONS TO PRODUCE NANOMATERIALS FOR  
ENERGY STORAGE APPLICATIONS

Joseph Michael Carlin Jr., Ph. D.

Cornell University 2019

Electrochemical energy storage is increasingly used in applications ranging from portable electronics to electric vehicles to grid-sized storage installations and the next generation of energy storage requires increased capacity, performance, and safety. To meet these demands, energy storage will rely more heavily on the use of nanostructured materials to improve performance. However, there are few ways to produce nanomaterials scalably while keeping them from being cost prohibitive. This work focuses on using electrospinning and air-controlled electrospaying techniques to prepare electrodes and separators for energy storage. These processes have the advantage of using inexpensive precursors, scalable production, and direct application of fiber mats and films and can overcome many of the shortcomings of conventional processes.

First, electrospinning is used to prepare free-standing, binder-free electrodes. Utilizing the natural non-woven mat formed by electrospinning, both carbon and carbon composite fiber sheets are prepared from polymer and precursor solutions and used directly as electrodes after heat treatment. These electrodes are used in supercapacitor, Li-ion, and Li-air energy storage applications.

Second, a combination of electrospinning and air-controlled electrospaying is used to prepare silicon fiber/RGO, direct-deposit anodes for Li-ion batteries. Silicon fibers are prepared by magnesiothermic reduction of electrospun silica fibers. Anodes are then prepared using a binder-free, water-based, direct-deposition method of electrospaying fibers with graphene sheets. After thermal treatment, reduced graphene oxide and silicon fiber anodes show high cycling capacity and rate capability. The system shows stability in accommodating silicon expansion, and the use of large diameter silicon fibers increased first coulombic efficiencies above 80%.

Finally, Li-ion battery separators are made using a combination of polymer and ceramic precursor. Electrospun separators have always shown excellent performance, but their large pore sizes can lead to short circuits and many of the common polymers used, such as PAN and PVDF, do not mitigate the risk of fire and other safety hazards. Through combinations of electrospinning and air-controlled electrospaying, as well as use of thermally resistant polymers with ceramic precursors, this work achieves thermally robust, flame-resistant separators with improved pore size distribution for safer, high rate Li-ion batteries.

## BIOGRAPHICAL SKETCH

Joseph Michael Carlin Jr. was born in 1989 in Madison, Wisconsin, to Joseph and Dawn Carlin. He grew up in Oxford, Ohio attending school in the Talawanda School District. In 2007 he began his college career at Miami University, joining the Paper Science program. He did research on the strength of paper tissue and towel under the tutelage of Professor Douglas Coffin. In his senior year he earned the Provost Student Academic Achievement Award. He went on to graduate from Miami's Honors Program in May 2011, earning Bachelors degrees in Chemical Engineering and Paper Science. In August 2011, Joseph started his doctoral program at the Robert Frederick Smith School of Chemical and Biomolecular Engineering at Cornell University. He joined Professor Yong Lak Joo's research group and focused on preparing electrode and separator materials from electrospinning and electrospraying for use in Li-ion batteries and other electrochemical energy storage applications. In August 2014, Joseph married Katelin (Ceronie) Carlin. He defended his thesis in August 2017 and then joined Axium Nano, LLC to continue research on non-woven battery separators.

To my wife, Kate, for sticking with me through this roller-coaster ride.

To my parents for their unwavering support and belief in my abilities.

To all my friends and family for their love and support.

## ACKNOWLEDGMENTS

For the better part of a decade I have worked on this thesis and there have been many twists and turns on the way to completing it. None of this would have been possible without the help of many different people. I would like to thank the professors who invested their time in me. First, I thank my advisor, Professor Yong Lak Joo, for all his guidance and assistance. Since arriving at Cornell, I have been excited to be a part of his lab and he rewarded that commitment time and time again helping me find my way as a researcher. Whether it was supporting me in trying to find answers to project obstacles, discussing new ways we could apply some of the unique materials we were creating, or sharing in the excitement of successes, he helped keep me motivated on the long journey. I would also like to thank my thesis committee members, Professor Margaret Frey and Professor Susan Daniel, for their advice and guidance. Finally, I would like to thank Professor Douglas Coffin, my undergraduate research advisor, for my first opportunity doing research. My opportunity to research non-woven materials began at Miami University and continued at Cornell.

I joined Professor Joo's lab with Dr. Brian Williams and I would like to specially thank him for years of research conversations, crazy brainstorming sessions, his help fixing equipment in the lab, his complete unselfishness to lend a hand, and most of all his friendship. There are many Joo group members who have also made my work possible: Prof. Jay Park, Prof. Ling Fei, Dr. Nate Hansen, Dr. Kyoung Woo Kim, Dr. Daewhan Cho, Dr. Jun Yin, Dr. Soshana Smith, Dr. Jangwoo Kim, Dr. Andrew Shah, Dr. Shubham Pinge, Dr. Mounica Divvela, Eric Chiang, Ghazal Shoorideh, Mohammed AlAmer, Kenville Hendrickson, Rachel Villamayor Huang, Christopher Klaassen and many other members who I worked with through the years. I love you all.

Finally, I would like to thank my friends and family who have been part of my life in Ithaca. To my close friends, Kyle and Nicole Watters, Justin Rosch, and Jason Boock, you are wonderful people I hope to stay in touch with always. To my sisters, Lindsey and Caitlin Carlin, for their enthusiasm and celebration of my work. To my parents who have always believed I would receive my Ph.D. and encouraged me to be my best. And to my lovely wife, Kate Carlin, who has put up with late nights, weird hours, thesis extensions, Ithaca winters, and many of the lows of graduate research, and stuck by me to support my dream. Starting my Ph.D. I did not know I was making such a big decision for both of us, but your commitment has made everything possible and I am glad that I can share this with you. I love you Kate.

## TABLE OF CONTENTS

Chapter 1: Introduction.....	1
1.1 Electrochemical Energy Storage.....	1
1.2 Electrospinning and Electrospaying.....	2
1.3 Lithium-Ion Batteries.....	5
1.4 Thesis Motivation and Scope of Work.....	9
1.5 References.....	12
Chapter 2: Electrospun, Freestanding Carbon and Composite Nanofiber Electrodes for Energy Storage Applications.....	15
2.1 Introduction.....	16
2.2 Experimental.....	20
2.3 Results and Discussion.....	24
2.4 Conclusions.....	53
2.5 References.....	55
Chapter 3: Magnesiothermic Reduction of Electrospun Silica Fibers used in AC- Electrosprayed Si/RGO Anodes .....	59
3.1 Introduction.....	60
3.2 Experimental.....	66
3.3 Results and Discussion.....	70
3.4 Conclusions.....	89
3.5 References.....	91
Chapter 4: Polyacrylonitrile/Ceramic Hybrid Asymmetric Separators for Lithium-Ion Batteries.....	93
4.1 Introduction.....	94
4.2 Experimental.....	98

4.3 Results and Discussion.....	103
4.4 Conclusions.....	121
4.5 References.....	122
Chapter 5: Electrospun Polyimide/Ceramic Hybrid Separators for Thermally Stable and High Rate Capability .....	125
5.1 Introduction.....	126
5.2 Experimental.....	130
5.3 Results and Discussion.....	134
5.4 Conclusions.....	149
5.5 Supporting Information.....	150
5.6 References.....	154
Chapter 6: Electrospun Polyimide Coated with a Ladder-Like Polysilsesquioxane by Air-Controlled Electrospaying for Improved Li-ion Battery Safety and High Rate Capability.....	157
6.1 Introduction.....	158
6.2 Experimental.....	163
6.3 Results and Discussion.....	167
6.4 Conclusions.....	183
6.5 References.....	184
Chapter 7: Recommendations for Future Work.....	189

## LIST OF FIGURES

- Figure 1.1.** Depiction of electrospinning process.
- Figure 1.2.** Depiction of electro spraying, air spraying, and air-controlled electro spray processes.
- Figure 1.3.** Depiction of lithium-ion battery discharge.
- Figure 2.1.** Pictures of carbon fiber trials showing (a) carbonized PAN fiber sheet formed between two ceramic plates, (b) PAN fibers electrospun to carbon felt (c) carbonized PAN fibers on carbon felt.
- Figure 2.2.** SEM images of carbonized PAN fiber morphology after treatments at (a) 1000°C, (b) 1200°C, and (c) 1400°C.
- Figure 2.3.** SEM imaging of carbonized PVP fibers carbonized at (a) 800°C, (b) 1000°C, (c) 1200°C, (d) 1400°C
- Figure 2.4.** BJH pore distribution plot for PAN carbonized fibers at 1000°C, 1200°C, and 1400°C.
- Figure 2.5.** BJH pore distribution plot for PVP carbonized fibers at 800°C, 1000°C, 1200°C, and 1400°C.
- Figure 2.6.** SEM imaging of fibers carbonized at 1000°C made from a 1:10 Super P: PAN solution.
- Figure 2.7.** BJH pore distribution plot for PAN carbonized fibers at 1000°C with and without Super P inclusion.
- Figure 2.8.** SEM images of PVP: Super P fibers after carbonization at 1000°C. Loadings of Super P were (a) 10 wt% Super P, (b) 20 wt% Super P, (c) 35 wt% Super P, and (d) 50 wt% Super P compared to the weight of PVP polymer in solution.
- Figure 2.9.** BJH plots showing the surface area contributions by pore size of Super P, PVP, and PVP/ Super P composites after carbonization at 1000°C.
- Figure 2.10.** SEM of PAN fibers carbonized at 1000°C for 8 hours with 5 wt% addition of GNRs.
- Figure 2.11.** SEM images of (a) as spun and (b) carbonized 17 wt% PAN/AAI fibers.

- Figure 2.12.** XRD of carbonized 17 wt% PAN/AAI fibers with labeled peaks for crystal structure.
- Figure 2.13.** BJH plots showing the surface area contributions by pore size of PAN and 17 wt% PAN/AAI fibers.
- Figure 2.14.** Magnetic properties of carbonized PAN/AAI samples from (a) the original work by Panels and (b) this work.
- Figure 2.15.** BJH plots showing the surface area contributions by pore size of carbonized PAN nanofibers and activated PAN carbon nanofibers.
- Figure 2.16.** CV plot showing the 5<sup>th</sup> cycle of a 10 mV/s sweep of a freestanding activated PAN carbon symmetric cell.
- Figure 2.17.** XRD showing crystal peaks of Mn<sub>3</sub>O<sub>4</sub> present in activated PAN/MnAcac samples.
- Figure 2.18.** SEM of 0.5:0.45 PAN:MnAcac fibers after activation treatment.
- Figure 2.19.** CV analysis of carbon/Mn<sub>3</sub>O<sub>4</sub> fibers. The scans showed low performance and non-ideal behavior at low scan rates of 1 and 10 mV/s.
- Figure 3.1.** A steel Swagelok reactor (1/2 in. fittings) used for magnesiothermic reduction of silica.
- Figure 3.2.** SEM images of the fibers and their fiber diameter distributions of (a,b) As spun PVP/TEOS fibers, (c,d) calcined silica fibers, and (e,f) silicon fibers after Mg reduction.
- Figure 3.3.** BJH pore distribution plot silica and silicon fibers.
- Figure 3.4.** XRD of silica fibers before and after Mg reduction. Mg reduction shows that the silica fibers were reduced to silicon.
- Figure 3.5.** SEM images of AC-electrosprayed GO sheets (left) and MWCNTs (right).
- Figure 3.6.** TGA analysis of AC-electrosprayed samples of the 2:1 Si fiber:RGO and the 120:40:8 Si fiber:RGO:MWCNT samples.
- Figure 3.7.** SEM images of silicon fiber anode preparations: (a) top view of a drop-casted 70/15/15 Si fiber/Super P/PAA, (b) top view of a direct deposit AC-electrosprayed Si fiber/GO anode, (c) cross-section of an AC-

electrosprayed Si/RGO anode, (d) cross-section of an AC-electrosprayed Si:RGO:MWCNT anode.

- Figure 3.8.** (a) the cycling performance of half-cells of silicon fiber slurries and direct-deposit electrospays. Slurries were kept at 0.1 A/g while AC-electrosprayed anodes show 0.1 and 1 A/g cycling. (b) The 1<sup>st</sup> cycle coulombic efficiency (CE) of cells tested.
- Figure 3.9.** Cycling performance of Si:RGO, Si:RGO:MWCNT, and HF-washed Si:RGO anodes prepared by the direct-deposit AC-electrospray method. Half-cells are tested for 5 cycles at 0.1 A/g and then 95 cycles at 1 A/g. Coulombic efficiency is charted for the HF-washed Si anode.
- Figure 3.10.** Rate capability of direct-deposit Si:RGO, Si:RGO:MWCNT, and HF-washed Si:RGO anodes from 0.1 A/g to 3 A/g.
- Figure 3.11.** SEM imaging: (a) and (b) show as spun PVP/TEOS/MWCNT samples. (c) fibers after calcination in air and (d) shows the air calcined fibers after Mg reduction. (e) precursor fibers after carbonization under N<sub>2</sub> environment and (f) shows the N<sub>2</sub> carbonized fibers after Mg reduction.
- Figure 3.12.** XRD analysis of the MWCNTs compared to the Mg reduced silicon fibers containing MWCNT.
- Figure 3.13.** Half-cell cycling performance of silicon fibers with internal MWCNTs prepared in conventional slurries.
- Figure 4.1.** SEM images of AC-electrosprayed PAN solutions: (a) 1 wt% at 0.015 ml/min, (b) 2 wt% at 0.03 ml/min, (c-d) 3 wt% at 0.06 ml/min, and (e-f) 4 wt% at 0.06 ml/min.
- Figure 4.2.** SEM images of AC-electrosprayed PAN with: (a) 90:10 wt DMF:NMP, (b) 80:20 wt DMF:NMP, (c) 70:30 wt DMF:NMP.
- Figure 4.3.** BJH pore distribution plot for PAN:PEO electrospays (70:30 DMF:NMP solvent).
- Figure 4.4.** BJH pore distribution plots of 50:50 wt PAN:PEO electrospays with different solvent makeups.
- Figure 4.5.** SEM images showing (a) the surface and (b) the cross-section of 50:50 wt PAN:PEO electrospayed films with a 70:30 wt DMF:NMP solvent.
- Figure 4.6.** Images of asymmetric membranes. (a) and (b) are SEM images of the fiber layers of a PAN separator and an 80:20 PAN/OPSZ separator

respectively. (c) and (d) are photos of PAN fibers sprayed with a red dye PAN particle solution showing the electro sprayed and electro spun sides, respectively.

**Figure 4.7.** SEM images of the AC-electro sprayed layers of PAN/OPSZ asymmetric membranes. (a) is from a 70:30 PAN/OPSZ ratio. (b) and (c) are from an 80:20 PAN/OPSZ separator.

**Figure 4.8.** SEM images of PAN particle stacking by AC-electro spray on PAN fibers. (a) shows 2 ml of 3 wt% PAN sprayed. (b) shows 1 ml of 1 wt% PAN sprayed. (c) shows 5 ml of 3 wt% PAN sprayed and (d) zoomed view of the red rectangle in (c).

**Figure 4.9.** Rate capability performance of PAN fiber, PAN and PAN/OPSZ asymmetric, and Celgard separators given by (top) specific capacity and (bottom) rate retention compared to 0.1 C rate.

**Figure 4.10.** SEM of the AC-electro sprayed surface an 80:20 PAN:OPSZ asymmetric separators. (a) the first particles collecting on the fibers. (b) a surface view showing the uniform PAN/OPSZ layer. (c) a cross-section pic showing the fiber and spray layer. (d) a zoomed image of a thin spray layer showing how particles collect in between the interfiber pores.

**Figure 4.11.** Full cell cycling of 15-micron thick PAN/OPSZ asymmetric separators: (a) 0.2 C cycling, (b) rate capability testing.

**Figure 5.1.** (a) The chemical structure of P84 co-polyimide and (b) the chemical structure of OPSZ (Durazane 1500 Slow Cure). In the OPSZ structure, R = -H or -CH<sub>3</sub>.

**Figure 5.2** FTIR spectrum of (a) OPSZ precursor and the ceramic formed during curing, and (b) the electro spun separators. The inset of (b) magnifies the peaks of interest of heat treated OPSZ.

**Figure 5.3** SEM and TEM images of electro spun separators. SEM images are (a) PI, (b) 95:5 PI:OPSZ, and (c) 90:10 PI:OPSZ. TEM are (d) PI, (e) 95:5 PI:OPSZ and (f) 90:10 PI:OPSZ fiber cross sections.

**Figure 5.4** Separator thermal performance in (a) TGA isotherms and (b) DSC measurement in air environment (exo up).

**Figure 5.5** (a) Thermal shrinkage was measured after holding materials at different temperatures for 1 hour. The area lost after 1 hour has been plotted for each separator type. (b) Image of Celgard after holding at 140°C for 1

- hour; (c) image of 90:10 P84:OPSZ separator after holding at 450°C for 1 hour.
- Figure 5.6** Flame testing: (a) Separator samples before flame testing. (b) Samples placed in tray and soaked with electrolyte. (c) The electrolyte is lit on fire. (d) Separator conditions post flame testing.
- Figure 5.7** (a) Nyquist plot from EIS of the SS-symmetrical cells with three layers of PI, 95:5 PI:OPSZ, 90:10 PI:OPSZ, and Celgard separators (b) Results of rate capability tests for the NCM811/graphite full cells with various separator membranes. Discharge rates reach 4C while charge rates are limited to 1C in cell tests.
- Figure 5.8** (a) and (b) show the cycling performance comparison of the PI, PI/OPSZ, and Celgard separators at (a) 0.5C and (b) 1C rates in NCM811/graphite full cells.
- Figure 5.S1** FTIR spectra of high-OPSZ content film (60:40 PI:OPSZ) versus electrospun PI and 90:10 PI:OPSZ.
- Figure 5.S2** A wettability comparison of Celgard and 90:10 P84:OPSZ. The picture is taken a few seconds after placing a drop of electrolyte on each separator.
- Figure 5.S3** (a) TGA and (b) DSC of dried-only PI and dried-only 90:10 PI:OPSZ samples compared to heat treated 90:10 PI:OPSZ (exo up).
- Figure 5.S4** Plot of areal shrinkage vs. holding temperature (1 hour) for dried, never heat treated, PI and PI:OPSZ separators.
- Figure 5.S5** Flame testing of dried, never heat-treated, PI and PI:OPSZ separators. (a) Samples before testing, (b) picture mid-test of electrolyte fire, and (c) post-electrolyte fire showing only the PI separator remained.
- Figure 6.1** (a) The chemical structure of P84 co-polyimide and (b) the chemical structure of the ladder-like polysilsesquioxane.
- Figure 6.2** TGA/DSC of the LPSQ precursor.
- Figure 6.3** FTIR spectra of the LPSQ precursor at different stages of curing. The inset is a magnified look at peaks of interest.
- Figure 6.4** XRD of the LPSQ precursor after varied heat treatments.

- Figure 6.5** (a) Solubility testing of LPSQ after different levels of thermal treatment and (b) LPSQ samples after testing in electrolyte.
- Figure 6.6** SEM imaging of PI/LPSQ separators. (a, b, c) PI/LPSQ samples after electro spray coating and before heat treatment of 0.055, 0.110, and 0.220 mg/cm<sup>2</sup> coatings, respectively. (d, e, f) PI/LPSQ samples after heat treatment of 0.055, 0.11, and 0.22 mg/cm<sup>2</sup> coatings, respectively. (g) PI fibers from reverse side of PI/LPSQ samples. (h) Cross-section of 0.11 mg/cm<sup>2</sup> electro sprayed sample and (i) 0.22 mg/cm<sup>2</sup> electro sprayed sample.
- Figure 6.7** Pore distribution comparison of PI fibers and 0.22 mg/cm<sup>2</sup> LPSQ-coated fibers.
- Figure 6.8** Thermal shrinkage was measured after holding materials at different temperatures for 1 hour. The area lost after 1 hour has been plotted for each separator type.
- Figure 6.9** Flame testing: (a) Separator samples before flame testing. (b) Samples placed in tray and soaked with electrolyte. (c) The electrolyte is lit on fire. (d) Separator conditions post flame testing.
- Figure 6.10** Nyquist plot from EIS of the SS-symmetrical cells with three layers of separators comparing the LPSQ-coated and Celgard separators.
- Figure 6.11** Results of rate capability tests for the NCM811/graphite full cells with various separator membranes. Discharge rates reach 4C while charge rates are limited to 1C in cell tests.
- Figure 6.12** Cycling performance comparison of the PI, LPSQ-coated PI, and Celgard separators at (top) 0.5C and (bottom) 1C rates in NCM811/graphite full cells.

## LIST OF TABLES

- Table 2.1.** Summary of fiber diameters for PAN and PVP carbonized fibers.
- Table 2.2.** Summary of BET data for PAN carbonized fibers. Microporous area refers to surface area provide by pores 2 nm or smaller.
- Table 2.3.** Summary of BET data for PVP carbonized fibers. Microporous area refers to surface area provide by pores 2 nm or smaller.
- Table 2.4.** Summary of conductivity data provided by four-point probe measurement for PAN and PVP carbonized fiber mats.
- Table 2.5.** Summary of BET data for PAN and PAN/Super P carbonized fibers at 1000°C.
- Table 2.6.** Summary of BET data for Super P, PVP carbon nanofibers and PVP/Super P carbon nanofibers fibers at 1000°C.
- Table 2.7.** Conductivity measurements for PVP and PAN carbon fibers with Super P added. Super P wt% reported is compared to the total weight of polymer in solution.
- Table 2.8.** BET summary of carbonized PAN and 17 wt% PAN/AAI fibers.
- Table 2.9.** BET summary of air activation of carbonized PAN fibers.
- Table 2.10.** Four-point probe testing of carbonized PAN/MnAcac/GNR fiber sheets for conductivity analysis.
- Table 3.1.** Suspension preparations for GO/Si fiber AC-electrospraying solutions.
- Table 3.2.** Summary of BET data for silica and silicon fibers. Microporous area refers to surface area provided by pores 2 nm or smaller.
- Table 3.3.** Summary of specific capacity and rate retention data of Figure 3.10 broken down by sample and current density.
- Table 3.4.** Fiber diameters of silica with MWCNT fibers at different stages of processing.
- Table 4.1.** Summary of AC-electrosprayed PAN solutions.

- Table 4.2.** BET summary for PAN:PEO electrospays (70:30 DMF:NMP solvent).
- Table 4.3.** BET summary for 50:50 wt PAN:PEO electrospays with different solvents.
- Table 5.1.** Fiber diameter, density, porosity, and electrolyte uptake of electrospun separator membranes.
- Table 5.2.** Physical properties of separators and their ionic conductivities calculated from EIS.
- Table 6.1.** LPSQ areal loading by spray time.
- Table 6.2.** Porosity, mean pore size, and electrolyte uptake of PI fiber and ACES coated separators.
- Table 7.1.** PI nanofiber materials strength comparison.

## LIST OF ABBREVIATIONS

ACES	Air-Controlled Electro spraying
EV	Electric Vehicle
SEM	Scanning Electron Microscopy
TEM	Transmission Electron Microscopy
FTIR	Fourier Transform Infrared Spectroscopy
TGA	Thermogravimetric Analysis
DSC	Differential Scanning Calorimetry
XRD	X-ray Diffraction
EIS	Electrochemical Impedance Spectroscopy
DMF	N, N-Dimethylformamide
LiPF <sub>6</sub>	Lithium Hexafluorophosphate
EC	Ethylene Carbonate
DEC	Diethyl Carbonate
DMC	Dimethyl Carbonate
OPSZ	Organopolysilazane
PDC	Polymer Derived Ceramic
PSSQ	Polysilsesquioxane
LPSQ	Ladder-Like Polysilsesquioxane
PAN	Polyacrylonitrile
PI	Polyimide
CTC	Charge Transfer Complex
PO	Polyolefin
PE	Polyethylene

# CHAPTER 1

## INTRODUCTION

### *1.1 Electrochemical Energy Storage*

A major challenge facing researchers today is how to store energy and use it efficiently. Electricity can be generated from many different sources including fuel-burning, solar power, nuclear power, wind power, and others, and the electricity generated is indispensable in all parts of our lives. Energy storage becomes more and more important with the continued demands for more electricity and the increasing diversity of energy sources. Applications ranging from batteries in our portable electronics or electric vehicles, to storage devices attached to alternative energy sources, to even grid-sized storage requires increased performance beyond what current energy storage devices can provide. High performance energy storage devices capable of efficient, versatile uses are becoming increasingly desirable [1].

Electrochemical energy storage is one of the main areas of focus for improving energy storage. Electrochemical energy storage includes all systems that store electricity in a chemical form, such as batteries, supercapacitors, fuel cells and flow batteries. These systems share several common features: energy-providing processes take place at an electrode/electrolyte interface, and electron and ion transport are separated [2].

To improve these systems, researchers have looked to nanostructured materials [3,4]. Nanostructured materials have many improved properties owing to their reduced dimensions and increased surface area to volume ratio. This is particularly useful in

electrochemical devices that feature interactions at surface interfaces to improve charge transport and reaction rates. Conventionally, nanomaterials have been produced by bottom-up approaches such as growth processes or template synthesis, but these have proven expensive and hard to scale. Use of a top down approach, such as electrospinning or electrospraying, could be used for simple, cost-effective fabrication of nanofibers.

### ***1.2 Electrospinning and Electrospraying***

Materials structured at the micron and nanoscale are essential to the development of energy storage electrodes and separators. Decreasing one or more dimensions to a micron or sub-micron level gives increased functionality due to increased surface area to volume ratio. One of the simplest and most scalable ways to form nanomaterials is electrospinning. Electrospinning is a process that creates high aspect ratio, continuous fibers from an electrically charged jet of polymer solution or polymer melt. The fibers range in diameters from a few microns down to a few nanometers [5]. Nanofibers from electrospinning have been applied to diverse, global issues including energy storage, healthcare, biotechnology, sensors, and environmental engineering [6, 7].

Significant interest in electrospinning came long after its discovery. The first patents utilizing electric spinning were granted in the early 1900s. J.F. Cooley, W.J. Morton, and Anton Formhals all hold patents for producing artificial threads using an electric field, but none understood why it occurred [8 - 10]. In 1964, Sir George Taylor published the mechanism showing how electric spinning worked through the

Taylor cone [11], which refers to the observed cone shape of the polymer solution from which a jet of charged particles projects out as a drawn fiber (electrospinning) or as a plume of droplets (electrospraying). Even with this understanding, it was not until the 1990s that electric spinning took off with the scientific community; Doshi and Renneker modernized the process and suggested several commercial uses for the fibers [12]. They also coined the term “electrospinning” and the method became more and more popular as a facile method to form sub-micron scale materials.

A basic electrospinning setup requires few materials: a syringe pump, a metal capillary, a high voltage source, and a grounded collector plate. In most cases, a polymer solution is pumped through a small stainless steel nozzle that is attached to the high voltage source (Fig. 1.1). The high voltage source gives the polymer solution particles charge, creating a repulsive force. With enough applied voltage, the repulsive force overcomes the surface tension of the polymer solution and a jet emanates towards the grounded collector. The jet is only stable near the tip of the needle. Due to repulsion of charged ions, the jet undergoes stretching and whipping known as bending instability [13, 14]. As solvent evaporates and polymer chains entangle, continuous, solid fibers are fabricated that form a non-woven mat at the grounded collector. The nanofiber mat can be used readily as a freestanding sheet with high porosity and high specific surface area.

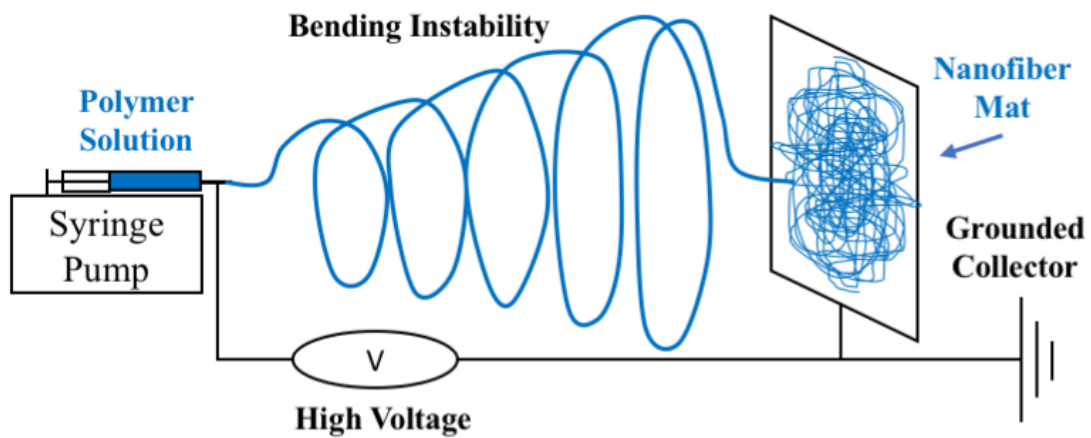


**Fig. 1.1.** Depiction of electrospinning process.

Electrospraying is a method of liquid atomization driven by electrical forces. It is in many ways the same process as electrospinning except instead of very fine fiber formation, the process is used to form droplets in the micron to submicron range. Much like electrospinning, electrospraying has been used for wide-ranging applications including thin film deposition, micro- and nanoparticles, pharmaceuticals, biotechnology, and energy storage [15-17]. Electrospraying uses the same setup as electrospinning: a syringe pump, a metal capillary, and a high voltage source. An applied voltage forms a Taylor cone and a jet is ejected. The two methods differ noticeably in the solution preparation. In general, electrospinning requires a high concentration solution of high molecular weight polymer to achieve the polymer chain entanglement needed for fiber formation. Electrospraying can be done with a dilute polymer solution, low molecular weight polymer in solution, or a suspension of particles void of polymer so that many different materials can be prepared with or without polymer.

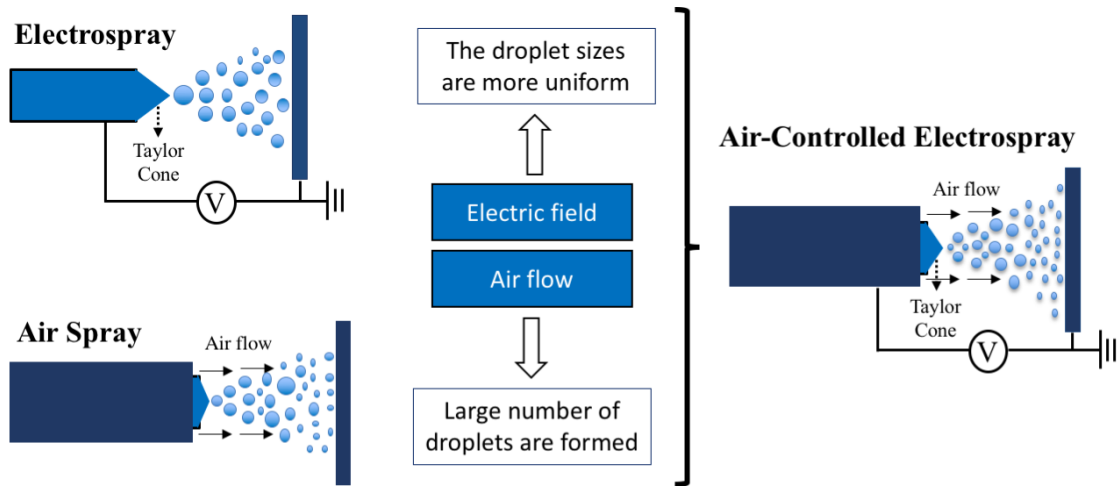


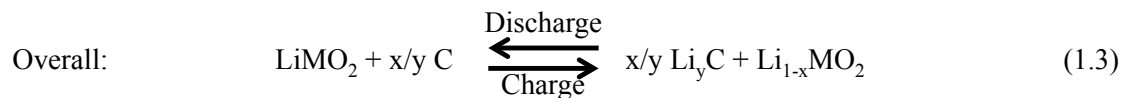
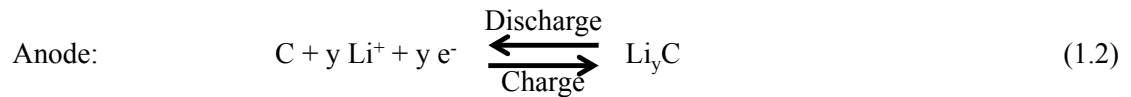
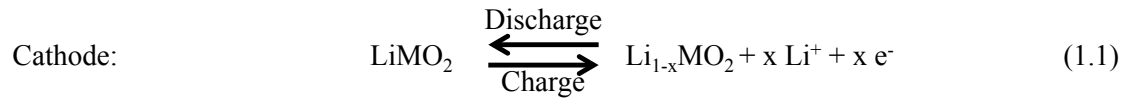
**Fig. 1.2.** Depiction of electro spraying, air spraying, and air-controlled electro spray processes.

Many conventional spraying systems utilize air flow to atomize solutions for droplet formation. The Joo group has worked recently with a combination of the two processes, utilizing both the electric field of electro spraying and the airflow of air spraying to create a process called air-controlled electro spraying (ACES). As depicted in Fig. 1.2, ACES uses two driving forces for atomization that together provides greater droplet formation with more uniform size distribution. ACES has been utilized for energy storage providing vast performance improvements for battery electrodes [18-22]. This thesis will further explore using combinations of electro spinning and ACES to address energy storage, and in particular, energy storage in lithium-ion batteries.

### ***1.3 Lithium-Ion Batteries***

Since their initial commercial release by Sony in the early 1990s, lithium-ion batteries have taken over the rechargeable battery industry due to their high energy

density, excellent rate capability, and high cycle life [23]. The batteries make use of lithium intercalating compounds for the anode and cathode. Graphite is typically used for the anode, though there is interest in incorporating silicon to improve the anode's capacity. The cathodes are typically Li metal oxides, including lithium cobalt oxide (LCO), lithium manganese oxide (LMO), lithium iron phosphate (LFP), lithium nickel cobalt aluminum oxide (NCA), and lithium nickel manganese cobalt oxide (NMC). LCO has been the favored cathode material since the first commercial batteries were produced, but due to the increasing cost of cobalt, blended cathode materials like NMC and NCA have gained more attention and are now the favored candidates for electric vehicle powertrains. The batteries charge and discharge as lithium ions transfer between the graphite and lithium metal oxide ( $\text{LiMO}_2$ ) host structures [24]:



In addition to electrode materials, Li-ion batteries cells contain a separator and an electrolyte. The separator is a porous membrane between the electrodes that prevents physical contact of electrodes and short circuiting but allows Li-ions to flow through. The most common separators are microporous polyolefin films including polypropylene (PP) and polyethylene (PE) membranes [25]. Li-ion battery liquid electrolytes consist of a lithium salt in an organic solvent. The most common salt used is lithium hexafluorophosphate ( $\text{LiPF}_6$ ) [26]. It is typically dissolved in ethylene

carbonate (EC) and a mix of one or more linear carbonate cosolvents such as diethyl carbonate (DEC), dimethyl carbonate (DMC), and ethyl methyl carbonate (EMC). EC-based solvents are excellent for battery use as they have high ionic conductivity, low viscosity, and form a protective, solid electrolyte interface (SEI) layer on graphite anodes. The SEI layer prevents sustained electrolyte decomposition and graphite exfoliation during battery cycling. A depiction of a discharging Li-ion battery is shown in Fig 1.3.

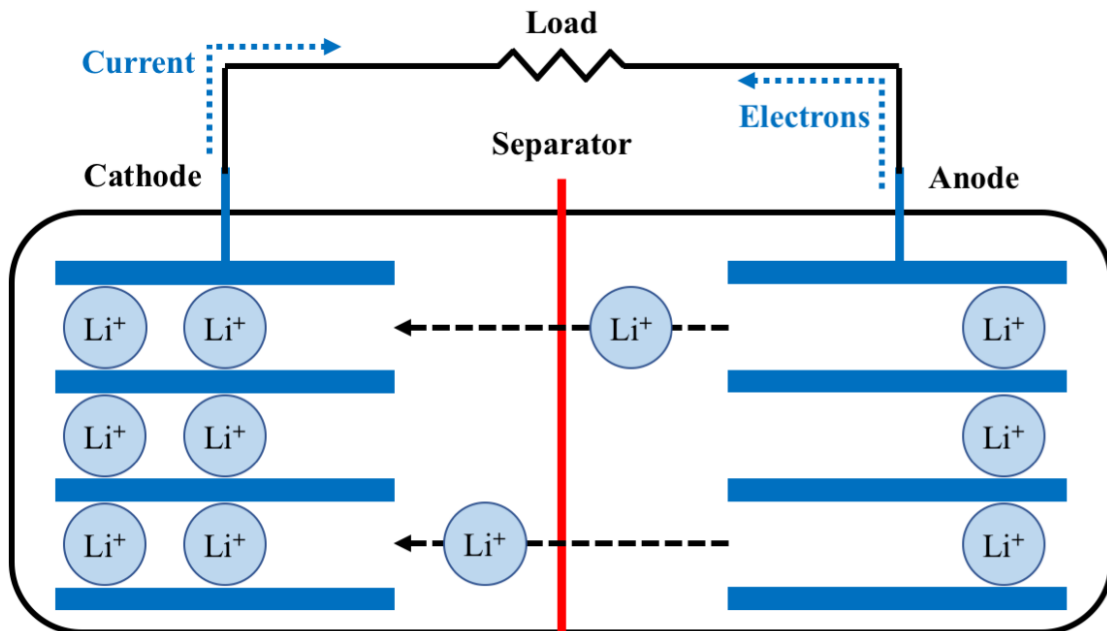


**Fig. 1.3.** Depiction of lithium-ion battery discharge.

From Sony's first Li-ion battery in 1991, the Li-ion market grew to \$2 billion in 2010 [27]. Li-ion batteries have taken over portable devices like cell phones, laptops, and digital cameras. Their use has expanded to other industries including hybrid and electric vehicles and as electrochemical energy storage for renewable energy sources. There are several limitations of current Li-ion batteries that need to be addressed as they move to these larger applications. In portable electronic devices, the

lithium-ion battery is generally the largest component. This becomes more problematic for electric vehicles, making improving energy density a priority for increasing driving range. This can be done by using higher capacity chemistries, such as silicon, or by optimizing current batteries and using more of the battery volume for capacity by making thicker electrodes and thinner separators.

The push for thinner separators is at odds with another limitation of Li-ion batteries – battery safety. There have been several high-profile examples of safety issues stemming from Li-ion batteries. The Samsung Galaxy Note 7 phone is a great example of how poor battery design and manufacturing can turn a small, portable device into a fire-causing hazard [28]. In trying to maximize volume of the battery, Samsung used a dangerously thin separator. Coupled with manufacturing flaws, the separator failed, and the batteries faced thermal runaway, fires, and explosive failures. Preparing larger packs of Li-ion batteries for vehicles magnifies the problem and safety has to be taken even more seriously, as exemplified by Boeing Dreamliner battery failures. In 2013, two Dreamliner planes had battery fires and all Dreamliner airplanes had to be grounded due to battery issues [29]. The batteries that caught fire could not be put out with the fire extinguishers on the plane, and even after the blazes were extinguished, the batteries still gave off heat and rekindled. Tesla electric vehicles have faced scrutiny, as they have a higher rate of fire death than internal-combustion-engine vehicles [30]. While we design batteries with enough energy capacity to take on long drives and replace internal-combustion engines, we must be careful to design batteries that do not introduce even more hazards or threat to human safety.

#### ***1.4 Thesis Motivation and Scope of Work***

Electrospinning and electrospraying are among the only top down approaches for the preparation of nanostructured materials. Functionality can be added with different polymers and inorganic materials like silica and silicon to achieve many different properties. Using scalable methods with cost effective, inorganic precursors, and not pre-formed nanoparticles, offer a solution to improve energy storage systems performance and safety. Both electrospinning and electrospraying also offer opportunities for direct deposit and immediate application of active materials, circumventing many of the processing steps associated with conventional material preparation. Finally, by combining electrospinning and electrospraying, several new architectures of materials can be achieved that can overcome limitations seen in pure electrospinning or electrospraying methods.

Chapter 2 focuses on an alternative method for electrode preparation instead of conventional casted slurries. In this work, we use electrospun fibers in their non-woven, continuous fiber form as freestanding sheets for direct application as electrodes. This process also does not use binders or additives and can form electrodes with only electrospinning and heat treatment. We first show how several carbon precursors can be used to form freestanding carbon fiber sheets by use of ceramic plates during heat treatment. It is shown that conductivity of the materials can be improved with addition of different conductive carbon materials, such as Super P and graphene nanoribbons, as well as through more aggressive heat treatments. We then expand into composite materials by using metal precursors in our polymer solutions.

First, a carbon/iron oxide fiber from a previous Joo group paper is remade as a free-standing sheet. Then carbon and carbon/Mn<sub>3</sub>O<sub>4</sub> fibers are prepared as electrodes for supercapacitor application.

In chapter 3, electrospinning and air-controlled electrospaying are used to prepare an RGO/silicon fiber direct-deposit anode. First, silica fibers are prepared by electrospinning. Silica fibers are reduced to silicon fibers using an established magnesium reduction and wash process. Electrospinning yields a uniform diameter of 1 to 2 micron diameter silicon fibers. Research has traditionally focused on nanoscale fibers and particles due to pulverization effects from alloying reactions that are mitigated at such small scale. However, there has been recent interest in micron silicon due to its improved 1<sup>st</sup> coulombic efficiencies, or decreased irreversible losses in the first cycle. Electrodes structured to permit for silicon expansion can improve cycle stability for micron-sized materials. A binder-free, conductive network is formed around the fibers by a direct-deposit method using air-controlled electrospaying of graphene oxide sheets with the micron-size silicon fibers. The direct-deposit method is water-based and avoids the use of polymer binders and the processing steps seen in conventional slurry casting. The graphene oxide sheets form protective layers that sandwich in silicon fibers while allowing for silicon expansion during lithiation. We show that there is possibility for micron silicon use in this system and discuss possible future improvements to address issues in performance.

In chapters 4, 5, and 6 we switch from electrode preparation to forming separators for Li-ion batteries with a strong focus on safety. In chapter 4, air-controlled electrospaying is used to form a dense, tortuous coating onto existing

electrospun, non-woven membranes. Polyacrylonitrile (PAN)/OPSZ fibers were previously studied by the Joo group and this work looks at coating an additional PAN/OPSZ layer onto the fiber framework. The pore-size of the non-woven membrane is decreased to avoid issues of short-circuiting while maintaining the high rate capability of PAN/OPSZ fiber separators.

Chapters 5 and 6 address thermal stability and flammability of separators to reduce the fire-related hazards seen in battery applications. Chapter 5 looks at the effect of moving from a PAN system to polyimide (PI) hybrid separators with OPSZ. It is shown that heat treatment of the hybrid fibers forms a flame-resistant material with excellent battery performance. In chapter 6, an electrospun PI nanofiber mat is coated by air-controlled electro spraying with a ladder-like polysilsesquioxane (LPSQ). This process separates the ceramic addition from the spinning process providing more flexibility in material choices. The ceramic provides improvements to thermal stability and flame resistance while reducing the large pore size of the electrospun framework and significantly improving battery safety without compromising ion transport and rate capability of the battery.

Finally, chapter 7 discusses several ways we could build on these unique electrospinning and electro spraying methods for use in new applications or for added functionality and performance. The methods developed here could have immediate use in separate application or be applied to logical next steps in improving material processes for energy storage applications.

## 1.5 References

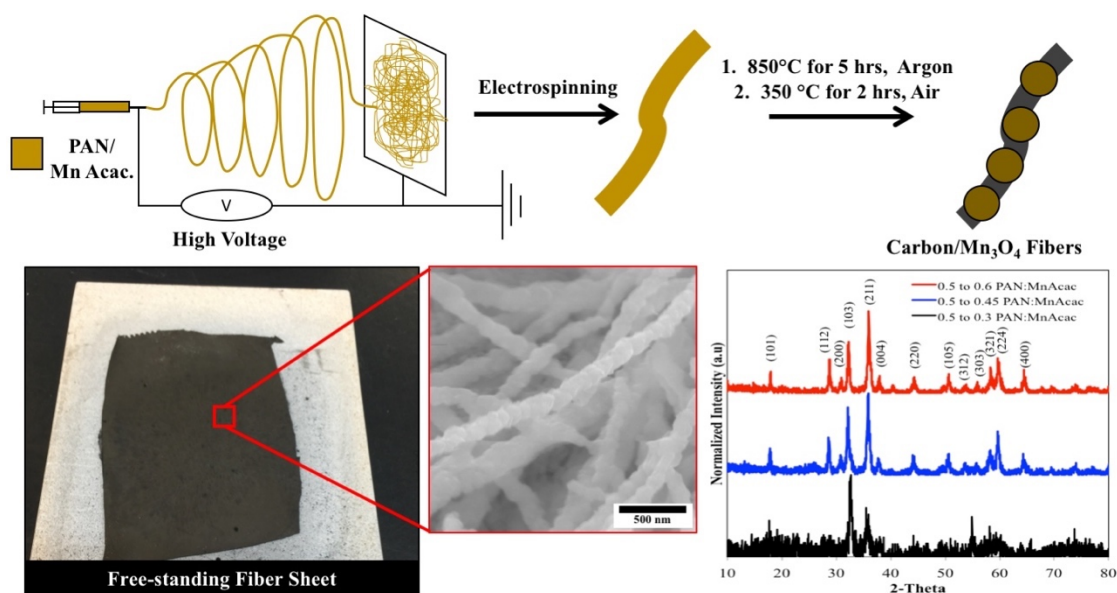
- [1] Liu, C., Li, F., Ma, L.-P. & Cheng, H.-M. Advanced Materials for Energy Storage. *Adv. Mater.* **22**, E28–E62 (2010).
- [2] Winter, M. & Brodd, R. J. What Are Batteries, Fuel Cells, and Supercapacitors? *Chem. Rev.* **104**, 4245–4270 (2004).
- [3] Zhang, X., Cheng, X. & Zhang, Q. Nanostructured energy materials for electrochemical energy conversion and storage: A review. *Journal of Energy Chemistry* **25**, 967–984 (2016).
- [4] Cavaliere, S., Subianto, S., Savych, I., Jones, D. J. & Rozière, J. Electrospinning: designed architectures for energy conversion and storage devices. *Energy Environ. Sci.* **4**, 4761 (2011).
- [5] Greiner, A. & Wendorff, J. H. Electrospinning: A Fascinating Method for the Preparation of Ultrathin Fibers. *Angew. Chem. Int. Ed.* **46**, 5670–5703 (2007).
- [6] Bhardwaj, N. & Kundu, S. C. Electrospinning: a fascinating fiber fabrication technique. *Biotechnology advances* **28**, 325–347 (2010).
- [7] Ramakrishna, S., Fujihara, K., Teo, W.-E., Yong, T., Ma, Z., & Ramaseshan, R. Electrospun nanofibers: solving global issues. *Materials Today* **9**, 40–50 (2006).
- [8] Anton, F. Process and apparatus for preparing artificial threads. US 1,975,504 (1934).
- [9] Cooley, J. F. Apparatus for electrically dispersing fluids. US 692,631 (1902).
- [10] Morton, W. J. Method of dispersing fluids. US 705,691 (1902).
- [11] Taylor, G. Disintegration of Water Drops in an Electric Field. *Proceedings of the Royal Society A: Mathematical, Physical and Engineering Sciences* **280**, 383–397 (1964).
- [12] Doshi, J. & Reneker, D. H. Electrospinning process and applications of electrospun fibers. *Journal of Electrostatics* **35**, 151–160 (1995).
- [13] Reneker, D. H., Yarin, A. L., Fong, H. & Koombhongse, S. Bending instability of electrically charged liquid jets of polymer solutions in electrospinning. *J. Appl. Phys.* **87**, 4531–4547 (2000).
- [14] Yarin, A. L., Koombhongse, S. & Reneker, D. H. Bending instability in electrospinning of nanofibers. *J. Appl. Phys.* **89**, 3018–3026 (2001).
- [15] Jaworek, A. Electro spray droplet sources for thin film deposition. *J Mater Sci* **42**, 266–297 (2006).
- [16] Jaworek, A. Micro- and nanoparticle production by electro spraying. *Powder Technology* **176**, 18–35 (2007).
- [17] Yurteri, C. U., Hartman, R. P. A. & Marijnissen, J. C. M. Producing Pharmaceutical Particles via Electro spraying with an Emphasis on Nano and

- Nano Structured Particles - A Review. *KONA Powder and Particle Journal* **28**, 91–115 (2010).
- [18] Fei, L., Yoo, S. H., Villamayor, R., Williams, B., Gong, S. Y., Park, S., Shin, K., & Joo, Y. L. Graphene Oxide Involved Air-Controlled Electro spray for Uniform, Fast, Instantly Dry, and Binder-Free Electrode Fabrication. *ACS Applied Materials & Interfaces* **9**, 9738–9746 (2017).
- [19] Lee, J., Ko, B., Kang, J., Chung, Y., Kim, Y., Halim, W., Lee J. H., & Joo, Y. L. Facile and scalable fabrication of highly loaded sulfur cathodes and lithium–sulfur pouch cells via air-controlled electro spray. *Materials Today Energy* **6**, 255–263 (2017).
- [20] Lee, J. H., Kang, J., Kim, S. W., Halim, W., Frey, M. W., & Joo, Y. L. Effective Suppression of the Polysulfide Shuttle Effect in Lithium– Sulfur Batteries by Implementing rGO–PEDOT:PSS-Coated Separators via Air-Controlled Electro spray. *ACS Omega* **3**, 16465–16471 (2018).
- [21] Halim, W., Lee, J. H., Park, S. M., Zhang, R., Sarkar, S., O’Neil, T., Chiang, E., & Joo, Y. L. Directly Deposited Binder-Free Sulfur Electrode Enabled by Air- Controlled Electro spray Process. *ACS Applied Energy Materials* **2**, 678–686 (2019).
- [22] Divvela, M. J., Zhang, R., Zhmayev, Y., Pinge, S., Lee, J. H., Kim, S. W., & Joo, Y. L. Control of formation of viscoelastic droplets and distribution of nano-inclusions in functional deposition for lithium–sulfur batteries. *Soft Matter* **15**, 6485–6494 (2019).
- [23] Armand, M. & Tarascon, J.-M. Building better batteries. *Nature* 1–6 (2008).
- [24] Reddy, T. & Linden, D. *Linden's Handbook of Batteries*. 4th ed., McGraw-Hill (2010).
- [25] Arora, P. & Zhang, Z. J. Battery Separators. *Chem. Rev.* **104**, 4419–4462 (2004).
- [26] Xu, K. Nonaqueous Liquid Electrolytes for Lithium-Based Rechargeable Batteries. *Chem. Rev.* **104**, 4303–4418 (2004).
- [27] Deimede, V. & Elmasides, C. Separators for Lithium-Ion Batteries: A Review on the Production Processes and Recent Developments. *Energy Technology* **3**, 453–468 (2015).
- [28] Mosur, P. Galaxy Note 7 Fires Caused by Battery and Design Flaws, Samsung Says. *The New York Times* (2017). Available at <https://www.nytimes.com/2017/01/22/business/samsung-galaxy-note-7-battery-fires-report.html>. (Accessed 11<sup>th</sup> November 2019)
- [29] Irfan, U. How Lithium Ion Batteries Grounded the Dreamliner. *Scientific American* (2014). Available at: <https://www.scientificamerican.com/article/how-lithium-ion-batteries-grounded-the-dreamliner/>. (Accessed 11<sup>th</sup> November 2019)

[30] Lopez, L. Life, death, and spontaneous combustion - here's why the debate about Tesla fires just got more fierce. *Business Insider* (2019). Available at: <https://www.businessinsider.com/why-tesla-cars-catch-on-fire-2019-4>. (Accessed 11<sup>th</sup> November 2019)

## CHAPTER 2

### ELECTROSPUN, FREESTANDING CARBON AND COMPOSITE NANOFIBER ELECTRODES FOR ENERGY STORAGE APPLICATIONS



#### Graphic Abstract

**Abstract:** Conventional electrode preparations utilize active material in casted slurries with conductive additive and polymer binder. This takes multiple processing steps, uses toxic solvent, and the added fillers decrease the concentration of active material in the casted electrode. Through electrospinning of polymer solutions we formed freestanding carbon fiber and all-carbon composite substrates with tunable conductivity, carbonizing precursor, and pore structure that can be used in application for energy storage. Additionally, in two examples, metal precursors are added to the spinning solution to form carbon/metal oxide nanofiber composites. To test the freestanding fabrication, we formed activated carbon and carbon/Mn<sub>3</sub>O<sub>4</sub> fiber sheets

and we attempted to use those for binder-free supercapacitor electrodes. In freestanding and slurry casted preparations, the electrodes showed poor performance in supercapacitor coin cells testing due to limitations of cell testing. The fabrication technique has proven successful outside of this work.

## ***2.1 Introduction***

While there has been a heavy focus on the development of high capacity batteries for use in portable electronics and electric vehicles, there is also a need for energy storage that can provide high power. Supercapacitors provide higher power and longer cycle life than batteries can, with some supercapacitors maintaining capacity for more than 10,000 cycles [1]. These could work in parallel with energy storage that has higher capacities and lower power, such as Li-ion batteries, where power from a supercapacitor could be provided for a few minutes to alleviate short term disturbances.

Supercapacitors fall into two classes: electrochemical double-layer capacitors (EDLC) and pseudocapacitors [2]. EDLCs function by non-faradic charge separation, or energy stored at an electrode's surface. With their capacitance directly linked to available surface area, EDLCs rely on high specific-surface area nanoporous materials, generally greater than 1000 m<sup>2</sup>/g [3]. Many different carbon materials are used as active materials for EDLC due to their conductivity and availability, including activated carbons [4-6], carbon aerogels [7], carbon nanotubes [8-10], and graphene [7,11]. Activated carbons are the most widely used active material due to their high surface area and relatively low cost and can be obtained from a variety of carbon-rich

organic precursors or polymers. After carbonization and activation, specific surface areas can reach 1000-3000 m<sup>2</sup>/g and capacitance of 100-200 F/g. Carbon nanotubes and graphene exhibit excellent conductivity and can be used as stand-alone electrode materials. However, due to their difficult fabrication processes and higher cost, they are more likely to be used in (1) all-carbon composite materials where they are inserted into an activated carbon matrix to improve the electrochemical performance or (2) used in hybrid materials as a conductive framework where pseudocapacitive functionalization is added to their structure for high capacitance [12].

Pseudocapacitors, in contrast to EDLCs, utilize quick redox reactions to store energy. Where the EDLC only involves rapid charge rearrangement and there is not a chemical reaction, pseudocapacitors' reliance on redox kinetics decreases the response rate of the capacitor [13]. The redox couples improve the capacitance but at a penalty to power. The redox couples are generally metal oxides, such as transition metal oxides including RuO<sub>2</sub> [14-15], Co<sub>3</sub>O<sub>4</sub> [16-17], NiO [18-19], and Fe<sub>3</sub>O<sub>4</sub> [20], or conducting polymers, such as polypyrrole or PEDOT [2, 21]. This work focuses on the use of manganese oxide as a promising supercapacitor material. Manganese oxides have been widely used due to their low cost, they are more environmentally friendly than other transition metal oxide systems, and they have a high theoretical specific capacitance [22-26]. Compared to the 100-200 F/g specific capacitance seen in EDLCs, the manganese oxides achieve more than 300 F/g, and at lower power, can achieve more than twice that. Like other metal oxides, they are resistors and have poor charge transport properties. More often, hybrid materials of carbon and manganese oxide are prepared. The conductivity of carbon and the high capacitance of manganese

oxide are used together to achieve high power and high energy density. In preparing hybrid electrodes (and EDLC electrodes) many report using a slurry casting process. Slurry preparation requires mixing of a grounded powder with polymer binder and conductive agents in a toxic solvent. This slurry has to be sonicated, mixed, bladed, calendared, and dried to prepare an electrode. An ideal system would be one in which the metal material and carbon co-exist in a robust structure and there is no slurry needed. If a material could be made from a one-solution system without the need for slurry casting, the processing would be greatly simplified and the electrode mass would only be active material.

Electrospinning is a facile fiber-formation technique where fibers are extruded from a polymer solution when an electric field is applied. Electrospinning can be used with carbonizing polymers to produce submicron fibers, followed by thermal treatment (carbonization), as a simple, cost-effective process for fabricating self-supported sheets of carbon nanofibers [27]. Due to their conductive nature, natural porosity, and ease of use, electrospun carbon nanofibers have been applied in electrodes for electrochemical energy storage including Li-ion batteries [28-29] and supercapacitors [30-33]. Electrospinning is also a cost-effective, top-down approach for making nanostructured composites that can be prepared from precursors or nanoparticle inclusions into the electrospinning solution. At the time of writing, there are many examples of electrospun carbon fibers with added functionalization, including carbon nanotubes [34-35], graphene [36], RuO<sub>2</sub> [37], MnO<sub>x</sub> [22], Ni [38], and metal sulfides [39], which underscores the advantage of the electrospinning process for preparing electrode materials.

Herein we show a method for formation of freestanding, one-solution non-woven supercapacitor electrodes. Starting from electrospinning polymers for carbon nanofibers, this work explores several ways to tune carbon nanofiber properties and builds to composite fiber sheets for hybrid supercapacitor electrodes through several stages:

1. Form freestanding carbon fiber mats while varying the carbonizing polymer, conductive carbon inclusions, and heat treatment to control several important properties.
2. Take previous Joo group work with carbon/iron precursor fibers and apply them to form a freestanding magnetic carbon/iron oxide sheet.
3. Form new carbon/metal oxide composite material from precursor solutions for direct application as a supercapacitor electrode.

First, we will show preparation of carbon nanofibers from two different polymers polyacrylonitrile (PAN) and polyvinylpyrrolidone (PVP). PAN solutions are prepared with an organic solvent (DMF), while PVP can be prepared with ethanol or water, and the two polymers could be utilized to accommodate a wider range of precursors with varying solubilities. Two carbon conductive additives are spun into the fibers, Super P and graphene nanoribbons (GNRs), and the effect of their loading on the sheet conductivity and fiber morphology are examined. The importance of the carbonizing heat treatment and its temperature is also explored. In each case we observe the effects on the conductivity of the carbon fiber and the fiber's pore structure.

Secondly, composite, freestanding fiber sheets are made from metal precursors added to the electrospinning solution. Previous work by the Joo group formed

magnetic fibers with a carbon/iron oxide hybrid and we repeat that work without losing the easy-to-use sheet structure. With this proven, a new preparation of carbon/Mn<sub>3</sub>O<sub>4</sub> is prepared with conductive carbon inclusions intended to be used as a binder-free, freestanding fibrous electrode for supercapacitors. There is additional comment on how the fabrication technique was used successfully in other Joo group efforts.

## ***2.2 Experimental***

### **2.2.1 Carbon nanofibers from PAN and PVP for freestanding carbon fiber sheets**

Carbon nanofibers were first prepared from PAN polymer solutions. PAN (Sigma-Aldrich, 150,000 MW) was dissolved in N,N-Dimethylformamide (DMF, Sigma-Aldrich) to form 12 wt% solutions. Solutions were stirred on a hot plate at 50°C for 2 hours and then mixed by vortex to achieve a homogeneous solution. Solutions were electrospun using a 20-gauge needle, 15 cm distance with 18 kV applied, and a flow rate of 0.02 ml/min. The electrospun fibers were then placed in between two ceramic plates for heat treatment. The ceramic plates are very important to forming a freestanding sheet, because without something keeping the fibers flat during heat treatment the fibers tend to curl and shrivel up. The PAN fibers were then stabilized in air at 1°C/min to 260°C for 1 hour. Once stabilized, fibers were carbonized at several different temperatures under inert environment.

In addition to PAN, we also worked with PVP (Sigma-Aldrich, 1,400,000 MW). Electrospinning solutions were prepared by dissolving 10 wt% solutions of PVP in ethanol and stirring for 2 hours. Electrospinning parameters included a 20-gauge

needle, 15 cm distance with 11 kV applied, and a 0.02 ml/min flow rate. Thermal treatment for carbonization was done in three stages. Fibers were first stabilized at 1°C/min to 150°C in air for 24 hours. The stabilized fibers were then pre-oxidized at 1°C/min to 360°C for 4 hours in air. Carbonization was done at several temperatures under inert environment.

To enhance conductivity several carbon additives were mixed into the electrospinning solutions. Two additives were tested: carbon black Super P and graphene nanoribbons (GNRs, from EMD). Both carbons were added to polymer solutions and were first stirred for an hour, and then sonicated for 30 minutes to disperse the carbons in solution.

Characterization of the freestanding fiber sheets includes SEM imaging, conductivity, and surface area tests. SEM was used to examine fiber morphology and find average fiber diameter and was done using a combination of a LEICA 440 and a TESCAN MIRA scope with samples coated using an Au-Pd sputter coater. 4-point probe testing was used for conductivity testing. A Micrometrics Gemini VII analyzer was used for N<sub>2</sub> physisorption analysis for specific surface area and pore size distribution with BET and BJH analysis.

### **2.2.2 Carbon/Magnetite freestanding sheets**

Previous Joo group member, Dr. Jeanne Panels, synthesized magnetically active carbon nanofibers/iron oxide composites, and that work is followed for electrospinning solutions and conditions [40]. To form carbon/iron oxide fibers, first a solution of 10 wt% PAN was prepared in DMF. To this solution, iron (III)

acetylacetonate (Sigma-Aldrich, AAI) was added in a 1:5 wt ratio of precursor: PAN. The solution was stirred on a hot plate at 50°C for 2 hours and then mixed by vortex briefly to obtain a uniform solution. The PAN/AAI solution was electrospun using a 20-gauge needle, 15 kV, 15 cm distance, and a flow rate of 0.008 ml/min. The resulting nanofiber mats were placed between two ceramic plates and heated in air at 1°C/min to 250°C for 30 min and subsequently carbonized at 3°C/min to 850°C for 2 hours under Argon.

In addition to the earlier stated characterizations, XRD analysis was used to determine the crystal formations of the iron precursor. This was done using a Scintag, Inc. theta-theta diffractometer using a Cu target and a step size of 0.02°.

### **2.2.3 Supercapacitor electrodes from carbon and carbon/Mn<sub>3</sub>O<sub>4</sub> sheets**

To test our freestanding approach in application, two different sheets were prepared. First, we prepared an activated carbon sheet from our PAN carbonized fiber solutions. Secondly, we formed a hybrid supercapacitor using PAN based carbon fibers with manganese oxide crystals.

Activated carbon was prepared by sending our freestanding electrospun PAN fiber sheets from part 1 through an additional air thermal treatment. The fibers were placed in a furnace at 10°C/min up to 350°C and held there for 2 hours. This process burns away some of the carbon, creating new pores and increasing the size of existing pores.

Hybrid fibers of carbon with manganese oxide were then prepared from PAN solutions. 10 wt% PAN in DMF were stirred on a hot plate at 50°C for 2 hours. Then

manganese (II) acetylacetonate (Sigma-Aldrich, Mn(Acac)) was added to form 50:30, 50:45, and 50:60 wt ratios of PAN:MnAcac in solution. The solutions were stirred at room temperature until the precursor dissolved. 2 mL volumes were electrospun with a 20-gauge needle, at 15 cm with 20 kV applied, and a 0.02 ml/min flow rate. After electrospinning, the fibers were heat treated in a three-step process. Nanofiber mats were placed between two ceramic plates and first heated in air at 1°C/min to 250°C for 1 hour and subsequently carbonized at 2°C/min to 850°C for 5 hours under Argon. Finally, the hybrid fibers were treated in air at 10°C/min to 350°C and held for 2 hours to activate the carbon portion and to form the manganese oxide crystals.

Thermal gravimetric analysis (TGA) was used to determine carbon and manganese oxide contents in the fibers. The TGA was ramped to 1000°C under air to burn off carbon, with carbon yield determined by the weight lost. In addition to previously stated characterization techniques, the activated carbon and carbon/manganese oxide were prepared as electrodes to evaluate their capacitance. Freestanding electrodes were punched out from the activated nanofiber sheets and used as prepared. Casted electrodes were prepared by mixing active material, Super P, and polyacrylic acid (PAA, 400,000 MW, Sigma Aldrich) in an 80/10/10 wt ratio in N-methyl-2-pyrrolidone (NMP, Sigma Aldrich). Electrodes were cast using a doctor blade and dried in a vacuum oven before use. Supercapacitors were assembled in a symmetric coin cell with a Celgard 2400 separator in between [41]. The electrolyte used for testing was 1M tetraethylammonium tetrafluoroborate (TEABF<sub>4</sub>) in propylene carbonate. Cells were then cycled from 0 to 3 V at low scan rates of 1 and

10 mV/s. Capacitance values were calculated for the CV curves by dividing the current by the voltage scan rate:

$$C = I/(dV/dt) \quad (2.1)$$

Where C is the capacitance, I is the current, and dV/dt is the scan rate. Specific capacitance reported is the capacitance for one electrode.

## ***2.3 Results and Discussion***

### **2.3.1 Freestanding carbon and carbon composite nanofiber sheets**

The most important aspect of this work is to prepare flat sheets of carbonized nanofibers for use as electrodes. Electrospun polymer nanofibers have the tendency to curl or crumple during heat treatment and there is no way to make the fiber mat flat again after heat treatment. Calcining or carbonizing precursor sheets has previously led to fibers that could only be used in application if they were chopped up or ground into a powder for slurry casting. Our first focus was to find a way to prepare sheets of carbon fibers that had the same utility as the spun polymer fiber sheets.

We first worked with small samples, 1 inch by 1 inch, sandwiched between two ceramic plates. Sandwiching the fibers kept them from curling. Later, after successful trials at small scale, we increased size to preparation of 4 inch by 3 inch samples. This is not the limit of the method, but it was the limit of our controlled atmosphere furnace; this method should work at larger scales than what is presented here.

An important factor in keeping a freestanding sheet through the carbonization process is whether the sheet is free to shrink as polymer burns off. In our study, PAN carbonized at 1000°C showed a carbon yield of 43% from the polymer fiber while PVP carbonized at the same temperature had a carbon yield of 8% ,showing much higher burn off and removal from its fiber structure. In general, low yield carbonizing polymers, like PVP, shrink more during the carbonization. Using the two flat plates design allows the fiber sheet to shrink in the x-y plane of the plate, but it cannot curl, fold up, or corrugate. Earlier attempts at making flat electrodes used restraining clips or tension in an attempt to keep the fiber sheets flat, and these electrodes tended to crack and split during carbonization. Figure 2.1 depicts the issue of restrained carbonization. The sample sandwiched between ceramic plates was allowed to shrink in area and shows no signs of cracking or breaking across the electrode (Figure 2.1a). In the second trial, PAN fibers were electrospun to a rough, carbon felt to try and restrain the fiber sheet and maintain the original area. Instead of carbon felt coated in carbon nanofibers, the carbonized nanofibers have split in many locations due to stress from resisting shrinkage.

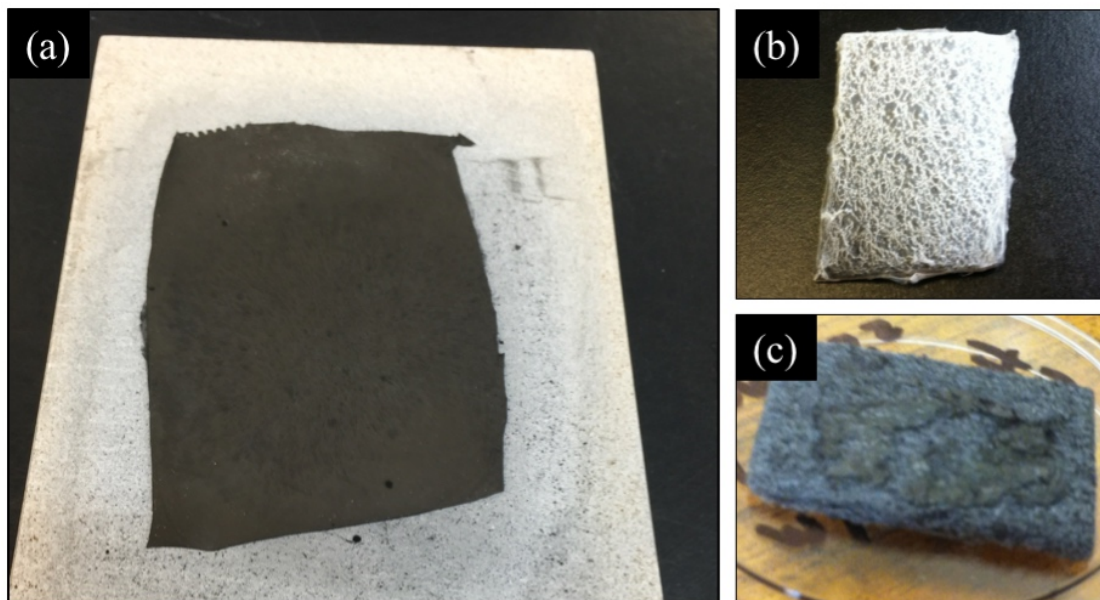


**Figure 2.1.** Pictures of carbon fiber trials showing (a) carbonized PAN fiber sheet formed between two ceramic plates, (b) PAN fibers electrospun to carbon felt (c) carbonized PAN fibers on carbon felt.

Using the ceramic plate method, we focused on the properties of the carbon fiber electrodes we could form and how the properties of the carbon sheets were affected by carbonization temperature. Two carbonizing polymers are shown here: PAN and PVP. They were chosen because they are easy to electrospin but have two different solvent types, providing flexibility in additional precursors or functional materials that could be dispersed in a carbon matrix. Samples were electrospun and then carbonized at temperatures ranging from 800°C to 1400°C and then fiber structure, conductivity, and pore structure were measured. Most trials used freestanding sheets with thicknesses of 100 microns. This is largely a matter of polymer loading and electrospinning time. Sheets have successfully been prepared in the range of 30-600 microns. While not examined in this work, thicker fiber mats could hold several advantages over casted slurries. Slurry casting works well with

thinner layers, but when trying to prepare higher thicknesses, the films tend to crack during drying.

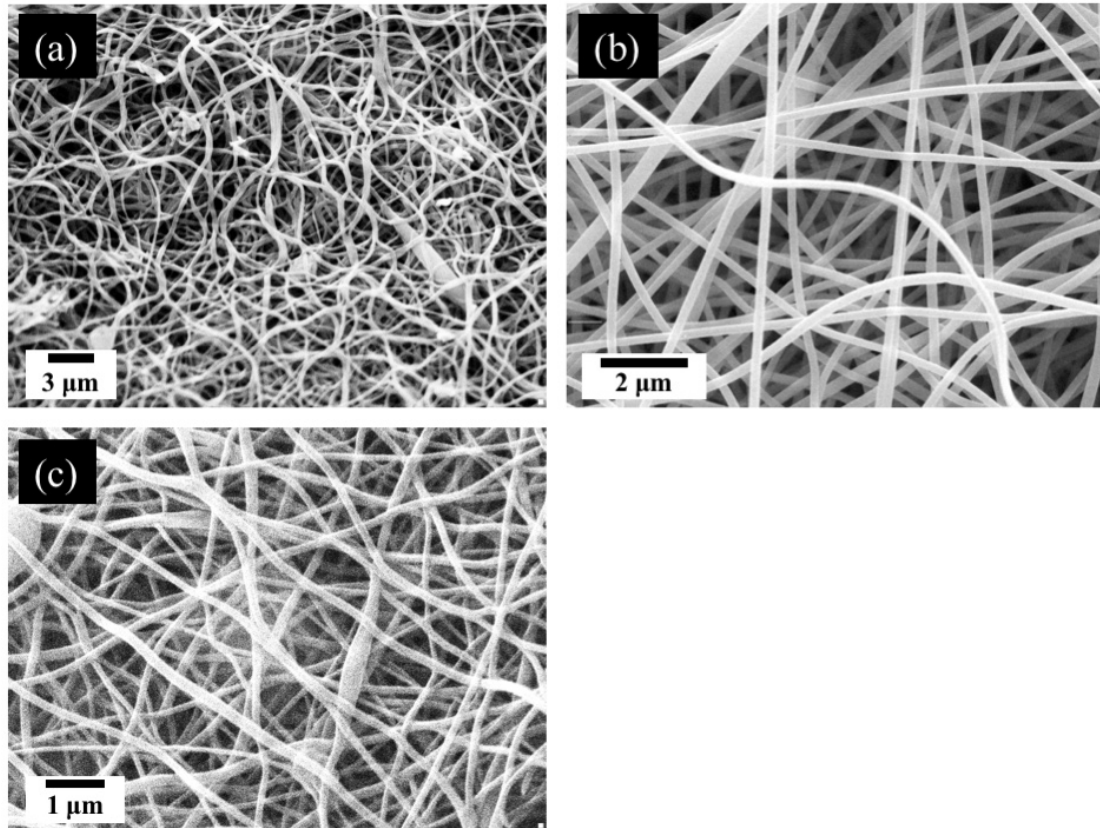


**Figure 2.2.** SEM images of carbonized PAN fiber morphology after treatments at (a) 1000°C, (b) 1200°C, and (c) 1400°C.

Figures 2.2 and 2.3 show SEM images of carbonized PAN and PVP fibers, respectively. The fiber diameters of both carbonized polymers are summarized in Table 2.1. Carbonized PAN fibers show smooth morphology with few beads and the morphology is maintained through high temperature treatments. As the carbonization temperature increases, the PAN fiber diameters decrease from around 230 nm at 1000°C to 130 nm at 1400°C. The shrinking does not affect the morphology of the carbon fibers.

The PVP carbon fibers have a smooth, uniform morphology free of beads. At higher temperatures the fibers appear more rigid and brittle. However, unlike PAN, the PVP carbon fibers show no significant change in diameter as carbonization temperature increased. Fiber size remains from 250-300 nm from 800-1400°C.

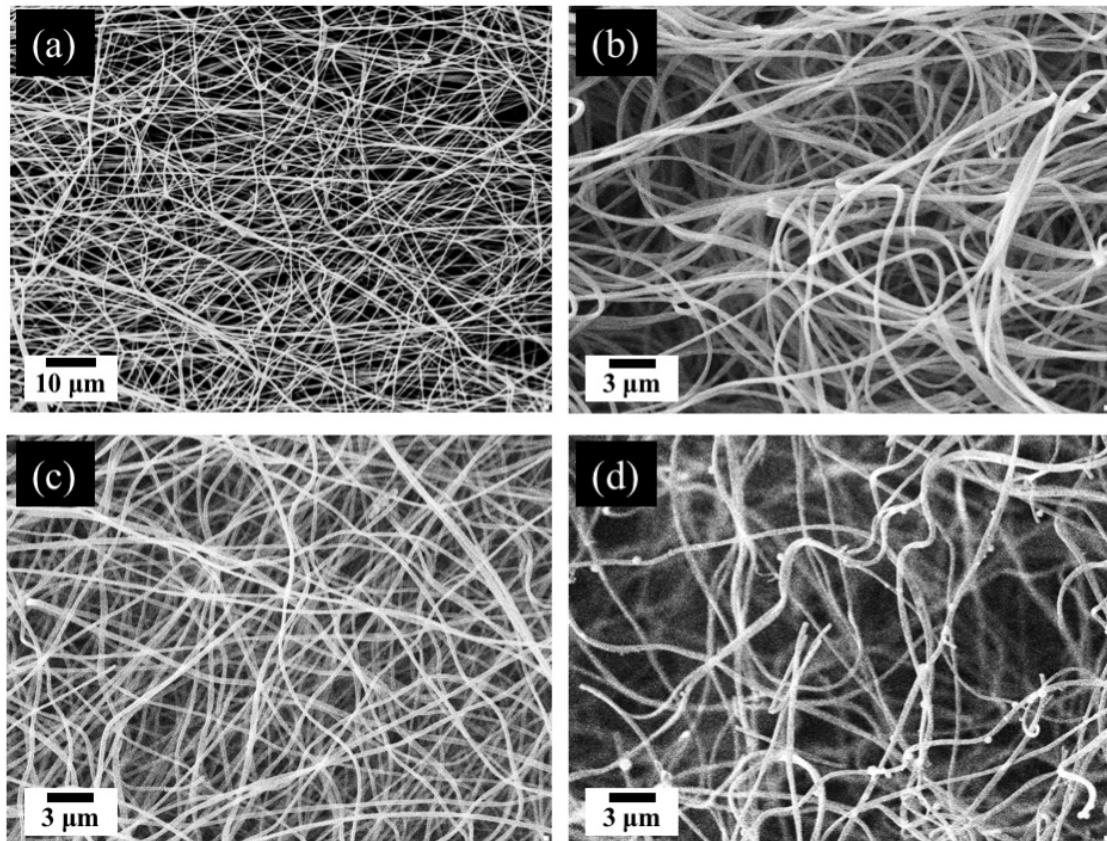


**Figure 2.3.** SEM imaging of carbonized PVP fibers carbonized at (a) 800°C, (b) 1000°C, (c) 1200°C, (d) 1400°C

**Table 2.1.**

Summary of fiber diameters for PAN and PVP carbonized fibers.

Polymer	Carbonization Temperature	Avg. Fiber Diameter (nm)	Std. Dev. (nm)
PAN	1000°C	229	45
	1200°C	198	29
	1400°C	130	12
PVP	800°C	286	189
	1000°C	267	36
	1200°C	249	35
	1400°C	305	39

The natural pores formed during the carbonization process are an additional focus for consideration. Physisorption analysis is used to evaluate the carbon fibers and two methods of reporting can establish how porous the carbon fibers are. BET surface area is reported as the total surface area of the carbon fiber and is split into a mesoporous area (pores larger than 2 nm) and microporous area (pores smaller than 2 nm). BJH method is used to get a distribution of pore sizes and their contribution to total surface area for pores 1.7 nm and larger. BJH will not include much of the microporous contribution from BET. The BET of PAN and PVP carbon fibers as a function of carbonization temperature is summarized for PAN and PVP in Tables 2.2 and 2.3, respectively. BJH pore distribution plots for PAN and PVP are shown in Figures 2.4 and 2.5, respectively.

**Table 2.2.**

Summary of BET data for PAN carbonized fibers. Microporous area refers to surface area provided by pores 2 nm or smaller.

Carbonization Temperature	BET (m <sup>2</sup> /g)	Mesoporous area (m <sup>2</sup> /g)	Microporous area (m <sup>2</sup> /g)
1000°C	152.3	44.7	107.6
1200°C	18.6	17.4	1.2
1400°C	41.5	29.8	11.7

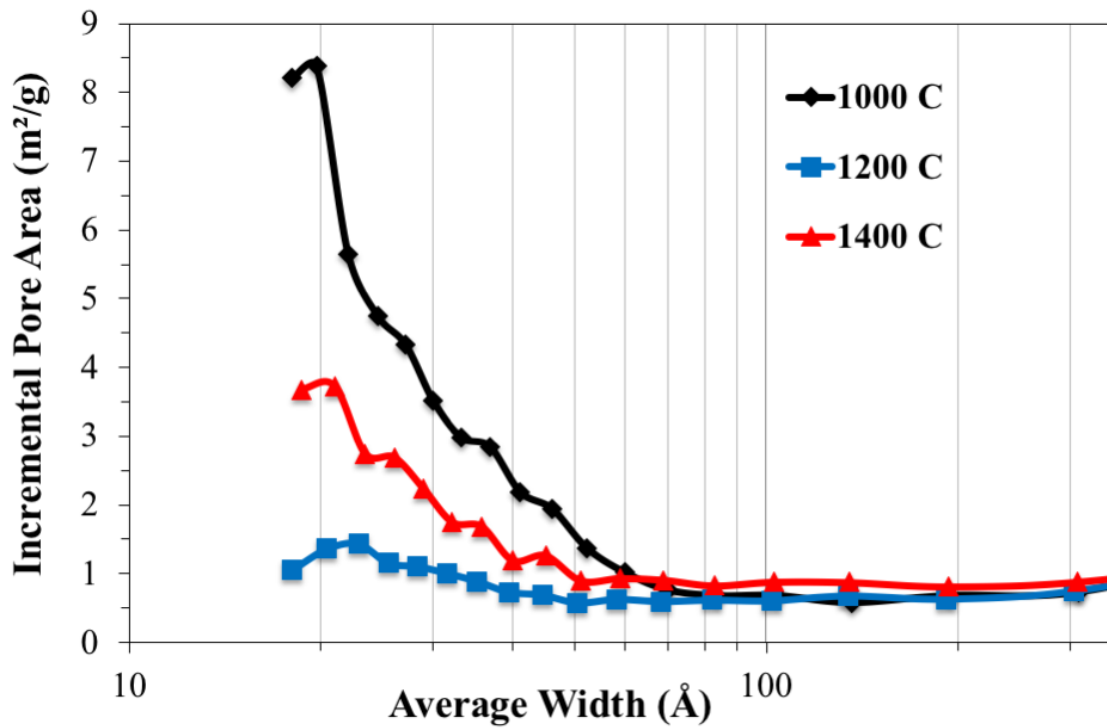


**Figure 2.4.** BJH pore distribution plot for PAN carbonized fibers at 1000°C, 1200°C, and 1400°C.

**Table 2.3.**

Summary of BET data for PVP carbonized fibers. Microporous area refers to surface area provided by pores 2 nm or smaller.

Carbonization Temperature	BET (m <sup>2</sup> /g)	Mesoporous area (m <sup>2</sup> /g)	Microporous area (m <sup>2</sup> /g)
800 C	623	42	581
1000 C	665	55	611
1200 C	674	58	616
1400 C	650	242	407

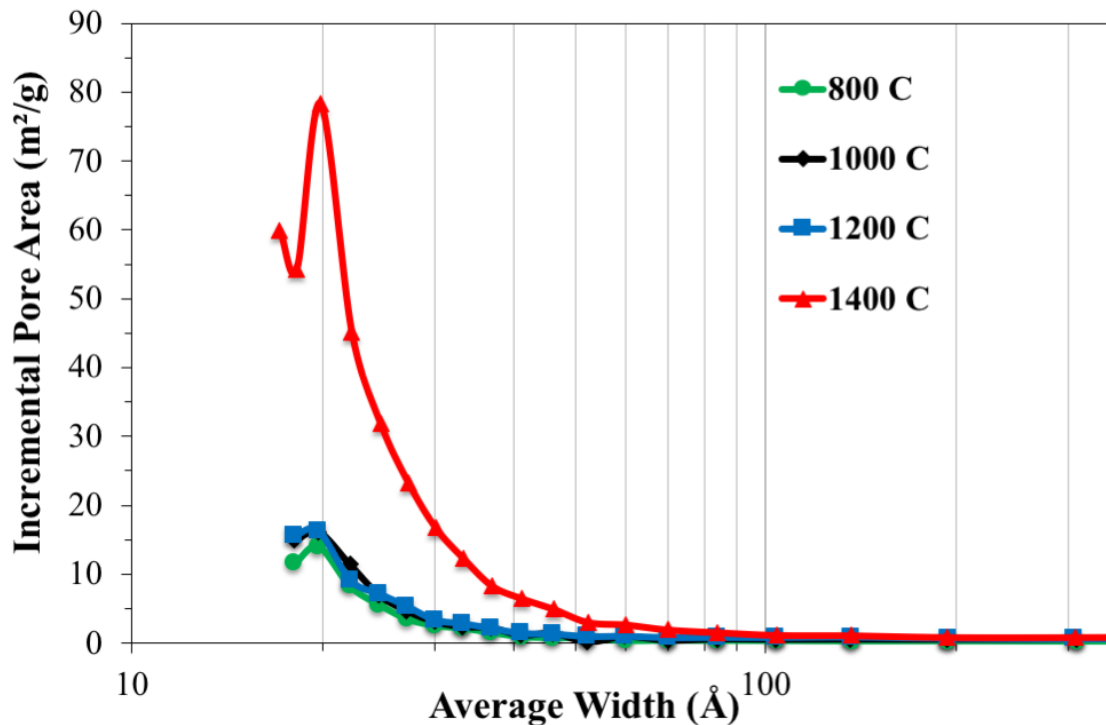


**Figure 2.5.** BJH pore distribution plot for PVP carbonized fibers at 800°C, 1000°C, 1200°C, and 1400°C.

There are several observations that can be made about the different pore structures of the two polymers. PVP naturally forms a higher surface area fiber than PAN and this is maintained for all tested carbonization temperatures. This is likely due to the much lower carbon yield of PVP than PAN, and much more burnoff takes place during the carbonization process, creating additional pores. The PAN carbon fibers lose surface area as they go from 1000°C to 1200°C. The loss of pores aligns with the

condensing of the carbon fiber seen in SEM. At 1400°C there is an increase which could be due to some additional burnoff in the structure increasing the size of the remaining pores, though the increase in surface area is not significant for supercapacitor purposes. PVP did not show this shrinking or condensing effect with carbonizing temperature, and the pore structures are relatively stable from 800 to 1400°C. At 1400°C, similar to PAN, there appears to be a shift in the size of the pores from the microporous range to pores just larger than 2 nm, which was confirmed by both BET and BJH analysis. Increase in pore size into this range could be useful for many different energy storage applications for porous carbon such as Li-S interlayers.

The four-point probe technique was used to find the conductivity of the freestanding carbon fiber mats and show how it changed with increasing temperature. Table 2.4 summarizes conductivity data measured for each polymer. As expected, both sets of carbonized fibers show a significant increase in conductivity from their polymer precursor. PAN carbon fibers show ~5x improvement in conductivity over the PVP carbon fibers, showing the important nature of how PAN forms a strong carbon structure. The internal pores of the carbonized PVP can also act as resistors, limiting the conductivity that can be achieved. There are significant conductivity improvements as the carbonizing temperature reaches above 1000°C or the holding time at 1000°C is increased. This is more apparent for PAN carbon fibers and correlates to the other characteristics we have seen, where there has been a condensing of the carbon structure and a reduction in pores. 1400°C is below the temperature range where we would expect graphitization of the carbon. It would be interesting to see the effect on the sheets properties of taking these carbon fiber sheets to

temperatures of 1800°C or higher and the effect it would have on the carbon nanofiber structure.

**Table 2.4.**

Summary of conductivity data provided by four-point probe measurement for PAN and PVP carbonized fiber mats.

Polymer	Carbonization Treatment	Conductivity (S/m)
PAN	As Spun	0.0018
	800°C 5 hours	55
	1000°C 20 min	145
	1000°C 8 hours	1204
	1200°C 2 hours	1100
	1400°C 1 hour	1240
PVP	As Spun	0.0003
	1000°C 20 min	44
	1200°C 2 hours	150
	1400°C 1 hour	200

In addition to pure polymer solutions, we also electrospun polymer solutions with added conductive carbon powders for all-carbon composites. Both PVP and low temperature carbonized PAN show lower conductivity values that may be improved by adding graphitic carbon to their structure. This could be important for making hybrid materials that cannot survive higher carbonization temperatures but require a conducting framework for electrochemical performance. Super P (carbon black) is a paracrystalline carbon that is both electrically conductive and inexpensive. It is often combined with polymer binders to form conductive slurries for active material. Super P was added in different loadings to the two polymer solutions. Super P could disperse much more easily in the ethanol solvent of the PVP solution and thus could be loaded to very high levels, as high as 50 wt% of total polymer loading, and remain spinnable. This will have an effect on the carbon yield for PVP fibers that is typically under 10%.

PAN solutions could disperse a moderate amount of Super P and it was tested up to 10 wt% compared to polymer.

SEM of carbonized PAN fibers with 10 wt% Super P inclusion is shown in Figure 2.6. The addition of Super P gives regions of smooth PAN-carbon and then regions of aggregated Super P that gives a rough, bumpy texture to the fiber. These aggregates stem from the poor dispersion in the PAN/DMF solution and limited how much carbon could be added.

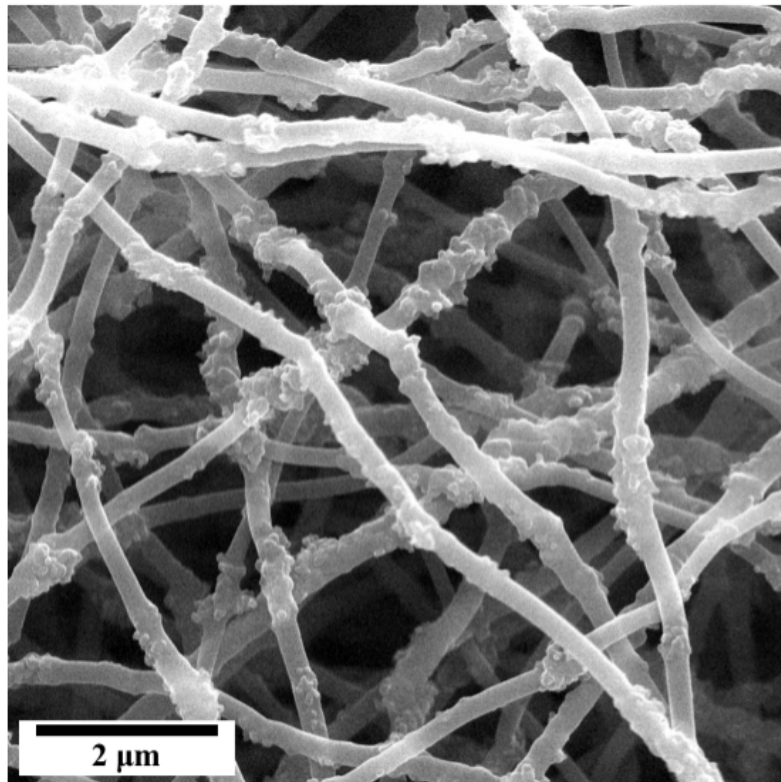


**Figure 2.6.** SEM imaging of fibers carbonized at 1000°C made from a 1:10 Super P: PAN solution.

The pore structure of the carbonized PAN with Super P is summarized in Table 2.5 and Figure 2.7. Both BET and BJH show a small shift to larger pore sizes, which may be from contributions of the Super P's own pores as well as some larger pores forming during carbonization of PAN due to Super P interrupting regions of the

polymer chains. A yield comparison of PAN fibers and PAN with 10 wt% addition of Super P carbonized at 1000°C showed that the PAN fibers had a higher yield without the Super P, as yield decreased from 43% to 37% with Super P addition. Super P has almost a 100% yield at 1000°C so the effect we are seeing is that the addition of any additive into the PAN matrix hurts the PAN carbonization process and adjusts the fiber properties negatively. The additional burnoff increased the pore size.

**Table 2.5.**

Summary of BET data for PAN and PAN/Super P carbonized fibers at 1000°C.

Carbon Sample	BET (m <sup>2</sup> /g)	Mesoporous area (m <sup>2</sup> /g)	Microporous area (m <sup>2</sup> /g)
PAN	152.3	44.7	107.6
PAN + 10 wt% Super P	146.0	51.3	94.7

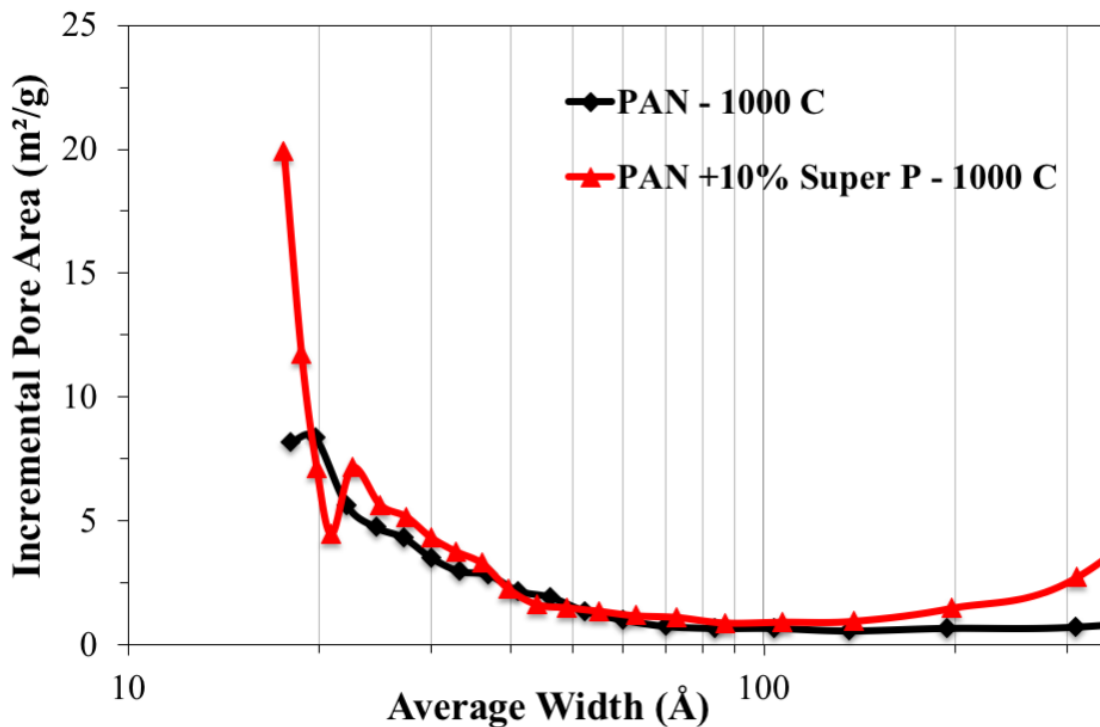


**Figure 2.7.** BJH pore distribution plot for PAN carbonized fibers at 1000°C with and without Super P inclusion.

Figure 2.8 shows the evolution of PVP carbon fibers at 1000°C as increasing amounts of Super P are added into the electrospinning solution. Loadings as high as 20 wt% of Super P can be evenly distributed throughout the PVP carbon fiber. While the fibers are not smooth, the Super P is not aggregated and is much more uniform along the fiber in the PVP matrix than it was in PAN. This could be very useful when preparing hybrid materials that would disperse or dissolve more easily in alcohol or water as a way to increase loadings. At 35 wt% Super P loading, there are more non-uniformities in fiber diameter and aggregation. At 50 wt% addition of Super P, some of the fiber morphology is lost and the fibers begin to resemble aggregates of Super P with fiber diameters varying significantly along the fiber.

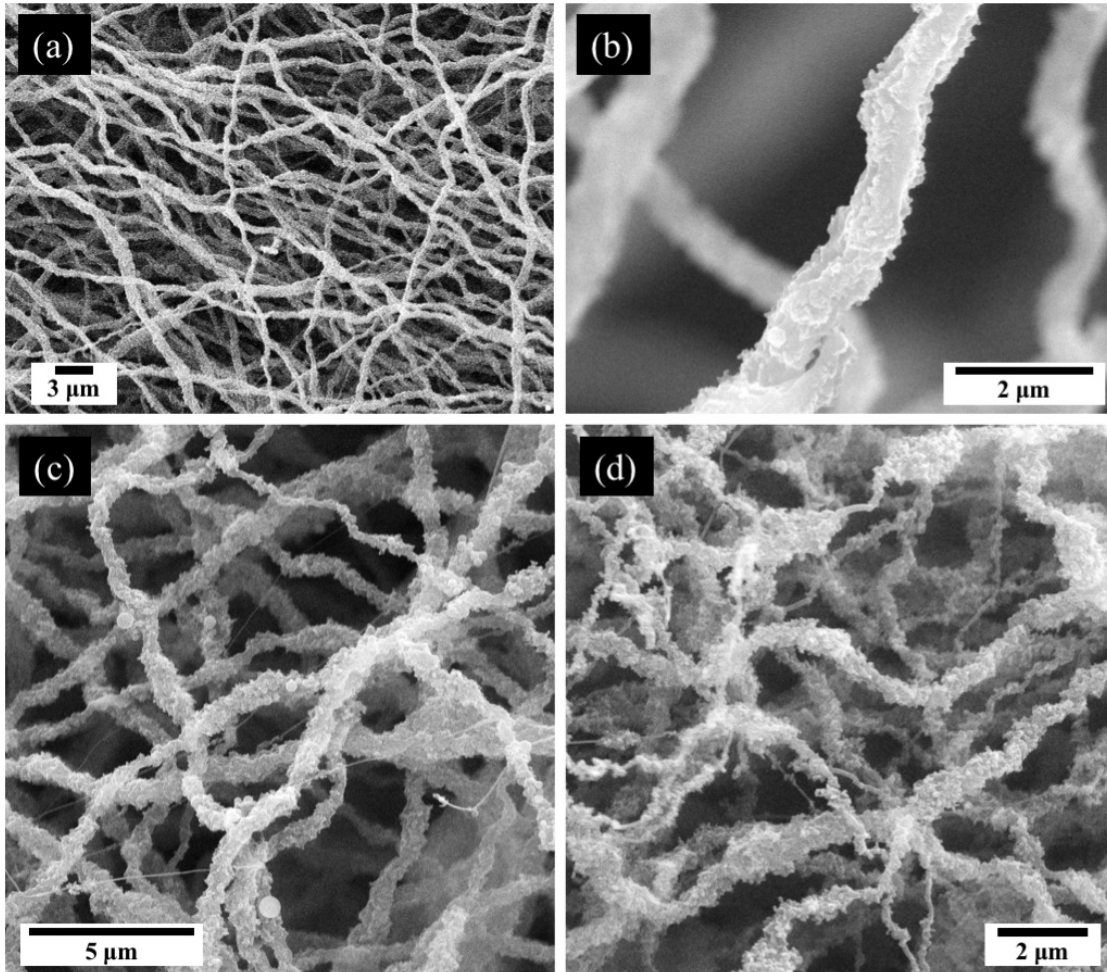


**Figure 2.8.** SEM images of PVP:Super P fibers after carbonization at 1000°C. Loadings of Super P were (a) 10 wt% Super P, (b) 20 wt% Super P, (c) 35 wt% Super P, and (d) 50 wt% Super P compared to the weight of PVP polymer in solution.

At such high Super P loadings, the PVP carbon fiber properties begin to represent more the characteristics of Super P. Specifically, we see a significant change in the pore structure of PVP carbon fibers as the Super P makes up the majority of the carbon nanofiber. Table 2.6 and Figure 2.9 summarize the pore data for Super P, PVP, and PVP/Super P composite fibers up to 20 wt% loading. Super P has a lower surface area than the PAN and PVP carbon nanofibers with few micropores. Super P has a large contribution of pores between 2 and 4 nm. As Super P ratio was increased in PVP carbon nanofibers, the total BET surface area and the micropore content

decreases significantly as more of the carbon in the nanofibers comes from Super P.

The BJH pore distribution reflects this change as composite fibers have a spike in pore size between 2-4 nm despite overall loss of surface area. While not addressed in this work, the addition of an activated carbon or a mesoporous carbon to the PVP carbon fiber matrix could make an excellent freestanding high-surface area carbon.

**Table 2.6.**

Summary of BET data for Super P, PVP carbon nanofibers and PVP/Super P carbon nanofibers fibers at 1000°C.

Carbon Sample	BET (m <sup>2</sup> /g)	Mesoporous area (m <sup>2</sup> /g)	Microporous area (m <sup>2</sup> /g)
Super P	73.3	10.9	62.4
PVP	757	710	47
PVP + 10 wt% Super P	270	160	110
PVP + 20 wt% Super P	237	59	178

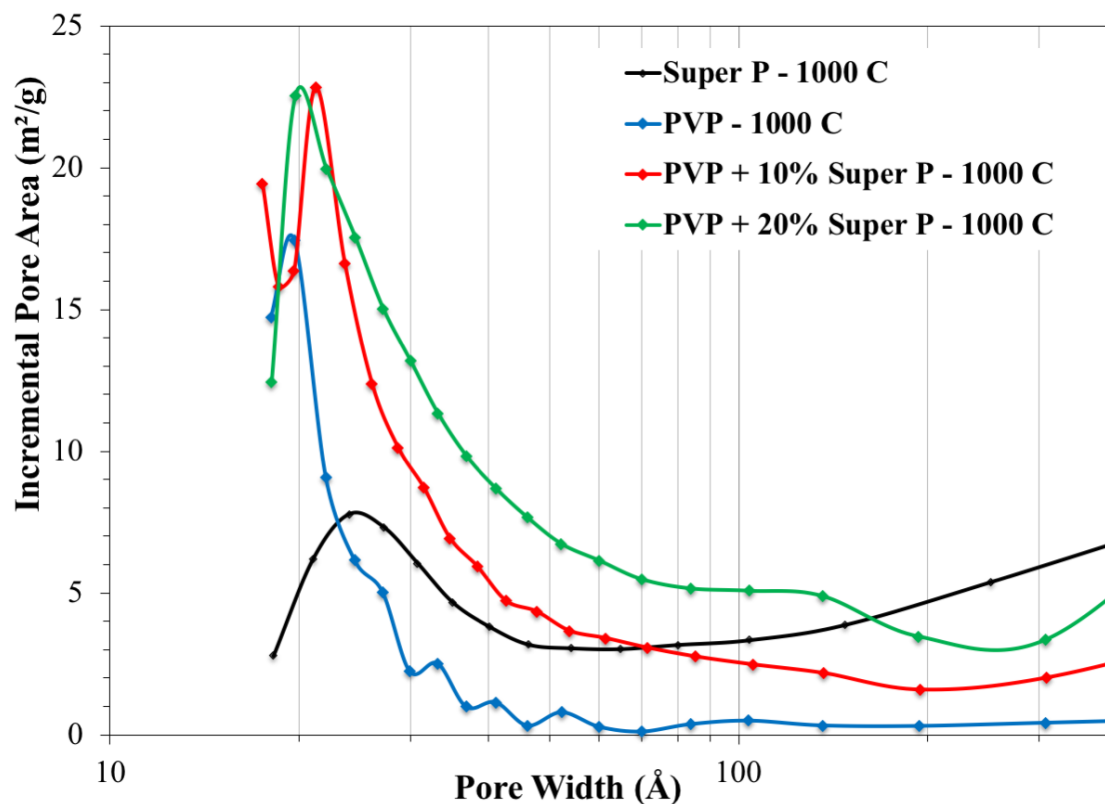


**Figure 2.9.** BJH plots showing the surface area contributions by pore size of Super P, PVP, and PVP/Super P composites after carbonization at 1000°C.

Conductivity data for carbon fiber sheets of both PAN and PVP with Super P, for a range of Super P loadings and carbonization treatments, can be found in Table 2.7. PAN carbon fibers showed their best conductivity performance with low additions of Super P, with 1% additions yielding the highest conductivity. The presence of an additive disrupts the cyclization reactions that are the source of high carbon yields for PAN, and limiting additions to 1 wt% added performance without compromising the PAN carbonization. This held true at both 1000°C for short duration and at 1200°C.

**Table 2.7.**

Conductivity measurements for PVP and PAN carbon fibers with Super P added. Super P wt% reported is compared to the total weight of polymer in solution.

Polymer	Carbonization Treatment	Super P wt%	Conductivity (S/m)
PVP	1000°C for 20 min	0	44
		10	211
		20	348
		35	332
		50	61
PAN	1000°C for 20 min	0	144
		1	701
		5	548
		10	449
PAN	1200°C for 2 hours	0	1103
		1	1229
		10	927

The addition of Super P had a much different effect on PVP carbon fibers than it did on PAN. PVP showed increasing conductivity at higher Super P loadings with conductivity peaking at 20-35 wt% loading compared to PAN. The Super P continued to improve performance until aggregation of the Super P ruined the nanofiber morphology. While PAN had a carbon yield over 40%, the carbon yield of PVP was

only 8% and it does not have the same cyclization process that can be disrupted. The addition of Super P improved the carbonized yield from 8% up to 18% yield at a 10 wt% Super P loading, and then 20% carbonized yield at a 20 wt% Super P loading. The fibers at these loadings are comprised primarily of Super P, and at higher loadings there is not enough carbonized PVP to hold everything together. The incorporation of such large loading of Super P had a significant effect on carbonized PVP properties and structure and increased the conductivity 5-7x the base PVP carbon.

We also briefly evaluated using graphene nanoribbons (GNRs) in PAN solution. GNRs are carbon nanotubes that have been unzipped to form high aspect ratio ribbons of graphene. GNRs are more conductive than Super P but far more expensive and thus are used in lower loadings. This is great for PAN carbon fibers where the inclusion amounts should be small. GNRs were added to PAN solution at 1, 3, and 5 wt% of PAN, and with sonication, the GNRs dispersed easily for electrospinning. SEM of the 5 wt% loading is shown in Figure 2.10. The fiber morphology was only slightly affected with fibers taking on a more flattened, ribbon-like appearance but overall morphology was smooth. There were no bumps or roughness as seen with Super P and the GNRs cannot be observed from the surface showing they are incorporated well into the PAN carbon nanofiber.

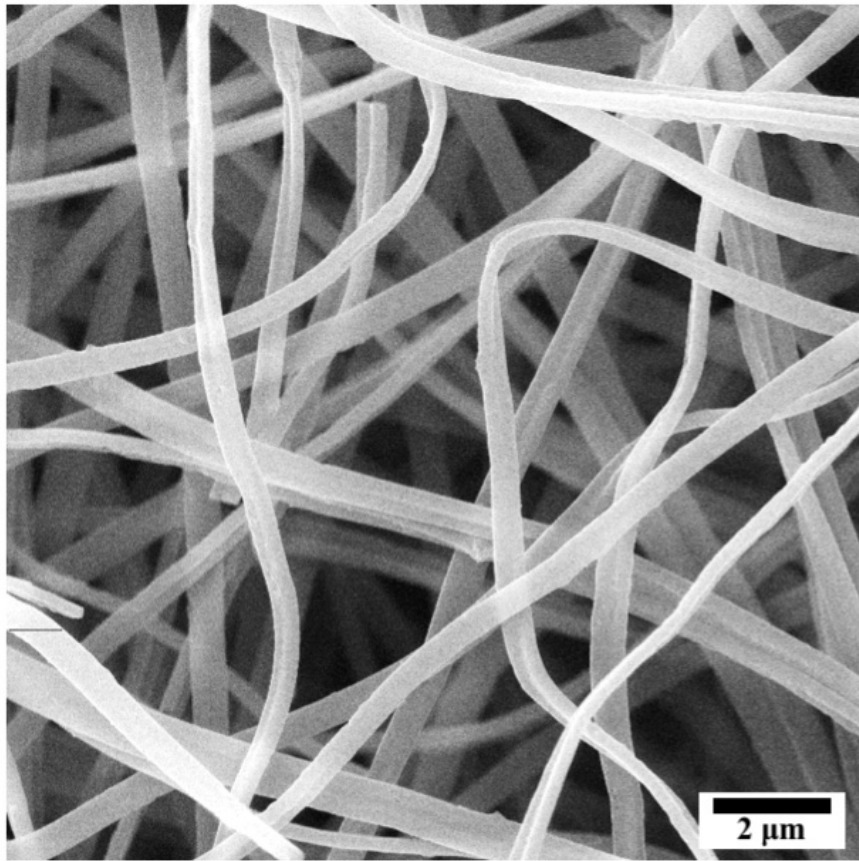


**Figure 2.10.** SEM of PAN fibers carbonized at 1000°C for 8 hours with 5 wt% addition of GNRs.

Conductivity tests show a greater improvement with GNRs than what was seen with Super P additions. After carbonization at 1000°C for 8 hours, the conductivity was 1204, 1739, 1237, and 1207 S/m for carbonized PAN, 1% GNR, 3% GNR, and 5% GNR, respectively. The conductivity was improved by over 40% from just 1% addition of GNRs, making it the most conductive PAN sample tested. Increasing loading of GNRs above 1% still led to decrease in carbonized PAN conductivity.

Working from two different polymer precursors we were able to form freestanding carbon nanofiber sheets with different properties. PAN carbonized sheets showed higher yield and conductivity to PVP sheets that could be very important as a conductive framework. While less conductive, the PVP carbon fiber sheets showed

great fiber morphology and higher surface area from pore formation than the PAN carbon fibers. The addition of conductive carbon improved the conductive qualities of both polymers at low carbonization temperatures. At higher temperatures, PAN fibers were more conductive with low loadings of conductive carbon or without inclusions as the PAN naturally forms a conducting carbon fiber that is interrupted by composites. GNRs worked better with PAN as loadings of 1% gave a significant conductive boost without hurting carbon yield. PVP continued to improve with conductive carbon loading until inclusions were high enough that fiber morphology began to suffer, and the fibers begin to resemble aggregated particles more than fibers.

### **2.3.2 Freestanding carbon fiber/ iron acetylacetonates mats**

After achieving freestanding carbon fiber mats with controllable properties, we moved onto metal precursors for hybrid composites. Previously, former Joo group member Dr. Jeanne Panels had formed  $\text{Fe}_3\text{O}_4$  (magnetite) and  $\text{Fe}_3\text{C}$  in carbonized PAN fibers [40]. The fibers had shown a magnetic quality due to the presence of magnetite and iron carbide. We replicated this work to form a magnetic freestanding sheet as proof of concept for our supercapacitor work.

Following Panels' work we electrospun PAN fibers in a 5:1 wt ratio with iron acetylacetonate (AAI), or a 17% AAI loading. After electrospinning, heat treatment was altered, and samples were stabilized at  $250^\circ\text{C}$  and carbonized at  $850^\circ\text{C}$  in between two ceramic plates. The samples formed a carbonized freestanding sheet that was  $\sim 100$  microns thick. The electrospun and carbonized fiber morphology were examined by SEM (Figure 2.12). Spun fibers were  $333 \pm 28$  nm and carbonized fibers were

114 +/- 14 nm diameters. Fiber morphology of both the as spun and carbonized samples were smooth and uniform. In the carbonized samples we can see that the iron precursor has formed small crystals distributed evenly along the fibers.

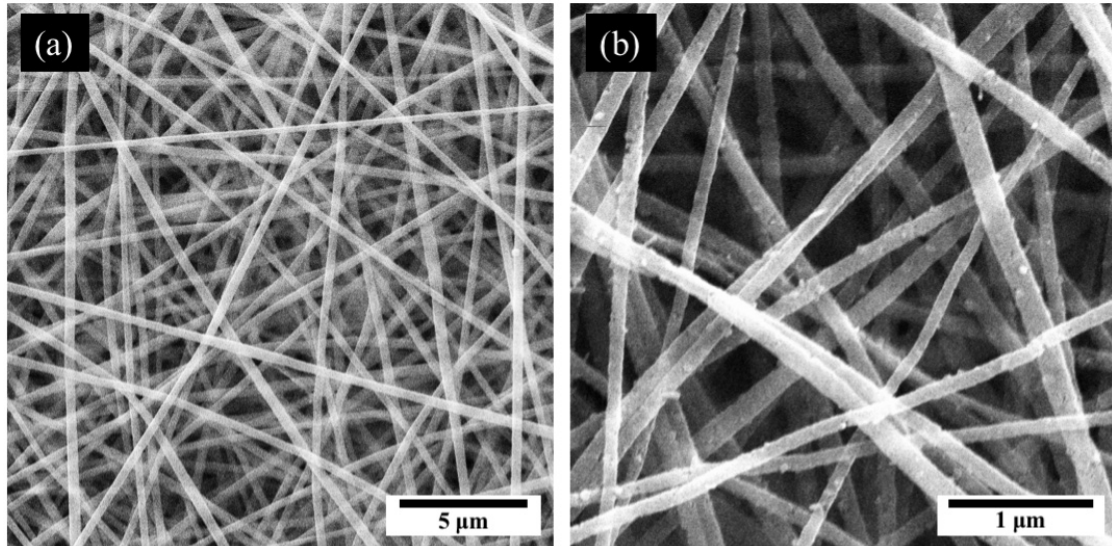


**Figure 2.11.** SEM images of (a) as spun and (b) carbonized 17 wt% PAN/AAI fibers.

Carbonized samples were analyzed by XRD to determine which iron crystals were formed in the fibers (Figure 2.12). XRD confirmed the presence of three different materials within the fibers: carbon,  $\text{Fe}_3\text{O}_4$ , and  $\text{Fe}_3\text{C}$ . The fibers match the crystal structures seen in Panels' original work. For our final goal of hybrid capacitors, iron oxide would be a useful redox material, but the significant iron carbide presence is not desired. This displays one of the issues of preparing materials in one-pot synthesis: we needed to carbonize the PAN fiber, but high temperatures and a carbon matrix were enough to form iron carbide instead of the desired iron oxide. This limits some of the freedoms we have when preparing carbon and metal oxides separately if we want to form an all-in-one composite fiber.

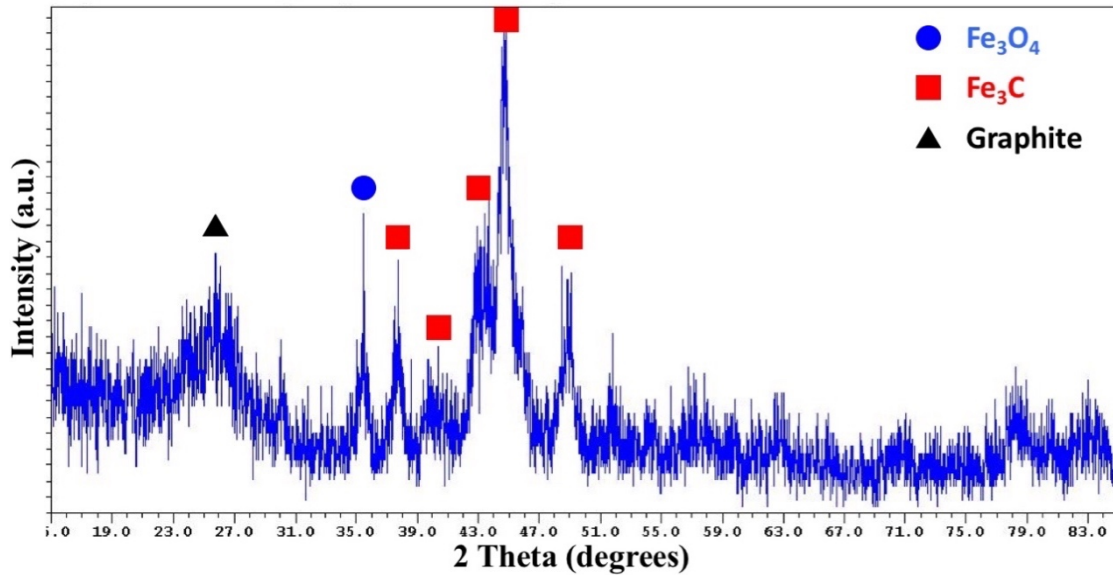


**Figure 2.12.** XRD of carbonized 17 wt% PAN/AAI fibers with labeled peaks for crystal structure.

A four-point probe was used to evaluate sheet conductivity. Based on our studies, 850°C is a low carbonization temperature and will not form highly conductive carbon fibers. The addition of metal crystals into the fibers improved the conductivity as the 17% PAN/AAI fibers had a higher conductivity of 290 S/m versus pure carbonized PAN with the same treatment with 55 S/m. With low temperature carbonization, conducting metals or conducting carbons could be much more important additions for PAN as the fibers will not be conductive on their own, relative to their 1000°C+ carbonization treatment.

Formation of iron oxide and iron carbide crystals affected the pore structure in the carbon fibers. Table 2.8 and Figure 2.13 summarize the BET and BJH data of carbonized PAN and PAN/AAI at 850°C. The metal addition had a significant impact on pore formation with additional pores formed at all size ranges. Pore contributions could be from the carbonized PAN and the iron crystals. A significant number of pores formed are at the mesoporous scale between 2-10 nm. This pore range is especially

useful for electrode structures because they are large enough to support diffusion of small molecules.

**Table 2.8.**

BET summary of carbonized PAN and 17 wt% PAN/AAI fibers.

Material	BET (m <sup>2</sup> /g)	Mesoporous area (m <sup>2</sup> /g)	Microporous area (m <sup>2</sup> /g)
Carbonized PAN	152	45	108
17 wt% PAN/AAI	611	361	250

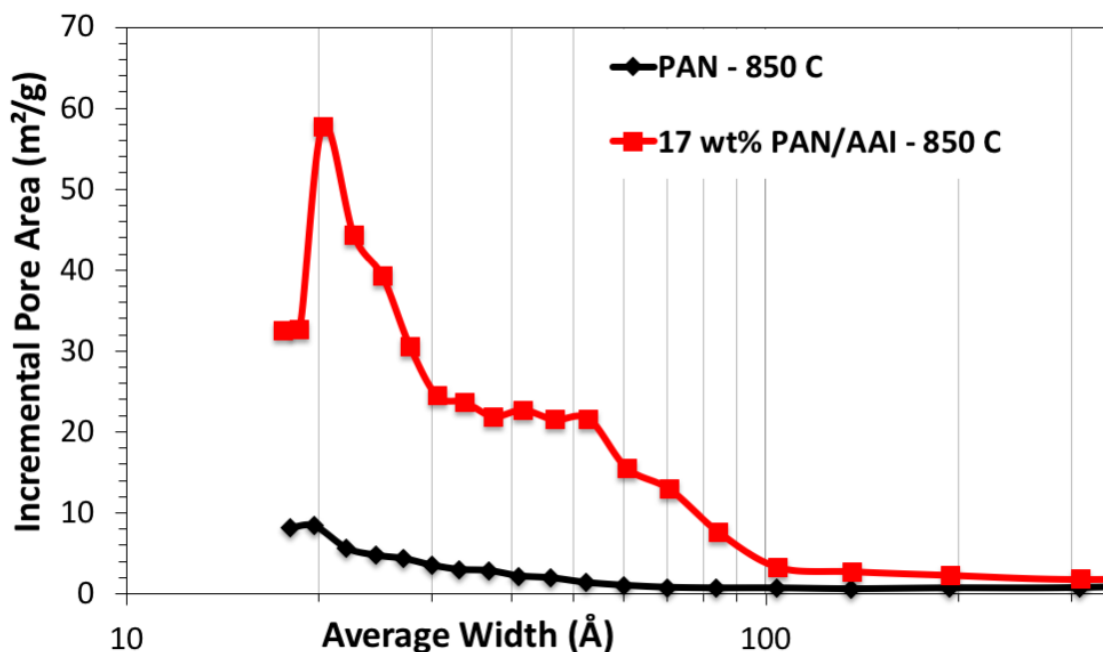


**Figure 2.13.** BJH plots showing the surface area contributions by pore size of PAN and 17 wt% PAN/AAI fibers.

We ran a final test was to confirm that the fiber sheets still had their magnetic quality. Figure 2.14 shows the original photograph taken by Panels and our new picture showing the prepared sheet. The thin sheet prepared could be used in direct application while the powder-like material from Panels' work would require slurry preparation and casting for application. Our samples had replicated the previous work in all respects but as a freestanding sheet. More importantly, it proved that we could form carbon composite sheets without jeopardizing sheet structure, as was seen with

carbon fibers. The formation of iron oxide and iron carbide together also brings in important design considerations for electrospinning composite materials. We have to consider whether or not forming a composite will make a high performing hybrid material, or if adverse effects from compromises on carbonization temperature would make the composite material unusable. In this work, iron oxide was dwarfed by the formation of iron carbide. High heat treatment with carbon present ruined the sample purity and in application that issue could be more important than whether the electrode was prepared by casting a slurry.

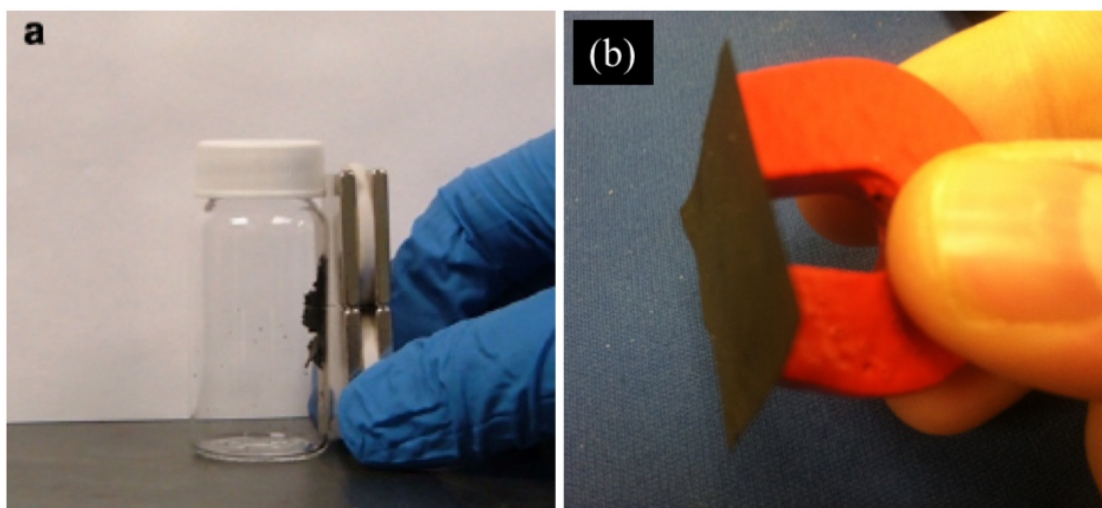


**Figure 2.14** Magnetic properties of carbonized PAN/AAI samples from (a) the original work by Panels and (b) this work.

### **2.3.3. Freestanding carbon/Mn<sub>3</sub>O<sub>4</sub> fiber mats for supercapacitors**

The main goal of this work was to form freestanding electrodes for supercapacitors and in this effort, we fell short. This section shows how we formed freestanding activated carbon and activated carbon/Mn<sub>3</sub>O<sub>4</sub>, but the supercapacitor test setup of coin cells prepared with a propylene carbonate electrolyte showed limited capacitance and did not work in freestanding or slurry casted approaches. The

electrode fabrication went well and should be considered for additional application but the cells in this work does not demonstrate their utility for energy storage.

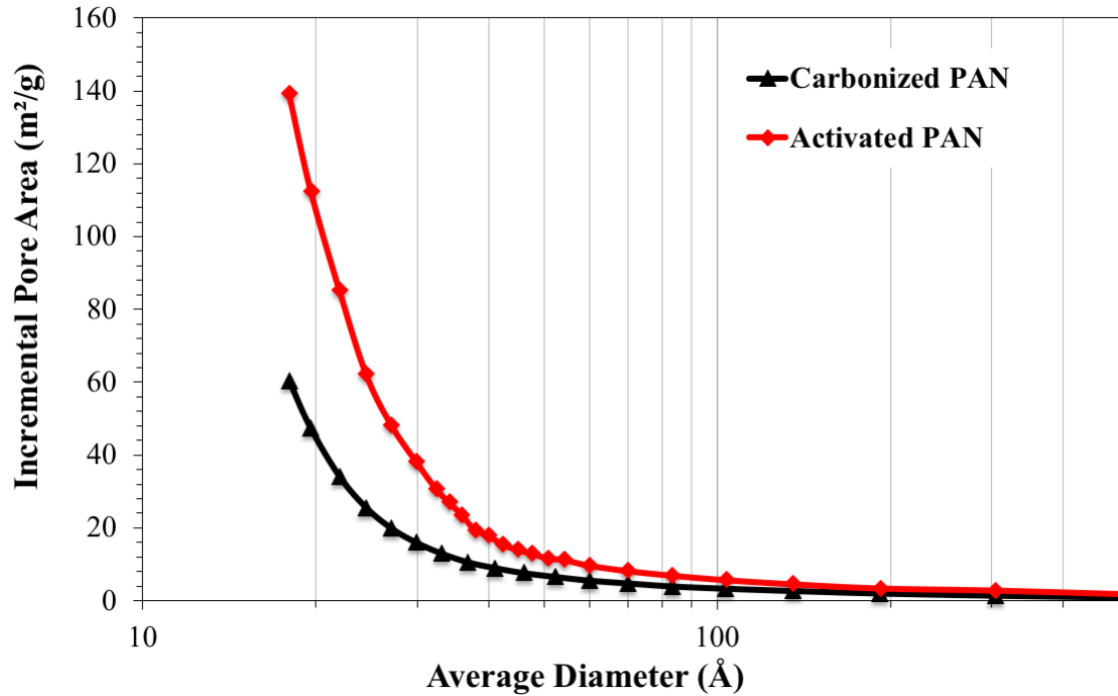
There are two classes of supercapacitors: high surface area carbon capacitors for EDLC and pseudocapacitors with hybrid materials that engage in fast, reversible redox reactions. To test the feasibility of our freestanding sheets for both classes of supercapacitors we prepared activated carbon and carbon/manganese oxide fiber sheets by electrospinning. We first prepared a carbonized PAN sheet for activated carbon fibers and then a PAN/manganese acetylacetonate sheet for activated carbon/Mn<sub>3</sub>O<sub>4</sub> hybrid fibers.

Activated carbon fiber sheets were prepared from the PAN carbon sheets developed before. Activation can be a physical or chemical process that is used to form pores and create more surface area for a material by eliminating the more reactive carbon atoms of the structure and creating pores. Physical activation can be done at high temperature with steam, carbon dioxide, air, or a mixture of these gases [42-44]. For this work, air activation was used to both burn out additional pores in carbon and to form metal oxide crystals that require oxygen. After carbonizing PAN fibers at 1000°C, an additional thermal treatment in air at 350°C was used to activate the carbon. Table 2.9. and Figure 2.15 give the BET and BJH surface area comparisons before and after activation.

**Table 2.9.**

BET summary of air activation of carbonized PAN fibers.

Sample	Total BET Area (m <sup>2</sup> /g)	Microporous Area (m <sup>2</sup> /g)	Larger Pore Area (m <sup>2</sup> /g)
Carbonized PAN	524	477	47
Activated PAN	913	780	132

**Figure 2.15.** BJH plots showing the surface area contributions by pore size of carbonized PAN nanofibers and activated PAN carbon nanofibers.

The carbonized PAN fibers showed much higher surface area than earlier tests of PAN carbon. This is an effect of humidity, which was not controlled during these experiments [45]. Activation further increased the microporous and mesoporous surface areas with BET surface area over 900 m<sup>2</sup>/g. The added pore structure is important for high capacity in super capacitors where charge is stored in a double layer at the carbon surface. Activated carbons can reach more than 3000 m<sup>2</sup>/g but 913 m<sup>2</sup>/g would have a high capacitance.

Activated carbon electrodes were punched out and directly used as electrodes for supercapacitors. Two activated carbon electrodes were assembled into a coin cell and tested by cyclic voltammetry (CV). The results of the CV were poor and showed both irregular shape of the CV and low capacitance, even at low sweep rates. In electric double layer capacitors (EDLCs) an ideal CV should be rectangular. From our CV sweeps (Figure 2.16) our CV shape was far from ideal and showed a capacitance of only 5 F/g. With typical EDLCs performing over 100 F/g and at higher sweep rates, there are issues with the coin cell approach and high resistance within the cell. Poor physical contact within the cell and no adhesion to a current collector could also be issues with using freestanding electrospun sheets in this supercapacitor setup. As will be shown in the next section, whether the fibers were freestanding or slurry cast was not the issue and the main issue was testing supercapacitors in coin cells.

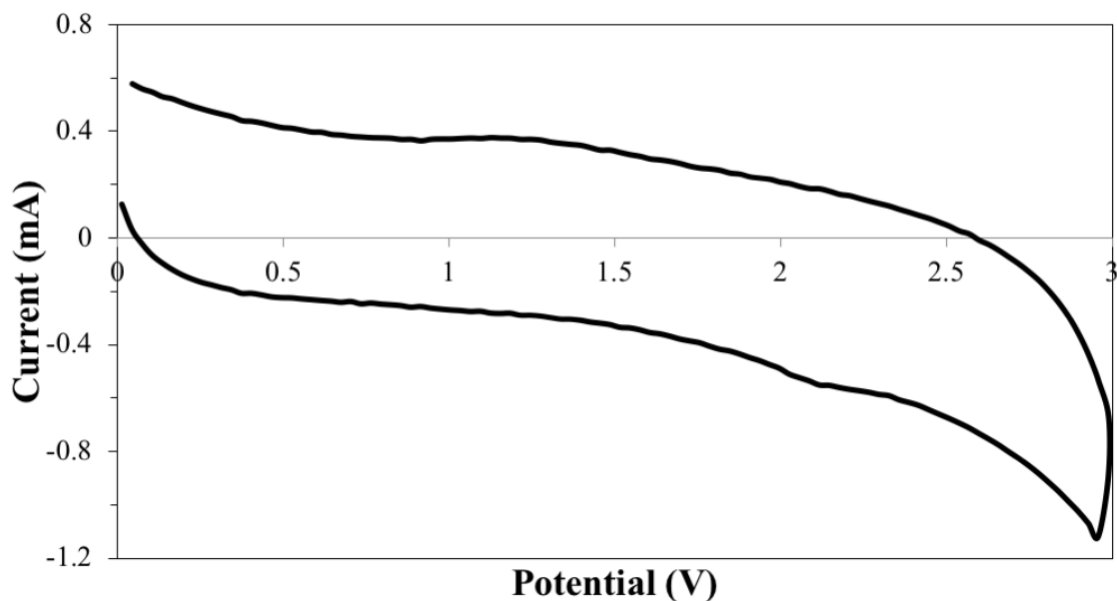


**Figure 2.16.** CV plot showing the 5<sup>th</sup> cycle of a 10 mV/s sweep of a freestanding activated PAN carbon symmetric cell.

We also prepared activated PAN carbon/Mn<sub>3</sub>O<sub>4</sub> sheets to be used as freestanding capacitors. Using similar chemistry to our iron oxide tests, manganese acetylacetonate (MnAcac) was used to form manganese oxide crystals within carbon fibers. Electrospun fibers had to be stabilized and carbonized to form carbon and the beginnings of manganese crystal. We used the activation step from before – air treatment at 350°C – to form the Mn<sub>3</sub>O<sub>4</sub> crystals and activate the carbon fibers. The goal was to form a hybrid material with a high surface area, conductive carbon matrix for the redox active Mn<sub>3</sub>O<sub>4</sub>. A hybrid fiber would give the increased capacitance of redox reactions while the carbon provided better electrochemical performance and its own capacitance.

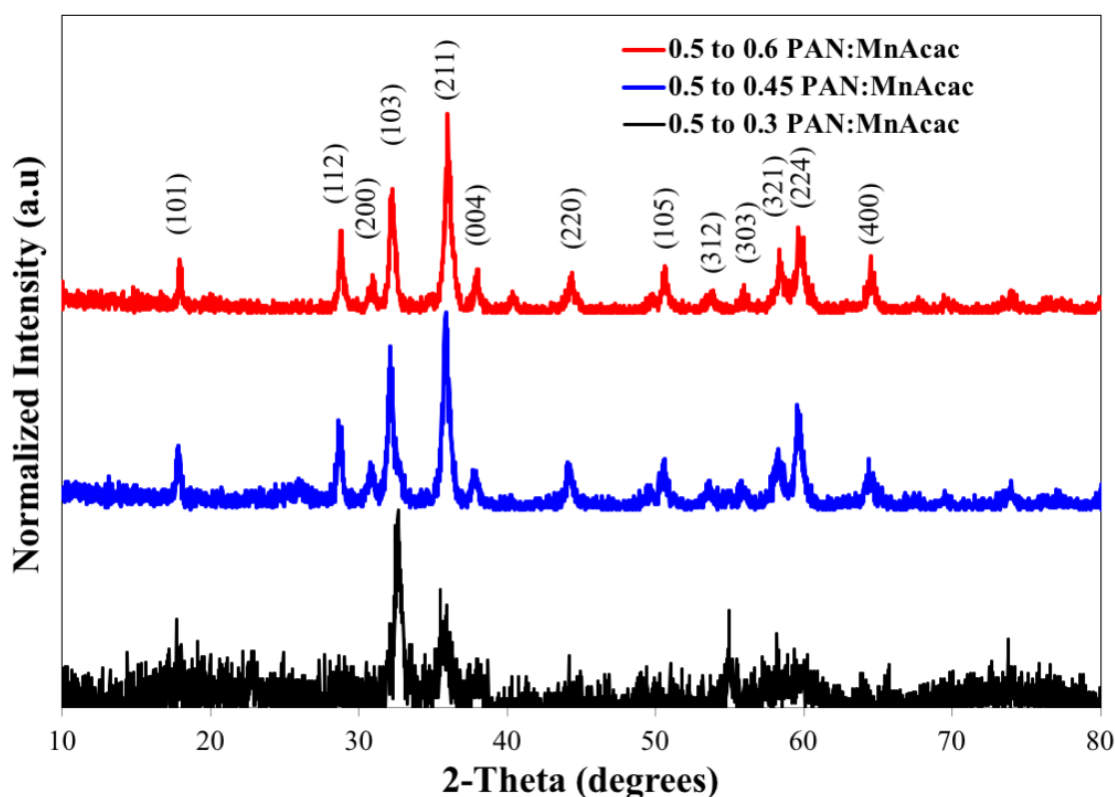


**Figure 2.17.** XRD showing crystal peaks of Mn<sub>3</sub>O<sub>4</sub> present in activated PAN/MnAcac samples.

PAN/MnAcac solutions were prepared in three weight ratios: 0.5:0.3, 0.5:0.45, and 0.5:0.6 g/g. All solutions were spinnable and formed freestanding sheets. XRD analysis was used to confirm  $\text{Mn}_3\text{O}_4$  crystal formation. Only  $\text{Mn}_3\text{O}_4$  is represented and undesirable oxides and carbides were avoided during heat treatment. Both the 0.5:0.45 and 0.5:0.6 loadings formed sharp  $\text{Mn}_3\text{O}_4$  peaks. TGA analysis was used to determine the  $\text{Mn}_3\text{O}_4$  loading of the 0.5:0.45 PAN:MnAcac sample and it showed that  $\text{Mn}_3\text{O}_4$  content was 59.2%. The 0.5:0.6 sample would have an even higher content and could have too much resistance for cell testing.

The 0.5:0.45 PAN:MnAcac fibers were examined with SEM after activation (Fig. 2.18). SEM shows the formation of uniform fibers with a crystalline morphology and not the smooth carbon fibers seen for the pure PAN case. The fibers are smaller than the PAN carbon fibers with an average diameter of  $132 \text{ nm} \pm 11 \text{ nm}$ .

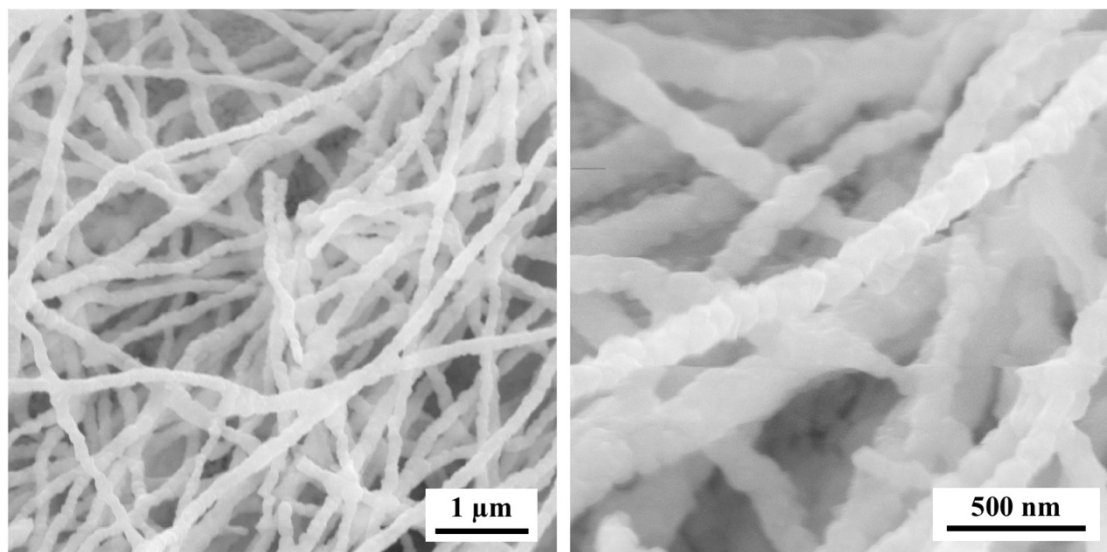


**Figure 2.18.** SEM of 0.5:0.45 PAN:MnAcac fibers after activation treatment.

The carbon/ $\text{Mn}_3\text{O}_4$  electrodes were not used as freestanding sheets due to the issues seen with the activated carbon fibers. A traditional slurry casting was prepared,

and samples were punched out and used in a symmetric coin cells for CV testing. Figure 2.19 shows the CV curves collected at two slow scan rates. The hybrid fibers had specific capacitance values of 22.9, 13.9 F/g at 1 and 10mV/s scan rates, respectively. Other projects in the literature put specific capacity values above 300 F/g and at faster scan rates. In addition to the low capacity we again see an irregular shape to the CV scan suggesting that the carbon/Mn<sub>3</sub>O<sub>4</sub> freestanding sheets coin cell assembly had high internal resistance.

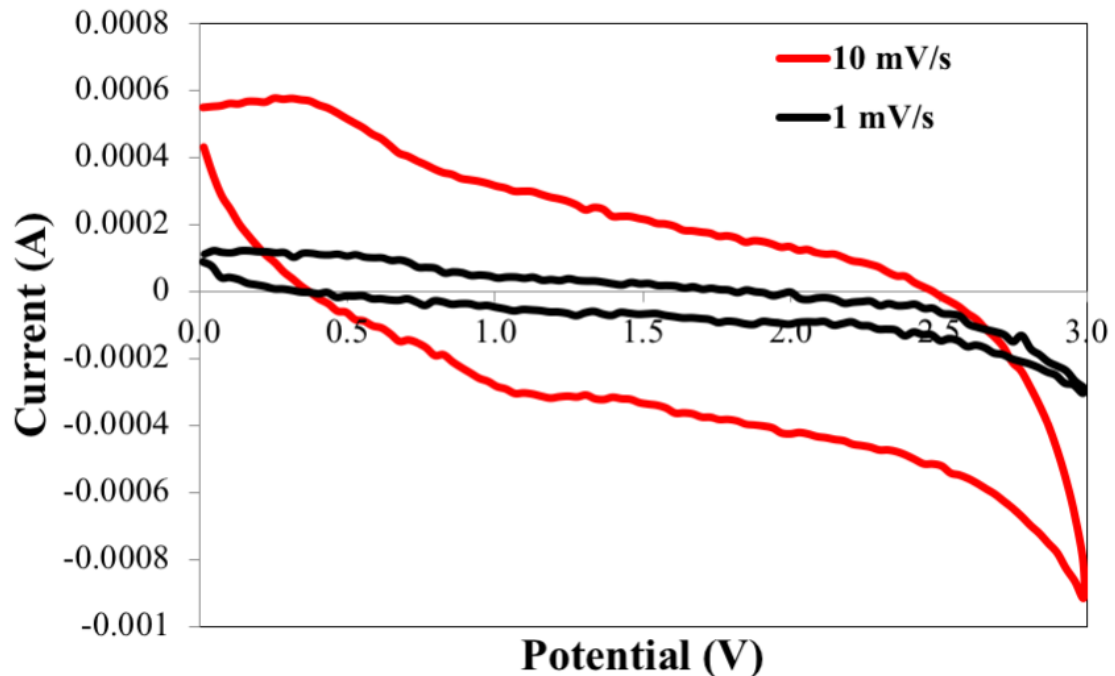


**Figure 2.19** CV analysis of carbon/Mn<sub>3</sub>O<sub>4</sub> fibers. The scans showed low performance and non-ideal behavior at low scan rates of 1 and 10 mV/s.

Before we moved on from this project, we wanted to combine all the elements into an activated carbon-GNR-Mn<sub>3</sub>O<sub>4</sub> composite to show the improvement of the conductivity of the carbon/Mn<sub>3</sub>O<sub>4</sub> fiber sheets as something that could be used again in another application or with an improved system for testing supercapacitor cells. From our work with pure carbon sheets, it was clear low temperature carbonization or

the large contents of additives would disrupt PAN carbon and limit conductivity. By adding a resistive metal oxide, the carbon/Mn<sub>3</sub>O<sub>4</sub> fibers' conductivity is further decreased. We prepared fiber sheets to see the effect of GNRs on the conductivity of the composite fibers. 5 wt% GNRs were added to a 0.5:0.45 PAN/MnAcac fiber and then heat treated as before to form activated carbon and Mn<sub>3</sub>O<sub>4</sub> with GNRs. The conductivity was measured after carbonization and again after activation of the fibers and reported in Table 2.10. The addition of GNRs doubled the conductivity of the activated fibers. The activation step hurt the conductivity significantly with the growth of Mn oxide crystals in the sample and the increased pore volume of the carbon increasing the fiber resistance. The GNRs could be highly effective in improving the electrochemical performance of freestanding electrodes in many applications.

**Table 2.10**

Four-point probe testing of carbonized PAN/MnAcac/GNR fiber sheets for conductivity analysis.

Sample	Carbonization Treatment	Conductivity (S/m)
50:45 PAN:MnAcac	Activated – 350°C	116
50:45 PAN:MnAcac	Carbonized – 800°C	555
+ 5% GNR	Activated – 350°C	218

## 2.4 Conclusions

This work has shown a simple method for producing freestanding carbon fiber sheets from both PAN and PVP polymers. This approach cuts out many conventional processing steps, is scalable, and begins from inexpensive precursors. When carbonized, the polymer fiber mats show high surface area, unique pore structure, and high conductivity when carbonized at higher temperatures. The electrospinning

process also easily forms all-carbon composites for incorporation of graphitic carbon samples to improve conductivity when lower temperature carbonization is required.

This approach can also incorporate metal precursors to form freestanding carbon/metal-based composite fiber mats. First, previous group work was replicated using a freestanding approach with carbon and iron acetylacetonate. We then focused on application of carbon fiber and composites to supercapacitor electrodes by forming activated PAN carbon and activated carbon/manganese oxide hybrid fibers. Both activated carbon and activated carbon/manganese oxide were prepared as freestanding electrodes. CV testing showed poor performance of the electrodes, likely due to poor contact and high resistance within the cells whether the electrodes were freestanding or casted slurries. The experiment could be redesigned in the future to reduce the resistance seen in testing or applied to other applications.

After this work was finished, the freestanding carbon and carbon/metal methods were applied by other group members. It was first applied to Li-ion batteries by Dr. Ling Fei. Dr. Fei formed carbon/metal sulfide fiber mats as anodes with no use of conductive binder or additives [Fei (2016)]. The fiber mats showed excellent capacity retention and rate capability for several different metal sulfides. Secondly, the freestanding carbon fiber sheets were used as electrodes in Li-air batteries by Dr. Jangwoo Kim [46]. In Dr. Kim's thesis work, the carbon fibers showed high initial capacity but limited cyclability. A layered approach combining carbon nanofibers with alternating conducting layers of Super P, as well as incorporating fusing of the layered material during stabilization, improved the Li-air cyclability. This modified method shows that the freestanding approach can incorporate other techniques while

maintaining binder-free, direct application as electrodes. Techniques proved in our supercapacitor trials were applied to form high performance electrodes in Li-ion batteries, improved cycling cathodes for Li-air batteries, and could be used in more applications due to its ease of formation and the range of precursors that can work in either PAN or PVP systems.

## 2.5 References

- [1] Dunn, B., Kamath, H. & Tarascon, J.-M. Electrical energy storage for the grid: a battery of choices. *Science* **334**, 928–935 (2011).
- [2] Simon, P. & Gogotsi, Y. Materials for electrochemical capacitors. *Nature Materials* **7**, 845–854 (2008).
- [3] González, A., Goikolea, E., Barrena, J. A. & Mysyk, R. Review on supercapacitors: Technologies and materials. *Renewable and Sustainable Energy Reviews* **58**, 1189–1206 (2016).
- [4] Simon, P. & Burke, A. Nanostructured carbons: double-layer capacitance and more. *Interface* (2008).
- [5] Du, X. *et al.* Preparation of activated carbon hollow fibers from ramie at low temperature for electric double-layer capacitor applications. *Bioresource Technology* **149**, 31–37 (2013).
- [6] Sevilla, M. & Mokaya, R. Energy storage applications of activated carbons: supercapacitors and hydrogen storage. *Energy Environ. Sci.* **7**, 1250–1280 (2014).
- [7] Lee, Y. J., Kim, G.-P., Bang, Y., Yi, J., Seo, J. G. & Song, I. K. Activated carbon aerogel containing graphene as electrode material for supercapacitor. *Materials Research Bulletin* **50**, 240–245 (2014).
- [8] An, K. H. *et al.* Supercapacitors Using Single-Walled Carbon Nanotube Electrodes. *Adv. Mater.* **13**, 497–500 (2001).
- [9] Chen, J. H. *et al.* Electrochemical characterization of carbon nanotubes as electrode in electrochemical double-layer capacitors. *Carbon* **40**, 1193–1197 (2002).
- [10] Kim, B., Chung, H. & Kim, W. Supergrowth of Aligned Carbon Nanotubes Directly on Carbon Papers and Their Properties as Supercapacitors. *J. Phys. Chem. C* **114**, 15223–15227 (2010).

- [11] Zhang, X., Zhang, H., Li, C., Wang, K., Sun, X. & Ma, Y. Recent advances in porous graphene materials for supercapacitor applications. *RSC Adv.* **4**, 45862–45884 (2014).
- [12] Borenstein, A., Hanna, O., Attias, R., Luski, S., Brousse, T. & Aurbach, D. Carbon-based composite materials for supercapacitor electrodes: a review. *J. Mater. Chem. A* **5**, 12653–12672 (2017).
- [13] Winter, M. & Brodd, R. J. What Are Batteries, Fuel Cells, and Supercapacitors? *Chem. Rev.* **104**, 4245–4270 (2004).
- [14] Hu, C.-C., Chang, K.-H., Lin, M.-C. & Wu, Y.-T. Design and Tailoring of the Nanotubular Arrayed Architecture of Hydrous RuO<sub>2</sub> for Next Generation Supercapacitors. *Nano Lett.* **6**, 2690–2695 (2006).
- [15] Wu, Z.-S., Wang, D.-W., Ren, W., Zhao, J., Zhou, G., Li, F., & Cheng, H.-M. Anchoring Hydrous RuO<sub>2</sub> on Graphene Sheets for High-Performance Electrochemical Capacitors. *Adv. Funct. Mater.* **20**, 3595–3602 (2010).
- [16] Yang, L., Cheng, S., Ding, Y., Zhu, X., Wang Z. L., & Liu, M. Hierarchical Network Architectures of Carbon Fiber Paper Supported Cobalt Oxide Nanonet for High-Capacity Pseudocapacitors. *Nano Lett.* **12**, 321–325 (2011).
- [17] Liao, Q., Li, N., Jin, S., Yang, G. & Wang, C. All-Solid-State Symmetric Supercapacitor Based on Co<sub>3</sub>O<sub>4</sub> Nanoparticles on Vertically Aligned Graphene. *ACS Nano* **9**, 5310–5317 (2015).
- [18] Lee, J. W., Ahn, T., Kim, J. H., Ko, J. M. & Kim, J.-D. Nanosheets based mesoporous NiO microspherical structures via facile and template-free method for high performance supercapacitors. *Electrochimica Acta* **56**, 4849–4857 (2011).
- [19] Ren, X., Guo, C., Xu, L., Li, T., Hou, L., & Wei, Y. Facile Synthesis of Hierarchical Mesoporous Honeycomb-like NiO for Aqueous Asymmetric Supercapacitors. *ACS Appl. Mater. Interfaces* **7**, 19930–19940 (2015).
- [20] Du, X., Wang, C., Chen, M., Jiao, Y. & Wang, J. Electrochemical Performances of Nanoparticle Fe<sub>3</sub>O<sub>4</sub>/Activated Carbon Supercapacitor Using KOH Electrolyte Solution. *J. Phys. Chem. C* **113**, 2643–2646 (2009).
- [21] Bryan, A. M., Santino, L. M., Lu, Y., Acharya, S. & D’Arcy, J. M. Conducting Polymers for Pseudocapacitive Energy Storage. *Chem. Mater.* **28**, 5989–5998 (2016).
- [22] Lee, E., Lee, T. & Kim, B.-S. Electrospun nanofiber of hybrid manganese oxides for supercapacitor: Relevance to mixed inorganic interfaces. *Journal of Power Sources* **255**, 335–340 (2014).
- [23] Bose, V. C. & Biju, V. Mixed valence nanostructured Mn<sub>3</sub>O<sub>4</sub> for supercapacitor applications. *Bulletin of Materials Science* **38**, 865–873 (2015).

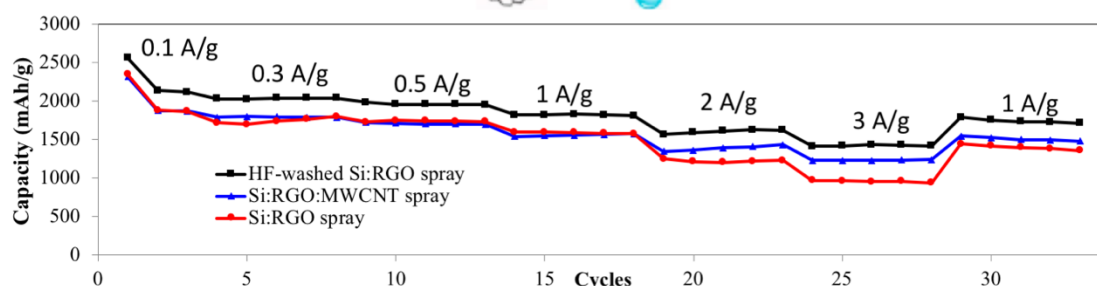
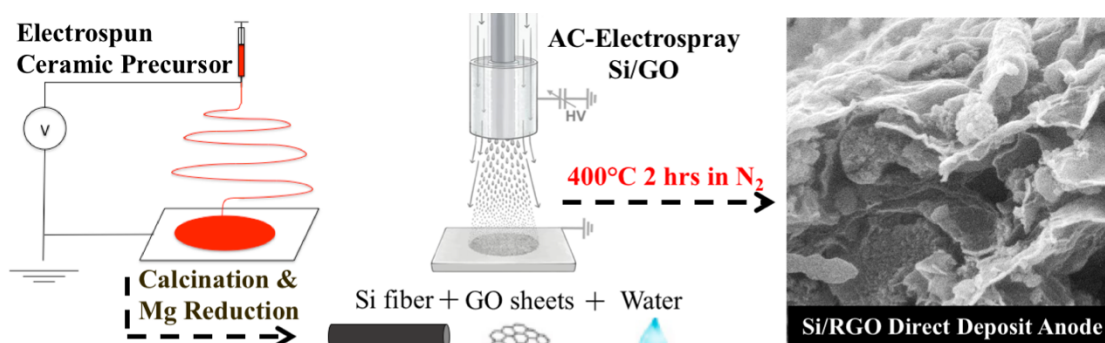
- [24] Xiong, T., Lee, W., Huang, X. & Xue, J. Mn<sub>3</sub>O<sub>4</sub>/Reduced graphene oxide based supercapacitor with ultra-long cyclic performance. *J. Mater. Chem. A* **5**, 12762–12768 (2017).
- [25] Suktha, P., Phattharasupakun, N., Dittanet, P. & Sawangphruk, M. Charge storage mechanisms of electrospun Mn<sub>3</sub>O<sub>4</sub> nanofibres for high-performance supercapacitors. *RSC Adv.* **7**, 9958–9963 (2017).
- [26] Lu, Q., Wang, X., Chen, M., Lu, B., Liu, M., Xing, T., & Wang, X. Manganese Dioxide/Ant-Nest-Like Hierarchical Porous Carbon Composite with Robust Supercapacitive Performances. *ACS Sustainable Chemistry & Engineering* **6**, 7362–7371 (2018).
- [27] Li, D. & Xia, Y. Electrospinning of Nanofibers: Reinventing the Wheel? *Adv. Mater.* **16**, 1151–1170 (2004).
- [28] Kim, C. *et al.* Fabrication of Electrospinning-Derived Carbon Nanofiber Webs for the Anode Material of Lithium-Ion Secondary Batteries. *Adv. Funct. Mater.* **16**, 2393–2397 (2006).
- [29] Ji, L. & Zhang, X. Fabrication of porous carbon nanofibers and their application as anode materials for rechargeable lithium-ion batteries. *Nanotechnology* **20**, 155705–8 (2009).
- [30] Kim, C. & Yang, K. S. Electrochemical properties of carbon nanofiber web as an electrode for supercapacitor prepared by electrospinning. *Appl. Phys. Lett.* **83**, 1216–1218 (2003).
- [31] Ju, Y.-W., Park, S.-H., Jung, H.-R. & Lee, W.-J. Electrospun Activated Carbon Nanofibers Electrodes Based on Polymer Blends. *J. Electrochem. Soc.* **156**, A489–6 (2009).
- [32] Mao, X., Hatton, T. A., & Rutledge, G. C. A review of electrospun carbon fibers as electrode materials for energy storage. *Current Organic Chemistry* **17**, 1390–1401 (2013).
- [33] Lin, H., Zhou, D., Niu, H., Jin, Q. & Qu, F. Synthesis of mesoporous graphitic carbon fibers with high performance for supercapacitor. *Electrochimica Acta* **159**, 116–123 (2015).
- [34] Ko, F. *et al.* Electrospinning of Continuous Carbon Nanotube-Filled Nanofiber Yarns. *Adv. Mater.* **15**, 1161–1165 (2003).
- [35] Guo, Q. *et al.* Supercapacitors based on hybrid carbon nanofibers containing multiwalled carbon nanotubes. *J. Mater. Chem.* **19**, 2810–7 (2009).
- [36] Zhou, Z. & Wu, X.-F. Graphene-beaded carbon nanofibers for use in supercapacitor electrodes: Synthesis and electrochemical characterization. *Journal of Power Sources* **222**, 410–416 (2013).

- [37] Ju, Y.-W. *et al.* A Hydrous Ruthenium Oxide-Carbon Nanofibers Composite Electrodes Prepared by Electrospinning. *J. Electrochem. Soc.* **154**, A192–6 (2007).
- [38] Li, J., Liu, E.-H., Li, W., Meng, X.-Y. & Tan, S.-T. Nickel/carbon nanofibers composite electrodes as supercapacitors prepared by electrospinning. *Journal of Alloys and Compounds* **478**, 371–374 (2009).
- [39] Fei, L., Williams, B. P., Yoo, S. H., Carlin, J. M. & Joo, Y. L. A general approach to fabricate free-standing metal sulfide@ carbon nanofiber networks as lithium ion battery anodes. *Chem. Commun.* **52**, 1501–1504 (2016).
- [40] Panels, J. E. *et al.* Synthesis and characterization of magnetically active carbon nanofiber/iron oxide composites with hierarchical pore structures. *Nanotechnology* **19**, 455612 (2008).
- [41] Stoller, M. D. *et al.* Using coin cells for ultracapacitor electrode material testing. *J Appl Electrochem* **41**, 681–686 (2011).
- [42] Rodriguez-Reinoso, F. & Molina-Sabio, M. Activated carbons from lignocellulosic materials by chemical and/or physical activation: an overview. *Carbon* **30**, 1111–1118 (1992).
- [43] Lee, K. J. *et al.* Activated carbon nanofiber produced from electrospun polyacrylonitrile nanofiber as a highly efficient formaldehyde adsorbent. *Carbon* **48**, 4248–4255 (2010).
- [44] Méndez, A. *et al.* Preparation of carbon-based adsorbents from pyrolysis and air activation of sewage sludges. *Chemical Engineering Journal* **108**, 169–177 (2005).
- [45] Williams, B. P. & Joo, Y. L. Tunable Large Mesopores in Carbon Nanofiber Interlayers for High-Rate Lithium Sulfur Batteries. *J. Electrochem. Soc.* **163**, A2745–A2756 (2016).
- [46] Kim, J. A study of engineering the cathode structures for improved performance in lithium batteries. (Cornell University, 2017).

## CHAPTER 3

### AIR-CONTROLLED ELECTROSPUN SLURRIES OF SILICON FIBERS WITH GRAPHENE OXIDE FOR BINDER-FREE SI/RGO ELECTRODE

#### FABRICATION



#### Graphic Abstract

**Abstract:** The development of lithium-ion anode materials with high capacity and high 1<sup>st</sup> coulombic efficiency has been a common research challenge in recent years. High capacity anodes have been made using silicon nanoparticles, but their high surface area causes significant losses of lithium ions in the first cycle. Coupled with their high cost, this has meant silicon nanoparticles have not been used in consumer batteries. Attempts to use a more affordable, lower surface area, micron-scale silicon faces pulverization issues and severe capacity fade. To address these needs, a multilayered silicon fiber/ reduced graphene oxide (RGO) suspension was directly

deposited onto current collectors with an air-controlled (AC) electrospaying method. The silicon fibers used were made via a magnesium reduction of silica fibers formed from electrospinning. The AC-electrospaying method has several advantages over the conventional slurry-cast approach in that it uses no binder or toxic solvents, sprays dry onto the current collector, and is also industrially scalable. Once sprayed, the electrodes were thermally annealed in a nitrogen atmosphere to form the Si/RGO composite. The fabricated electrodes feature layers of silicon fibers sandwiched in RGO sheets forming a conductive network while also accommodating the mechanical stress from silicon volume expansion. The electrochemical performance of the Si/RGO electrodes shows much better performance than traditional casted preparations and can cycle repeatedly at rates up to 1 A/g. Reversible capacities in half cells can reach more than 1600 mAh/g at 0.1 A/g and 800 mAh/g at the high rate of 1 A/g (based on combined Si/RGO mass). The AC-electrospaying method is a scalable approach to prepare micron-scale silicon anodes.

### ***3.1 Introduction***

Commercial Li-ion batteries use graphite-based anodes due to their excellent conductivity and cycle life. In order to meet goals of decreasing the size of batteries for portable electronics and electric vehicles, higher energy densities must be achieved, and it is necessary to find replacements for low energy density carbon. Lithium metal alloys, such as Sn and Si, are highly promising materials to replace carbon as some of the most energy dense materials [1]. While carbon can lithiate to  $\text{LiC}_6$  with a theoretical specific capacity of 372 mAh/g, tin lithiates to  $\text{Li}_{22}\text{Sn}_5$  for 990

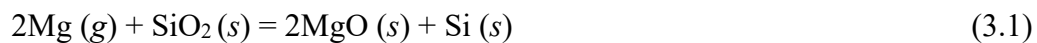
mAh/g and silicon lithiates to  $\text{Li}_{12}\text{Si}_5$  for 4200 mAh/g. With more than 10 times the energy density of carbon, silicon use in batteries could significantly improve the specific energy of lithium ion batteries. However, the materials that have the highest capacity for lithium storage also go through significant expansion during lithiation. Silicon goes through a 320% volume change during lithium insertion and extraction, while carbon only changes by 12% [2]. This expansion leads to material fracture of the alloy particles and disintegration of the anode known as pulverization. Pulverization causes severe capacity fade of the battery and makes silicon unusable for batteries, and must be prevented. While carbon has a moderate energy density, its small volume expansion enables stable cycling hundreds to thousands of times without suffering breaks, giving the batteries excellent capacity retention.

This has led researchers to develop ways to accommodate the volume expansion and protect against pulverization. While many methods have been tested, two have gained significant attention: (1) use of nanoscale silicon to minimize the silicon volume and mitigate the stress of expansion [3] and (2) the use of carbon composite structures to suppress Si volume expansion and provide charge transport pathways for improved electrochemical performance [4]. Together these methods can give stable cycling with higher energy density anodes [5-11]. However, there are drawbacks to both methods. In most cases, the nanostructured silicon and carbon have complex synthesis, are prohibitively expensive, and the composites are made by difficult fabrication. While more energy dense, these electrodes could not replace inexpensive graphite electrodes in battery production.

An additional issue with using silicon nanoparticles and nanowires is that they have high surface areas and they suffer from low initial coulombic efficiency (CE) [12]. In the first cycle, solvents in Li-ion batteries react with lithium at the electrode to form a solid electrolyte interphase (SEI) that cause irreversible capacity loss. By using high surface area nanosilicon, much more lithium is consumed in the first cycle. This requires a difficult prelithiation process or the addition of excess cathode material to account for the lithium lost forming the SEI, hurting energy density. Recently, micron-scale silicon has gained interest due to their cheaper cost, availability, and their better initial CE [13-14]. While there could be many advantages to silicon microparticles, if the micron silicon is not adequately protected, the pulverization of micron silicon exposes new surface area and forms additional SEI, and the efficiency drops and capacity fades quickly. Li from the Cui group at Stanford reported a method to form graphene cages around 1-3  $\mu\text{m}$  Si microparticles [14]. The cages allowed the silicon inside to expand and fracture while maintaining electrical contact with graphene and preventing additional SEI formation inside the cage stabilizing coulombic efficiency. With much lower surface area, the graphene caged particles had much higher first CE, reaching 93.2% - comparable to graphite. While highly effective, growing graphene cages around the particles was process intensive and could not be easily scaled. Until a scalable method of fabricating anodes with micron scale silicon that is protected from pulverization is developed, improving the energy density of lithium ion batteries will be expensive and difficult to increase for consumer applications.

Electrospinning is a facile fabrication process to produce micron to sub-micron fibers [15]. The unique fiber diameter range is below what can be easily achieved

through milling, and as a top-down approach, electrospinning is ideal for preparing micron diameter silicon. There are many examples in the literature of using electrospinning to form silicon fibers for Li-ion anodes [16-19]. In general, silica precursor solutions are electrospun, calcined to form silica fibers, and then reduced to form silicon. The reduction of silica fibers to form silicon fibers was only made viable by the development of magnesium reduction in 2007. There have been other methods that could reduce silica to silicon, but they did not maintain the structural properties through the process and the fiber morphology was lost. Carbothermal reduction requires temperatures at or above 2000°C, which is above the silicon melting point [20]. Silicon reduction can be done using molten salts at 850°C but the reduced materials still do not retain the microscale morphology of the reactants [21]. In 2007, the Sandhage group reported a magnesiothermic reduction that could reduce silica to pure silicon while maintaining intricate nanostructures [22]. The reduction utilizes magnesium gas to form magnesia and silicon from silica.



Solid magnesium is added into a reactor with silica. The two reactants are kept separate. The reactor is then heated to the melting point of magnesium so that a magnesium vapor phase forms and diffuses into the silica sample for reaction. The magnesia formed can be removed by dilute HCl wash yielding silicon. It is important to note that this reaction forms three different silicon-based products: unreacted silica,

silicon, and magnesium silicide. Magnesium can react with silica but also reacts with silicon:



Excess magnesium and mixing of the reactants needed to be avoided.  $\text{Mg}_2\text{Si}$  can be also be washed from the products with HCl. After using Mg reduction, while the 3D nanostructures are maintained, there is an increase in the specific surface area of the reactant after magnesia removal.

A more recent advancement was an improvement in temperature control for Mg reduction. The reduction of silica is highly exothermic, so complete mixing with Mg would lead to high local temperatures. These temperatures are high enough to melt silicon and lose the silicon nanostructure. The Ji group reported that the addition of NaCl into a mixture of silica and Mg to the reactor scavenges the heat from the reaction due to its large heat of fusion at  $800^\circ\text{C}$  [23]. They showed through several tests that local temperatures fall in the range of  $840 - 1100^\circ\text{C}$ . Without salt added, temperatures were above  $1300^\circ\text{C}$ . This improvement allows for a more scalable, large batch reaction of mixed magnesium and silica and has already been applied to silicon anode preparations [24-25]. Temperature control could also provide an outlet for other compounds to be mixed into the reactor, such as placing carbon in the silica material. Where previously carbon and silicon together would form silicon carbide due to the high local temperatures, the salt's presence could allow for silica/carbon composite materials' reduction to silicon/carbon.

Micron-scale silicon fibers can be prepared by electrospinning silica fibers and reducing them using a scalable magnesium/salt reduction. For Li-ion battery use, the fibers will need a conductive coating that can accommodate the stresses of volume expansion and maintain electrical contact with the silicon. More importantly, the coating should be added with a scalable, cost-effective process that can be used to make more energy dense batteries possible. Recently, a technique was reported by our group for preparing directly deposited binder-free active materials with GO by using air-controlled electrospinning [26]. A suspension of graphene oxide sheets and silicon nanoparticles in water formed a layered film when electrospun. The GO layers sandwiched silicon NPs in between the sheets, forming a protective layer for silicon expansion and providing a 3D conductive network for charge transport. The film sprayed dry and formed robust sheets without the use of binder or toxic solvents. The suspension was sprayed directly to current collectors and was then heat treated in inert environment to reduce the GO, increasing the layer's conductivity, to form an RGO/Si anode. The heat-treated electrodes could be used directly as electrodes without any other post processing. When tested, the cells showed exceptional cycle stability cycling above 1500 mAh/g for over 100 cycles at 1 A/g.

This work will build off the results with silicon nanoparticles to test several aspects of electrospinning GO and the use of micron-scale silicon. First, silicon fibers are prepared by electrospinning silica precursors and reducing silica fibers with magnesium. We evaluate whether silicon fibers require an HF-wash post reduction to remove partially reduced/unreacted silica, as HF is hazardous to add to a process. The HF-washed and unwashed silicon are prepared as anodes by conventional casted

slurries and by air-controlled electrospinning deposition. The anodes are cycled for 100 cycles at high current density (1 A/g) to gauge the success of RGO layers to mitigate pulverization of micron silicon fibers and maintain cycle life. Additionally, rate capability of the GO process was not previously tested. In this work, RGO/Si anodes are tested at higher current densities up to 3 A/g. To improve rate capability, MWCNT are added into the GO suspension for higher conductivity and improved charge transport. Finally, addition of MWCNT into the silica precursor solutions as a way to form silicon/MWCNT composite fibers is tested and shown as a potential direction for future work.

## ***3.2 Experimental***

### **3.2.1 Mg Reduced silica fibers for RGO/Si anodes**

Silica fibers were prepared by electrospinning silica precursor. First a solution of 3.5 g of ethanol, 1g of acetic acid (glacial), and 0.75 g of PVP (1,400,000 MW, Sigma Aldrich) were mixed together. A second solution was prepared with 4 g of distilled water and 1.5 g of TEOS. Water and TEOS were stirred together for 10 minutes before being added to the ethanol/acetic acid/PVP solution. The combined sol-gel was stirred by vortex for 1 minute and then set in a sonication bath for 30 minutes. After sonication, the sol-gel was gently stirred for 30 minutes before electrospinning. Electrospinning parameters used a 20-gauge needle, 0.02 ml/min flow, 15cm distance, and 15kV applied. Electrospun fibers were calcined at 650°C for 4 hours in air at 5°C/min.

Silica samples were then ground up and placed into a salt solution of water and NaCl. Silica:NaCl weight ratio was kept at 1:10 as described by Luo *et al* [23]. The solution was stirred and sonicated for an hour each and then dried in a vacuum oven. Once dried, the powder was moved to an Argon-filled glove box. A 1:1.1 weight ratio of silica to Mg powder (50 mesh, Sigma Aldrich) was ground together with a mortar and pestle and placed in a Swagelok steel reactor (Fig 3.1). The reactor was then placed in a tube furnace under Argon flow and heated at 5°C/min to 725°C for 6 hours. Once cooled the powder goes through a two-step washing process: 1) rinse with ethanol and water and 2) soak in 2M HCl (Sigma Aldrich) for 4 hours. This removes deposited magnesium oxide but any unreacted or partially reacted SiO<sub>2</sub> would remain. For unreacted SiO<sub>2</sub> removal, the powder was also washed with a dilute 5 wt% HF solution.



**Figure 3.1.** A steel Swagelok reactor (1/2 in. fittings) used for magnesiothermic reduction of silica.

Suspensions of silicon fiber, GO sheets (Dongjin Semichem), and multiwalled carbon nanotubes (EMD) were prepared in distilled water. The tested suspensions are listed in Table 3.1. Samples were stirred for an hour and sonicated for 30 minutes before electrospaying. AC-electrospaying was used to deposit ~1mg of material onto 2cm<sup>2</sup> copper foil circles as Li-ion anodes. A 13/17 gauge co-axial nozzle was used

with 25 psi air pressure, 20 kV, 20 cm collector distance, and 0.05 ml/min flow rate. Once deposited, the anodes were heat treated in a tube furnace to reduce GO (RGO). Electrodes were heated to 400°C for 2 hours at 2°C/min under nitrogen environment.

**Table 3.1.**

Suspension preparations for GO/Si fiber AC-electrospraying solutions.

ID	HF wash?	Si Fiber (mg)	GO (mg)	MWCNT (mg)	H <sub>2</sub> O (g)
2:1 Si:GO	No	120	60	0	8
120:40:8 Si:GO:MWCNT	No	120	40	8	8
2:1 HF Si:GO	Yes	120	60	0	8

For comparison, silicon fiber anodes were prepared by a conventional slurry preparation. A solution of silicon fibers, Super P, and polyacrylic acid (PAA, 3,000,000 MW, Sigma Aldrich) in a 70:15:15 weight ratio was ground together by mortar and pestle with N-methyl-2-pyrrolidone solvent (NMP, Sigma Aldrich). Once homogeneous, the solution was drop-casted onto copper foil circles and dried in a vacuum oven overnight. These were tested for the three different Si samples: the partially reduced Si, the HF washed Si, and the Si with intrafiber MWCNTs.

Electrochemical testing was carried out using CR2032 size coin cells. Half-cell Li-ion battery testing used the prepared anodes with a Celgard 2400 separator, Li foil as a cathode, and a 1M LiPF<sub>6</sub> electrolyte solution (MTI). Cell cycling used a voltage range of 0.01 to 1.5 V. Anodes were cycled at 0.1 A/g for 5 cycles and then increased to 1 A/g for 95 cycles. All rate capability tests began at 0.1 A/g and increased current

every 5 cycles up to 3 A/g. Charge and discharge currents were matched each cycle until high currents were reached. Charge current was not increased above 1 A/g.

### 3.2.2 Preparation of silicon fibers with internal MWCNTs

For improved cycling and rate capability of micron-size silicon fibers, silicon with MWCNTs in the core of the fiber were developed. These are named Si@MWCNT to denote MWCNTs are within the fibers and not just in a GO suspension with them. SiO<sub>2</sub>@MWCNTs are prepared similarly to the silica fibers except 42.7 mg of MWCNTs are added to the 4g of distilled water before TEOS is added. The water and MWCNTs were sonicated for 30 minutes to disperse the MWCNTs and then TEOS was added. Nothing else was changed in solution preparation. Electrospinning parameters were also largely the same except that a larger needle, 18-gauge instead of 20-gauge, was used due to increased viscosity of the solution. Due to burnoff of MWCNT near 600°C in air, heat treatment needed adjustment, and two different heat treatments were tested for the MWCNT samples: 1) a lower temperature calcination at 500°C for 4 hours in air at 5°C/min and 2) carbonization reaction at 650°C for 4 hours in nitrogen at 5°C/min. The carbonization in N<sub>2</sub> will have silica, MWCNTs, and carbonized PVP after heat treatment. PVP is burnt off in the previous air treatments at 500°C and 600°C. Both samples are reduced separately using the same magnesium reduction method. The two samples are notated as Si@MWCNT (calcined at 500°C) and C/Si@MWCNT (carbonized at 650°C).

### ***3.3 Results and Discussion***

#### **3.3.1 Mg Reduced silica fibers for RGO/Si anodes**

Preparation of micron-scale silicon fibers began with electrospinning a TEOS sol-gel. Typical TEOS sol-gels increase in viscosity until they reach a short time period where they are spinnable. To avoid having a short spinning period, PVP was added to aid fiber formation. During calcination, PVP is burned away and the TEOS forms a silica fiber. Once calcined, the silica fibers were placed in a reactor with elemental magnesium and heated to be reduced to silicon. A wash process was used to remove all magnesium products. The fibers at this time are a combination of silicon and some unreacted or partially reduced silica. Purified silicon fibers that were washed with dilute HF will be notated as HF washed Si fibers.

Figure 3.2 shows SEM images of the fiber morphology at each stage and the fiber size distributions. The average fiber diameters are  $1950 \text{ nm} \pm 775 \text{ nm}$ ,  $762 \text{ nm} \pm 368 \text{ nm}$ , and  $983 \text{ nm} \pm 560 \text{ nm}$  for the spun PVP/TEOS, calcined silica, and silicon fibers respectively. Fiber size distributions show our final silicon fibers at the desired diameter of micron scale with all fibers falling in the range of 0.4-3.2  $\mu\text{m}$ . An important physical change in the silicon fibers, compared to its previous polymer or silica forms, was that the fibers became very brittle and they have a chopped appearance. Instead of long, continuous fibers, the silicon fibers are now 5 to 10  $\mu\text{m}$  in length. The brittleness has been an issue in trying to use the silicon fibers as a freestanding sheet like our approach in other electrospinning applications, but it is not an issue for AC-electrospraying. The brittleness largely comes from the mesopores formed inside the silicon fibers during the reduction. Table 3.2 and Figure 3.3 shows

the N<sub>2</sub> physisorption pore data before and after magnesium reduction. As was seen in the original work by Bao *et al.*, the removal of oxygen by Mg vapor maintains the overall structure of the silica material but creates additional pore surface area [22]. BET analysis shows that the overall surface area is similar before and after reduction, but a large number of micropores in the silica structure have increased to the mesoporous range and they are clearly depicted in the BJH pore distribution.

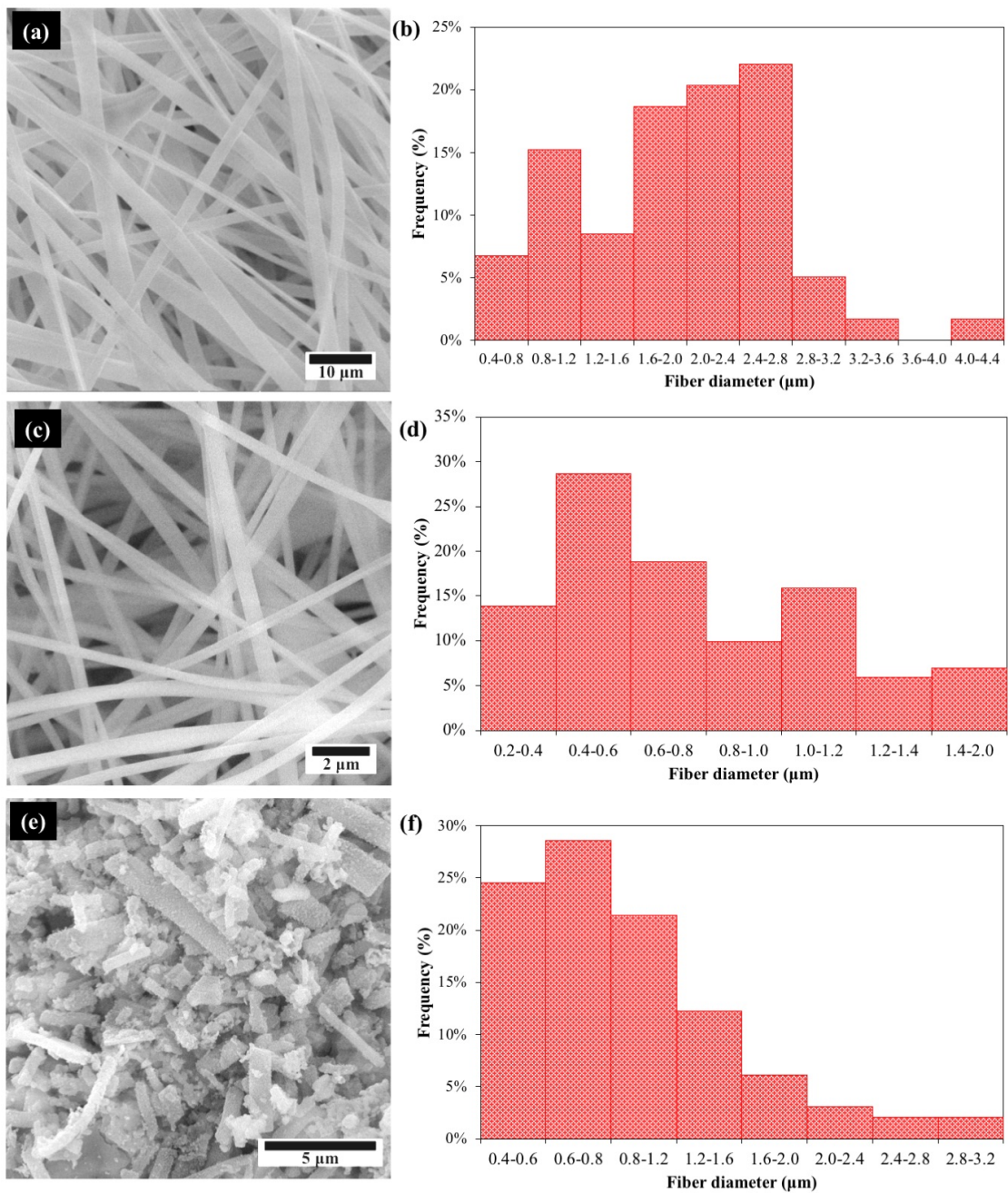


**Figure 3.2.** SEM images of the fibers and their fiber diameter distributions of (a,b) As spun PVP/TEOS fibers, (c,d) calcined silica fibers, and (e,f) silicon fibers after Mg reduction.

**Table 3.2.**

Summary of BET data for silica and silicon fibers. Microporous area refers to surface area provided by pores 2 nm or smaller.

Sample	BET (m <sup>2</sup> /g)	Mesoporous area (m <sup>2</sup> /g)	Microporous area (m <sup>2</sup> /g)
Silica Fibers	116.2	32.3	83.9
Silicon Fibers	161.2	137.2	24.0

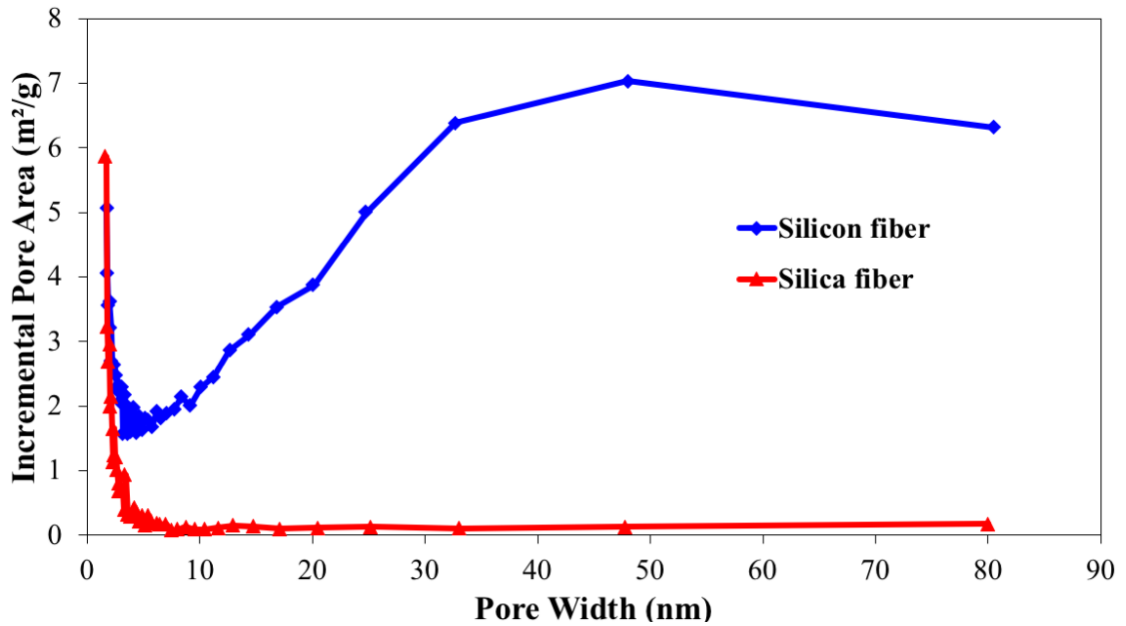


**Figure 3.3.** BJH pore distribution plot silica and silicon fibers.

The reduction of silica to silicon was confirmed by XRD. Figure 3.4 shows the XRD of the fibers before and after Mg reduction. The silica sample shows an expected broad peak between 20 and 30 degrees of amorphous silica. After reduction, XRD shows sharp peaks that correlate to those of silicon.

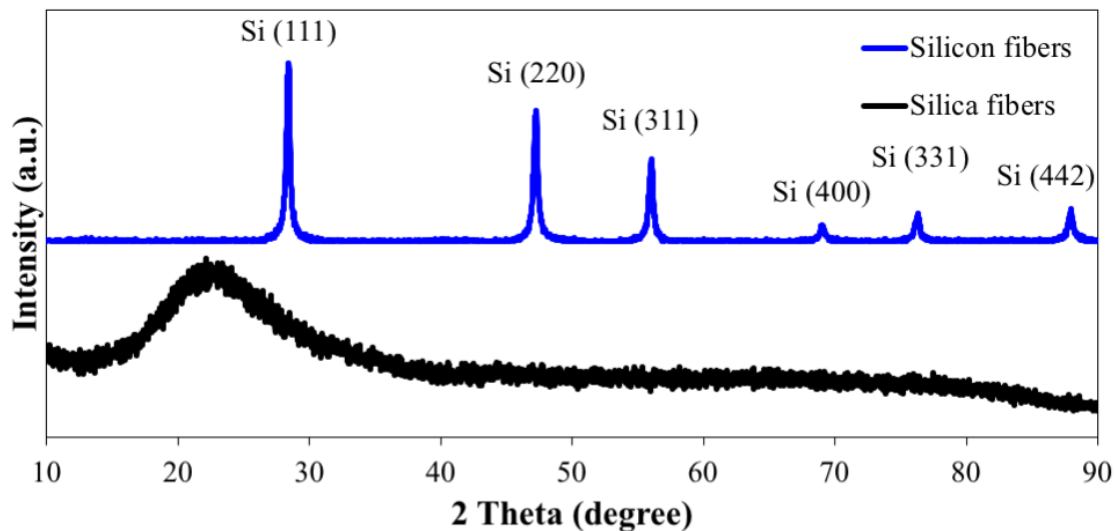


**Figure 3.4.** XRD of silica fibers before and after Mg reduction. Mg reduction shows that the silica fibers were reduced to silicon.

Silicon fibers were then mixed with GO sheets and MWCNT in suspensions for direct deposition onto copper current collectors. These two carbon nanomaterials serve different purposes for anode performance. The use of GO is required for direct deposition due to its natural adhesive properties and avoids the use of binder. When a GO-suspension is sprayed, it forms a layered film on a current collector. Additionally, that layering has been shown by Fei *et al.* to trap particles and fibers during the electrospinning process [26]. GO is not the most conductive carbon, but by reducing GO (RGO) the electrical conductivity is improved. MWCNTs are added purely for electrical conductivity improvement. In general, these highly graphitic carbon tubes have better conductivity than the further oxidized carbons, like GO and RGO, and can aid charge transfer from the resistive silicon fibers to the RGO network. An additional advantage is that both GO and MWCNTs can be dispersed in water and the electrospinning process can avoid toxic solvents. As previously stated, this avoids many of the issues with current industrial practices. Figure 3.5 shows SEM images of

both GO and MWCNTs. The GO sheets have been electrospayed showing their layering. The GO sheets have widths in the range of 10-20 microns and can easily entrap the 1- $\mu\text{m}$  diameter fibers. The MWCNTs have an average diameter of 75 nm.

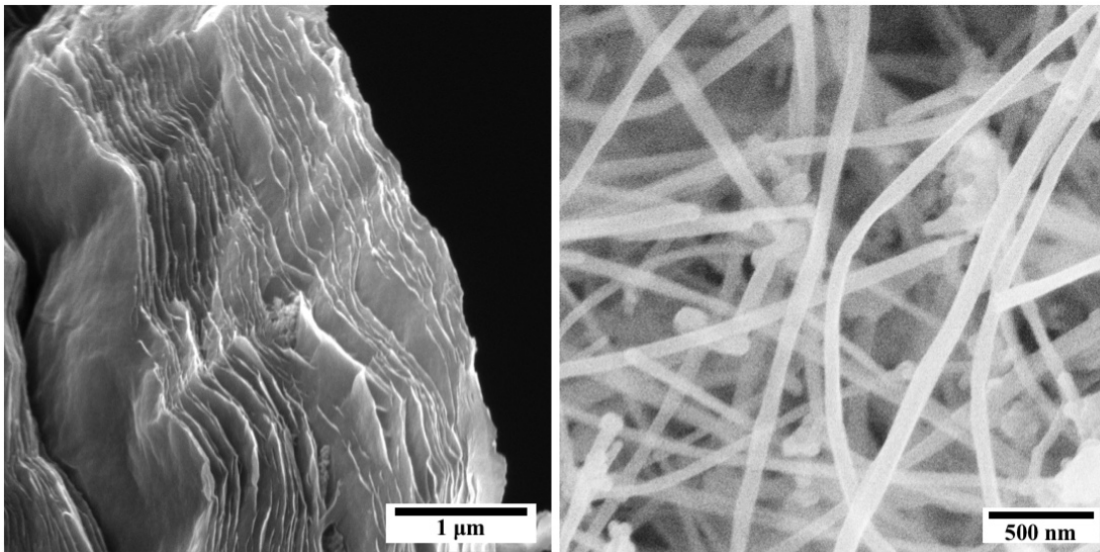


**Figure 3.5.** SEM images of AC-electrospayed GO sheets (left) and MWCNTs (right).

Five different anode preparations were evaluated to test for the effect of direct deposit fabrication, MWCNT additions, and silicon purity:

1. 70/15/15 Si fiber/Super P/PAA drop-casted slurries
2. 2:1 Si fiber/RGO AC-electrospayed direct-deposit anodes
3. 70/15/15 HF-washed Si fiber/Super P/PAA drop-casted slurries
4. 2:1 HF-washed Si fiber/RGO AS-electrospayed direct-deposit anodes
5. 120:40:8 Si fiber/RGO/MWCNT AC-electrospayed direct-deposit anodes

Solutions of GO and silicon fibers were electrospayed with and without MWCNT.

When MWCNT were added, they replaced a portion of the GO additions in an attempt to keep the total silicon loading equal across all electrospayed samples. The samples were then heat treated in  $\text{N}_2$  to thermally reduce GO and form 2:1 Si:RGO and 120:40:8 Si:RGO:MWCNT anodes. The electrospayed films were first characterized

by TGA to confirm the silicon content in each sample (Figure 3.6). RGO burned off at 400°C while MWCNT burned off at 600°C. The 2:1 Si:RGO samples had an 80% silicon content found from the minimum value of the TGA. Two minimums were evaluated in the RGO/MWCNT sample to give approximately 82% silicon. The two preparations had similar silicon contents for electrochemical testing.

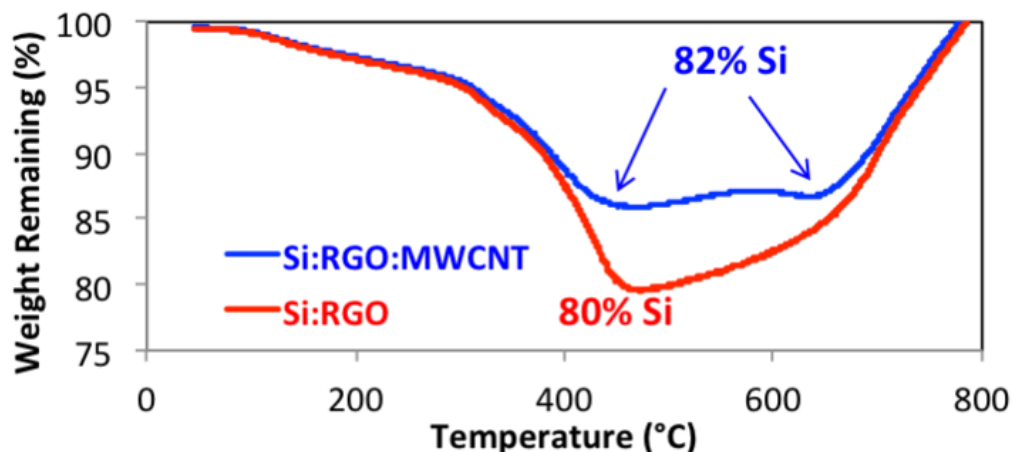


**Figure 3.6.** TGA analysis of AC-electrosprayed samples of the 2:1 Si fiber:RGO and the 120:40:8 Si fiber:RGO:MWCNT samples.

SEM images of the prepared anodes are shown in Figure 3.7. The drop-casted slurry shows the silicon fibers are in clumps surrounded by conductive binder. The binder will offer limited protection to the micron diameter silicon fibers. The AC-electrosprayed direct-deposit anodes show a surface of smooth GO sheets and silicon fiber pieces. One issue with this preparation is that there are exposed silicon fibers on the surface not protected by GO. Future work with this process could involve capping the anodes with a pure GO AC-electrospray to protect all silicon. Cross-section images show that silicon fibers are sandwiched within the RGO layers. Additionally, looking at the cross section of the Si:RGO:MWCNT sample we can see the MWCNTs dispersed into the layers with the silicon fibers.

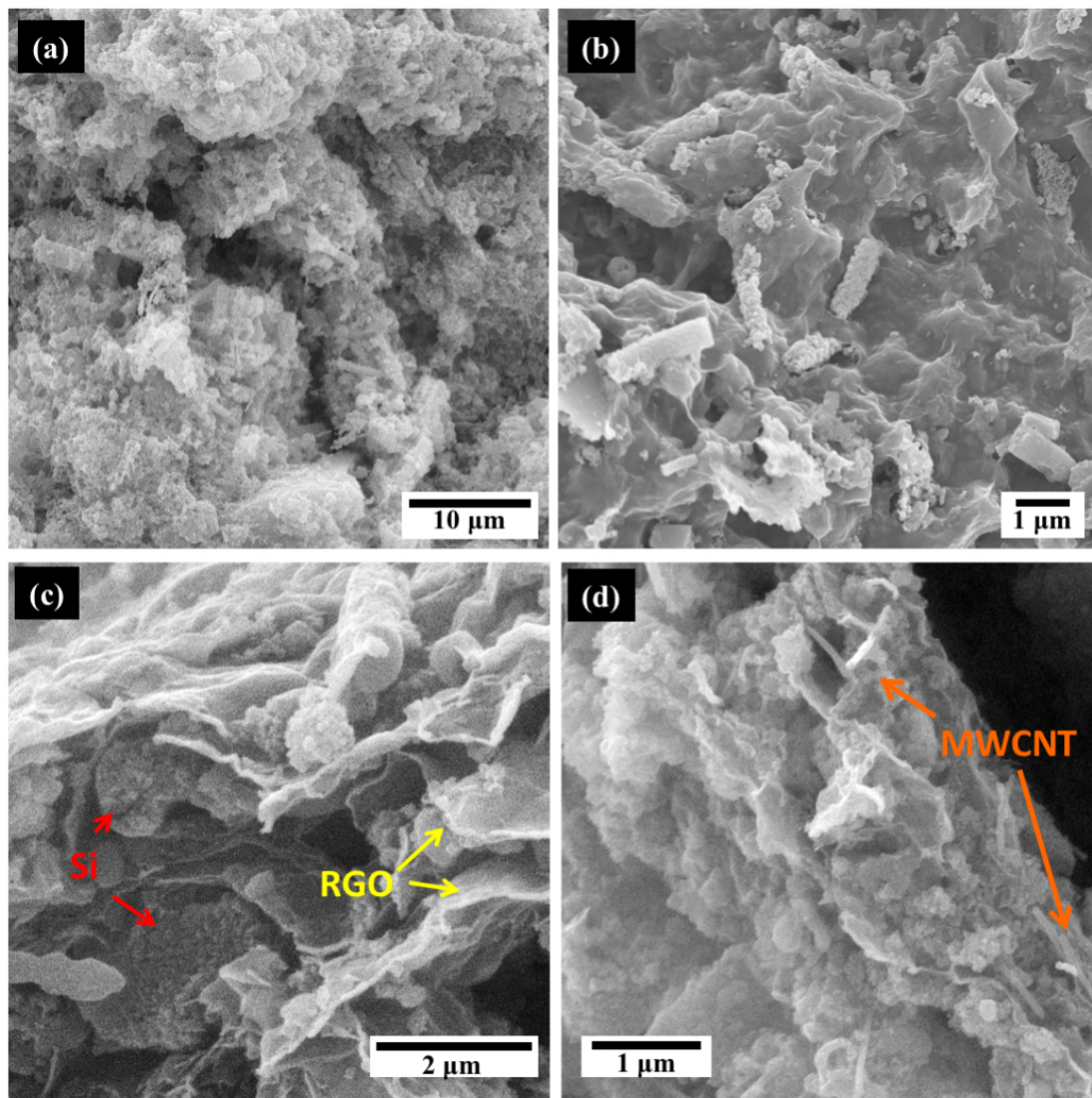


**Figure 3.7.** SEM images of silicon fiber anode preparations: (a) top view of a drop-casted 70/15/15 Si fiber/Super P/PAA, (b) top view of a direct deposit AC-electrosprayed Si fiber/GO anode, (c) cross-section of an AC-electrosprayed Si/RGO anode, (d) cross-section of an AC-electrosprayed Si:RGO:MWCNT anode.

The prepared anodes were assembled into half cells with Li metal for evaluation. Figure 3.8 compares early cycles of drop-casted slurries and AC-electrosprayed silicon, as well as the effect of HF-washing and purifying the silicon fibers. Silicon fibers have two notations. Si fiber refers to reduced silica fibers that have had magnesium products rinsed away with HCl. The HF-washed Si fibers were

prepared the same way but with an additional washing in dilute HF to remove any unreacted silica. This HF washing step is not easy to industrialize, as it is the most hazardous chemical needed to prepare the silicon fibers and requires strict safety precautions. If the use of HF can be avoided when making our Si fiber/RGO anodes, then it would be beneficial to scaling the process.

The drop-casted slurries were tested at 0.1 A/g in the voltage range of 0.01-1.5 V. The direct-deposit anodes, with better protection and conductivity, were cycled at 0.1 A/g for 5 cycles before increasing to 1 A/g current density. All capacity measurements account for total electrode mass – silicon, binder, Super P, RGO, and MWCNTs – and not just silicon. The silicon loading for the slurries (70%) are lower than the loading in the direct-deposit anodes (80-82%) and should show a lower initial capacity.

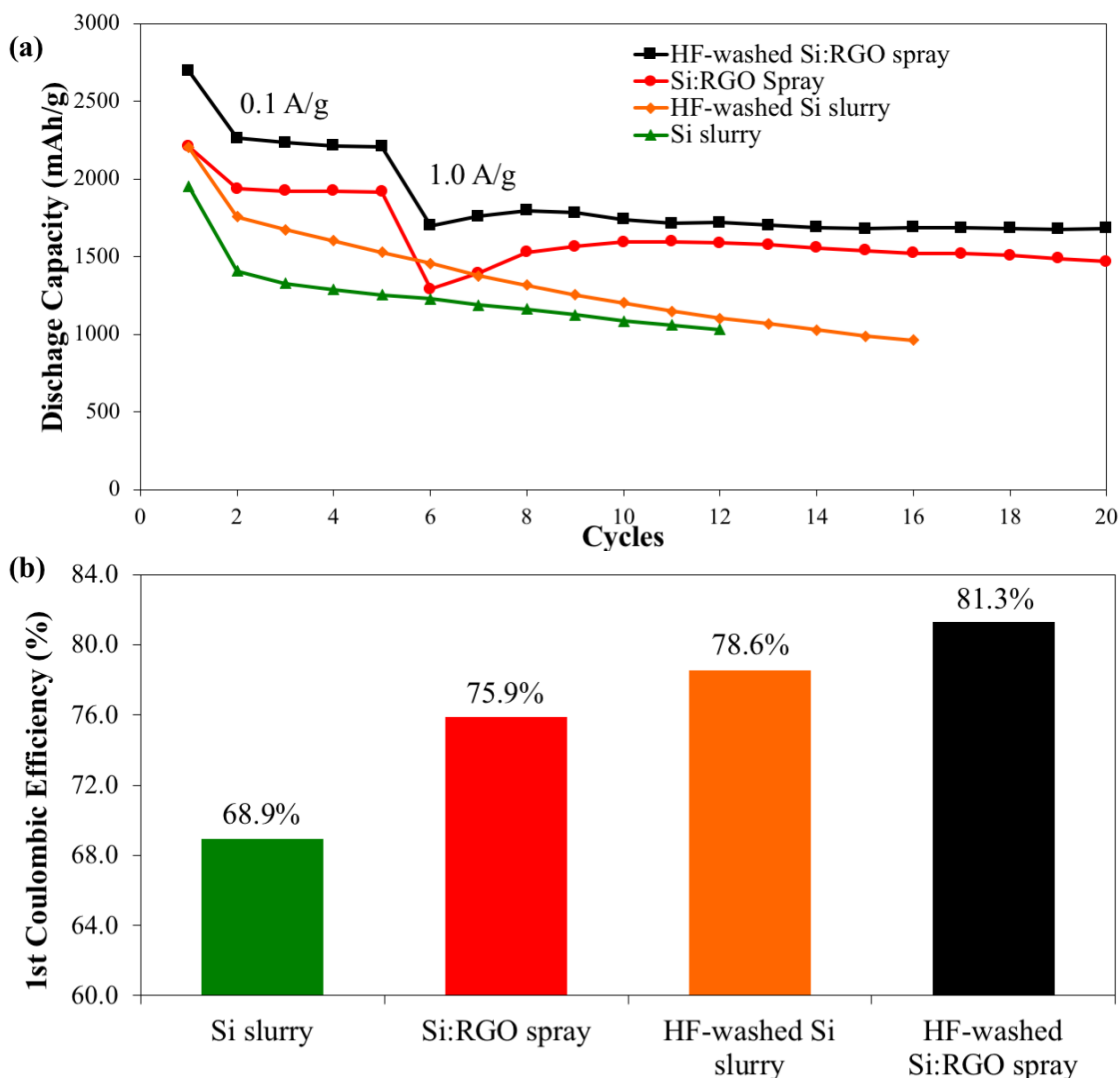


**Figure 3.8.** (a) the cycling performance of half-cells of silicon fiber slurries and direct-deposit electrosprays. Slurries were kept at 0.1 A/g while AC-electrospayed anodes show 0.1 and 1 A/g cycling. (b) The 1<sup>st</sup> cycle coulombic efficiency (CE) of cells tested.

Cycling performance shows several important effects of both the AC-electrospaying method and the purity of the silicon after HF-washing. Drop-cast electrodes show a steady decline in capacity at low current density. The micron-sized silicon immediately has issues in the casted approach. The electrospayed samples show steady cycling and limited capacity loss in early cycles. Even when the electrospayed anodes increase current density 10-fold to 1 A/g, they show a more

stable cycling capacity. The HF-washed silicon also has a significant effect on the capacity. There is a shift in the graphs with the increased purity, as non-electroactive silica has been removed from the samples. The HF-washed Si:RGO sprayed sample and the Si:RGO sprayed sample cycle above 2200 mAh/g and 1900 mAh/g at 0.1 A/g respectively. At 1 A/g the samples cycle at high capacities above 1700 and 1500 mAh/g for HF-washed Si:RGO and Si:RGO respectively. The improvements from direct-deposit and HF washing can be observed in the initial cycle from the coulombic efficiency. The electrospayed, HF-washed silicon shows the highest CE of 81.3%. The electrospayed anodes outperformed the casted anodes, but the HF-washing is more significant to the 1<sup>st</sup> CE as both the HF-washed slurry and electrospayed anodes outperformed the impure silicon anodes. The impurities still present are hurting anode performance through consumption of lithium or undesirable side reactions. In practice, additional cathode material must be added to account for 1<sup>st</sup> cycle losses making it imperative to have high 1<sup>st</sup> CE.

With a focus on the cycle life of direct-deposit anodes, Figure 3.9 shows a full 100 cycles for the 3 AC-electrospayed preparations. This is an extension of Figure 3.8 where cells ran 5 cycles at 0.1 A/g and now runs 95 cycles at 1 A/g. The 120:40:8 Si:RGO:MWCNT sample has also been added for comparison.

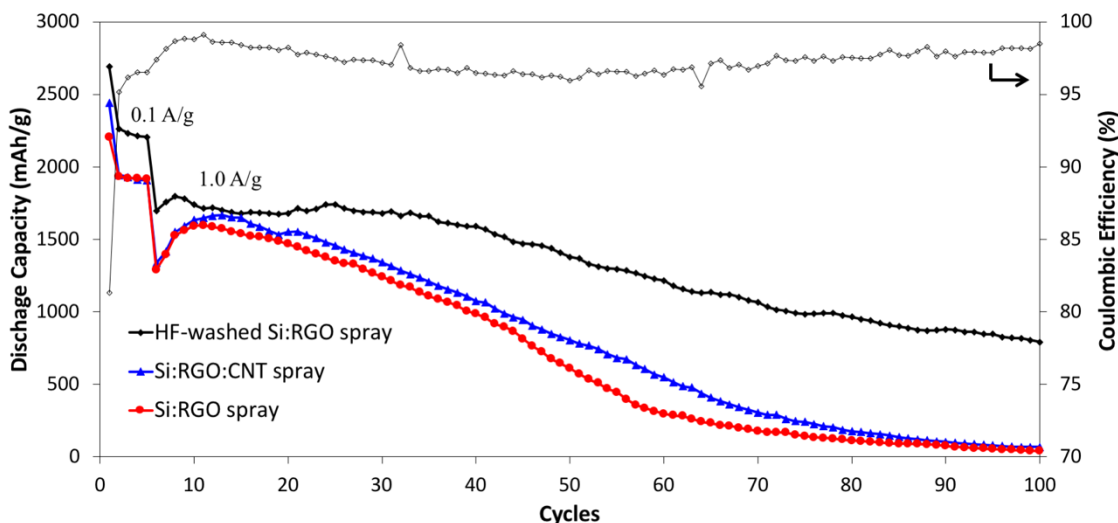


**Figure 3.9.** cycling performance of Si:RGO, Si:RGO:MWCNT, and HF-washed Si:RGO anodes prepared by the direct-deposit AC-electrospray method. Half-cells are tested for 5 cycles at 0.1 A/g and then 95 cycles at 1 A/g. Coulombic efficiency is charted for the HF-washed Si anode.

Cycling shows that only the HF-washed silicon sample can survive 100 cycles at 1 A/g. The unwashed silicon fibers, with and without MWCNTs present, remain above 1000 mAh/g for only 40 cycles and steadily lose all capacity by 100 cycles. The HF-washed Si:RGO spray shows remarkable capacity and capacity retention for micron-sized silicon. The HF-washed samples had a specific capacity of 1700 mAh/g in its 6<sup>th</sup> cycle and slowly decreased to 800 mAh/g by 100 cycles for a 46.5% capacity retention at 1 A/g. This is quite strong for such high silicon loading and a relatively high current density although it would be problematic for any real application. One concern for this approach is the coulombic efficiencies during cycling. The coulombic efficiencies (charted for the HF-washed silicon) are above 95% but carbon covered silicon can achieve far closer to 100%. The consistent loss of capacity and the lower coulombic efficiency are a sign that pulverization is occurring, but at a far lower rate than is demonstrated in other anode preparation methods.

The rate capability of the three direct-deposit anodes was also tested. Electrochemical tests began at charge/discharge currents of 0.1 A/g for 3 cycles and increased every 5 cycles with 3 A/g as the highest discharge current density. Charging current density was limited to a max of 1 A/g. The cycling data is shown in Figure 3.10 and the capacities at each rate and the rate retention are summarized in Table 3.3. The specific capacity values are taken from the third cycle at each rate and the rate retention is compared to the specific capacity at 0.1 A/g.

**Table 3.3.**

Summary of specific capacity and rate retention data of Figure 3.10 broken down by sample and current density.

Current Density (A/g)	Si:RGO spray		Si:RGO:MWCNT		HF Si:RGO spray	
	Capacity (mAh/g)	Rate Ret. (%)	Capacity (mAh/g)	Rate Ret. (%)	Capacity (mAh/g)	Rate Ret. (%)
0.1	1866	100.0%	1871	100.0%	2115	100.0%
0.3	1737	93.1%	1794	95.9%	2038	96.4%
0.5	1746	93.6%	1704	91.1%	1960	92.7%
1	1591	85.3%	1555	83.1%	1832	86.6%
2	1201	64.4%	1392	74.4%	1613	76.3%
3	953	51.1%	1227	65.6%	1434	67.8%

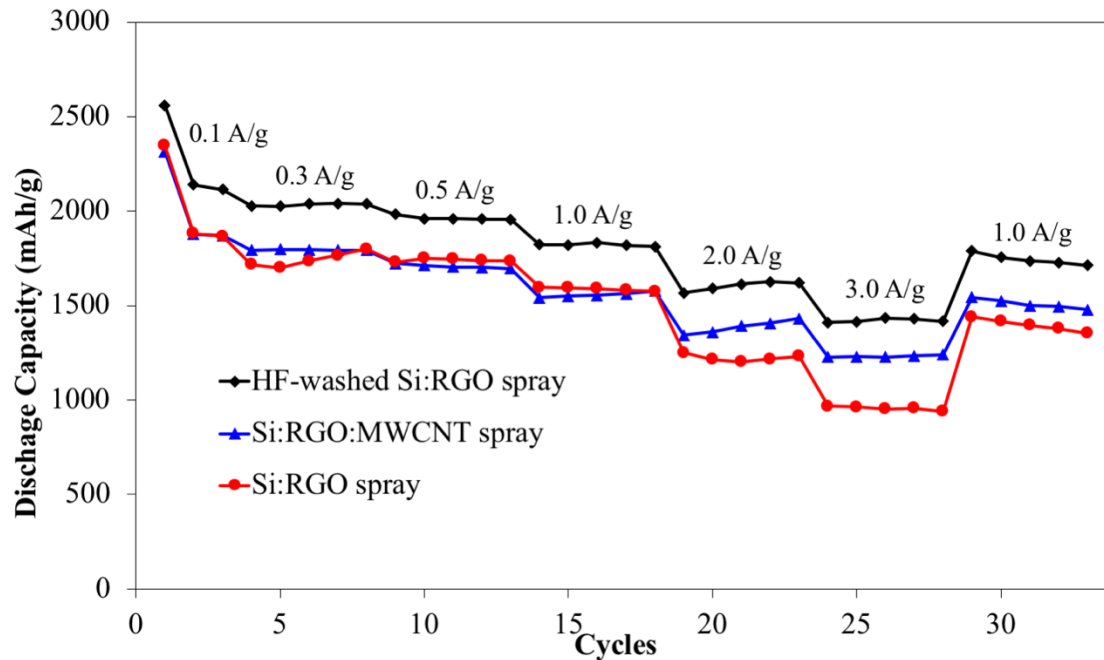


**Figure 3.10.** Rate capability of direct-deposit Si:RGO, Si:RGO:MWCNT, and HF-washed Si:RGO anodes from 0.1 A/g to 3 A/g.

All three samples show excellent rate capability with reversible capacities of 953, 1227, and 1434 mAh/g for Si:RGO, Si:RGO:MWCNT, and HF-washed Si:RGO samples respectively. These values correspond to half or 2/3 of their 0.1 A/g capacities at a 30-fold increase in current density. Similar to the cycling data, the HF-washed silicon sample shows a higher capacity at all current densities, but the removal of

impurities led to an improvement in the rate retention at all tested current densities. The Si:RGO:MWCNT also demonstrated a high rate retention with more than 10% improvement over the Si:RGO spray at current densities of 2 and 3 A/g. The MWCNTs did not help cycling stability but improving the charge transport was important for high rate application. The HF-washing is important to the first coulombic efficiency and the cycle life of micron-size silicon, and it improves rate capability significantly without adding graphitic carbon. That processing step would be necessary for any silicon prepared by Mg reduction.

### **3.3.2 MWCNT placement inside silicon fibers (future direction)**

Our work Si fibers showed that using MWCNTs in place of RGO could improve rate capability without decreasing the active material loading but had almost no effect on their cycle life and stability. This surface-level addition of MWCNT may not have aided the cycling of the Si fibers, but MWCNT could be more impactful if the MWCNTs were inside the silicon fibers. By forming our fibers with electrospinning, there is an opportunity to apply the conductive carbon precursor solution and disperse the MWCNTs along the fibers. The question is whether the MWCNTs can survive the high heats of calcination and Mg reduction needed to form silicon, or if the addition of carbon into these reactions creates undesirable side products, such as carbides. Calcination at 550°C is below the burnoff temperature seen in the TGA for MWCNT. The Mg reduction is hugely exothermic and can create large local temperatures above 1200°C. This temperature is more than enough for C and Si to react to form SiC. By using the salt in the reduction to scavenge heat, local

temperatures remain lower, possibly below 1000°C, and the SiC should not form yielding silicon with intrafiber conductive carbon for fast charge transport.

PVP/TEOS/MWCNT fibers were prepared by electrospinning. The fibers were then heat treated by two methods: 1) low-temperature calcination in air and 2) normal temperature carbonization in an inert environment. Low-temperature calcination risked MWCNT burnoff and carbonization risked carbide formation. TGA was used to determine carbon contents of these fibers. The SiO<sub>2</sub>@MWCNT samples (air calcined) showed 5 wt% carbon content – all due to MWCNT. Based on initial loadings, 9 wt% MWCNT content was expected, so almost half of the MWCNTs were lost during calcination. It may be possible to decrease calcination temperature to maintain more of the MWCNTs. The C/SiO<sub>2</sub>@MWCNT fibers (carbonized) had 12.6 wt% carbon with about 9% due to MWCNTs and 3.6% from carbonized PVP polymer. Both fiber preparations were used in Mg reductions.

SEM imaging of the spun fibers, the calcined/carbonized fibers, and the Mg reduced fibers are shown in Figure 3.11. The fiber diameters are reported in Table 3.4. The fiber morphology is maintained in both cases through Mg reduction. Air calcined samples' diameters vary, with many small diameter fibers present after calcination that are not clearly present in the reduced sample – possibly broken into unmeasurable pieces. After reduction, MWCNT can be seen in both samples. The fibers prepared with MWCNTs are not as uniform as the polymer/precursor approach, but the micron size was maintained.

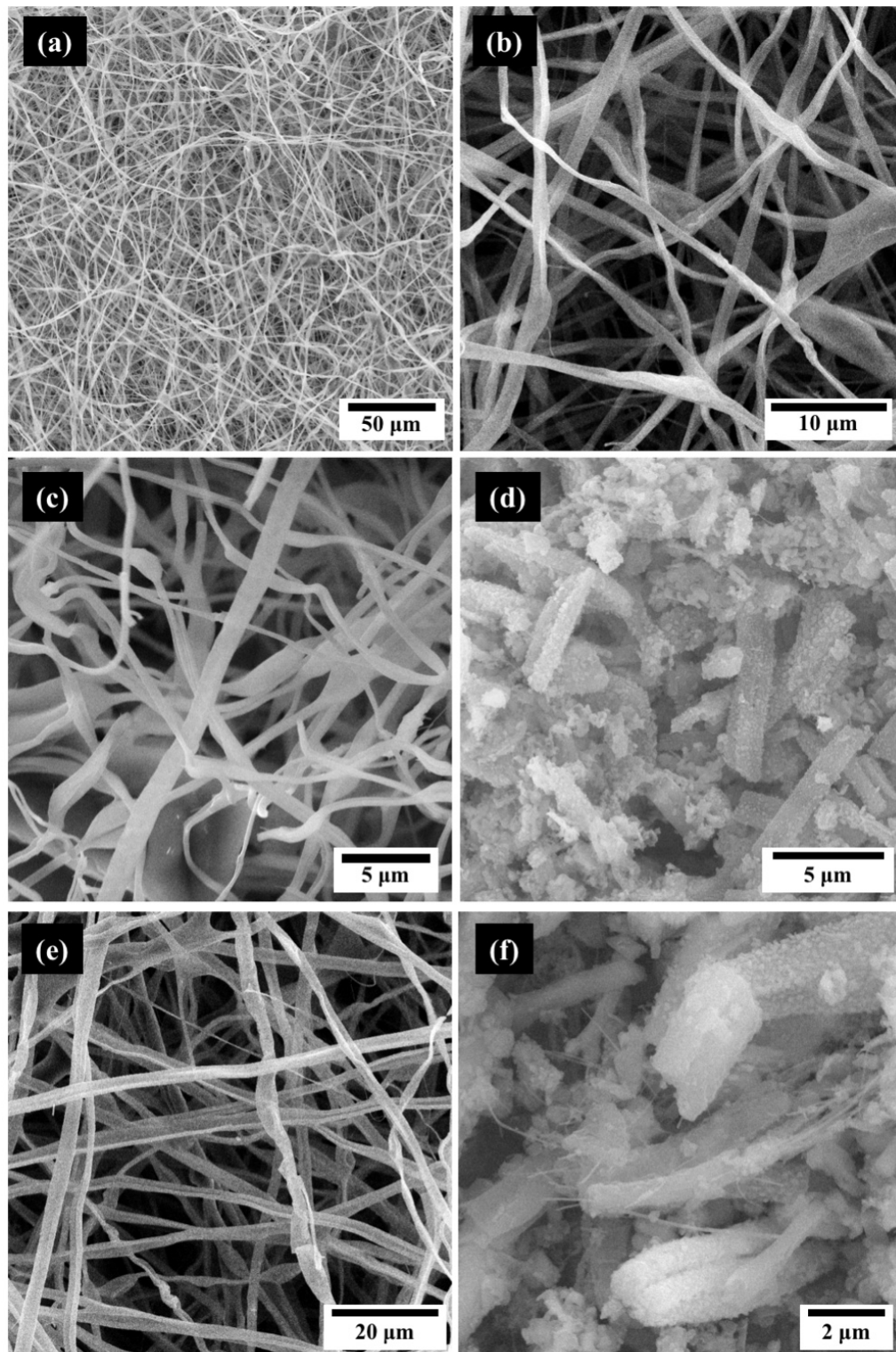


**Figure 3.11.** SEM imaging: (a) and (b) show as spun PVP/TEOS/MWCNT samples. (c) fibers after calcination in air and (d) shows the air calcined fibers after Mg reduction. (e) precursor fibers after carbonization under N<sub>2</sub> environment and (f) shows the N<sub>2</sub> carbonized fibers after Mg reduction.

**Table 3.4.**

Fiber diameters of silica with MWCNT fibers at different stages of processing.

<b>Heat Treatment</b>	<b>Fiber Diameter (nm)</b>
As Spun Precursor/CNT	1130 +/- 420
Calcine 550°C under air	650 +/- 460
Air calcined Si@CNT	1370 +/- 515
Carbonize 650°C under N2	2110 +/- 620
N2 carbonized Si@CNT	880 +/- 395

XRD was used to check for silicon, side reactions, and MWCNT presence and is shown in Figure 3.12. MWCNTs show a strong peak at  $\sim 28^\circ$  for graphitic carbon. This peak should be present in any sample containing MWCNT. The carbonized samples show peaks for several different materials including silicon, graphitic carbon, and an additional peak between 30 to 40 degrees. Though the peaks are not sharp, this is the area we would expect to see SiC peaks form. The air calcined sample shows strong silicon signatures and a weak bump at  $\sim 28^\circ$ , confirming that MWCNTs are present but in smaller concentrations than in the carbonized sample. There is no indication of a peak between 30 and 40 degrees for the air calcined sample.

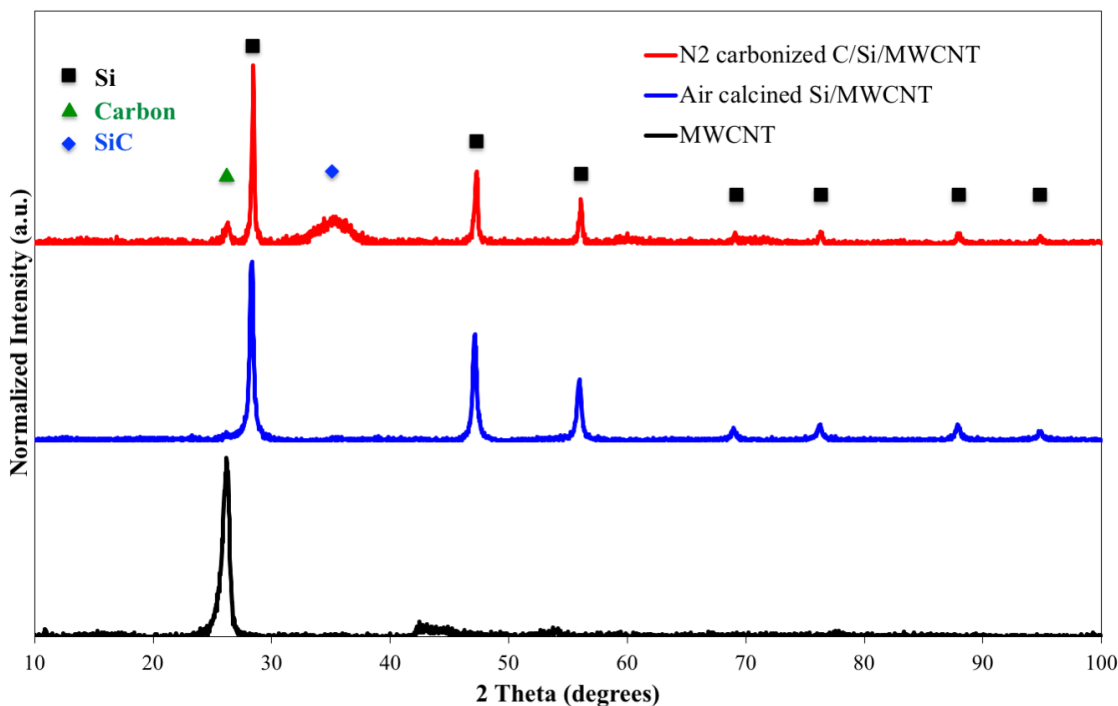


**Figure 3.12.** XRD analysis of the MWCNTs compared to the Mg reduced silicon fibers containing MWCNT.

The two samples were prepared in slurries to check their electrochemical viability (70/15/15 fiber/Super P/PAA). The drop-casted anodes were put in half-cells and cycled for 100 cycles. These results are shown in Figure 3.13. The air calcined sample was tested at 0.1 A/g for 10 cycles and then due to good performance, the current density was increased to 0.5 A/g. The carbonized sample was only tested at 0.1 A/g and showed very poor performance: 734 mAh/g initial capacity, 30.5% 1<sup>st</sup> CE, and a cycling capacity below 50 mAh/g by the 10<sup>th</sup> cycle. Despite a high silicon presence, the carbonization caused too many side reactions and had no significant capacity. The air calcined sample shows promise as an anode material: an initial capacity of 1700 mAh/g and a 1<sup>st</sup> CE of 75.5% without the use of electrospinning deposition or an HF wash, is a 7% boost. After 90 cycles at 0.5 A/g the fibers still showed a capacity of 300 mAh/g – similar to that of graphite.

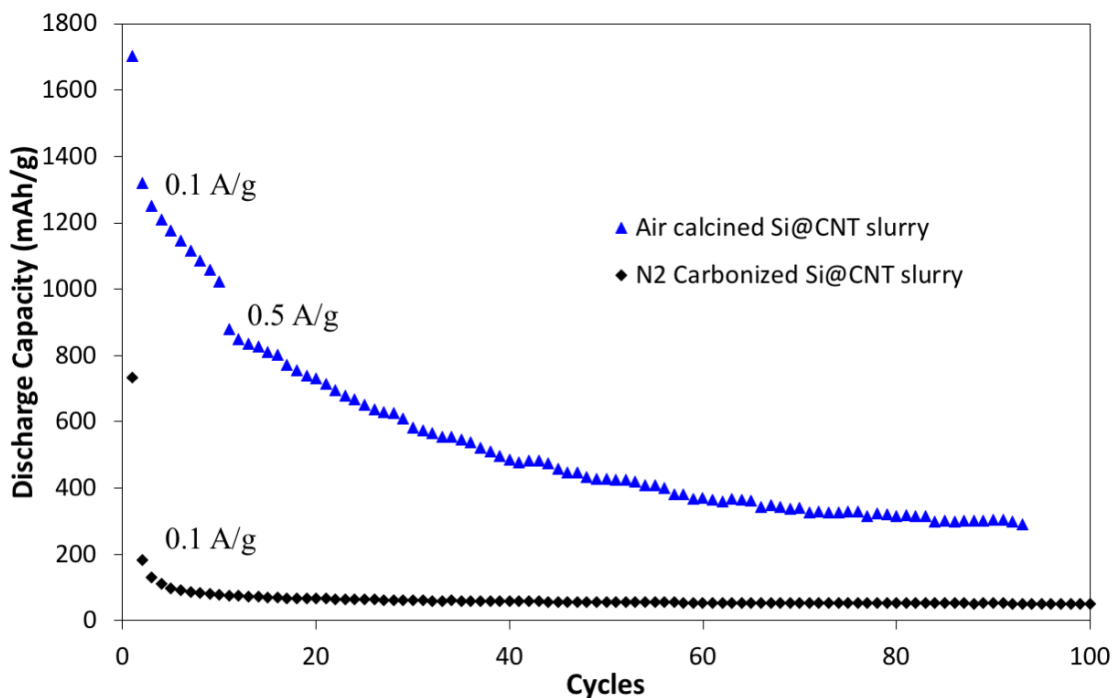


**Figure 3.13.** half-cell cycling performance of silicon fibers with internal MWCNTs prepared in conventional slurries.

The Si@MWCNT samples have not been used with the binder-free, AC-electrospinning method. Future work with this project should focus first on decreasing calcination temperature to prevent MWCNT burnoff. An HF-washed 2:1 Si@MWCNT/RGO anode should show improvements to 1<sup>st</sup> CE, rate capability, and cycle life.

### 3.4 Conclusions

Binder-free anodes prepared by direct-deposit using AC-electrospinning of GO sheets have been shown to be a versatile method for high performance anode preparation. Previous work in the Joo group focused on AC-electrospinning GO anodes utilized silicon nanoparticles that avoid pulverization issues, but they are cost prohibitive to use and their high surface area gives low 1<sup>st</sup> CE. This work explored the

use of micron-scale silicon in the GO-system by preparing electrospun silicon microfibers, as well as ways to optimize the conductivity and performance of the electrodes. Several anodes of silicon microfibers were prepared by AC-electrospraying. While there were clear signs of pulverization and capacity fade, the AC-electrospray approach exhibited a significant improvement in retention, cycle life, and rate capability compared to a slurry casted approach, and showed that the reduced graphene oxide layers can accommodate some stresses of volume expansion. Both a high purity, HF-washed silicon and an unwashed silicon with MWCNTs present could maintain 65% of their 0.1 A/g capacity at 3 A/g. Additionally, the high purity silicon fiber showed significantly less capacity fade. HF-washed silicon went 100 cycles at high current density and maintained a capacity over 800 mAh/g – more than twice the capacity of commercial graphite. Perhaps most important for consideration of this approach, the HF-washed silicon fibers showed 1<sup>st</sup> CE above 80%, reducing the large number of Li-ions lost in the first cycle.

Finally, preliminary work was done for a future iteration of this project in which conductive carbon would be placed inside the silicon fibers. A conductive network through the core of the fibers could have the strongest effect, as charge transport through large diameter fibers could be dramatically improved. While there are ways to prepare silicon particles below 10-micron diameters, electrospinning is the only scalable method to form silicon microparticles or microfibers with conductive additives at their core.

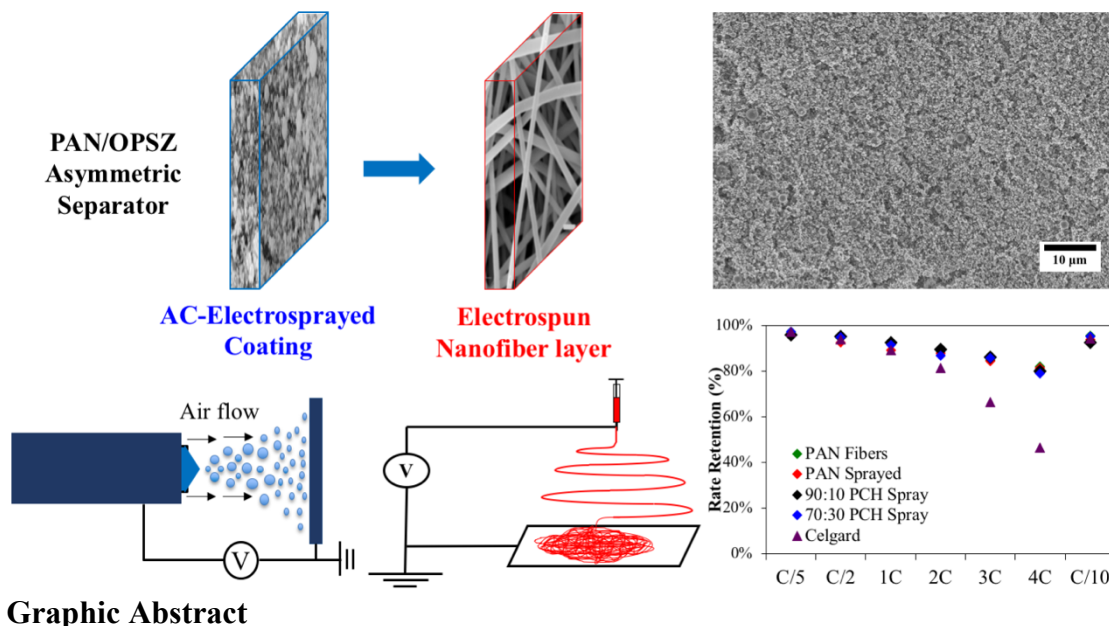
### 3.5 References

- [1] Scrosati, B. & Garche, J. Lithium batteries: Status, prospects and future. *Journal of Power Sources* **195**, 2419–2430 (2010).
- [2] Zhang, W.-J. A review of the electrochemical performance of alloy anodes for lithium-ion batteries. *Journal of Power Sources* **196**, 13–24 (2011).
- [3] Chan, C. K. *et al.* High-performance lithium battery anodes using silicon nanowires. *Nature Nanotech* **3**, 31–35 (2007).
- [4] Kasavajjula, U., Wang, C. & Appleby, A. J. Nano- and bulk-silicon-based insertion anodes for lithium-ion secondary cells. *Journal of Power Sources* **163**, 1003–1039 (2007).
- [5] Cui, L.-F., Yang, Y., Hsu, C.-M. & Cui, Y. Carbon–Silicon Core–Shell Nanowires as High Capacity Electrode for Lithium Ion Batteries. *Nano Lett.* **9**, 3370–3374 (2009).
- [6] Park, M.-H. *et al.* Silicon Nanotube Battery Anodes. *Nano Lett.* **9**, 3844–3847 (2009).
- [7] Hu, L. *et al.* Silicon-Carbon Nanotube Coaxial Sponge as Li-Ion Anodes with High Areal Capacity. *Adv. Energy Mater.* **1**, 523–527 (2011).
- [8] Ji, L. *et al.* Graphene/Si multilayer structure anodes for advanced half and full lithium-ion cells. *Nano Energy* **1**, 164–171 (2012).
- [9] Chabot, V. *et al.* Graphene wrapped silicon nanocomposites for enhanced electrochemical performance in lithium ion batteries. *Electrochimica Acta* **130**, 127–134 (2014).
- [10] Zhang, W. *et al.* Journal of Power Sources. *Journal of Power Sources* **312**, 216–222 (2016).
- [11] Ma, Y. *et al.* Facile synthesis of Si-C nanocomposites with yolk-shell structure as an anode for lithium-ion batteries. *Journal of Alloys and Compounds* **704**, 599–606 (2017).
- [12] Fuller, T. F. Bigger and better. *Nat. Energy* 1–2 (2016).  
doi:10.1038/nenergy.2016.3
- [13] Wang, C. *et al.* Self-healing chemistry enables the stable operation of silicon microparticle anodes for high-energy lithium-ion batteries. *Nature Chemistry* **5**, 1042–1048 (2013).
- [14] Li, Y. *et al.* Growth of conformal graphene cages on micrometre-sized silicon particles as stable battery anodes. *Nat. Energy* **1**, 15029 (2016).
- [15] Greiner, A. & Wendorff, J. H. Electrospinning: A Fascinating Method for the Preparation of Ultrathin Fibers. *Angew. Chem. Int. Ed.* **46**, 5670–5703 (2007).
- [16] Yoo, J.-K., Kim, J., Jung, Y. S. & Kang, K. Scalable Fabrication of Silicon Nanotubes and their Application to Energy Storage. *Adv. Mater.* **24**, 5452–5456 (2012).

- [17] Cho, D. *et al.* Facile Synthesis of Porous Silicon Nanofibers by Magnesium Reduction for Application in Lithium Ion Batteries. *Nanoscale Res Lett* 1–8 (2015). doi:10.1186/s11671-015-1132-8
- [18] Jung, J.-W., Lee, C.-L., Yu, S. & Kim, I.-D. Electrospun nanofibers as a platform for advanced secondary batteries: a comprehensive review. *J. Mater. Chem. A* **4**, 703–750 (2015).
- [19] Weihan, L., Linchao, Z. & Ying, W. Nanostructured electrode materials for lithium-ion and sodium-ion batteries via electrospinning. *Science China Materials* (2016).
- [20] Gribov, B. G. & Zinov'ev, K. V. Preparation of high-purity silicon for solar cells. *Inorganic materials* (2003).
- [21] Yasuda, K., Nohira, T., Takahashi, K., Hagiwara, R. & Ogata, Y. H. Electrolytic Reduction of a Powder-Molded SiO<sub>2</sub> Pellet in Molten CaCl<sub>2</sub> and Acceleration of Reduction by Si Addition to the Pellet. *J. Electrochem. Soc.* **152**, D232 (2005).
- [22] Bao, Z. *et al.* Chemical reduction of three-dimensional silica micro-assemblies into microporous silicon replicas. *Nature* **446**, 172–175 (2007).
- [23] Luo, W. *et al.* Efficient Fabrication of Nanoporous Si and Si/Ge Enabled by a Heat Scavenger in Magnesiothermic Reactions. *Sci. Rep.* **3**, (2013).
- [24] Wang, W. *et al.* Monodisperse Porous Silicon Spheres as Anode Materials for Lithium Ion Batteries. *Sci. Rep.* **5**, 8781 (2015).
- [25] Favors, Z. *et al.* Towards Scalable Binderless Electrodes: Carbon Coated Silicon Nanofiber Paper via Mg Reduction of Electrospun SiO<sub>2</sub> Nanofibers. *Sci. Rep.* **5**, 8246 (2015).
- [26] Fei, L. *et al.* Graphene Oxide Involved Air-Controlled Electrospray for Uniform, Fast, Instantly Dry, and Binder-Free Electrode Fabrication. *ACS Appl. Mater. Interfaces* **9**, 9738–9746 (2017).

## CHAPTER 4

### POLYMER/CERAMIC HYBRID ASYMMETRIC SEPARATORS FOR LITHIUM-ION BATTERIES



**Abstract:** A combination of electrospinning and air-controlled (AC) electrospaying were used to form an asymmetric separator for Li-ion batteries. Polyacrylonitrile (PAN) and ambient temperature-curable organopolysilazane (OPSZ) were used to form a PAN/polymer-derived ceramic (PDC) fiber layer and AC-electrosprayed layer in a two-step process. The fiber layer provides a porous support and foundation while the AC-electrosprayed layer reduces pore size and acts as a safety measure to prevent short-circuiting. This addresses the problem of increasing pore sizes for electrospun fibers at low thicknesses. The combined process is used to fabricate 15-micron thick asymmetric separators without calendaring. In rate capability testing, the asymmetric

PAN/PDC separators display high rate capability with 85.3% of their 0.1C capacity at 4C rate.

#### ***4.1 Introduction***

Lithium ion batteries are lightweight, display high energy density, and have long cycle life, making them excellent energy storage devices for portable electronics and now electric vehicles [1-3]. Consumers expect smaller batteries and longer battery life when they purchase new electronics and cars, and so there is a continuous push to improve the energy density of batteries. While it does not take part in the electrochemical reactions, the battery separator is a target for improved energy density. A separator serves as a physical barrier between the anode and cathode to prevent short circuiting while also allowing Li-ion transport between the electrodes. Thinner separators improve batteries' energy density by taking up less volume in the cell, but the separator must still provide the safety measures needed to prevent dead batteries, battery fires, or explosions. Most commercial batteries use polyolefin microporous films for separators, including polypropylene (PP) and polyethylene (PE). Polyolefin films are used due to their high mechanical strength, great chemical stability, low cost, and low thicknesses [4]. Commercial polyolefins can be manufactured that are thinner than 10-microns [5]. However, while they can be produced extremely thin, there are drawbacks to battery performance when using polyolefin materials. Polyolefins do not have good compatibility with Li-ion batteries' carbonate-based electrolytes due to polyolefin's non-polar, hydrophobic properties [6, 7]. Additionally, the extruded microporous films have low porosity relative to other

separator fabrication processes. Taken together, the polyolefin films have poor electrolyte wetting, low electrolyte uptake, and display poor ion transport properties hurting cell cycle life and rate performance.

To overcome these drawbacks, researchers have focused on the electrospinning process as a way to make separators with electrophilic polymers and higher porosity [8]. Electrospinning forms a non-woven membrane of submicron diameter fibers with minimal thickness and small pore size [9]. These membranes have high porosity with average porosities of 70-80% compared to the 40-50% achieved by microporous films [5, 10]. The increase in porosity significantly improves ion diffusion through the separator. Secondly, electrospinning works with a wide range of polymers, including many polymers that have more electrophilic properties than polyolefins. There are many reported electrospun polymer separators including polyacrylonitrile (PAN) [11], polyvinylidene fluoride [12], poly(vinylidene fluoride-co-hexafluoropropylene) [13], polyethylene terephthalate [14], meta-aramid [15], and polyimide [16]. PAN fiber separators prepared by Cho *et al.* had ionic conductivities more than double that of a commercial PP film and displayed much better cycle life at 0.5C rate. PAN fibers had more than 82.5% capacity retention compared to the commercial polyolefin film's 68.7% retention [11]. In general, the electrospun separators demonstrate increased electrolyte wetting, uptake, and retention compared to polyolefin materials, which yields higher ionic conductivities, rate capability, and capacity retention.

The ionic conductivity of the electrospun polymer separators can be further enhanced with the addition of inorganic ceramic materials [17, 18]. Ceramic fillers can be incorporated into electrospinning solutions to form composite separators, with the

most common fillers being SiO<sub>2</sub> and Al<sub>2</sub>O<sub>3</sub> nanoparticles [19-22]. In addition to improving ionic conductivity, the ceramic fillers improve electrolyte wetting, thermal stability, and cycling stability. Ceramic nanoparticles can reach loadings of ~10% before aggregation of particles in the fibers causes battery performance to wane. Higher ceramic loadings and better dispersion in nanofibers can be achieved by working with ceramic precursors instead of ceramic nanofibers [23-27]. Precursor approaches achieve ceramic loadings greater than 20%; more than doubling what has been reported for preformed nanoparticles. Recent work by Dr. Soshana Smith used a low temperature curing organopolysilazane (OPSZ) to form PAN fiber separators with 26% polymer derived ceramic (PDC) content [25]. The PDC was well dispersed through the fiber as well as formed a surface, shell-layer. The PDC improved ionic conductivity through electrolyte interactions at the fiber surface as well as disrupting PAN's ability to crystallize for increased amorphous regions, giving batteries excellent rate capability and cycling retention.

Despite the many listed advantages and performance improvements of using electrospun separators over polyolefin films, electrospun separators are not being used in batteries for consumer electronics or electric vehicles. One significant issue facing electrospun separators are the continued efforts to decrease separator thicknesses to improve battery energy density. Electrospun separators are unique among non-woven materials, with their pore size distribution below 1-micron at separator thicknesses ranging from 25-40 microns. Producing electrospun separators below 25 microns risks an increase in pore size above 1 micron as well as the formation of straight-through pores that could both cause short-circuiting. Current technology already uses

separators thinner than can be produced safely by electrospinning. Samsung made waves with their Samsung Galaxy Note 7 phones using a 6-7 micron separator. The Note 7 battery had the thinnest separator seen in a phone with a 5-micron polyolefin layer and 1-micron of  $\text{Al}_2\text{O}_3$  on each side [28]. Tesla model S batteries use an 18-micron separator containing a 13-micron polymer layer and a 5-micron  $\text{Al}_2\text{O}_3$  coating [29]. Electric vehicles are focused on using a thicker separator than phone batteries, but that is still a difficult target for electrospun separators to reach safely and the target thickness could reduce with time. Additional processing to reduce pore size could make electrospun separators a reality if it can be done scalably and maintains the advantages of the electrospun fiber mats.

In recent years, the Joo group has worked with the air-controlled (AC) electro spraying technique as a way to prepare stand-alone electrode films and uniform coatings on separators, and was effective in Li-ion and Li-sulfur battery efforts [30-32]. AC-electro spraying could be just as effective in the preparation of film-like and coated separators with morphologies that minimize pore size for safer batteries. As a solution-based process, AC-electro spraying can form separators with electrophilic PAN/PDC, which will minimize separator resistance of a denser film. This work will focus on two unique approaches to prepare thinner separators by using AC-electro spraying:

1. A freestanding AC-electro sprayed PAN film to form an interconnected film with pores added by removal of a sacrificial polymer
2. An AC-electro sprayed dense PAN/PDC particle layer formed as a coating on a PAN/PDC electrospun fiber framework.

The first approach focuses on making a thin film more similar to the polyolefin microporous films than an electrospun non-woven, but with PAN instead of the poor performing polyolefin materials. Pores will be formed by removing a sacrificial polymer in a water bath. The second approach focuses on reducing the pore size of electrospun separators by coating the fiber mat with a dense, tortuous particle layer. A PAN/PDC particle layer is formed that fills in and covers the large interfiber pores on the surface layer. The electrospun layer's thickness can be reduced without increasing the risk of short circuiting.

## ***4.2 Experimental***

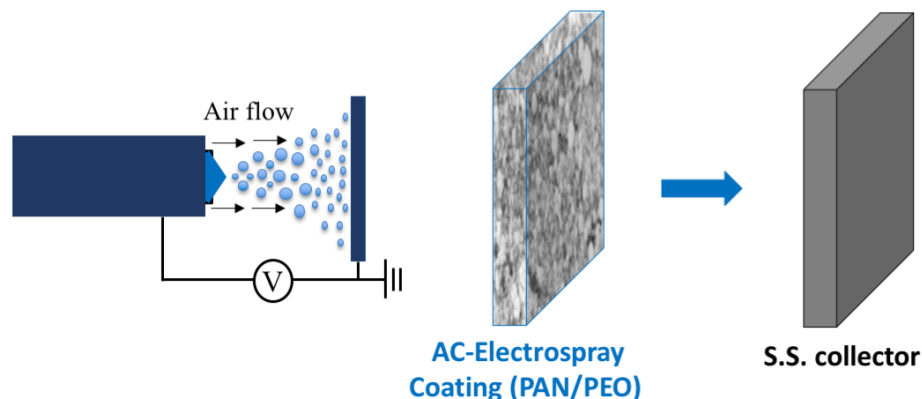
### **4.2.1 Materials**

Several materials were used in electrospinning and electrospraying separators. Polymers, solvents, and additives included: polyacrylonitrile (PAN, Mw = 200,000, Polysciences), PAN (Mw = 150,000, Sigma-Aldrich), polyethylene oxide (PEO, Mw = 10000, Sigma-Aldrich), sodium chloride (VWR), zinc chloride (VWR), N,N-Dimethylformamide (DMF, Sigma-Aldrich), N-methyl pyrrolidone (NMP, Sigma-Aldrich), and Durazane 1500 Slow Cure organopolysilazane (OPSZ, EMD Performance Materials). Several materials were also used to evaluate cell performance including: Celgard 2400 polypropylene separators, lithium cobalt oxide cathodes (LiCoO<sub>2</sub>, MTI Corporation), graphite anodes (MTI Corporation), and 1M LiPF<sub>6</sub>-EC/DMC/DEC electrolyte (MTI Corporation).

#### 4.2.2 Preparation of freestanding AC-electrosprayed separators

Three sets of trials were prepared to try and form porous, freestanding polymer sheets using AC-electrospraying. First, PAN ( $M_w = 150,000$ ) was dissolved in DMF in concentrations from 1 to 4 wt%. These were stirred at 60°C for 12 hours to obtain homogeneous solutions before electrospaying. AC-electrospraying parameters used a 14:18 gauge co-axial needle, 10 psi of air ran through the shell, the distance was 25 cm, and a voltage of 20 kV was used. PAN concentration and flow rate were varied and will be discussed in the results section. The samples were electrospayed directly to a stainless steel grounded collector. Adhered films were removed from the collectors by first placing the collector in a water bath. The collected films were dried at 95°C. This process was used for all freestanding membranes and is depicted in Scheme 4.1.

Secondly, to improve an interconnected structure, a mixed solvent of DMF with NMP was used. NMP is a less volatile solvent than DMF and does not evaporate as readily during electrospay. This ensures that the droplets formed would still have residual solvent as they hit the collector. 3 wt% PAN solutions were made in 90:10, 80:20, and 70:30 wt ratio of DMF:NMP. AC-electrospraying parameters used a 14:18 gauge co-axial needle. Air at 10 psi ran through the shell, solution flow was 0.06 ml/min, the distance was 25 cm, and a voltage of 20 kV was used. While not spraying dry, this method sprays dry enough that it does not drip and can be worked with immediately without the need to dry and remove NMP.



**Scheme 4.1.** Preparation of freestanding PAN separators by AC-electrospraying PAN/PEO to S.S. collector.

With an interconnected PAN film, two trials were prepared for pore formation. First, PEO ( $M_w=10000$ ) was added to 3 wt% PAN solutions in 70:30 wt DMF:NMP. PEO loadings were tested for PAN:PEO wt ratios of 80:20, 60:40, 50:50, 40:60, and 20:80. Additionally, to see if NMP use affected pore formation in the films, we also sprayed the 50:50 wt PAN:PEO in pure DMF and 50:50 wt DMF:NMP. All samples used the same AC-electrospraying parameters as before: 10 psi of air, 25 cm distance, 20 kV, and 0.060 ml/min flow rate. Water-soluble PEO was then removed from the membrane in the water bath used for film collection to produce a porous film.

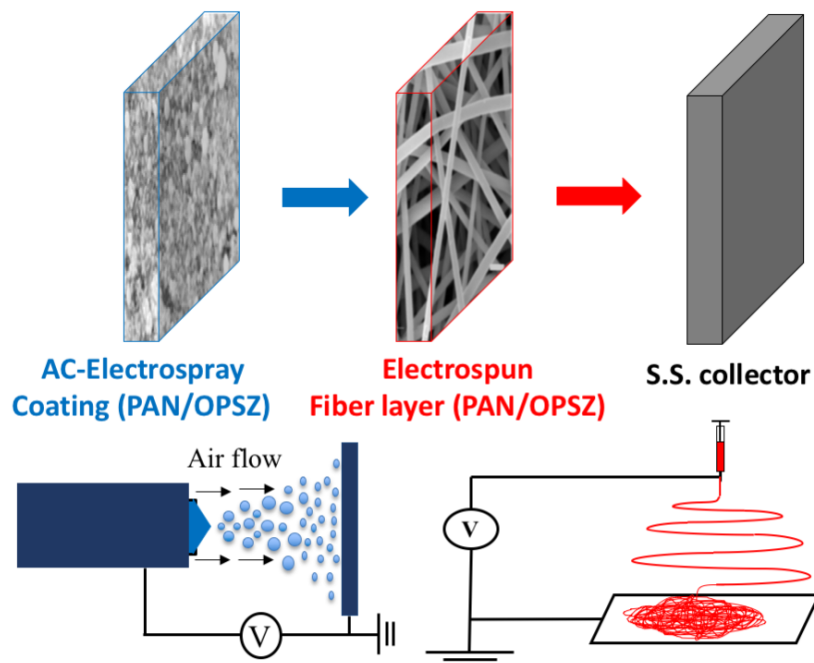
Characterization of the freestanding membranes includes SEM imaging and  $N_2$  physisorption analysis. SEM was done using a TESCAN MIRA FE-SEM to look at spray morphology and pore formation. Pore size and surface area was quantified using a Micrometrics Gemini VII analyzer to prepare BET and BJH analysis.

#### 4.2.3 Preparation of asymmetric separators

The preparation of an asymmetric Li-ion separator is depicted in Scheme 4.2. The fiber layer of the asymmetric membranes was prepared using electrospinning. The

electrospinning solution was prepared by dissolving PAN ( $M_w = 200,000$ ) in DMF to form an 8 wt% solution. The solution was stirred at 50°C for several hours to obtain a homogeneous solution. Just prior to electrospinning, OPSZ was added for concentrations of 10, 20, and 30 wt% compared to PAN. The mixture was stirred on a vortex mixer for 2 minutes to ensure thorough mixing. The PAN/OPSZ solution was electrospun at a flow rate of 0.2 ml/min for pure PAN, 0.15 ml/min for 90:10 and 80:20 PAN/OPSZ solutions, and 0.1 ml/min for 70:30 PAN/OPSZ. A 20-gauge needle was used with a 16 cm distance between needle tip and collector, and 17.5 kV was applied to the needle. 25-micron thick membranes were prepared by electrospinning 0.25 ml. For thin asymmetric membranes (10-12 micron fiber layer), 0.15 ml was spun.

The coated layer of the asymmetric membrane was prepared using AC-electrospraying. The spray was applied directly to the electrospun PCH fiber sheets on grounded collectors. The electrospaying solutions were prepared by dissolving 3 wt% PAN ( $M_w=150000$ ) in DMF and stirring at 50°C for 2 hours to obtain a homogeneous solution. For PAN/OPSZ separators, OPSZ was added to PAN solutions 15 minutes before electrospaying. AC-electrospraying parameters used a 14:18 gauge co-axial needle, 10 psi ran through the shell, solution flow was 0.015 ml/min, the distance was 25 cm, and a voltage of 20 kV was used. Once electrospayed, asymmetric samples were dried at 120°C for 12 hours to ensure the removal of all residual solvent as well as aid in the curing of any OPSZ.



**Scheme 4.2** Preparation of PAN/OPSZ asymmetric hybrid separators

Two different thicknesses of asymmetric separators were prepared. Initial membranes used a 25-micron fiber layer with 2 ml of PAN and PAN/OPSZ solutions sprayed on top to form 40-50 micron thick separators. Later, thin separators were produced using ~12 microns of fibers with 0.5 ml sprayed over the top to form 15-micron thick separators.

In addition to previous characterization techniques, asymmetric separators were also tested in Li-ion full cells in CR2032 sized coin cells. Full cells were assembled using commercial  $\text{LiCoO}_2$  cathode, graphite anode, and 1M  $\text{LiPF}_6$  electrolyte from MTI. The separator and electrodes were dried in a vacuum oven overnight to remove excess moisture. Cells were assembled in an argon-filled glove box. Cell cycling was carried out at a voltage range between 2.5 – 4.2 V at 0.2 C (1 C = 140mA/g). Cells were discharged at 0.1 C, 0.2 C, 0.5 C, 1 C, 2 C, 3 C, 4 C, and 0.1

C respectively. Cell charging was kept at 0.1 C for 0.1 C discharge cycles, and 0.2 C for all other rates.

### 4.3 Results and Discussion

#### 4.3.1 Preparation of a freestanding AC-electrosprayed separator

PAN was first AC-electrosprayed at a range of concentrations and flow rates to test morphologies achieved. The test parameters and the resulting morphologies are summarized in Table 4.1. SEM images of several trials are shown in Figure 4.1. The PAN solutions all sprayed relatively dry with each spray forming particles and/or fibers even at high rates. Increasing flow rates further than those listed led to large droplets leaving the needle tip and forming drips on the collector. At low polymer concentration, 1-2 wt%, independent particles are formed. At 3 wt% and higher, there is a transition away from particles towards beads on a string formation, and eventually fibers. From the SEM it is also observed that the PAN particles are not coating evenly across the surface but form honeycomb-shaped build-ups. The DMF-only trials did not form interconnected structures as the sprays are too dry.

**Table 4.1**  
Summary of AC-electrosprayed PAN solutions.

PAN Concentration (wt% in DMF)	Solution Flow Rate (ml/min)	Morphology
1%	0.0075	Polymer particles
	0.015	
2%	0.015	Polymer particles
	0.03	
3%	0.03	Micron size polymer beads on a string
	0.06	
4%	0.03	Beaded fibers
	0.06	

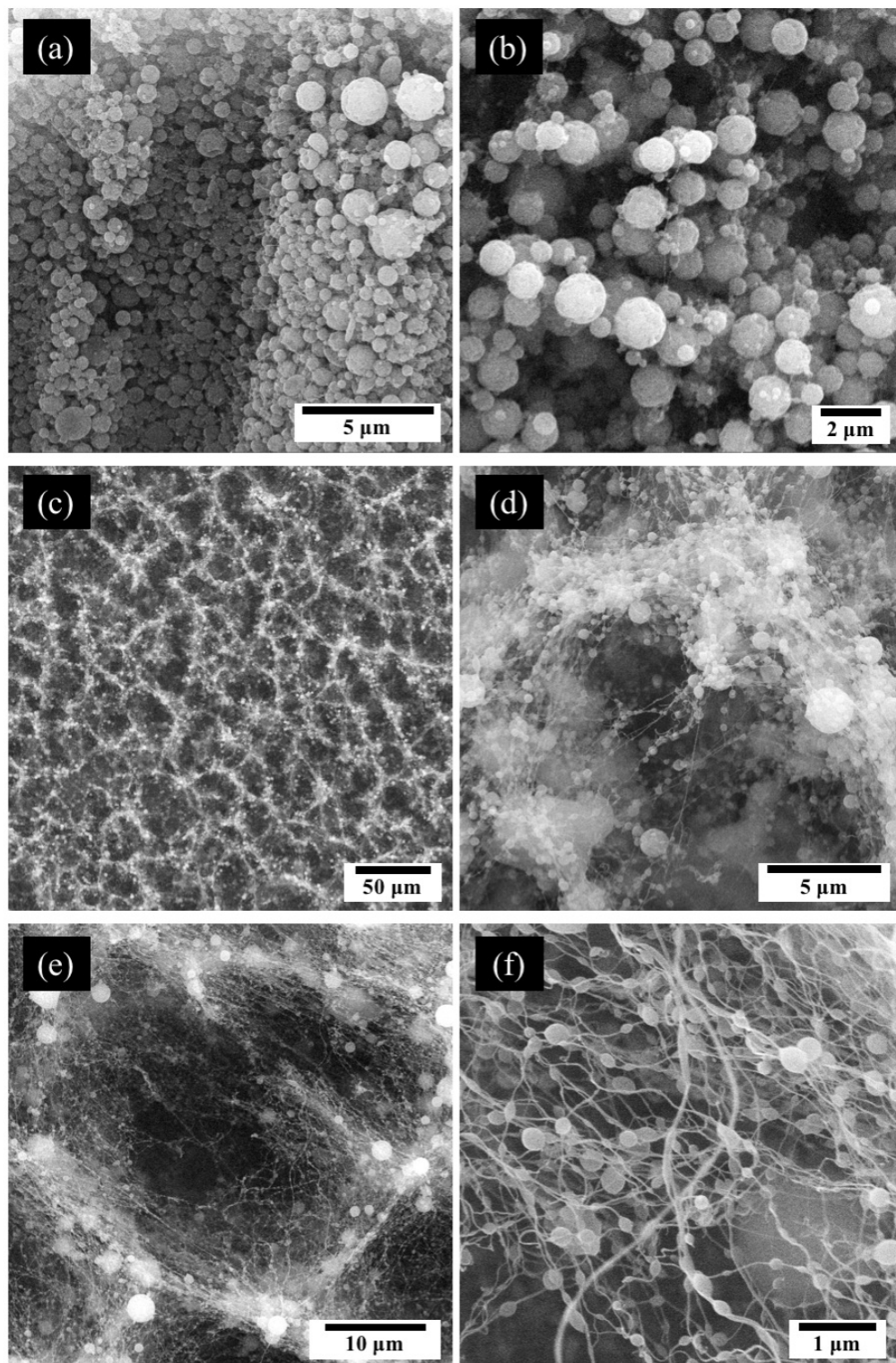


**Figure 4.1.** SEM images of AC-electrosprayed PAN solutions: (a) 1 wt% at 0.015 ml/min, (b) 2 wt% at 0.03 ml/min, (c-d) 3 wt% at 0.06 ml/min, and (e-f) 4 wt% at 0.06 ml/min.

It was important that the electro sprayed membrane had a more interconnected structure to form a freestanding film. The addition of a non-volatile solvent reduces the evaporation rate and allows for more residual solvent for more film-like morphology at the collector. To tune residual solvent, 3 wt% PAN was prepared in varied ratios of DMF/NMP mixtures. Figure 4.2 shows SEM images depicting the evolution towards a continuous film as NMP ratio was increased to 30 wt% of total solvent. With 20% NMP usage, it is clear a film has formed and can be seen folded up on the SEM tab. At 30% NMP, the film is more solid and shows fewer particle-like structures at its surface. The residual solvent seemed to mitigate much of the uniformity issue of particle/fiber stacking seen in the PAN spray in pure DMF, and it improves with increased NMP. There are still surface structures, but they do not show significant stacking. With NMP, AC-electrospraying formed PAN films similar to what could be formed by conventional casting, but they were prepared in a mostly dry state and did not require long drying times to form. A non-porous film could be applied to a roll-to-roll process without the need for a heating section to remove solvent.

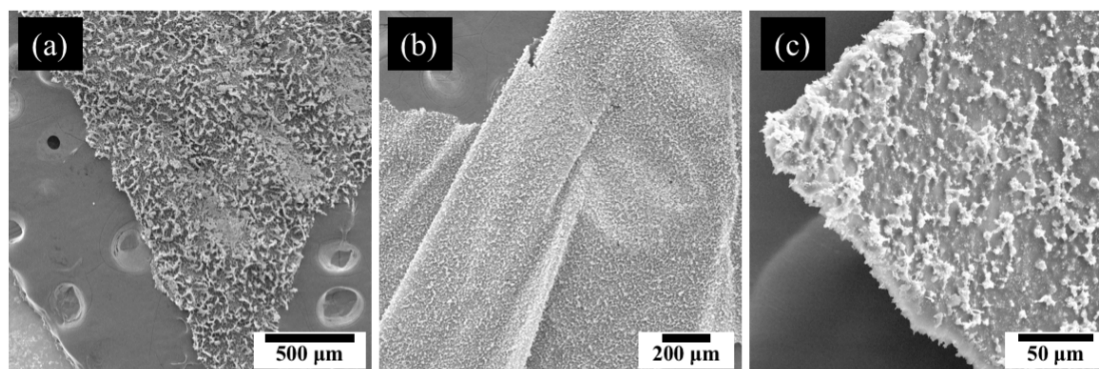


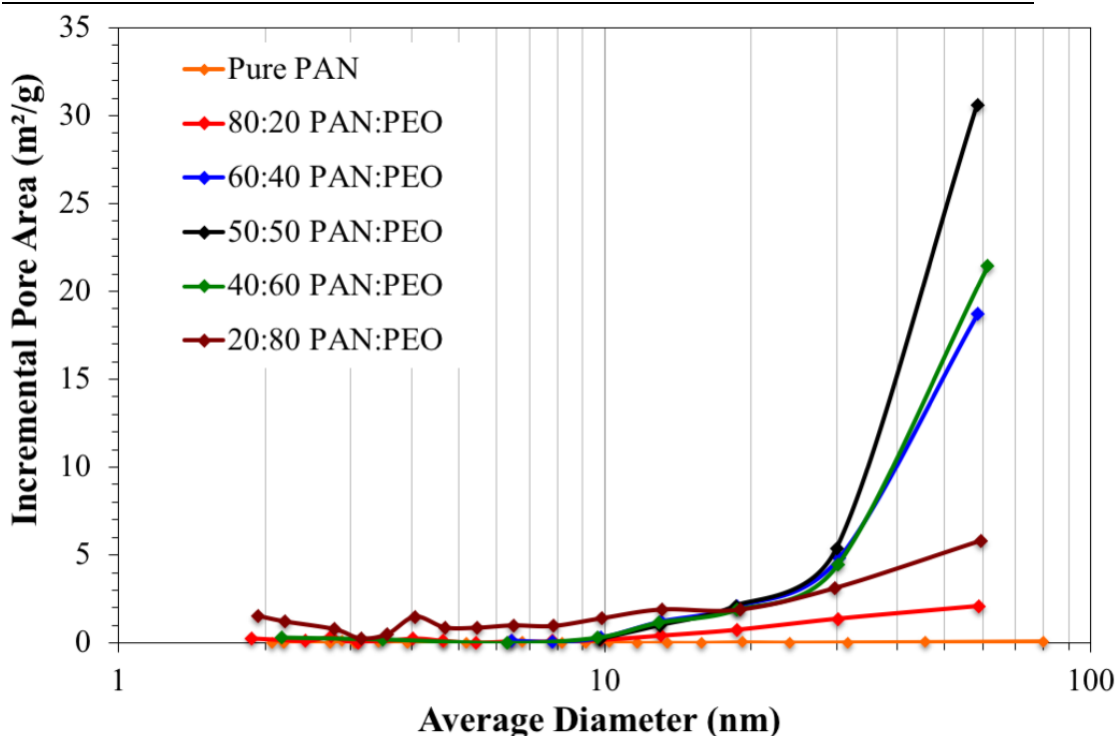
**Figure 4.2.** SEM images of AC-electrosprayed PAN with: (a) 90:10 wt DMF:NMP, (b) 80:20 wt DMF:NMP, (c) 70:30 wt DMF:NMP.

Formation of an interconnected, freestanding PAN film was the first objective. However, without a system of pores running through the film, ion transport would be blocked. To add pores, PEO was added to the PAN solution as a sacrificial polymer and was removed from the film after spraying by dissolving it in a water bath. The ratio of PAN:PEO was varied in 70:30 wt ratio of DMF:NMP to evaluate the effect of increasing amounts of sacrificial polymer. The washed films were evaluated by physisorption analysis and the BET summary and BJH pore distribution are reported in Table 4.3 and Figure 4.3. BET analysis shows that pure PAN samples were non-porous films and that all pores formed in other films were from PEO removal. As PEO content increased, there was an increase in microporous and mesoporous surface area. Surface area was largest when 60% of electrospayed polymer was PEO. Beyond that, PEO addition did not significantly affect pore formation. The surface area created by sacrificial polymer is significant – electrospun polymer fibers have surface areas  $\sim 10$  m<sup>2</sup>/g. The 50:50 PAN:PEO ratio has the largest formations of mesopores and was used for continued analysis.

**Table 4.2.**

BET summary for PAN:PEO electrospays (70:30 DMF:NMP solvent).

PAN:PEO (wt ratio)	BET (m <sup>2</sup> /g)	Microporous area (m <sup>2</sup> /g)	Mesoporous area (m <sup>2</sup> /g)
Pure PAN	0.85	0.66	0.19
80 to 20	9.3	2.4	6.9
60 to 40	24.4	4.1	20.3
50 to 50	32.8	7.1	25.7
40 to 60	47.4	29.6	17.8
20 to 80	35.2	6.6	28.6

**Figure 4.3.** BJH pore distribution plot for PAN:PEO electrospays (70:30 DMF:NMP solvent).

In addition to examining pore effects in 70:30 DMF:NMP solutions, the NMP ratio was changed while keeping PAN:PEO constant. 50:50 wt PAN:PEO solutions were also electrospayed in pure DMF and in 50:50 DMF:NMP solvents. Table 4.3 and Figure 4.4 show the BET and BJH results for the varied solvent ratio. The NMP ratio shows no immediate pattern. The pores forming in the electrospayed films seem

only reliant on the PAN/PEO ratio and not on the solvent. The NMP has significant effects on membrane morphology but not on pore space.

**Table 4.3.**

BET summary for 50:50 wt PAN:PEO electrospays with different solvents.

Solvent Mix	BET (m <sup>2</sup> /g)	Microporous area (m <sup>2</sup> /g)	Mesoporous area (m <sup>2</sup> /g)
Pure DMF	49.7	4.7	45.0
70:30 wt DMF:NMP	32.8	7.1	25.7
50:50 wt DMF:NMP	40.7	4.6	36.1

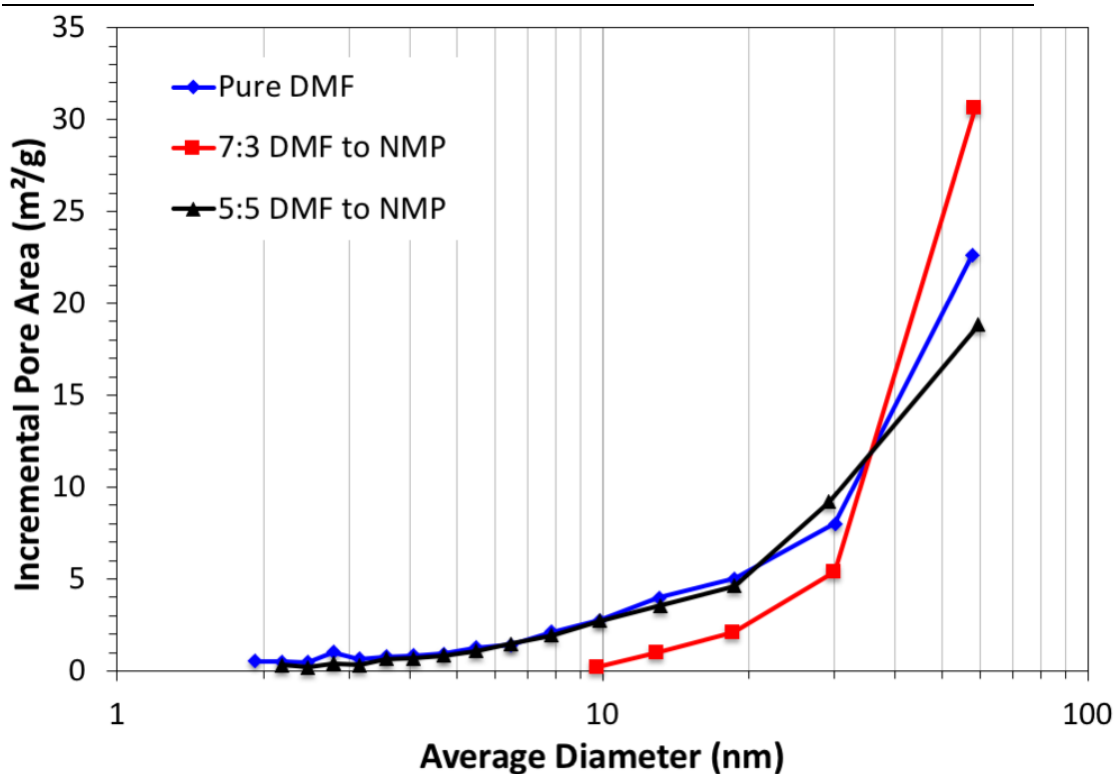


**Figure 4.4.** BJH pore distribution plots of 50:50 wt PAN:PEO electrospays with different solvent makeups.

For electrochemical testing, freestanding porous PAN membranes were prepared with a thickness of 13-15 microns. The samples were punched out and placed in full cells. However, no tested freestanding films allowed for ion transport and the cells could not cycle. SEM imaging was used to look at porous membranes (Figure 4.5). The pores created appear to be mostly surface level and are not interconnected

through the film structure. The cross-section appears almost solid. Trying to work with a thick layer of polymer may require a different approach to build pores such as polymer assembly to build a pore network. Alternatively, this work will focus on coating an electrospayed layer onto a porous fiber network without the need for pore formation.

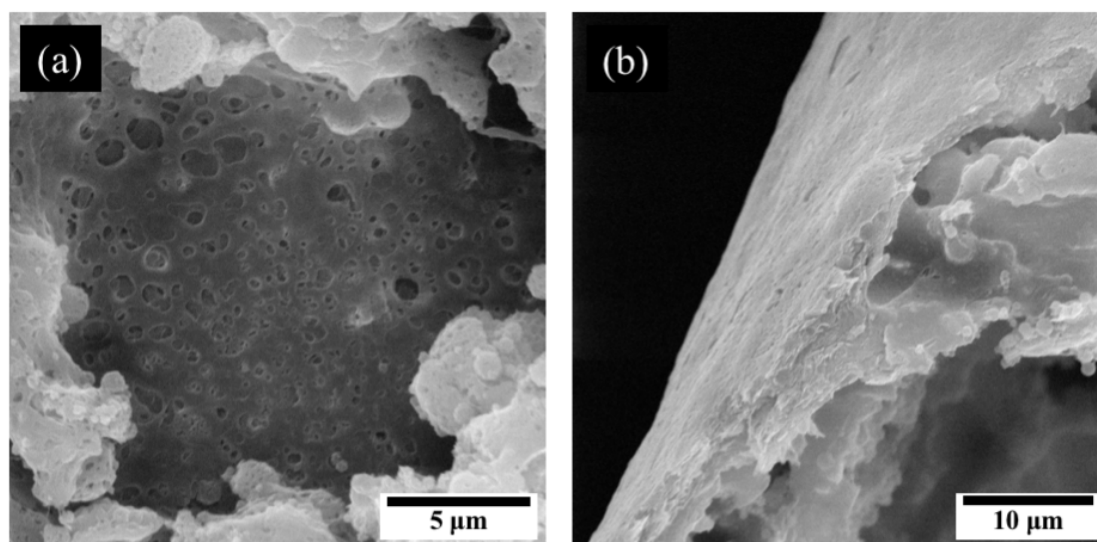


**Figure 4.5.** SEM images showing (a) the surface and (b) the cross-section of 50:50 wt PAN:PEO electrospayed films with a 70:30 wt DMF:NMP solvent.

#### 4.3.2 Preparation of an asymmetric membrane for Li-ion battery

The sacrificial polymer did not form the pores necessary for ion transport, and the freestanding electrospayed membranes were not able to function as Li-ion battery separators. The sprays with residual solvent were necessary to form strong, easy to handle films, but there was not a natural porous structure. By contrast, the dry sprays without NMP formed highly porous collections of particles and beaded fibers that would allow ion transport but could not be a standalone separator. The focus in approach 2 is on how a dry spray can be applied to electrospun separators in order to

avoid the need for a freestanding film. Electrospaying can address pore size of electrospun membranes by forming a thin layer of densely packed particles to clog interfiber pores with a tortuous, nanoparticle layer. The sprayed particle layer, unlike the connected film in approach 1, is weak by itself and requires a substrate. An asymmetric separator combining a fiber layer with a dry electrospayed layer could bring necessary safety to high performance separators.

Asymmetric separators were prepared by first electrospinning PAN and PAN/OPSZ fiber mats, followed by AC-electrospaying a layer of dilute PAN and PAN/OPSZ solutions. Earlier electrospaying showed that PAN at 3 wt% in pure DMF, at 0.015 ml/min can form a layer of submicron scale particles. Once electrospayed, morphology of both sides of the asymmetric separators were examined by SEM. First, Figure 4.6 shows SEM of the fiber layers from the uncoated side. For both pure PAN and 80:20 PAN/OPSZ layers, there are no signs of spray or residual solvent soaking through. The fiber morphologies are smooth and show no sign of beads or other non-uniformities. The PAN fibers have an average diameter of 370 nm +/- 50 nm and the 80:20 PAN:OPSZ fibers have a diameter of 390 nm +/- 40 nm. To see if solvent or sprayed solution penetrates through the fiber layer, red dye was added to the sprayed solutions. Also depicted in Figure 4.6 are the sprayed and reverse sides of the dye sprayed separator, which show that the sprayed solution does not soak through and that the fiber layer should be unaffected by the AC-electrospayed coating.

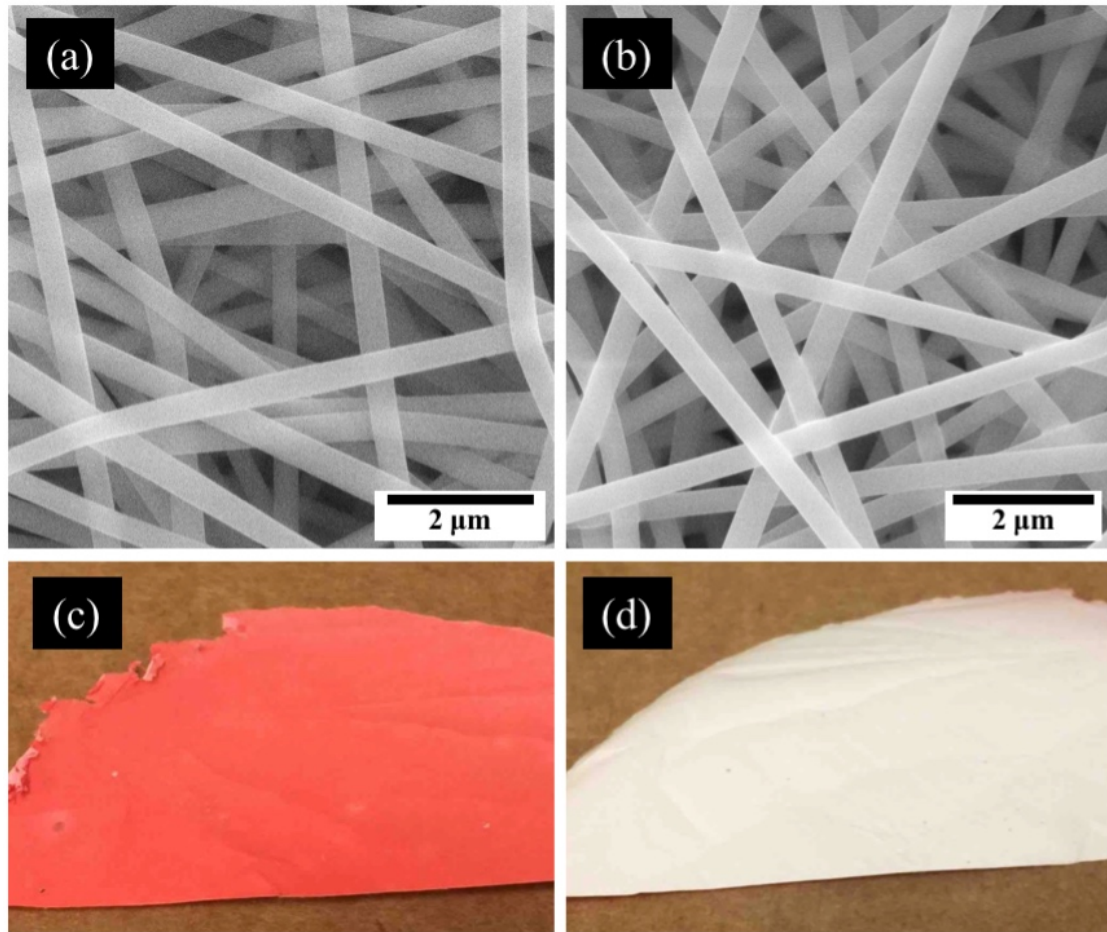


**Figure 4.6.** Images of asymmetric membranes. (a) and (b) are SEM images of the fiber layers of a PAN separator and an 80:20 PAN/OPSZ separator respectively. (c) and (d) are photos of PAN fibers sprayed with a red dye PAN particle solution showing the electrospayed and electrospun sides, respectively.

The AC-electrosprayed side and cross-section of PAN/OPSZ sprays and SEM of the coatings are shown in Figure 4.7. The PAN/OPSZ particles spray uniformly over the fiber surface in a tight packing. The large interfiber pores have been filled with a tortuous path of particles. Unlike many bladed coatings of particles and binder, this sprayed layer has a natural porosity to it and is the same PAN/OPSZ material that makes up the fiber layer. Increased loading of spray can add 10s of microns to the separator thickness if desired.

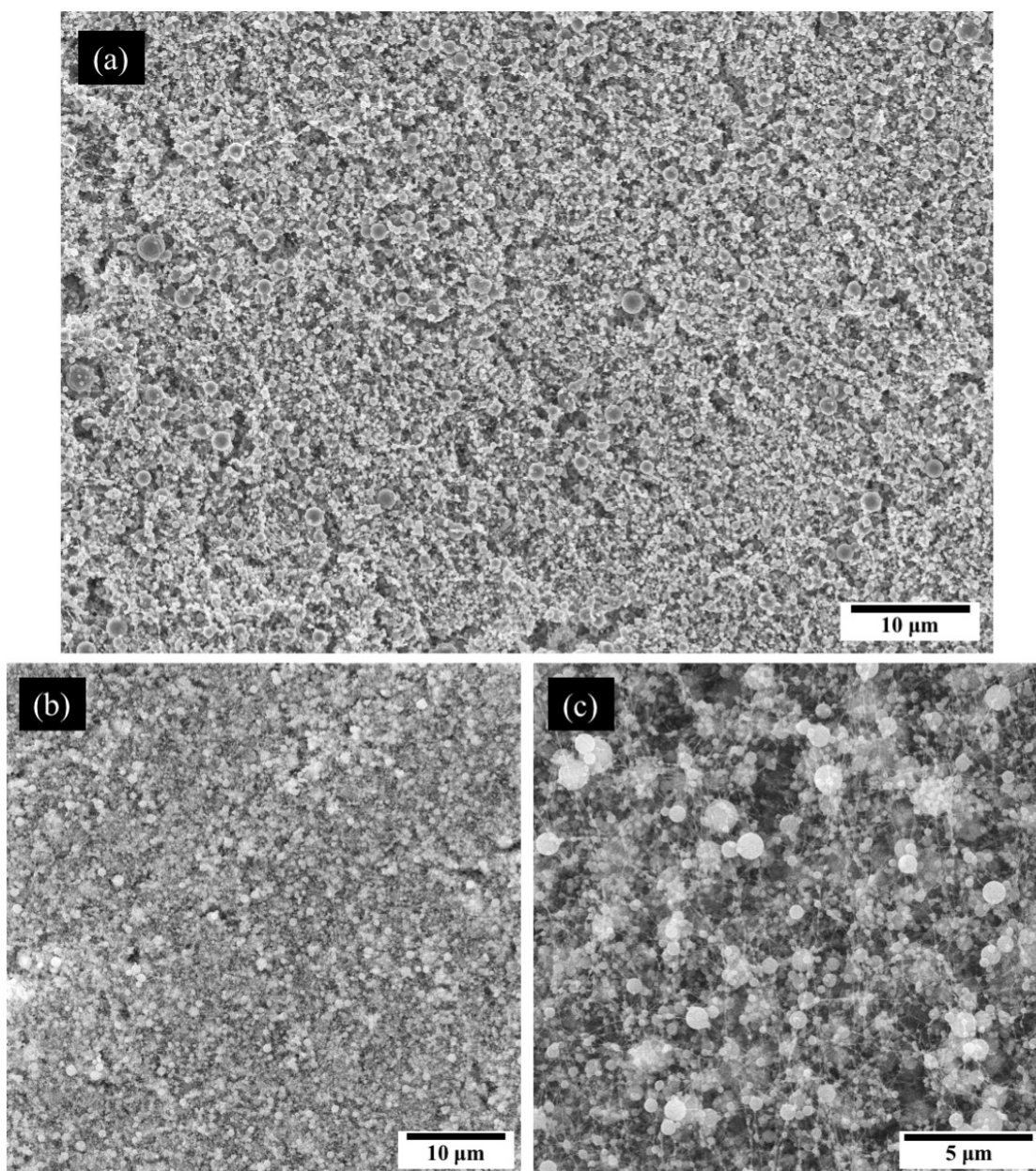


**Figure 4.7.** SEM images of the AC-electrosprayed layers of PAN/OPSZ asymmetric membranes. (a) is from a 70:30 PAN/OPSZ ratio. (b) and (c) are from an 80:20 PAN/OPSZ separator.

While the PAN/OPSZ sprayed evenly across the fiber surface, PAN solutions did not. From earlier studies, electrospayed PAN particles tended to agglomerate and stack on themselves to form uneven coatings and large surface structures. These were particularly prevalent when spraying higher concentrations of PAN. SEM images in

Figure 4.8 show clearly that pure PAN does not spray uniformly over a surface. The particles stack, forming what could be described as walls of PAN. Image (a) and (b) show particle stacking of 3 and 1 wt% solutions, showing that the phenomenon happens even at low concentration. The stacking effect creates large gaps in the sprayed layer, and there is direct access to the fiber structure directly not seen in the PAN/OPSZ layers. Continued spraying of PAN does not improve the uniformity but only creates larger PAN structures. Image (c) shows walls of PAN particles that have fallen over under their weight which are more than 50 microns tall. The particle size and morphology are similar to what is seen in the PAN/OPSZ sprays, except in the unevenness across the surface. This seems to be an electrostatic issue of PAN solutions. The addition of either PEO or OPSZ to the PAN solutions was shown to mitigate the effects and lead to smoother sprays. PAN-only coatings should not be used for forming asymmetric separators for Li-ion batteries. The PAN sprays leave interfiber pores unfilled while making the separator thicker, hurting energy density without improving battery safety.

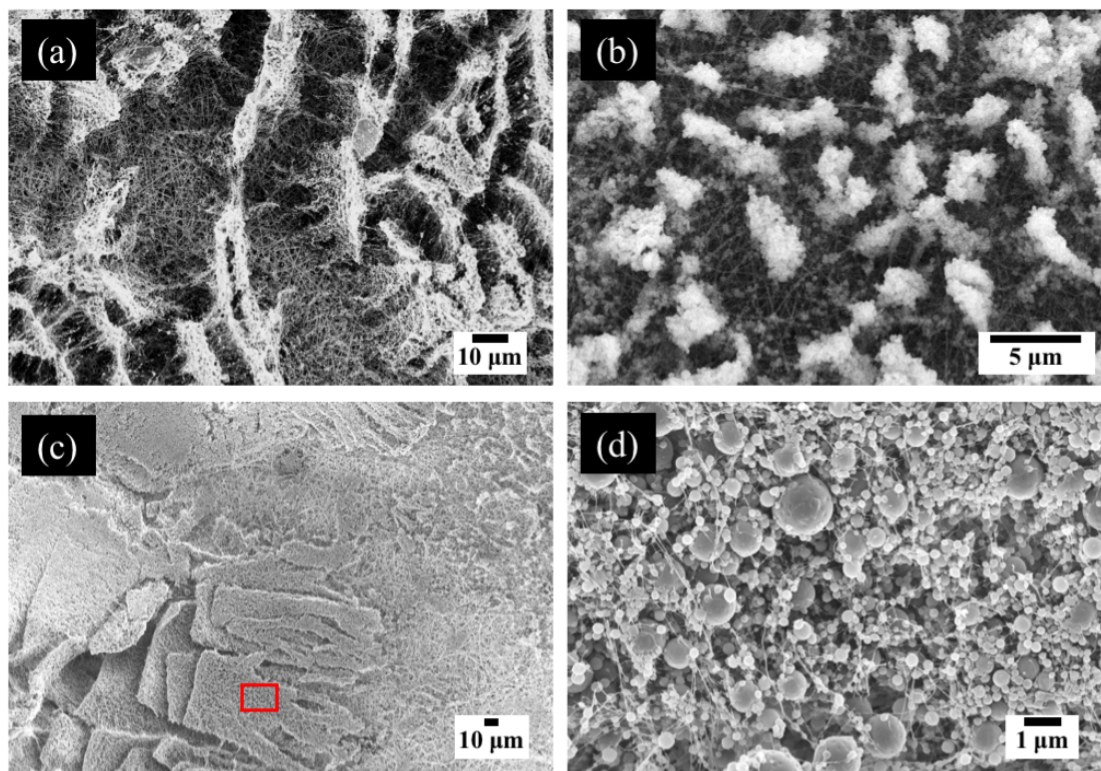


**Figure 4.8.** SEM images of PAN particle stacking by AC-electrospray on PAN fibers. (a) shows 2 ml of 3 wt% PAN sprayed. (b) shows 1 ml of 1 wt% PAN sprayed. (c) shows 5 ml of 3 wt% PAN sprayed and (d) zoomed view of the red rectangle in (c).

PAN and PAN/OPSZ AC-electrosprayed asymmetric separators were prepared in Li-ion full cells with  $\text{LiCoO}_2$  cathodes and graphite anodes. PAN/OPSZ membranes were dried at  $120^\circ\text{C}$  to form PAN/PDC. PAN fibers and Celgard (PP) separators were used for comparison. The PAN fiber membranes and Celgard were 25 microns in thickness and the electrosprayed separators were 40 microns thick. The initial tests were focused on rate capability of the separators and how the added electrosprayed layer affects performance. Figure 4.9 shows the rate performance of the different separators, plotted first in terms of specific capacity per cycle and then by rate retention at each tested rate. Rate retention was used because the initial capacity varied significantly from cell to cell. This is attributed to uneven loading of active material in

the commercial electrodes, as some samples achieve specific capacities above theoretical limits and must have higher active contents than what was reported. Direct comparison of specific capacities cannot be used, but how well the cells maintained their capacities at high rates can be evaluated and compared. Rate retention is given in terms of C rate and is based off the reversible capacity of the cells at 0.1 C, making it independent of active loading.

There is no significant difference between the cell performance of PAN fiber and PAN asymmetric separators. This is expected as the PAN sprayed layer leaves wide gaps for accessing the PAN fiber separator and would not add significant resistance to the base fiber layer. The sprayed layer has no effect on electrochemical performance and safety aspects. The PAN/PDC asymmetric separators performed very well. Both 90:10 and 70:30 wt PAN/PDC separators showed more than 79% rate retention at 4 C. This is well above the Celgard performance and in line with the PAN fiber reference. The PAN/PDC asymmetric separators' rate retention was slightly below that of pure PAN fiber separators at 82%, but well above the commercial Celgard sample that averaged below 50% at 4 C rate. This data suggests that the sprayed dense layer hurts the rate performance of the separators. With the decrease in porosity as well as the added thickness of the spray, it was expected that ionic conductivity would decrease. By using ionically conducting PDC and maintaining a natural system of pores, the ionic conductivity loss is not significant, and the separators maintain high rate performance similar to that of electrospun fibers. Finally, the PDC content did not have a significant effect on the rate capability, as has been shown by several previous publications. One possible reason for this is that the

improvement is hard to see in the data due to the electrode quality. The electrodes have already proven to have non-uniform active content and some strange cycling behaviors, and thus it is difficult to quantify how much better one separator is performing than another. A second possibility is that the PAN/PDC separators (other than Celgard) are accommodating the Li-ion transport needed at 4 C and the capacity loss is due primarily to the electrode kinetics so that all the higher ionic conductivity separators perform similarly. A more stressful system including higher electrode loadings and faster charging rates could draw out a stronger distinction and the importance of high PDC content. Nevertheless, the PAN/PDC asymmetric separators displayed excellent cell performance.

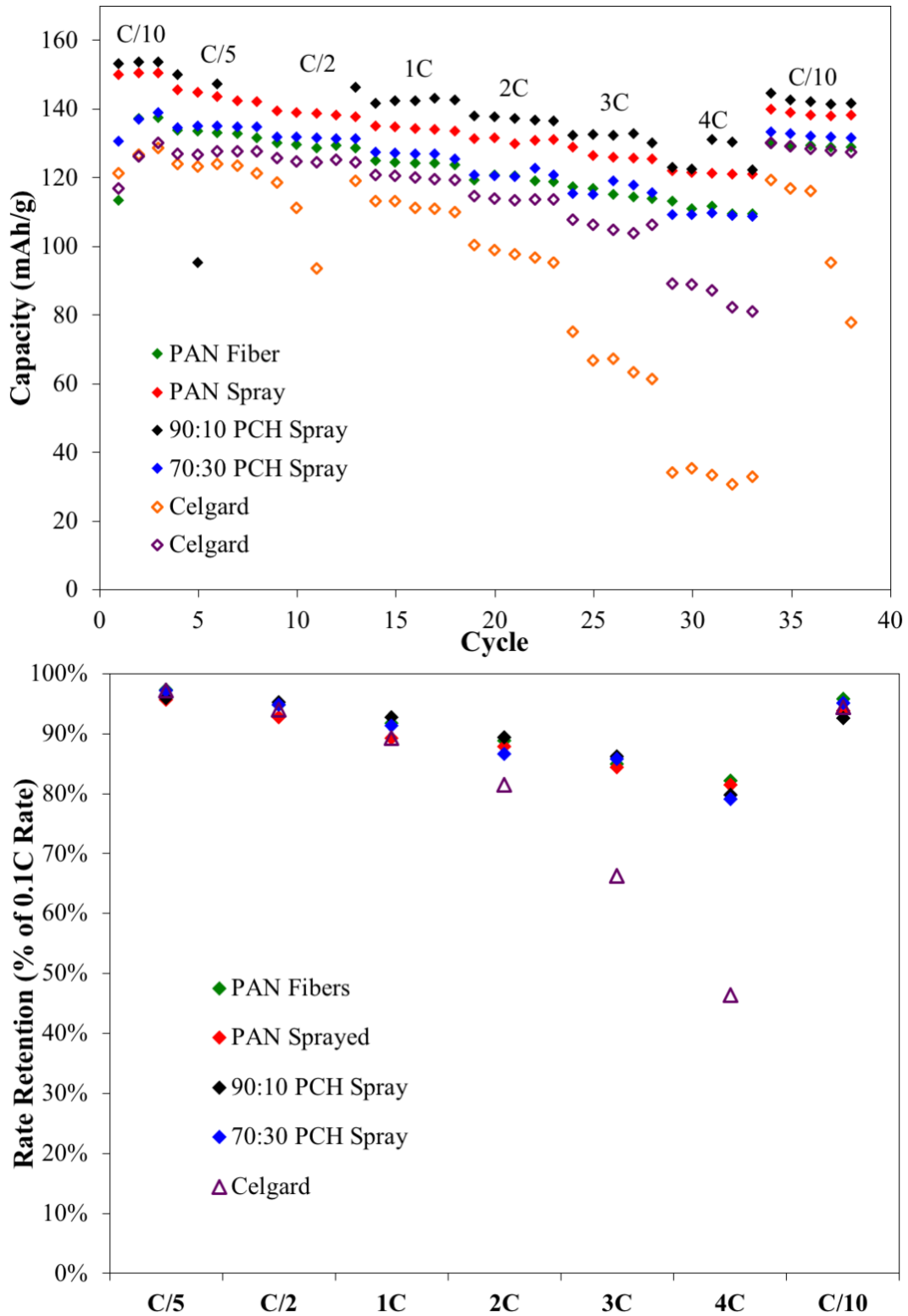


**Figure 4.9.** Rate capability performance of PAN fiber, PAN and PAN/OPSZ asymmetric, and Celgard separators given by (top) specific capacity and (bottom) rate retention compared to 0.1 C rate.

The first cell tests met the initial challenge of electrospaying a separator that showed competitive battery performance. This did not accomplish our goal of determining whether we could effectively decrease the thickness of electrospun separators, as the tested separators were more than 40 microns thick. To meet this objective, 15-micron thick separators were prepared using a 10-12 micron fiber layer and 3-5 micron electrospayed coating over the surface. Both the fibers and coating used 80:20 wt PAN/OPSZ solution. Figure 4.10 contains SEM images of the thinner separators.

The SEM images show several important aspects of how the sprayed layer forms. First, because thin polymer strings connect the particles, the initial layers are draped over the surface layer of fibers. These particles do not penetrate past the first layer. The layer continues to build and can form a uniform layer with much smaller polymer loading than was used in the initial tests. A sprayed layer only a few microns thick forms without gaps or open access to the fiber layer. Cross-sectional images confirm the clear distinction in the fiber and spray layer. In high magnification, a thin particle layer can be seen, with particles filling the gaps in between fibers.

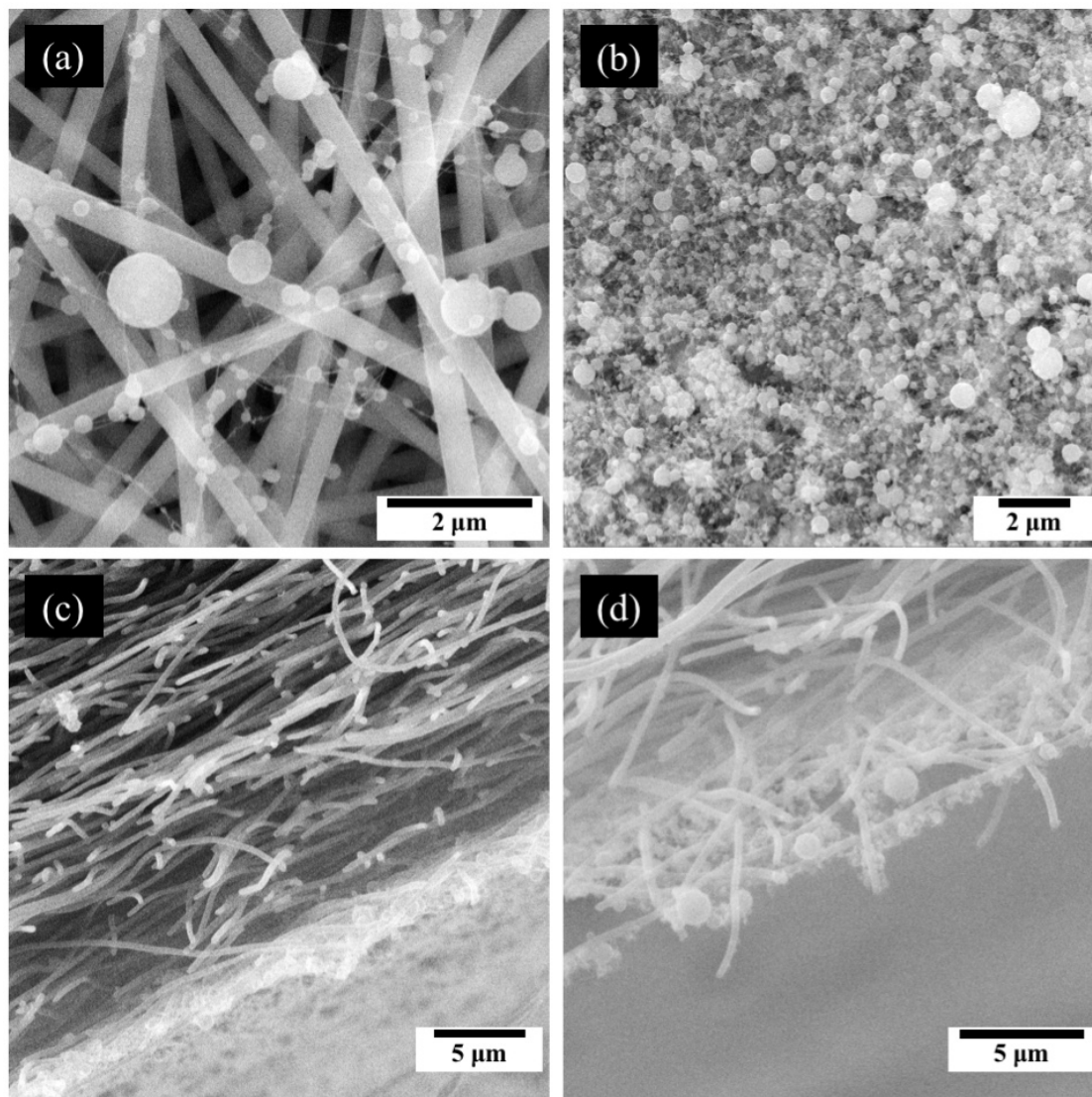


**Figure 4.10.** SEM of the AC-electrosprayed surface an 80:20 PAN:OPSZ asymmetric separators. (a) the first particles collecting on the fibers. (b) a surface view showing the uniform PAN/OPSZ layer. (c) a cross-section pic showing the fiber and spray layer. (d) a zoomed image of a thin spray layer showing how particles collect in between the interfiber pores.

15-micron thick 80:20 PAN:OPSZ separators were assembled into Li-ion full cells as before. Both 0.2 C cycling and rate capability were tested using the MTI brand electrodes. For comparison, several rate capability cells were also assembled with Celgard separators. The Celgard cells skipped the 0.1 C cycles and start at 0.2 C and will display no data for the first three 0.1 C cycles. Cell data is shown in Figure 4.11.

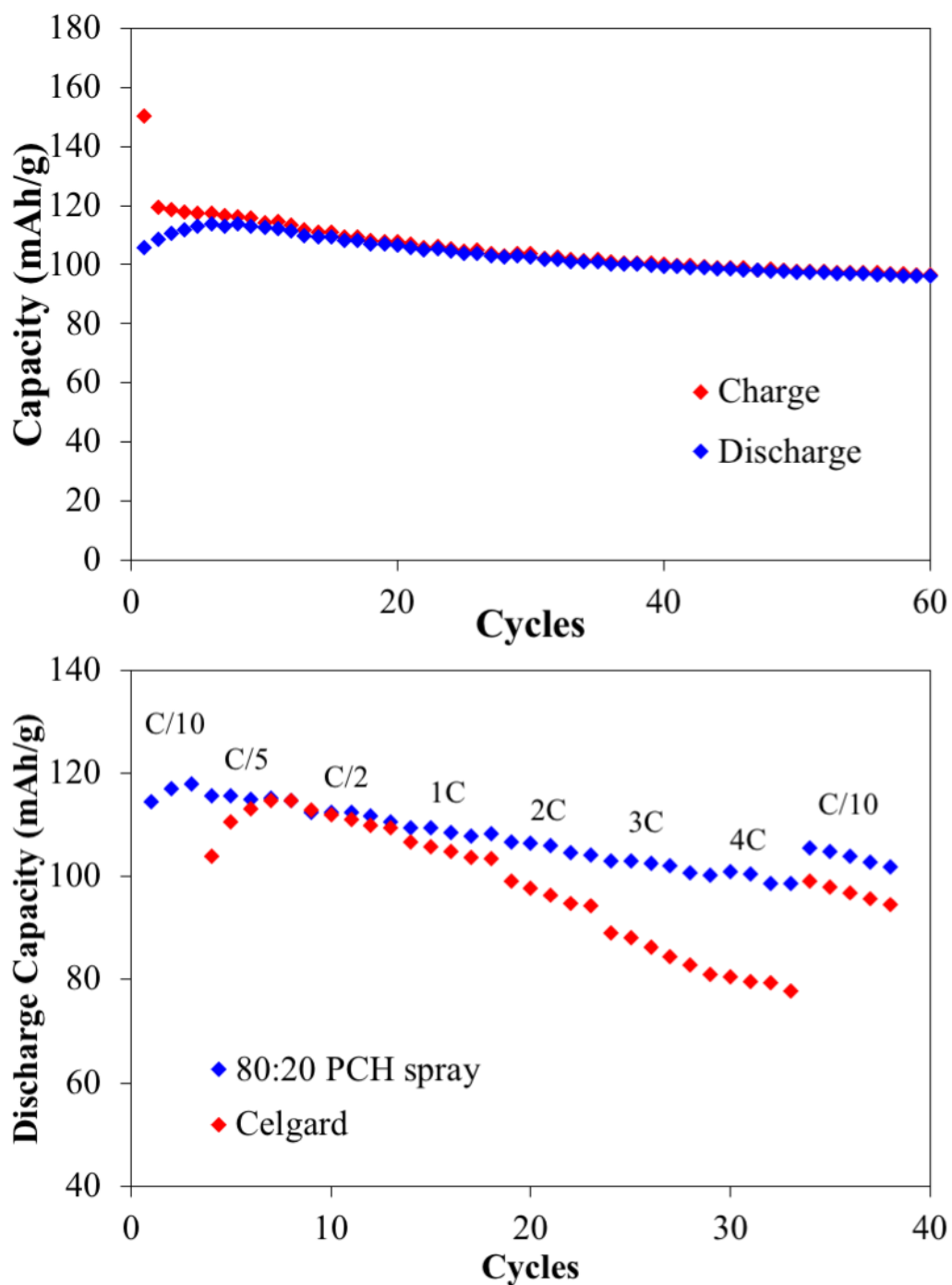


**Figure 4.11.** Full cell cycling of 15-micron thick PAN/OPSZ asymmetric separators: (a) 0.2 C cycling, (b) rate capability testing.

Despite the issues with the electrodes, the PAN/PDC asymmetric separators show steady cycling at 0.2 C and high rate capability. After 50 cycles at 0.2 C, the

cells with asymmetric separators maintained 85% of their capacity. Much of this seems to be due to early losses in capacity that then stabilize. In rate capability, the asymmetric separators performed significantly better than Celgard. At rates below 1 C, the performance of both separators overlaps, but as rates increased, the higher ionic conductivity of the asymmetric separator gives better rate retention. The PAN/PDC separators exhibit 92.1% rate retention at 1 C and 85.3% at 4 C. Cells containing thin asymmetric separators cycled stably and at high rates, proving the asymmetric concept works.

#### ***4.4 Conclusions***

Two preparations of AC-electrosprayed PAN/OPSZ separators were prepared for Li-ion batteries to address short-circuiting risks associated with electrospun fiber separators. First, a freestanding film was fabricated by AC-electrospraying. A sacrificial polymer was used to create pores through the film, but the polymer removal did not form a system of continuous pores to allow for ion transport. In a second process, an original asymmetric separator technique was developed by combining electrospun fibers with an AC-electrosprayed coating. The first trials used a thick coating layer onto electrospun fiber separators to form 40-50 micron thick separators. With a porous sprayed layer formed with high PDC content, the asymmetric separators exhibited similar performance to a purely electrospun non-woven separators and demonstrated excellent rate capability in Li-ion full cells. Thick asymmetric PAN/PDC separators retained more than 79% of their 0.1 C capacity at 4 C. A second trial focused on thinner asymmetric separators tested 15-micron thick separators. The

thinner separators showed no short-circuiting issues and even better rate capability, retaining 85.3% of their 0.1 C capacities at 4 C. Combining AC-electrospraying with electrospinning improved battery safety without hurting the high performance of electrospun separators.

The two chapters to follow shift from PAN/OPSZ materials to new, flame-resistant materials. PAN/OPSZ separators are highly flammable – the OPSZ even increases the flammability. The importance of flame resistance and the development of a new polymer/precursor system are discussed in chapters 5 and 6. Chapter 6 revisits the spin/spray combination developed here to form high safety, high battery performance separator materials.

#### **4.5 References**

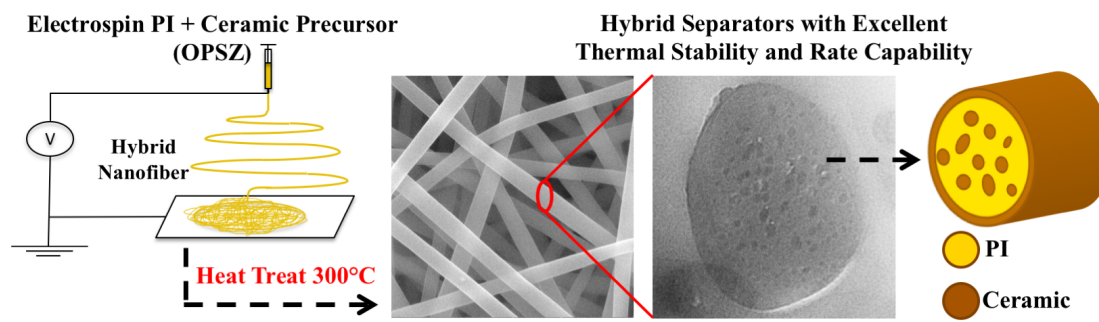
- [1] Tarascon, J.-M. & Armand, M. Issues and challenges facing rechargeable lithium batteries. *Nature* (2001).
- [2] Armand, M. & Tarascon, J.-M. Building better batteries. *Nature* 1–6 (2008).
- [3] Ding, Y., Cano, Z. P., Yu, A., Lu, J. & Chen, Z. Automotive Li-Ion Batteries: Current Status and Future Perspectives. *Electrochemical Energy Reviews* **2**, 1–28 (2018).
- [4] Arora, P. & Zhang, Z. J. Battery Separators. *Chem. Rev.* **104**, 4419–4462 (2004).
- [5] Deimede, V. & Elmasides, C. Separators for Lithium-Ion Batteries: A Review on the Production Processes and Recent Developments. *Energy Technology* **3**, 453–468 (2015).
- [6] Zhang, S. S. A review on the separators of liquid electrolyte Li-ion batteries. *Journal of Power Sources* **164**, 351–364 (2007).
- [7] Huang, X. Separator technologies for lithium-ion batteries. *J Solid State Electrochem* **15**, 649–662 (2010).
- [8] Lee, H., Yanilmaz, M., Toprakci, O., Fu, K. & Zhang, X. A review of recent developments in membrane separators for rechargeable lithium-ion batteries. *Energy Environ. Sci.* **7**, 3857–3886 (2014).

- [9] Jung, J.-W., Lee, C.-L., Yu, S. & Kim, I.-D. Electrospun nanofibers as a platform for advanced secondary batteries: a comprehensive review. *J. Mater. Chem. A* **4**, 703–750 (2015).
- [10] Waqas, M. *et al.* Recent Development in Separators for High-Temperature Lithium-Ion Batteries. *Small* **15**, 1901689 (2019).
- [11] Cho, T.-H. *et al.* Battery performances and thermal stability of polyacrylonitrile nano-fiber-based nonwoven separators for Li-ion battery. *Journal of Power Sources* **181**, 155–160 (2008).
- [12] Liang, Y. *et al.* Heat treatment of electrospun Polyvinylidene fluoride fibrous membrane separators for rechargeable lithium-ion batteries. *Journal of Power Sources* **240**, 204–211 (2013).
- [13] Li, X. *et al.* Polymer electrolytes based on an electrospun poly(vinylidene fluoride-co-hexafluoropropylene) membrane for lithium batteries. *Journal of Power Sources* **167**, 491–498 (2007).
- [14] Hao, J. *et al.* A novel polyethylene terephthalate nonwoven separator based on electrospinning technique for lithium ion battery. *Journal of Membrane Science* **428**, 11–16 (2013).
- [15] Lee, J. H., Manuel, J., Lie, Y., Park, K. E., Park, W. H. & Ahn, J.-H. High Temperature Resistant Electrospun Nanofibrous Meta-Aramid Separators for Lithium Ion Batteries. *Journal of Nanoscience and Nanotechnology* **16** 10724–10729 (2016).
- [16] Miao, Y.-E., Zhu, G.-N., Hou, H., Xia, Y.-Y. & Liu, T. Electrospun polyimide nanofiber-based nonwoven separators for lithium-ion batteries. *Journal of Power Sources* **226**, 82–86 (2013).
- [17] Croce, F., Appetecchi, G. B., Persi, L. & Scrosati, B. Nanocomposite polymer electrolytes for lithium batteries. *Nature* **394**, 456–458 (1998).
- [18] Nunes-Pereira, J. & Costa, C. M. Polymer composites and blends for battery separators: State of the art, challenges and future trends. *Journal of Power Sources* **281**, 378–398 (2015).
- [19] Jung, H.-R., Ju, D.-H., Lee, W.-J., Zhang, X. & Kotek, R. Electrospun hydrophilic fumed silica/polyacrylonitrile nanofiber-based composite electrolyte membranes. *Electrochimica Acta* **54**, 3630–3637 (2009).
- [20] Shayapat, J., Chung, O. H. & Park, J. S. Electrospun polyimide-composite separator for lithium-ion batteries. *Electrochimica Acta* **170**, 110–121 (2015).
- [21] Fu, Q. *et al.* Mechanically Reinforced PVdF/PMMA/SiO<sub>2</sub> Composite Membrane and Its Electrochemical Properties as a Separator in Lithium-Ion Batteries. *Energy Technology* **6**, 144–152 (2017).
- [22] Wang, Y., Wang, S., Fang, J., Ding, L.-X. & Wang, H. A nano-silica modified polyimide nanofiber separator with enhanced thermal and wetting properties

- for high safety lithium-ion batteries. *Journal of Membrane Science* **537**, 248–254 (2017).
- [23] Zhang, F., Ma, X., Cao, C., Li, J. & Zhu, Y. Poly (vinylidene fluoride)/SiO<sub>2</sub> composite membranes prepared by electrospinning and their excellent properties for nonwoven separators for lithium-ion batteries. *Journal of Power Sources* **251**, 423–431 (2014).
- [24] Yanilmaz, M., Lu, Y., Zhu, J. & Zhang, X. Silica/polyacrylonitrile hybrid nanofiber membrane separators via sol-gel and electrospinning techniques for lithium-ion batteries. *Journal of Power Sources* **313**, 205–212 (2016).
- [25] Smith, S. A., Park, J. H., Williams, B. P. & Joo, Y. L. Polymer/ceramic co-continuous nanofiber membranes via room-curable organopolysilazane for improved lithium-ion battery performance. *J Mater Sci* **52**, 3657–3669 (2016).
- [26] Smith, S. A., Williams, B. P. & Joo, Y. L. Effect of polymer and ceramic morphology on the material and electrochemical properties of electrospun PAN/polymer derived ceramic composite nanofiber membranes for lithium ion battery separators. *Journal of Membrane Science* **526**, 315–322 (2017).
- [27] Chen, S., Zhang, Z., Li, L. & Yuan, W. Covalently-Bonded Poly(vinyl alcohol)-Silica Composite Nanofiber Separator with Enhanced Wettability and Thermal Stability for Lithium-Ion Battery. *ChemistrySelect* **3**, 13365–13371 (2018).
- [28] Loveridge, M. *et al.* Looking Deeper into the Galaxy (Note 7). *Batteries* **4**, 3–11 (2018).
- [29] Uitz, M. *et al.* Aging of Tesla's 18650 Lithium-Ion Cells: Correlating Solid-Electrolyte-Interphase Evolution with Fading in Capacity and Power. *J. Electrochem. Soc.* **164**, A3503–A3510 (2017).
- [30] Fei, L. *et al.* Graphene Oxide Involved Air-Controlled Electrospray for Uniform, Fast, Instantly Dry, and Binder-Free Electrode Fabrication. *ACS Appl. Mater. Interfaces* **9**, 9738–9746 (2017).
- [31] Lee, J. H. *et al.* Effective Suppression of the Polysulfide Shuttle Effect in Lithium–Sulfur Batteries by Implementing rGO–PEDOT:PSS-Coated Separators via Air-Controlled Electrospray. *ACS Omega* **3**, 16465–16471 (2018).
- [32] Divvela, M. J. *et al.* Control of formation of viscoelastic droplets and distribution of nano-inclusions in functional deposition for lithium–sulfur batteries. *Soft Matter* **15**, 6485–6494 (2019).

## CHAPTER 5

### ELECTROSPUN POLYIMIDE/CERAMIC HYBRID NANOFIBERS FOR THERMALLY STABLE LI-ION BATTERY SEPARATORS



#### Graphic Abstract

**Abstract:** Nanofibrous polyimide (PI)/ceramic hybrid separators were formed by electrospinning to provide high rate performance and excellent thermal and fire resistance for Li-ion batteries. Composite nanofibers were prepared from a PI solution mixed with a varied loading of an organopolysilazane ceramic precursor (OPSZ) functionalized with trialkoxysilyl groups. The PI:OPSZ fibers were heat treated at 300°C to crosslink the PI and crosslink and cure the ceramic precursor, improving both the thermal stability and the electrochemical performance of the material. The use of the functionalized OPSZ creates a uniformly blended polymer/ceramic hybrid structure with ceramic domains throughout the fiber and a ceramic shell layer at the fiber surface. The added ceramic content greatly decreases thermal shrinkage with separators having 10% precursor inclusion, achieving less than 20% areal shrinkage after holding at 450°C for 1 hour, as well as showing excellent flame resistance. Additionally, the surface level ceramic improves the ionic conductivity above that of the pure polymer nanofibers and yields significant improvements in battery test

compared to reference polyolefin films. The hybrid fibers offer a large improvement to battery performance and safety and are stable in extreme conditions.

### **5.1 Introduction**

Due to their high energy density, high efficiency, and long cycle life, lithium-ion batteries are used in personal electronics and increasingly in electric vehicles (EVs) [1]. The demand for EVs has put a focus on battery safety and the fires and explosions that can result from cell abuse, crashes, and other accidents [2-4]. The separator is vital to battery safety, acting as a physical barrier between the electrodes. Currently, polyolefin microporous films are used in lithium-ion batteries due to their high strength, chemical stability, low cost, and low thicknesses [5]. There are several drawbacks to their use stemming from intrinsic characteristics of the polypropylene (PP) and polyethylene (PE) used to form the separators. The polymers have poor electrolyte wettability and electrolyte uptake due to their non-polar, hydrophobic properties. This is compounded by the low porosity of commercial microporous films (approximately 40-50%) yielding low ion transport in battery cells and limiting the rate capability of the batteries [6]. More importantly, commercial polyolefin separators cannot maintain battery safety in the event of cell abuse or high temperatures, as they have poor thermal stability. PE and PP have low melting points at 120-130°C and 165°C respectively. At elevated temperatures they exhibit large thermal shrinkage before melting, allowing electrode contact and leading to thermal runaway and possible battery fire [4, 6-8]. Ceramic coatings have been applied to polyolefin separators that improve their thermal stability and they show decreased shrinking at

temperatures near their melting point [9, 10]. However, coated polyolefin separators still break down at elevated temperatures and the coating layer does not overcome the issues of the polyolefin's low melting point. Separators for EVs should overcome the drawbacks of conventional polyolefin microporous separators and demonstrate improved electrochemical performance as well as excellent thermal stability.

Electrospinning has garnered significant attention as a technique to form non-woven separators for Li-ion batteries and can address many of the shortcomings of polyolefin microporous films [11]. Electrospinning is a scalable process to produce continuous, uniform fibers with diameters ranging from nanometers to a few microns. The process results in a highly porous fiber network providing much higher porosities than commercial polyolefin films, with porosities above 60% [12]. The increase in porosity improves diffusion through the separator and can correlate to an increased ionic conductivity. Electrospinning is also versatile in using a wide range of polymers with properties that avoid the drawbacks of polyolefins. With a focus on safety, research has been driven towards electrospinning thermally stable polymers such as polyimides [13-17]. Polyimide (PI) is thermally stable to temperatures above 400°C with not melting point and can avoid the thermal shrinkage issues and safety concerns that occur with polyolefin separators at temperatures at 135°C and above [18]. In addition to improved thermal stability, Miao *et al.* found PI nanofibrous separators have better electrolyte wettability and better battery performance with higher capacity, lower resistance, and higher rate capability compared to a Celgard reference [13].

In addition to the added thermal stability, inorganic ceramic fillers are added as a way to improve the electrochemical performance [19-21]. This has been applied to

electrospun PI separators, and ceramics have been added in two different approaches: ceramic addition to the spinning solution [22-25] and ceramic addition once the fiber mat is formed in a second step [26-29]. Wang et al. added up 5 wt% SiO<sub>2</sub> nanoparticles to their spinning solution and improved the wettability and battery performance of a pure polyimide separator [23]. To try and increase particle dispersion throughout the fibers, Chen et al. used TiO<sub>2</sub> nanoparticles functionalized with short chain polymers in a co-spin of PI and PVDF-HFP [24]. Battery performance was improved by nanoparticle functionalization, but nanoparticle loading was limited to 2%. It is difficult to achieve good dispersion of ceramic fillers, high loading, and placement at the fiber surface when using nanoparticle additions. Ceramic addition can also be done in post processing with a PI nanofibrous scaffold. This has included Al<sub>2</sub>O<sub>3</sub> nanoparticle/PVDF-HFP coatings by dipcoating [26], combined SiO<sub>2</sub> and Al<sub>2</sub>O<sub>3</sub> nanoparticle coatings by dipcoating [27], boehmite nanoparticle coatings by blade coating [28], and electrostatic spray coating with a combination of polyamic acid and TEOS precursor [29]. In all cases, the addition of ceramic improved the thermal stability and wettability of the separators. However, the gains from improved electrolyte interaction were offset by loss of porosity and electrolyte uptake leading to minimal gains in ionic conductivity and increased bulk resistance in the cell from the added layer.

Many of the advantages of ceramic fillers can be achieved without the drawbacks of ceramic nanoparticles by incorporating ceramic precursors to separators. Organopolysilazanes (OPSZ) are polymers in which silicon and nitrogen atoms alternate to form a ceramic precursor backbone. When coupled with trialkoxysilyl

functional group, OPSZs can cure at low temperatures in the presence of moisture, resulting in highly cross-linked polymers, with Si-O-Si bonds in place of Si-N-Si, that have ceramic properties [30, 31]. While this does form a polymer derived ceramic (PDC), additional heat treatment up to 300°C improves the conversion of the ceramic precursor and there is mass loss as additional volatile groups are removed [31]. In previous studies by Smith et al. [32, 33], liquid OPSZ was added to polyacrylonitrile (PAN) solution to form PAN/PDC hybrid fibers with low temperature moisture curing (120°C). With use of miscible OPSZ, fabrication kept to a one-step electrospinning process, increased the overall ceramic loading in the fibers, selectively formed a ceramic shell to the nanofibers, and avoided aggregation seen in higher loadings of nanoparticles. It was also observed that OPSZ with increased trialkoxysilyl content formed bicontinuous domains of polymer and PDC blended through the fibers [33]. This led to improved properties including the ionic conductivity, cycling stability, and rate capability. However, the use of PAN and no heat treatment of the ceramic precursor meant that thermal stability was limited and the separator material was flammable, making it unsafe for EV use.

In this work, the safety concerns and flammability are addressed with a PI/PDC nanofiber separator fabricated by an electrospinning process. OPSZ is incorporated into a PI spinning solution to form a hybrid polymer/precursor fibrous material with precursor well distributed throughout. The polymer/precursor fibers are then heat treated at 300°C to improve the properties of the PI and form PDC from the OPSZ. At temperatures near and above the  $T_g$ , polyimides form charge-transfer complexes (CTCs), a type of intra- and intermolecular bond [34, 35]. These

temperature-driven bonds improve the chemical and thermal stability of the PI. The OPSZ precursor also benefits from heat treatment improving the precursor conversion, rendering it more thermally stable and flame resistant. We have varied the ceramic precursor loading to demonstrate the effect of ceramic content on thermal and cycling performance. In addition, we evaluated several thermal properties with and without heat treatment to determine the effect of thermal annealing. We aim to show that the PI:OPSZ hybrid fibers are improved by increased precursor loading and heat treatment, addressing the needs for both battery safety and performance in EV applications.

## ***5.2 Experimental***

### **5.2.1 Preparation of electrospun separators**

PI and PI/ceramic non-woven separators were prepared using electrospinning. P84, a commercially available PI, was purchased from HP Polymer Inc. P84 is a copolyimide of 3,3'-4,4'-benzophenone tetracarboxylic dianhydride (BTDA) with 80% 2,4-diaminotoluene (TDI) and 20% 4,4'-methylenedianiline (MDI). The ceramic precursor used was Durazane 1500 Slow Cure organopolysilazane (OPSZ) purchased from durXtreme GmbH, which features a high content of trialkoxysilyl functional group. The chemical structures of P84 and OPSZ are shown in Figure 5.1. The electrospinning solution was prepared by first dissolving PI in N,N-Dimethylformamide (DMF). The solution was stirred at 50°C for 4 hours to dissolve the polymer and then cooled to room temperature. For hybrid separators, OPSZ was added shortly before electrospinning. Three solutions were prepared: 22wt% PI in

DMF, 22wt% PI in DMF with 5 wt% OPSZ relative to PI, and 20wt% PI in DMF with 10 wt% OPSZ relative to PI. For complete mixing, solutions were stirred on a vortex mixer for two minutes after OPSZ addition and then stirred gently for an hour to reduce bubbles in the solution.

PI and PI/OPSZ solutions were electrospun using a 19-gauge needle at a 0.01 ml min<sup>-1</sup> flow rate. 20kV was applied to the needle and a grounded collector was placed 18 cm away. Once electrospun, the fiber samples were heat treated for further cross-linking of the PI and curing of the ceramic precursor. Samples were placed between ceramic blocks and held at 300°C for 4 hours in air. After heat treatment, fiber samples were roll calendered to 20 to 25µm thicknesses. A polypropylene microporous film, Celgard 2400, was used for comparison studies to conventional separators.

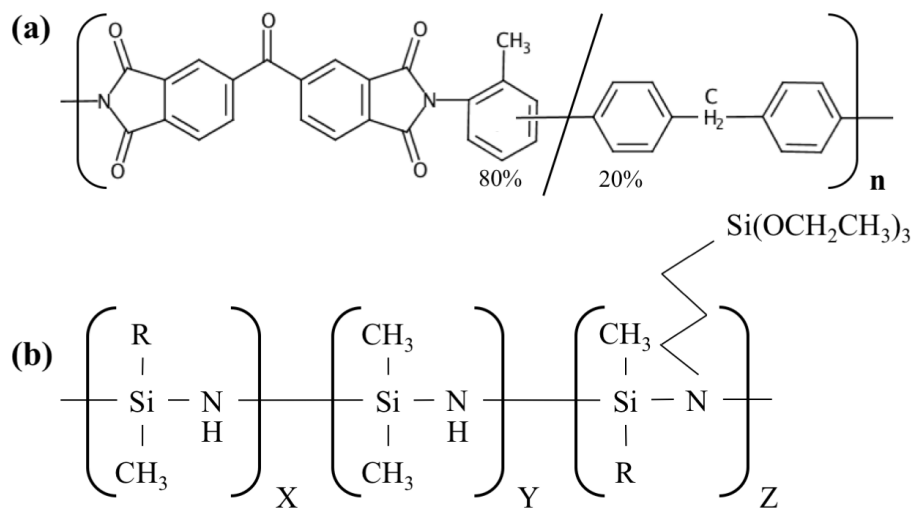


**Figure 5.1.** (a) The chemical structure of P84 co-polyimide and (b) the chemical structure of OPSZ (Durazane 1500 Slow Cure). In the OPSZ structure, R = -H or -CH<sub>3</sub>.

### 5.2.2 Material Characterization

The fiber morphology and diameter were examined using scanning electron microscopy (SEM) using a Tescan Mira3 FESEM with a 15 kV beam voltage. The morphology of fiber cross-sections was investigated using transmission electron microscopy (TEM) with a FEI Tecnai F20 TEM. Fourier transform infrared (FTIR) spectra were obtained in the range of 4000-600  $\text{cm}^{-1}$  with a resolution of 4  $\text{cm}^{-1}$  for 64 scans using a PerkinElmer Frontier FT-IR spectrometer. Thermal stability was first characterized through thermogravimetric analysis (TGA) and differential scanning calorimetry (DSC). The tests were run simultaneously using a Netzsch STA 449 F3 Jupiter apparatus in an open alumina boat under air environment from 25°C to 1000°C at 10°C  $\text{min}^{-1}$  heating rate. Ceramic content in hybrid fibers was also determined by TGA. Thermal shrinkage of the separators (6 x 6 cm) was observed by measuring the dimensional change after heat treatment at varied temperatures for 1 hour using equation 5.1:

$$\text{Shrinkage (\%)} = (A_i - A_f) / A_i \times 100\% \quad (5.1)$$

where  $A_i$  and  $A_f$  are the initial and final areas of the separator, respectively [9]. Tests of flame resistance of separators (6 x 6 cm) were conducted by igniting liquid-electrolyte soaked separators, observing the burning process, and calculating the dimensional change using equation 5.1. Electrolyte uptake was calculated using equation 5.2:

$$\text{Electrolyte Uptake (\%)} = (M_{\text{wet}} - M_{\text{dry}}) / M_{\text{dry}} \times 100\% \quad (5.2)$$

where  $M_{\text{dry}}$  and  $M_{\text{wet}}$  are the masses of the dry and wet separator, respectively. The porosity of the separators was calculated by the *n*-butanol uptake method using equation 5.3:

$$\text{Porosity (\%)} = 1 - (M / \rho_{\text{PI}} \times V) \quad (5.3)$$

where  $M$  is the separator weight,  $\rho_{\text{PI}}$  is the density of PI (P84), and  $V$  is the apparent volume of the separator.

### 5.2.3 Electrochemical Characterization

Electrochemical tests were carried out in CR2032 coin cells. Ionic conductivity testing was conducted using electrochemical impedance spectroscopy (EIS) on a Bio-Logic SP-150 potentiostat. Three separators were sandwiched between two stainless steel (SS) spacers inside a cell to obtain an average resistance [36]. AC impedance measurements were conducted at an amplitude of 5 mV over a frequency range of 100 kHz to 100 Hz. Ionic conductivity was calculated by equation 5.4:

$$\sigma = d / (R_b \times A) \quad (5.4)$$

where  $R_b$  is the bulk resistance from EIS,  $d$  is the combined thickness of the three separator layers, and  $A$  is the effective area of the SS spacer.

Battery performance was evaluated with full cells consisting of a NMC811 cathode and a graphite anode from NEI Corporation. Both electrodes had a composition of 90/5/5 weight ratio of active material / PVDF binder / conductive carbon. NMC811 active loading was  $10.4 \text{ mg cm}^{-2}$  and graphite active loading was  $6 \text{ mg cm}^{-2}$ . The electrolyte used in all tests was 1M  $\text{LiPF}_6$  in 4/4/2 volume ratio of EC/DEC/DMC with 10 wt% FEC addition (PuriEL from soulbrain MI). Cell performance was evaluated on an Arbin BT-2043 battery testing system in a voltage range of 3.0 – 4.3 V. Cycling tests were carried out at 0.5 and 1.0 C charge and discharge rates ( $1 \text{ C} = 170 \text{ mA g}^{-1}$ ). Rate capability of cells was tested at matching charge and discharge rates of 0.1, 0.2, 0.5, and 1 C, and then discharge rates of 2 and 4 C with charge rates kept at 1 C, before returning to 0.1 C.

### ***5.3 Results and Discussion***

#### **5.3.1 Material properties of electrospun separators**

FTIR analysis was used to examine the presence of cured ceramic precursor in the fibers. The OPSZ precursor (Fig. 5.2A) shows several characteristic peaks for a Si-NH-Si backbone including a Si-NH-Si bending mode at  $1168 \text{ cm}^{-1}$  and a NH stretching mode at  $3402 \text{ cm}^{-1}$ . Additionally, there is a SiH bending mode at  $2140 \text{ cm}^{-1}$  from the precursor backbone and a doublet peak at  $1126 \text{ cm}^{-1}$  and  $1060 \text{ cm}^{-1}$  from the trialkoxysilyl ( $\text{Si-OCH}_2\text{CH}_3$ ) functional group. A combination of low temperature moisture curing and  $300^\circ\text{C}$  heat treatment of OPSZ precursor leads to loss of or reduction in these peaks as OPSZ is hydrolyzed and cross-linked by condensation reactions at these sites [30, 31]. Forming PDC yields several key ceramic properties

for improved thermal stability and battery performance [33]. After heat treating the precursor there is new peak at 1020 representing Si-O-Si stretching replacing the Si-N-Si bonds. The OPSZ also contains an easily recognizable peak for identification from non-hydrolyzable Si-CH<sub>3</sub> at 1270 cm<sup>-1</sup>. The PI:PDC fibers were examined for peaks in the same regions for the presence of treated and untreated OPSZ (Fig. 2B). The PI:PDC fibers show small peaks at 1020 cm<sup>-1</sup> and 1270 cm<sup>-1</sup> that are not present in the pure PI sample, indicating the presence of PDC. There are no new peaks at any of the precursor hydrolyzable locations indicating a fully cross-linked PDC from the heat treatment. Due to the presence of PI groups in the spectra, to better show the ceramic presence, films were cast using a 60:40 wt ratio of PI:OPSZ that were heat treated and then evaluated with FTIR (Fig. 5.S1). The samples confirm the peaks seen in the lower OPSZ loadings, and show with better resolution that we obtain a cross-linked ceramic in our PI:PDC hybrid materials with an Si-O-Si backbone through moisture curing and heat treatment.

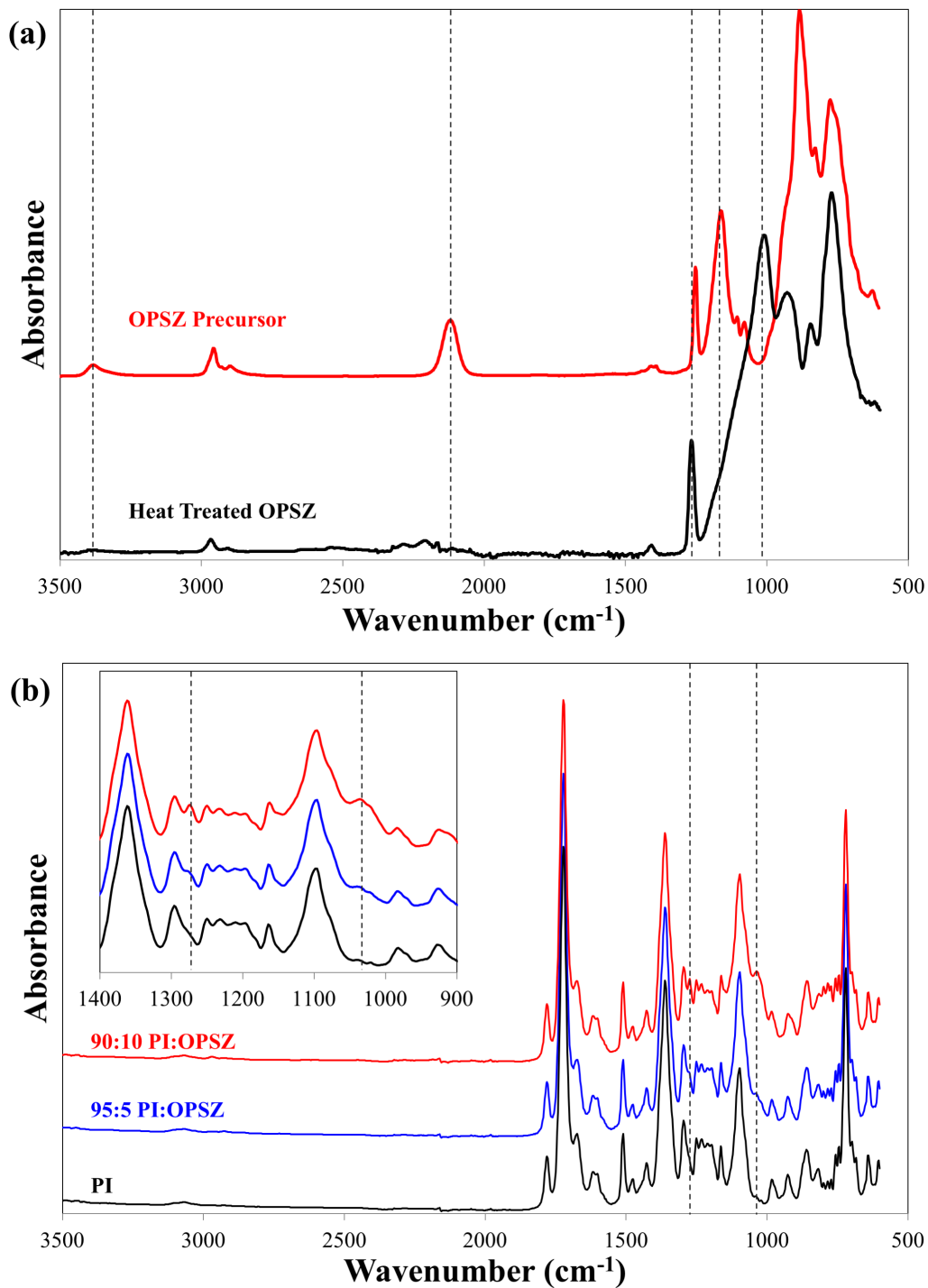


**Figure 5.2.** FTIR spectrum of (a) OPSZ precursor and the ceramic formed during curing, and (b) the electrospun separators. The inset of (b) magnifies the peaks of interest of heat treated OPSZ.

The morphology and fiber diameters of the heat-treated, calendered separators were investigated using SEM, and images are shown in Figure 5.3. The diameters of the prepared fibers are uniform and have an average diameter around 320 nm for all OPSZ loadings. The addition of OPSZ can increase the viscosity of the spinning solution and cause larger fiber diameters, but the 10% OPSZ addition started with a lower solution concentration to account for the change. The fiber morphologies are smooth and free of defects such as beads. The calendered fibers do show some signs of fiber flattening at fiber junctions, which is less significant with increased OPSZ loading, likely due to ceramic domains in the fibers making them less compressible.

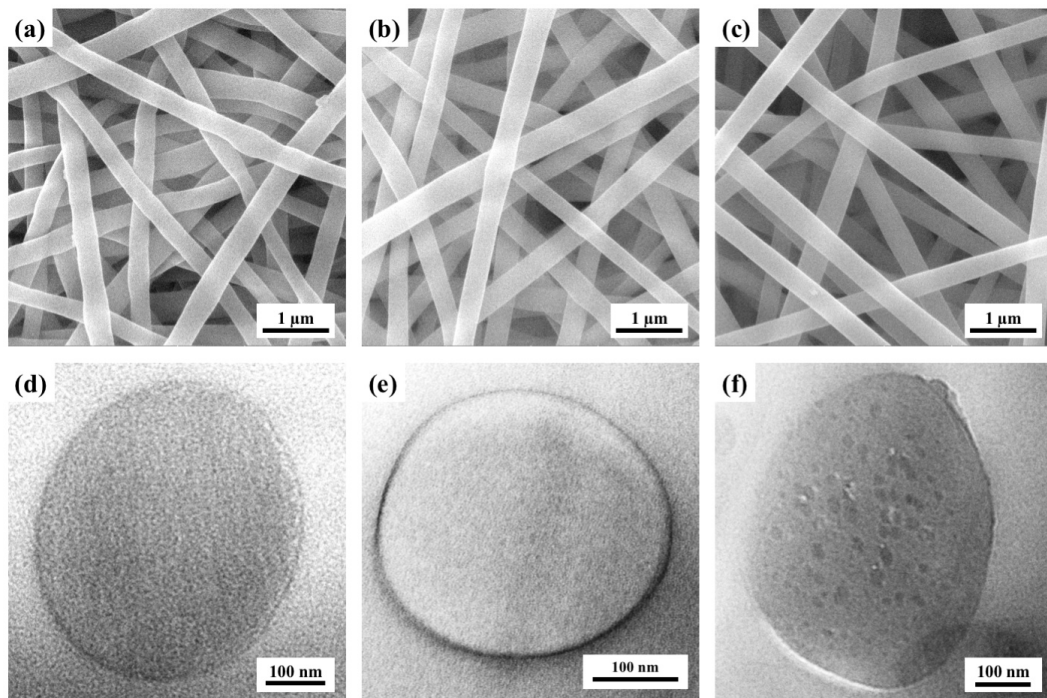


**Figure 5.3.** SEM and TEM images of electrospun separators. SEM images are (a) PI, (b) 95:5 PI:OPSZ, and (c) 90:10 PI:OPSZ. TEM are (d) PI, (e) 95:5 PI:OPSZ and (f) 90:10 PI:OPSZ fiber cross sections.

TEM was used to examine the ceramic morphology within the fibers (Fig. 5.3 d-f). The PI fiber cross section shows no distinguishing features. With OPSZ addition,

domains of PDC can be found at the fiber surface and within the PI matrix. Both the 5% and 10% loading show a thin shell layer on the outside of the nanofiber that is 5-6 nm thick for 95:5 PI:OPSZ fibers and 7-8 nm for 90:10 PI:OPSZ fibers. This ceramic layer is similar to layers seen in previous works with OPSZ precursor [32, 33] and this unique morphology cannot be replicated with nanoparticles. Within the fiber, the PDC content varies more significantly with OPSZ loading as the OPSZ domains selectively form at the fiber surface and excess OPSZ forms domains at the fiber core. The fibers with 10% OPSZ loading have increased occurrence of PDC domains as well as increased size. The average domain size inside the fibers are between 5 to 10 nm for 95:5 PI:OPSZ fibers and 15-20 nm for 90:10 PI:OPSZ fibers. These PDC domains will influence electrolyte interactions and battery performance as well as improving the thermal stability of the nanofiber separators.

Separators were evaluated to determine their density, porosity, and electrolyte uptake and their properties are listed in Table 5.1. High porosity, wettability, and uptake of electrolyte are important aspects to reducing the separator's resistance in the cell. The porosity of the electrospun separators is much higher than that of a commercial PP film, Celgard 2400, providing more void space for electrolyte to fill and easier diffusion of Li-ions through the separator. The PI and hybrid separators also demonstrated much better wetting with electrolyte that quickly soaked into the porous fiber mats (Fig 5.S2). These two traits influenced the much higher electrolyte uptake for electrospun separators, which was around 600% compared to 97% for Celgard. The electrolyte uptake did not vary significantly with OPSZ addition. With similar fiber diameter, porosity, and the high affinity of PI materials for polar electrolyte

solvents, the uptake was not improved with the addition of OPSZ but remained mostly constant.

**Table 5.1.**

Fiber diameter, density, porosity, and electrolyte uptake of electrospun separator membranes.

Sample	Fiber Diameter (nm)	Density (mg cm <sup>-3</sup> )	Porosity (%)	Electrolyte Uptake (%)
Celgard 2400	NA	0.58	41	97
PI	318 ± 62	0.43	69.2	628
95:5 PI:OPSZ	322 ± 54	0.42	68.8	606
90:10 PI:OPSZ	316 ± 38	0.42	70.1	599

### 5.3.2 Thermal stability, thermal shrinkage, and flammability

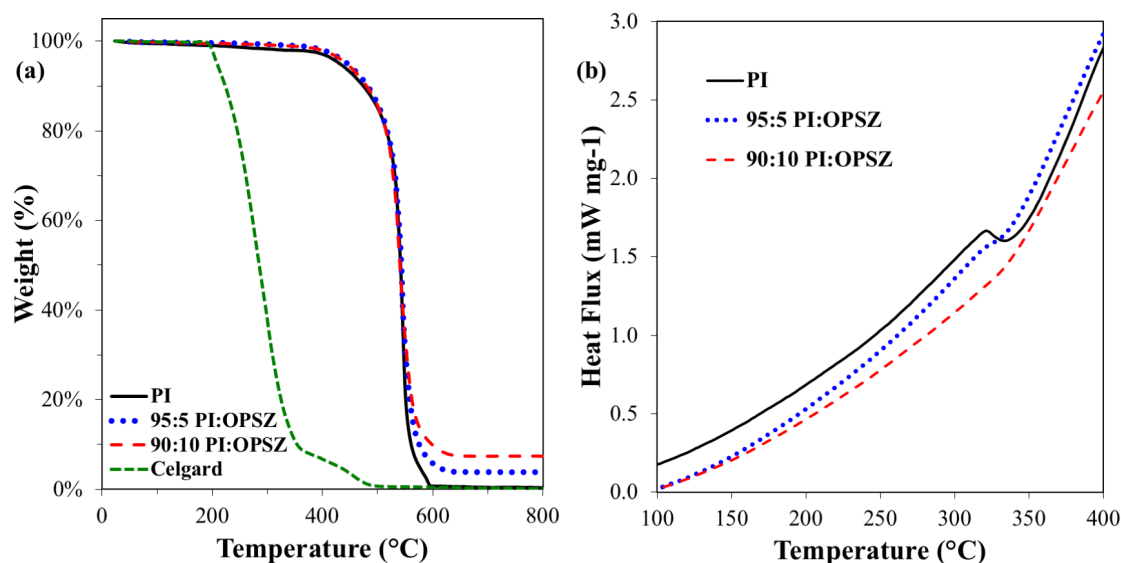


**Figure 5.4.** Separator thermal performance in (a) TGA isotherms and (b) DSC measurement in air environment (exo up).

TGA was used to determine the weight percent inclusion of OPSZ in the nanofibers as well as to demonstrate the excellent thermal stability of the PI and PI:PDC separators. The TGA results shown in Figure 5.4a indicate high onset temperature of mass loss for all PI-based separators. Celgard loses 5% mass by 210°C,

while the PI and PI:OPSZ separators lose 5% mass at 450°C. The addition of ceramic does not affect the decomposition of PI polymer and the PI and PI:PDC separators align closely. At high temperatures, the ceramic contents can be determined with 3.7% and 7.3% ceramic for the 5 and 10 wt% precursor loadings respectively. DSC results up to 400°C in Figure 5.4b shows only a glass transition for polyimide at 318°C. With the addition of OPSZ, the endothermic peak is diminished with 5% loading, and only a slope shift can be seen with 10% loading as the PDC interrupts the polymer matrix. The TGA and DSC show that the separators have the excellent intrinsic thermal stability of PI, and OPSZ addition does not significantly change the properties. Additionally, to measure the effect of the heat treatment, TGA and DSC were also run for samples only dried at 120°C for 24 hours and were not heat treated at 300°C (Fig. 5.S3). The fibers with OPSZ that only went through low-temperature curing show additional mass loss from 200°C to 300°C that corresponds to exothermic peaks in the DSC seen in both the OPSZ-containing fiber samples and the OPSZ precursor. The heat treatment is necessary for further condensing of the ceramic.

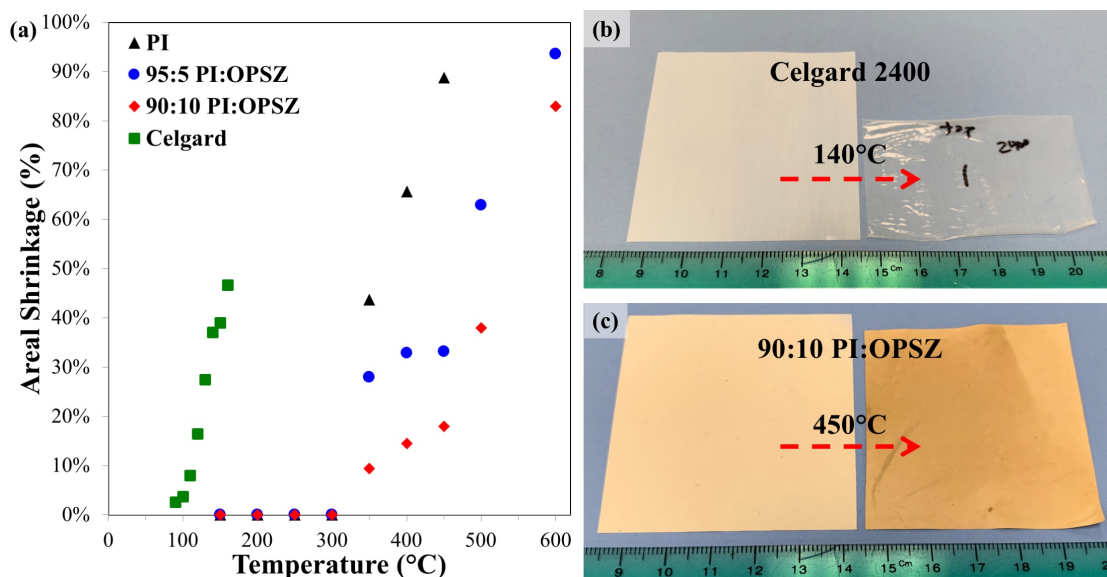


**Figure 5.5.** (a) Thermal shrinkage was measured after holding materials at different temperatures for 1 hour. The area lost after 1 hour has been plotted for each separator type. (b) Image of Celgard after holding at 140°C for 1 hour; (c) image of 90:10 P84:OPSZ separator after holding at 450°C for 1 hour.

Thermal shrinkage is evaluated by taking 6-cm squares of the separator materials and placing them in a furnace at set temperatures for 1 hour. The areas of the samples are measured before and after the thermal aging and the area lost is plotted in Figure 5.5. Celgard was evaluated over a temperature range of 90°C to 170°C and showed significant shrinkage above 100°C. The shrinkage was in the stretched, machine direction and is depicted in image (b) of Figure 5.5. There is no directionality in the shrinkage from the electrospun separators. The PI and PI:PDC separators were heat treated at 300°C and show no shrinkage at lower temperatures. At 350°C the PI and 95:5 PI:OPSZ separator show significant shrinkage, losing 43.7% and 28%, respectively, while the 90:10 PI:OPSZ separator achieves 9.4%. The 90:10 PI:OPSZ separators, with a more prevalent shell layer and larger ceramic domains, demonstrate greater thermal stability with only 18.0% areal shrinkage at 450°C. At temperatures above 450°C, as seen in the TGA tests, the PI deteriorates and burns off quickly. The PI separators did not survive 500°C aging and the PI deterioration contributed to significant shrinkage in the PI:PDC systems. The PI:PDC samples maintain a small square of pure ceramic at 600°C.

To test the effect of heat treatment on the separators, PI and PI:OPSZ fiber separators were dried at 120°C and were never heat treated. These samples were tested at temperature increments up to 300°C (Fig. 5.S3). Pure PI fibers showed minor shrinkage at 300°C with only 2% area loss. The hybrid fibers showed significant

shrinkage, beginning at 200°C, that increased with OPSZ content. At 300°C, the dried-only 90:10 PI:OPSZ shows 26.8% areal shrinkage, which the heat treated separator only displayed above 450°C. The heat curing of the OPSZ precursor to PDC is essential to the thermal stability of the separator.

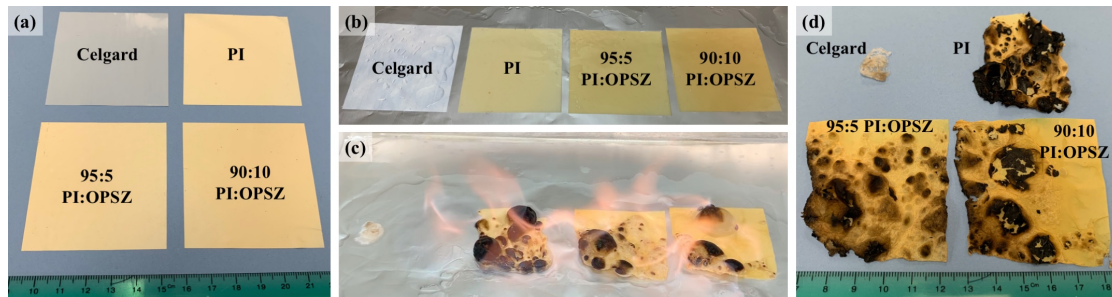


**Figure 5.6.** Flame testing: (a) Separator samples before flame testing. (b) Samples placed in tray and soaked with electrolyte. (c) The electrolyte is lit on fire. (d) Separator conditions post flame testing.

The flame resistance of the separators was tested by burning electrolyte. 6-cm squares of each material were placed in an aluminum pan with 20-ml of electrolyte. Figure 5.6 shows the conditions once the electrolyte was lit with a torch and the fire was allowed to burn until the electrolyte was consumed. The Celgard quickly shrinks and melts. The PI and hybrid samples show some bubbling across the surface and singeing from gas evolution by the electrolyte but they remained physically intact and held form. The shrinkage was 44.0%, 14.2%, and 7.8% for PI, 95:5 PI:OPSZ, and 90:10 PI:OPSZ respectively. Similar to the thermal shrinkage, the non-flammable ceramic shell layer and ceramic domains within the fibers protect the separator and improved the flame resistance of the separator. The test was repeated for dried, and never heat-treated samples, and the change was drastic (Fig. 5.S4). Pure PI fibers shrink by 92.5% forming a small square of material. Without any thermal crosslinking or formation of CTCs, the PI separator cannot stand up to the flame as well as the

annealed samples. The addition of dried only, untreated OPSZ is disastrous. Neither the 5% or 10% OPSZ samples survive the flame test and completely break down in the electrolyte fire with no separator material left for area measurement. Uncured OPSZ is a flammable agent running through and around the fibers and additional OPSZ led to faster breakdown in the flames. The annealing of PI and curing of the ceramic precursor become even more important for flame resistance to add safety to Li-ion batteries.

### 5.3.3 Electrochemical testing

The ionic conductivity of the separators represents how quickly Li-ions can transfer through the separator during charge and discharge and can be calculated by EIS. The Nyquist plot in Figure 5.7a was generated from EIS results for the four separators. The inset is a zoomed image near the x-axis. The x-intercept of each plot represents the bulk resistance,  $R_b$ , in each cell attributed to the triple-stacked separators. The intercept was determined by a linear fit and then divided by 3 to find the resistance for individual separator layers. This resistance value is then used to determine the ionic conductivity for each separator material. The average properties, resistance values, and ionic conductivities for the stacked separators are listed in Table 5.2. As seen in previous works with PI nanofibers, the larger porosity of the nanofiber mat and improved wettability led to a 45% increase in ionic conductivity compared to Celgard. The addition of ceramic further improves the ionic conductivity with 81% and 150% increases compared to Celgard for 95:5 PI:OPSZ and 90:10 PI:OPSZ separators respectively. While the three electrospun separators' high porosities aid ion diffusion in the cell, the ceramic content is significant in decreasing separator

resistance, and increased OPSZ loading increased ionic conductivity. Ceramic fillers improve ionic conductivity by acting as plasticizers to decrease polymer crystallinity as well as acting as Lewis acid-base centers promoting salt dissociation freeing more Li-ions [19, 20]. The surface layer of ceramic in the PI:PDC fibers enhances these interactions by direct contact with the liquid electrolyte and greatly increasing the ionic conductivity.

**Table 5.2.**

Physical properties of separators and their ionic conductivities calculated from EIS

Separator	Avg. Thickness ( $\mu\text{m}$ )	Avg. Bulk Resistance ( $\Omega$ )	Ionic conductivity ( $\text{mS cm}^{-1}$ )
Celgard 2400	25.0	1.34	0.96
PI	20.3	0.75	1.40
95:5 PI:OPSZ	20.0	0.59	1.74
90:10 PI:OPSZ	20.7	0.44	2.39

Separators went through several battery evaluations to test the separator effects on battery rate capability and cyclability (Fig. 5.7). All tests started with several formation cycles at 0.1C. Averaged across all cell tests, the electrospun separators improved the first cycle coulombic efficiency in the full cells, reaching 85.5%, 85.6%, and 85.8% for PI, 95:5 PI:OPSZ, and 90:10 PI:OPSZ, respectively, compared to 83.7% for Celgard. The electrospun separators also achieved a higher first charge capacity compared to Celgard, and, coupled with their increased coulombic efficiency, led to a significant increase in initial discharge capacities with 191.3, 191.4, 192.7, and 185.0  $\text{mAh g}^{-1}$  for PI, 95:5 PI:OPSZ, 90:10 PI:OPSZ, and Celgard respectively. The high electrolyte uptake and better wettability improve the cell in the first cycle.

Rate capability testing for the PI and hybrid separators can be seen in Figure 5.7b. The PI and PI:PDC separators have similar results at milder conditions with the ceramic addition becoming more important as rates reach 1C and higher. Celgard cells, with lower first cycle coulombic efficiency and ionic conductivity, start at lower capacity and retain less capacity as charge rates increase. When increasing the discharge rate to 2C (1C charge), higher ionic conductivity is more significant, and the PI:PDC separators retain more capacity than the pure PI separator. This effect is most pronounced at 4C discharge (1C charge), and the effect of increased ceramic can be seen with 10% OPSZ cells performing better than the PI and 5% OPSZ cells. Compared to their C/10 capacities of 191 mAh g<sup>-1</sup>, there is a 37.5%, 33.7%, and 25.5% retention at 4C discharge (1C charge) for the 90:10 PI/OPSZ, 95:5 PI:OPSZ, and pure PI separators respectively. The Celgard cells retain only 16.0% of their capacity at 4C discharge. When returning to C/10 rate, all cells showed good recovery. The electrospun separator cells recover more than 96% of their first cycle capacity and Celgard cells recover 93%.

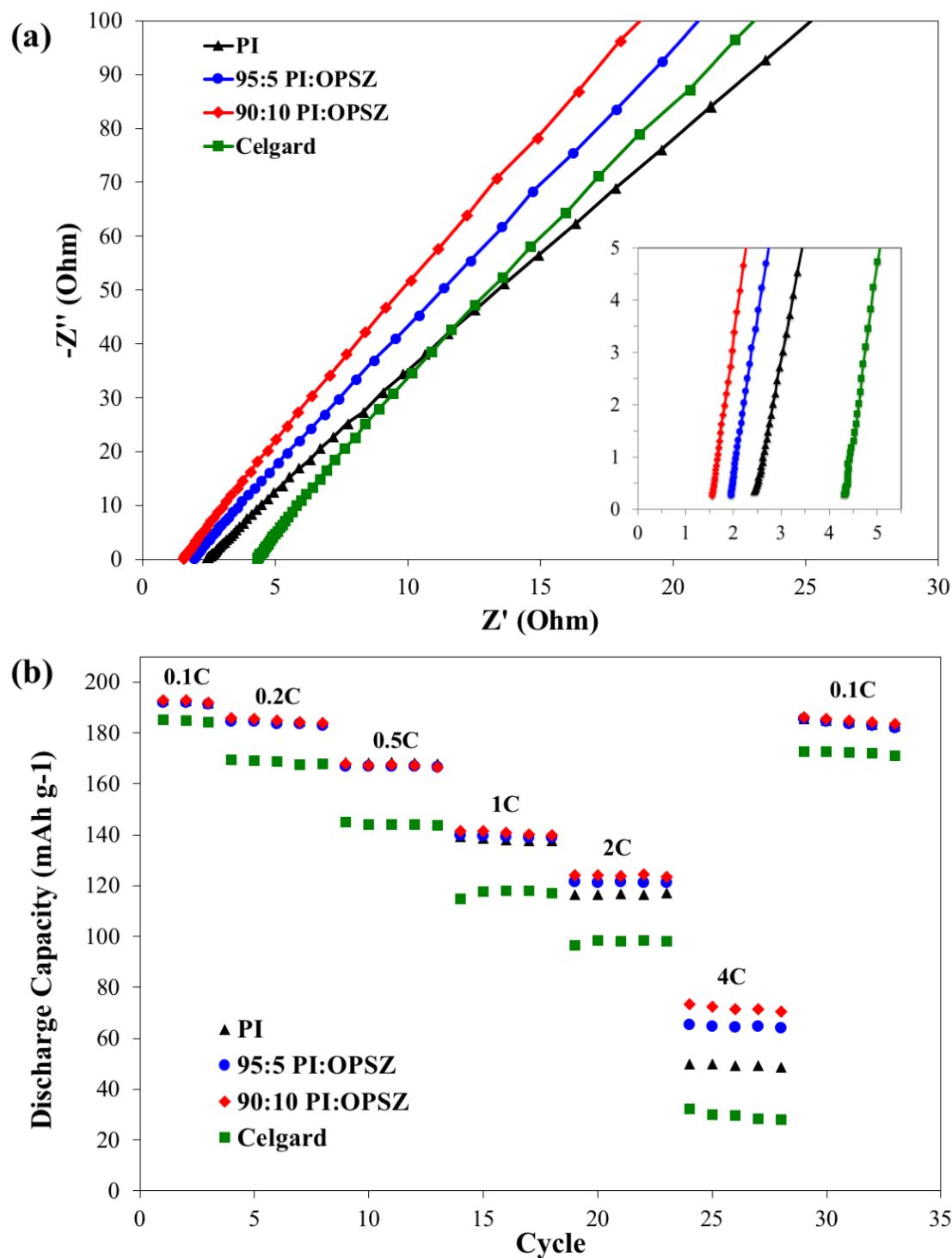


**Figure 5.7.** (a) Nyquist plot from EIS of the SS-symmetrical cells with three layers of PI, 95:5 PI:OPSZ, 90:10 PI:OPSZ, and Celgard separators (b) Results of rate capability tests for the NCM811/graphite full cells with various separator membranes. Discharge rates reach 4C while charge rates are limited to 1C in cell tests.

Figure 5.8a and 5.8b show the cycling performance of electrospun PI and PI:OPSZ separators compared to Celgard at 0.5C and 1C rates in NMC 811/graphite full cells. At 0.5C, electrospun separators start at 170-175 mAh g<sup>-1</sup> while Celgard starts at 148 mAh g<sup>-1</sup>. After 250 cycles the hybrid separators showed the highest capacity retention, retaining 67.9%, 75.1%, 76.1% and 77.8% for Celgard, PI, 95:5 PI:OPSZ, and 90:10 PI:OPSZ respectively. The test was then run at higher rate and for more cycles, testing at 1C for 500 cycles. As seen in the first case, the cells containing the electrospun separators, with their higher electrolyte uptake, wettability, and ionic conductivity, perform much better than the polyolefin film. The electrospun separators start at 140-144 mAh g<sup>-1</sup> while Celgard starts at 127 mAh g<sup>-1</sup>. After 500 cycles, the full cells' retention aligns with the ionic conductivities of the separators with the 90:10 PI:OPSZ separator exhibiting the best performance. The cells showed 56.1%, 62.6%, 64.4%, and 69.2% retention for Celgard, PI, 95:5 PI:OPSZ, and 90:10 PI:OPSZ, respectively.

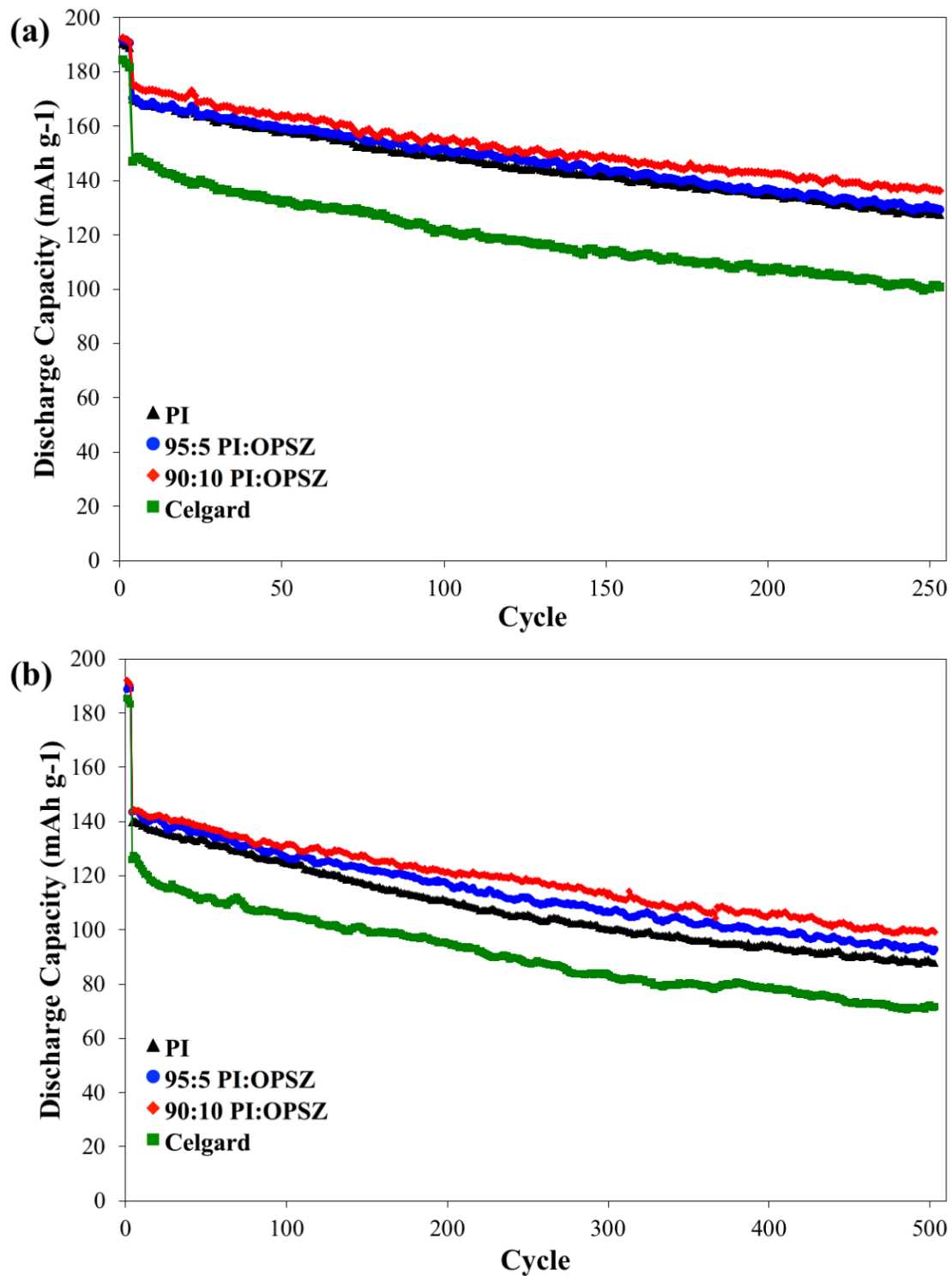


**Figure 5.8.** (a) and (b) show the cycling performance comparison of the PI, PI/OPSZ, and Celgard separators at (a) 0.5C and (b) 1C rates in NCM811/graphite full cells.

#### ***5.4 Conclusions***

PI and OPSZ solutions have been electrospun and heat treated to form PI:PDC separators. The use of a polysilazane precursor with a  $\text{Si}(\text{OCH}_2\text{CH}_3)_3$  chain enabled high ceramic loading, ceramic blending throughout the fiber without aggregation, and ceramic domains both within the fiber as well as forming a shell layer. The thermal treatment at  $300^\circ\text{C}$  enabled advantageous material changes for both the polymer and the ceramic precursor as the hybrid separators have demonstrated both improved battery performance and improved safety compared to the PP film reference and the pure PI electrospun separator. In particular, the 10% loading of OPSZ added protection to the fiber separator and demonstrated minimal thermal shrinkage and excellent flame resistance, demonstrating much improved safety over polyolefin and PI materials. All electrospun separators exhibited high ionic conductivity, capacity retention at high battery charge/discharge rates, and battery cyclability. The ceramic shell layer of the PI:PDC fibers further improved electrolyte interactions and ionic conductivity, and at 10% OPSZ inclusion the NMC 811/graphite full cells retained 69.2% of their capacity after 500 cycles at 1C rate, and more than doubled the capacity of the polyolefin cells at 4C discharge rate. PI:PDC separators address the thermal issues seen as safety hazards in electric vehicles and improve the performance of the batteries over their lifetime.

## 5.5 Supporting Information

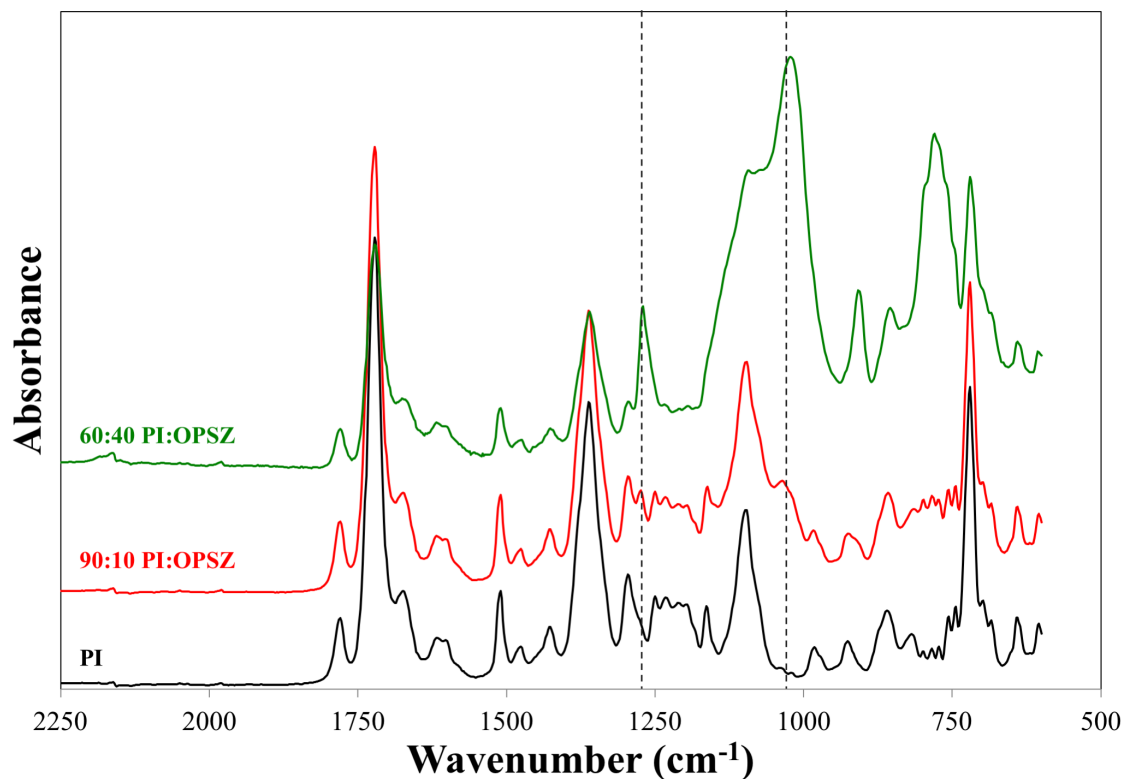


**Figure 5.S1.** FTIR spectra of high-OPSZ content film (60:40 PI:OPSZ) versus electrospun PI and 90:10 PI:OPSZ.

In order to better see the ceramic curing in the hybrid fibers, films with increased OPSZ content were prepared, dried, and heat treated at 300°C. Figure 5.S1. Show the spectra comparison of the hybrid film versus the PI and 90:10 PI:OPSZ fibers. The two peaks of interest are the additional peaks at 1280 cm<sup>-1</sup> and at 1040 cm<sup>-1</sup> seen in the hybrid film and fiber but not in the pure PI fiber. These represent the non-hydrolyzable Si-CH<sub>3</sub> group and Si-O-Si bonds, respectively showing the presence of cured OPSZ ceramic in the hybrid materials.

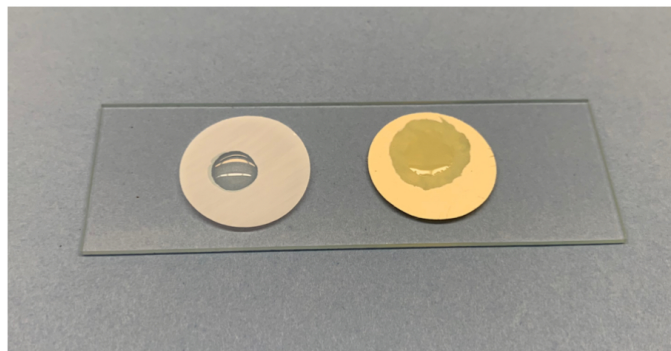


**Figure 5.S2.** A wettability comparison of Celgard and 90:10 P84:OPSZ. The picture is taken a few seconds after placing a drop of electrolyte on each separator.

The wettability of the separators was compared with a drop of electrolyte.

Placed at the same time, the electrolyte immediately starts to wet the electrospun separators and quickly spreads relative to the Celgard separator.

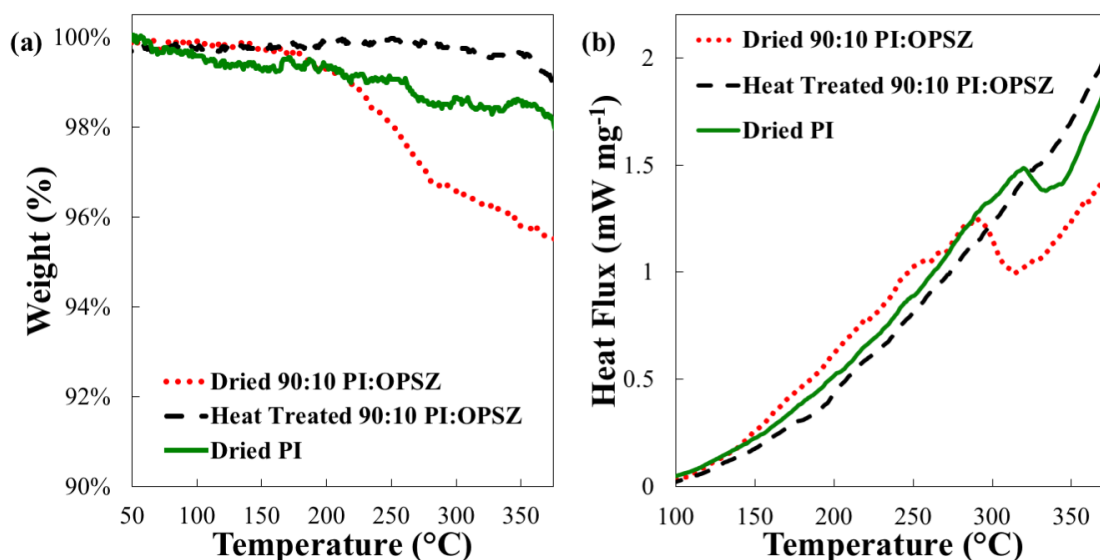


**Figure 5.S3.** (a) TGA and (b) DSC of dried-only PI and dried-only 90:10 PI:OPSZ samples compared to heat treated 90:10 PI:OPSZ (exo up).

Heat treatment of PI:OPSZ fibers at 300°C promotes further condensing of the OPSZ precursor into PDC. Figure 5.S3 shows that samples that were only dried at 120°C, and only go through low temperature moisture curing of OPSZ, go through additional mass loss by 300°C in TGA. Dried PI fibers exhibit mass loss as well, however, the dried PI:OPSZ fibers show additional contributions from the OPSZ

precursor with a sharper mass drop from 230°C to 300°C. This mass loss corresponds to a broad exothermic peak seen in DSC spectra of the PI:OPSZ fibers 230 to 300°C. The dried PI and heat treated PI:OPSZ fibers do not exhibit these peaks or mass loss. This additional condensing of the OPSZ precursor and reduction of volatile organic groups is necessary for the PI:PDC fiber's excellent thermal stability.

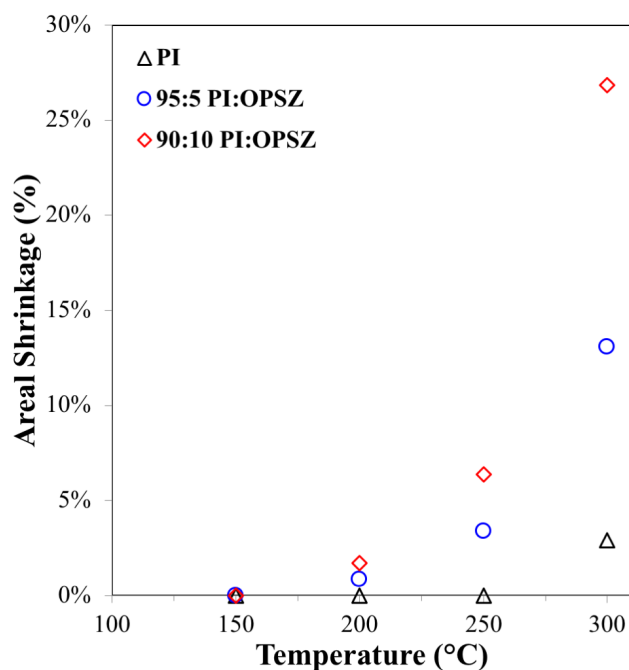


**Figure 5.S4.** Plot of areal shrinkage vs. holding temperature (1 hour) for dried, never heat treated, PI and PI:OPSZ separators.

PI separators show little change in thermal shrinkage in 300°C without annealing with no shrinkage until 300°C and area loss is 2.9%. The OPSZ samples show significant thermal shrinkage above 200°C without heat treatment to cure the ceramic. Increasing OPSZ precursor content decreases thermal stability. At 300°C the hybrid separators show 13.1% and 26.8% area loss for 95:5 and 90:10 PI:OPSZ separators respectively.

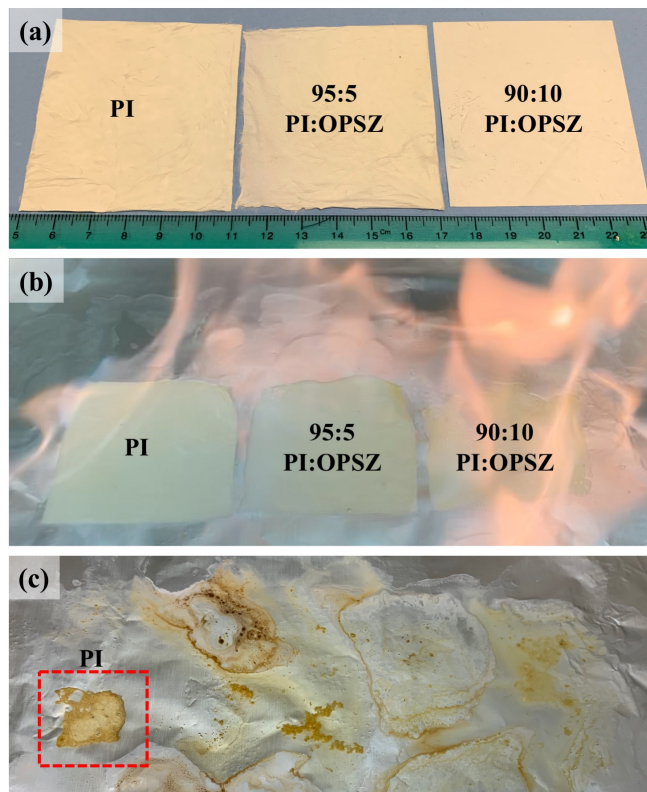


**Figure 5.S5.** Flame testing of dried, never heat-treated, PI and PI:OPSZ separators. (a) Samples before testing, (b) picture mid-test of electrolyte fire, and (c) post-electrolyte fire showing only the PI separator remained.

The PI separator shows much more significant shrinkage in the electrolyte fire without annealing. PI shrunk by 44.0% with annealing and by 92.5% without. PI:OPSZ samples completely break down in the fire and the addition of more uncured OPSZ precursor seems to make the breakdown more rapid. Picture (c) in Figure 5.S5 shows that the PI:OPSZ separators have no separator left but have deposited in bits across the aluminum foil.

## 5.6 References

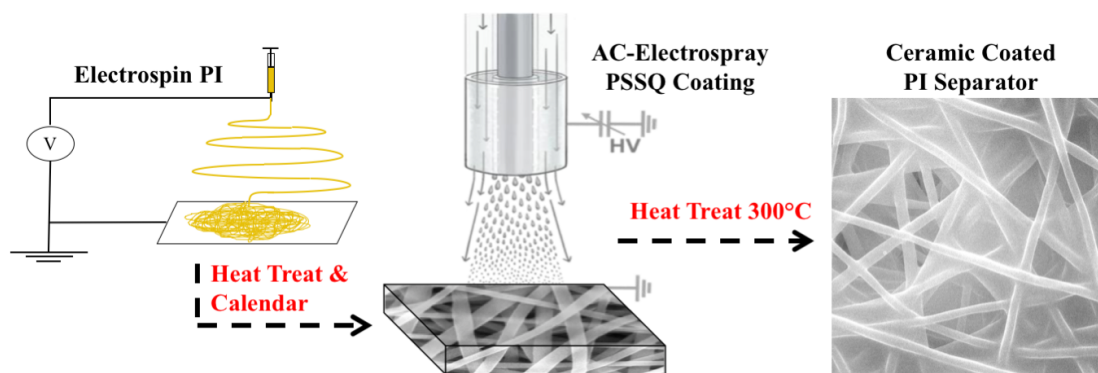
- [1] Ding, Y., Cano, Z. P., Yu, A., Lu, J. & Chen, Z. Automotive Li-Ion Batteries: Current Status and Future Perspectives. *Electrochemical Energy Reviews* **2**, 1–28 (2018).
- [2] Lu, L., Han, X., Li, J., Hua, J. & Ouyang, M. A review on the key issues for lithium-ion battery management in electric vehicles. *Journal of Power Sources* **226**, 272–288 (2013).
- [3] Rezvanizani, S. M., Liu, Z., Chen, Y. & Lee, J. Review and recent advances in battery health monitoring and prognostics technologies for electric vehicle (EV) safety and mobility. *Journal of Power Sources* **256**, 110–124 (2014).
- [4] Feng, X., Ouyang, M., Liu, X., Lu, L., & He, X. Thermal runaway mechanism of lithium ion battery for electric vehicles: A review. *Energy Storage Materials* **10**, 246–267 (2018).
- [5] Arora, P. & Zhang, Z. J. Battery Separators. *Chem. Rev.* **104**, 4419–4462 (2004).
- [6] Zhang, S. S. A review on the separators of liquid electrolyte Li-ion batteries. *Journal of Power Sources* **164**, 351–364 (2007).
- [7] Huang, X. Separator technologies for lithium-ion batteries. *J Solid State Electrochem* **15**, 649–662 (2010).
- [8] Wang, Q., Ping, P., Zhao, X., Chu, G., Sun, J., & Chen, C. Thermal runaway caused fire and explosion of lithium ion battery. *Journal of Power Sources* **208**, 210–224 (2012).
- [9] Liu, H., Xu, J., Guo, B. & He, X. Preparation and performance of silica/polypropylene composite separator for lithium-ion batteries. *J. Mater. Sci.* **49**, 6961–6966 (2014).
- [10] Jeon, H., Yeon, D., Lee, T., Park, J., Ryou, M.-H., Lee, & Y. M. A water-based Al<sub>2</sub>O<sub>3</sub> ceramic coating for polyethylene-based microporous separators for lithium-ion batteries. *Journal of Power Sources* **315**, 161–168 (2016).
- [11] Jung, J.-W., Lee, C.-L., Yu, S. & Kim, I.-D. Electrospun nanofibers as a platform for advanced secondary batteries: a comprehensive review. *J. Mater. Chem. A* **4**, 703–750 (2015).
- [12] Deimede, V. & Elmasides, C. Separators for Lithium-Ion Batteries: A Review on the Production Processes and Recent Developments. *Energy Technology* **3**, 453–468 (2015).
- [13] Miao, Y.-E., Zhu, G.-N., Hou, H., Xia, Y.-Y. & Liu, T. Electrospun polyimide nanofiber-based nonwoven separators for lithium-ion batteries. *Journal of Power Sources* **226**, 82–86 (2013).

- [14] Jiang, W., Liu, Z., Kong, Q., Yao, J., Zhang, C., Han, P., & Cui, G. A high temperature operating nanofibrous polyimide separator in Li-ion battery. *Solid State Ionics* **232**, 44–48 (2013).
- [15] Wang, Q., Song, W.-L., Wang, L., Song, Y., Shi, Q., & Fan, L.-Z. Electrospun polyimide-based fiber membranes as polymer electrolytes for lithium-ion batteries. *Electrochimica Acta* **132**, 538–544 (2014).
- [16] Wu, D., Shi, C., Huang, S., Qiu, X., Wang, H., Zhan, Z., Zhang, P., Zhao, J., Sun, D., & Lin, L. Electrospun Nanofibers for Sandwiched Polyimide/Poly(vinylidene fluoride)/Polyimide Separators with the Thermal Shutdown Function. *Electrochimica Acta* **176**, 727–734 (2015).
- [17] Cao, L., An, P., Xu, Z. & Huang, J. Performance evaluation of electrospun polyimide non-woven separators for high power lithium-ion batteries. *Journal of Electroanalytical Chemistry* **767**, 34–39 (2016).
- [18] Ding, Y., Hou, H., Zhao, Y., Zhu, Z. & Fong, H. Electrospun polyimide nanofibers and their applications. *Progress in Polymer Science* **61**, 67–103 (2016).
- [19] Croce, F., Appetecchi, G. B., Persi, L. & Scrosati, B. Nanocomposite polymer electrolytes for lithium batteries. *Nature* **394**, 456–458 (1998).
- [20] Salem N., Abu-Lebdeh Y. (2012) Effect of Nanoparticles on Electrolytes and Electrode/Electrolyte Interface. In: Abu-Lebdeh Y., Davidson I. (eds) *Nanotechnology for Lithium-Ion Batteries*. Nanostructure Science and Technology. Springer, Boston, MA.
- [21] Nunes-Pereira, J. & Costa, C. M. Polymer composites and blends for battery separators: State of the art, challenges and future trends. *Journal of Power Sources* **281**, 378–398 (2015).
- [22] Shayapat, J., Chung, O. H. & Park, J. S. Electrospun polyimide-composite separator for lithium-ion batteries. *Electrochimica Acta* **170**, 110–121 (2015).
- [23] Wang, Y., Wang, S., Fang, J., Ding, L.-X. & Wang, H. A nano-silica modified polyimide nanofiber separator with enhanced thermal and wetting properties for high safety lithium-ion batteries. *Journal of Membrane Science* **537**, 248–254 (2017).
- [24] Chen, W., Liu, Y., Ma, Y. & Yang, W. Improved performance of lithium ion battery separator enabled by co-electrospinning polyimide/poly(vinylidene fluoride-co-hexafluoropropylene) and the incorporation of TiO<sub>2</sub>-(2-hydroxyethyl methacrylate) *Journal of Power Sources* **273**, 1127–1135 (2015).
- [25] Liu, J., Liu, Y., Yang, W., Re, Q., Li, F., & Huang, Z. Lithium ion battery separator with high performance and high safety enabled by tri-layered SiO<sub>2</sub>@PI/m-PE/SiO<sub>2</sub>@PI nanofiber composite membrane. *Journal of Power Sources* **396**, 265–275 (2018).

- [26] Lee, J., Lee, C.-L., Park, K. & Kim, I.-D. Synthesis of an Al<sub>2</sub>O<sub>3</sub>-coated polyimide nanofiber mat and its electrochemical characteristics as a separator for lithium ion batteries. *Journal of Power Sources* **248**, 1211–1217 (2014).
- [27] Liang, X., Yang, Y., Jin, X., Huang, Z. & Kang, F. The high performances of SiO<sub>2</sub>/Al<sub>2</sub>O<sub>3</sub>-coated electrospun polyimide fibrous separator for lithium-ion battery. *Journal of Membrane Science* **493**, 1–7 (2015).
- [28] Zhong, G., Wang, Y., Wang, C., Wang, Z., Guo, S., Wang, L., Liang, X., & Xiang, H. An AlOOH-coated polyimide electrospun fibrous membrane as a high-safety lithium-ion battery separator. *Ionics* **25**, 2677–2684 (2019).
- [29] Sun, G., Dong, G., Kong, L., Yan, X., Tian, G., Qi, S., & Wu, D. Robust polyimide nanofibrous membrane with porous-layer-coated morphology by in situ self-bonding and micro-crosslinking for lithium-ion battery separator. *Nanoscale* **10**, 22439–22447 (2018).
- [30] Marceaux, S., Bressy, C., Perrin, F.-X., Martin, C. & Margailan, A. Development of polyorganosilazane–silicone marine coatings. *Progress in Organic Coatings* **77**, 1919–1928 (2014).
- [31] Müller, S., de Hazan, Y. & Penner, D. Effect of temperature, humidity and aminoalkoxysilane additive on the low temperature curing of polyorganosilazane coatings studied by IR spectroscopy, gravimetric and evolved gas analysis. *Progress in Organic Coatings* **97**, 133–145 (2016).
- [32] Smith, S. A., Park, J. H., Williams, B. P. & Joo, Y. L. Polymer/ceramic co-continuous nanofiber membranes via room-curable organopolysilazane for improved lithium-ion battery performance. *J. Mater. Sci.* **52**, 3657–3669 (2017).
- [33] Smith, S. A., Williams, B. P. & Joo, Y. L. Effect of polymer and ceramic morphology on the material and electrochemical properties of electrospun PAN/polymer derived ceramic composite nanofiber membranes for lithium ion battery separators. *Journal of Membrane Science* **526**, 315–322 (2017).
- [34] Vanherck, K., Koeckelberghs, G. & Vankelecom, I. F. J. Crosslinking polyimides for membrane applications: A review. *Progress in Polymer Science* **38**, 874–896 (2013).
- [35] Barsema, J., Klijnstra, S., Balster, J., van der Vegt, N., Koops, G., & Wessling, M. Intermediate polymer to carbon gas separation membranes based on Matrimid PI. *Journal of Membrane Science* **238**, 93–102 (2004).
- [36] Landesfeind, J., Hattendorff, J., Ehrl, A., Wall, W. A. & Gasteiger, H. A. Tortuosity Determination of Battery Electrodes and Separators by Impedance Spectroscopy. *J. Electrochem. Soc.* **163**, A1373–A1387 (2016).

## CHAPTER 6

### ELECTROSPUN POLYIMIDE NANOFIBERS COATED WITH A LADDER-LIKE POLYSILSESQUOXANE BY AIR-CONTROLLED ELECTROSPRAYING FOR IMPROVED LI-ION BATTERY SAFETY AND HIGH RATE CAPABILITY



#### Graphic Abstract

**Motivation:** In Chapter 5, a process was described in which separator materials were prepared using a hybrid solution of PI and OPSZ in a facile, two-step process of electrospinning and heat treatment. There are several limitations to this process for both scale-up and further improvements to the separator material. The OPSZ is highly reactive, and in choosing polymers to pair with the precursor, we were limited to P84 and a few other co-polyimides. Co-polyimides are already imidized, but due to being co-polymers, maintain solubility in solutions such as DMF. There is more interest in working with PI precursor material, polyamic acid (PAA), and polymer blends to try to improve the strength of electrospun separators; however, the OPSZ reacts immediately with the precursors and other polymers and they cannot be electrospun. Additionally, the OPSZ can cause gelling of solutions. In the work described in Chapter 5, OPSZ was limited to 10% loading when paired with P84 due to gelling at higher loadings. This

loading falls short of work done by Dr. Soshana Smith, who reached 30% OPSZ loading when paired with PAN [1]. The increased ceramic content above 10% had shown further increases in ionic conductivity but is not possible with our previous approach. Having chemicals in solution that react and gel in real time would also be much more difficult to scale for eventual use in EVs. The one-solution electrospinning method limits what we can design to what can be achieved with compatible chemicals. Chapter 6 is focused on a process that maintains the scalability of electrospinning, but is not limited to the compatibility of putting everything into one solution, and should allow for more freedom in polymer and precursor choice and control for a PI/Ceramic separator or other future combinations.

### ***6.1. Introduction***

Lithium-ion batteries (LIBs), having high energy density, great rate capability, and long cycle life, have found wide application in mobile devices and computers and increasing use as electrochemical storage systems for renewable energy and electric vehicles (EVs) [2, 3]. In most commercial LIBs, microporous polyolefin (PO) films are used as the battery separator to prevent physical contact of battery electrode and influence Li-ion transport across the cell. Their low cost, low thickness, high mechanical strength, and high chemical stability have contributed to their common usage [4]. However, several properties of the PO films are disadvantageous for battery use, stemming from the low porosity of the microporous films and the intrinsic material properties of the POs used as separator material, polypropylene (PP) and polyethylene (PE). The POs have poor electrolyte wettability due to their non-polar properties [5, 6].

Combined with the microporous films' low porosity, PO separators exhibit low electrolyte uptake and ionic conductivity, limiting battery performance and rate capability. More importantly, POs offer limited battery safety due to their low melting point temperatures (120-130°C for PE and ~165°C for PP) and significant areal shrinkage at temperatures above 90°C [5-8]. When used in EVs, the battery could experience hazardous conditions or physical abuse, causing elevated temperatures that are well above the limits of POs. When shrinkage of the separator occurs, there is further contact of battery electrodes, subsequent thermal runaway, and possible battery explosion [9, 10]. For increased EV use, thermal safety issues must be addressed with materials that can withstand elevated temperatures. Separators for future EVs should have excellent thermal stability as well as promote ion diffusion through the cell.

There have been many attempts to improve the thermal stability of PO films, mainly through applied coatings or grafting of inorganic ceramics to the separator surfaces [11-13]. The ceramic additions improve thermal shrinkage, however, at temperatures above the melting point of the polyolefin, the material is still unstable and would allow for contact of the electrodes. Other coating efforts include additions of highly thermally stable polymer coatings and binders, such as polyimide (PI) [14-16]. The use of PI improves thermal shrinkage further but does not fix the issues of the PO melting point. Additionally, while ceramics and polyimide are more electrophilic materials than POs, the addition of these surface level enhancements does not decrease the resistance of the bulk PO in the cell. No significant improvement is seen in cell performance, and in some cases, there is even diminished cell performance. Much of this could be due to the thick, binder-heavy coatings needed to adhere to the PO surface.

The coatings on PO separators do not prevent the safety issues in hazardous conditions, and they do not decrease the cell resistance of the POs that is needed for EV use.

An alternative to adding a protective coating is to begin with a separator framework that is already thermally stable [17]. As a scalable process for forming high porosity nanofibrous separators, electrospinning has been a research focus as a way to overcome many of the shortcomings of PO microporous films [18]. Electrospinning is a simple technique for preparing non-woven separator materials with uniform fiber size, high permeability, small pore size, and an interconnected open pore structure that can be used with many different polymers [19]. By working from an electrospun fiber framework, we are no longer limited to using PP and PE to form an ionically conducting, thermally stable separator. Instead of using PI as a coating for a PO separator, electrospinning is used to form PI nanofiber separators [20-24]. PIs are thermally stable to temperatures reaching 400°C, have no melting point, and can avoid the thermal shrinkage issues and safety issues seen in PP and PE. PI is also more electrophilic, and with much higher separator porosity, PI electrospun separators achieve greater ionic conductivity, rate capability, and battery performance. The thermal properties and flame resistance can be improved further with addition of a ceramic coating [25-27]. The ceramic coating improves the electrolyte wetting, but a thick polymer and particle coating covers much of the fiber mat's open pore structure, which is needed for ion diffusion, and there is not a significant increase in battery performance. A method that could add ceramic content to the fiber mat and penetrate into the fiber layers without the addition of binder would give the thermal stability advantage, as well as improve battery performance, and requires a material with both ceramic and adhesive properties.

Polysilsesquioxanes (PSSQs) are organic-inorganic hybrid materials that feature a structure of Si-O-Si bonds with functional end groups with an empirical structure of  $(\text{RSiO}_{3/2})_n$ . [28]. The end groups make PSSQ soluble in many organic solvents and cause it to easily disperse in most polymer matrices. These materials can be cross-linked at temperatures exceeding 100°C or with UV-radiation, condensing the PSSQ and forming a chemically resistant, thermally stable hybrid material. Due to their high inorganic content and thermal stability, PSSQs have been investigated for development of nanocomposites; they have recently garnered increased interest for Li-ion battery applications, including battery electrolytes [29, 30], and as additions to separator materials including nanoparticles in a non-woven separator [31], grafting material for electrospun separator [32], and as an inorganic binder for a ceramic coating [33]. PSSQs come in different structures including random, cage, and ladder-like polysilsesquioxanes (LPSQs). LPSQs are a double-stranded organosilicate and possess high thermal resistance as well as easily forming films [34, 35]. These properties are ideal for forming a thermally stable, binderless layer within a pre-existing fiber framework for battery separator applications.

To address challenges from a one-pot electrospinning solution for forming polymer/ceramic separators, this work presents a technique for making a PI nanofiber framework by electrospinning which is then coated and infused with a LPSQ via air-controlled electro spraying (ACES or AC-electro spraying). ACES is a technique that makes use of both high-pressure air and an electrical field to break up a solution into small droplets to coat a surface and has already been applied to several battery applications for electrodes and separators [35-40]. Solvent evaporation occurs during

the spraying process, allowing for higher flow rates and avoiding the significant drying process needed in dipcoating or blade coating. Here, an LPSQ solution is spray coated across the fiber surface with residual solvent, infusing into the surface layers of polymer fibers without soaking the substrate. This process forms a combined PI/LPSQ layer and does not form a separate LPSQ layer on top of a PI fiber separator. By using LPSQ this process avoids use of any polymer binders to adhere the ceramic material to the polymer fiber scaffold. Previous efforts by the Joo group focused on OPSZ, but OPSZ is a more expensive material and was better suited to a one-solution preparation, as it formed a ceramic sheath layer from a combined PI/precursor solution. OPSZ is not needed for a separated spin/spray fabrication and LPSQ holds several advantages in cost, spraying morphology, and high solubility in DMF. In this work, a 300°C heat treatment is used to cross-link the LPSQ coating and remove some of the functional end groups to form a PI/ceramic-rich layer in the separator and reduce the solubility of the LPSQ in polar solvents. The heat treatment also benefits the PI nanofibers, as at temperatures nearing the  $T_g$  (318°C) polyimides form charge transfer complexes (CTCs) [41, 42]. CTCs are a type of intra- and intermolecular bond that improves the PI's chemical resistance and thermal stability. We aim to show that an asymmetric separator containing a PI nanofiber matrix with a dense PI/LPSQ layer formed by ACES and heat treatment yields a thermally robust, flame-resistant separator with excellent battery performance for use in EVs.

## **6.2. Methods**

### **6.2.1 Preparation of coated PI separator**

PI non-woven membranes were prepared using electrospinning. P84, a commercially available PI, was purchased from HP Polymer Inc. P84 is a co-polyimide of 3,3'-4,4'-benzophenone tetracarboxylic dianhydride (BTDA) with 80% 2,4-diaminotoluene (TDI) and 20% 4,4'-methylenedianiline (MDI) and is drawn in Figure 6.1a. The electrospinning solution was prepared by dissolving PI in N,N-Dimethylformamide (DMF) for a 22wt% concentration. The solution was stirred at 50°C for 4 hours and then cooled to room temperature. The PI solution was electrospun using a 19-gauge needle, a 0.01 ml min<sup>-1</sup> flow rate, 20 kV applied to the needle, and the grounded collector set 18 cm away. After spinning, the fibers were placed between ceramic plates and heat treated at 300°C for 4 hours in air. The samples were then roll calendered to 25- $\mu$ m thickness.

Once calendered, the PI membranes were coated with LPSQ (one-sided) by ACES. The ceramic precursor used is an LPSQ with acrylate and methyl groups from Dongjin Semichem (Fig. 6.1b). The LPSQ was dissolved in DMF to form a 10 wt% solution. The PI nanofiber membrane was coated by ACES using an air atomizing nozzle (iSpray, part 1/8J-SU11), 25 kV voltage, a 27-cm gap to the sample, a 0.25 ml min<sup>-1</sup> flow rate, and 30 PSI of air pressure. The loading of ceramic was controlled by the time sprayed. Once coated, separators were heat treated at 300°C for 4 hours and were then ready for use. A polypropylene microporous film, Celgard 2400, was used for comparison studies to conventional separators.

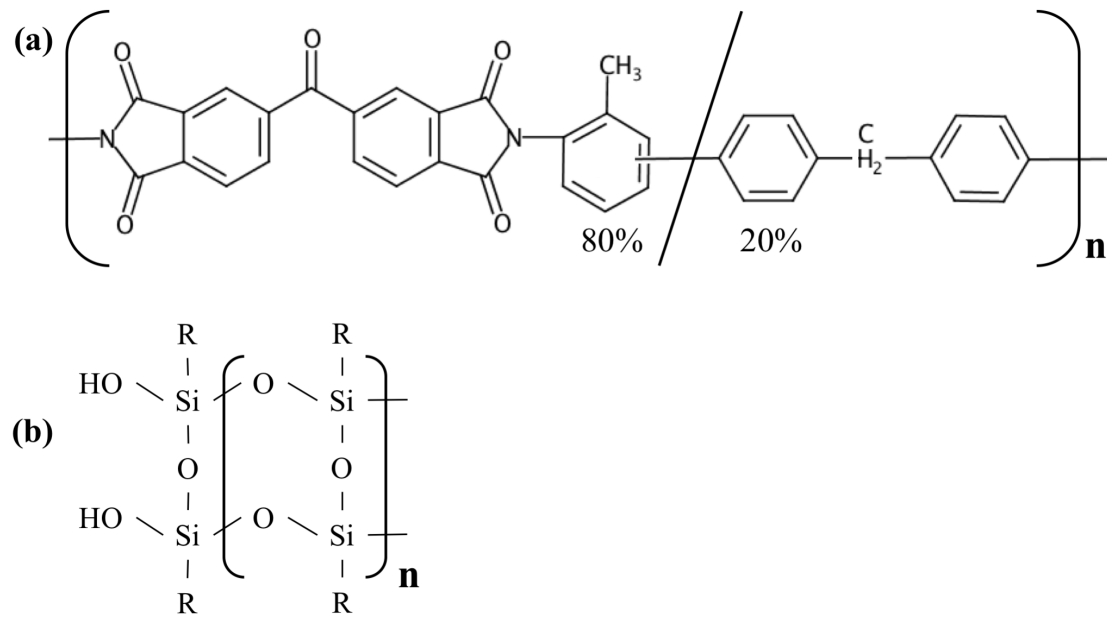


**Figure 6.1.** (a) The chemical structure of P84 co-polyimide and (b) the chemical structure of the ladder-like polysilsesquioxane.

### 6.2.2 Material Characterization

The fiber and coating morphologies and fiber diameter were examined using scanning electron microscopy (SEM) using a Tescan Mira3 FESEM with a 15 kV beam voltage. Fourier transform infrared (FTIR) spectra were obtained in the range of 4000-600  $\text{cm}^{-1}$  with a resolution of 4  $\text{cm}^{-1}$  for 64 scans using a PerkinElmer Frontier FT-IR spectrometer. Wide angle X-ray diffraction (XRD) patterns were recorded from 5° to 70° for all prepared separators using a Bruker D8 Advance ECO powder diffractometer with a 1 kW Cu-K $\alpha$  source. Thermal information about the LPSQ and its heat treatment was characterized through thermogravimetric analysis (TGA) and differential scanning calorimetry (DSC). The tests were run simultaneously using a Netzsch STA 449 F3 Jupiter apparatus under air environment from 25°C to 1000°C at 10°C/min heating rate. Areal ceramic loading on the fiber mat was determined by

burning off the polymer in a furnace held at 900°C in air and measuring the remaining inorganic content. Thermal shrinkage of the separators (4 x 4 cm) was observed by measuring the dimensional change after heat treatment at varied temperatures for 1 hour using equation 6.1:

$$\text{Shrinkage (\%)} = (A_i - A_f) / A_i \times 100\% \quad (6.1)$$

where  $A_i$  and  $A_f$  are the initial and final areas of the separator, respectively [43]. Tests of flame resistance of separators (4 x 4 cm) were conducted by igniting liquid-electrolyte soaked separators and observing the burning process and calculating the dimensional change using equation 6.1. Electrolyte uptake was calculated using equation 6.2:

$$\text{Electrolyte Uptake (\%)} = (M_{\text{wet}} - M_{\text{dry}}) / M_{\text{dry}} \times 100\% \quad (6.2)$$

where  $M_{\text{dry}}$  and  $M_{\text{wet}}$  are the masses of the dry and wet separator, respectively. The porosity of the separators was calculated by the *n*-butanol uptake method using equation 6.3:

$$\text{Porosity (\%)} = (M_{\text{BuOH}} / \rho_{\text{BuOH}}) / (M_{\text{BuOH}} / \rho_{\text{BuOH}} + M_{\text{dry}} / \rho_{\text{PI}}) \times 100\% \quad (6.3)$$

Where  $M_{\text{BuOH}}$  is the weight of *n*-butanol absorbed,  $M_{\text{dry}}$  is the weight of the dry separator,  $\rho_{\text{BuOH}}$  is the density of *n*-butanol, and  $\rho_{\text{PI}}$  is the density of PI (P84). A capillary flow porometer (Porous Media Inc., NY) was used to characterize pore size distribution of the fabricated membranes from the dry and wet flow curves.

### 6.2.3 Electrochemical Characterization

Electrochemical tests were carried out in CR2032 coin cells. Ionic conductivity testing was done using electrochemical impedance spectroscopy (EIS) on a Bio-Logic SP-150 potentiostat. Three separators were sandwiched between two stainless steel (SS) spacers inside a cell to obtain an average resistance [44]. AC impedance measurements were done at amplitude of 5 mV over a frequency range of 300 kHz to 100 Hz. Ionic conductivity was calculated by equation 6.4:

$$\sigma = d / (R_b \times A) \quad (6.4)$$

where  $R_b$  is the bulk resistance from EIS,  $d$  is the combined thickness of the three separator layers, and  $A$  is the effective area of the SS spacer.

Battery performance was evaluated with full cells consisting of an NMC811 cathode and a graphite anode from NEI Corporation. Both electrodes had a composition of 90/5/5 weight ratio of active material / PVDF binder / conductive carbon. NMC811 active loading was  $10.4 \text{ mg cm}^{-2}$  and graphite active loading was  $6 \text{ mg cm}^{-2}$ . The electrolyte used in all tests was 1M LiPF<sub>6</sub> in 4/4/2 volume ratio of EC/DEC/DMC with

10 wt% FEC addition (PuriEL from soulbrain MI). Cell performance was evaluated on an Arbin BT-2043 battery testing system in a voltage range of 3.0 – 4.3 V. Cycling tests were carried out at 0.5 and 1.0 C charge and discharge rates (1C = 170 mA g<sup>-1</sup>). Rate capability of cells was tested at matching charge and discharge rates of 0.1, 0.2, 0.5, and 1C, and then discharge rates of 2 and 4C with charge rates kept at 1C, before returning to 0.1C.

### ***6.3. Results and Discussion***

#### **6.3.1 Material properties of separators**

LPSQ is soluble in DMF due to the presence of several organic functional groups on its ladder structure, which allows for a highly loaded liquid precursor solution for electrosprayed coatings. The presence of these groups, such as the precursors' acrylate groups, contribute to solubility not only in polar solvents, but also in carbonate-based electrolytes. If left untreated before cell assembly, the precursor's solubility would be an issue as it could dissolve out of the separator into the lithium-ion battery electrolytes. In this work, heat treatment was employed to cross-link the LPSQ and remove polar functional groups. Samples include untreated LPSQ, LPSQ aged in low temperature at 120°C for 12 hours, and LPSQ heat treated at 300°C for 4 hours.

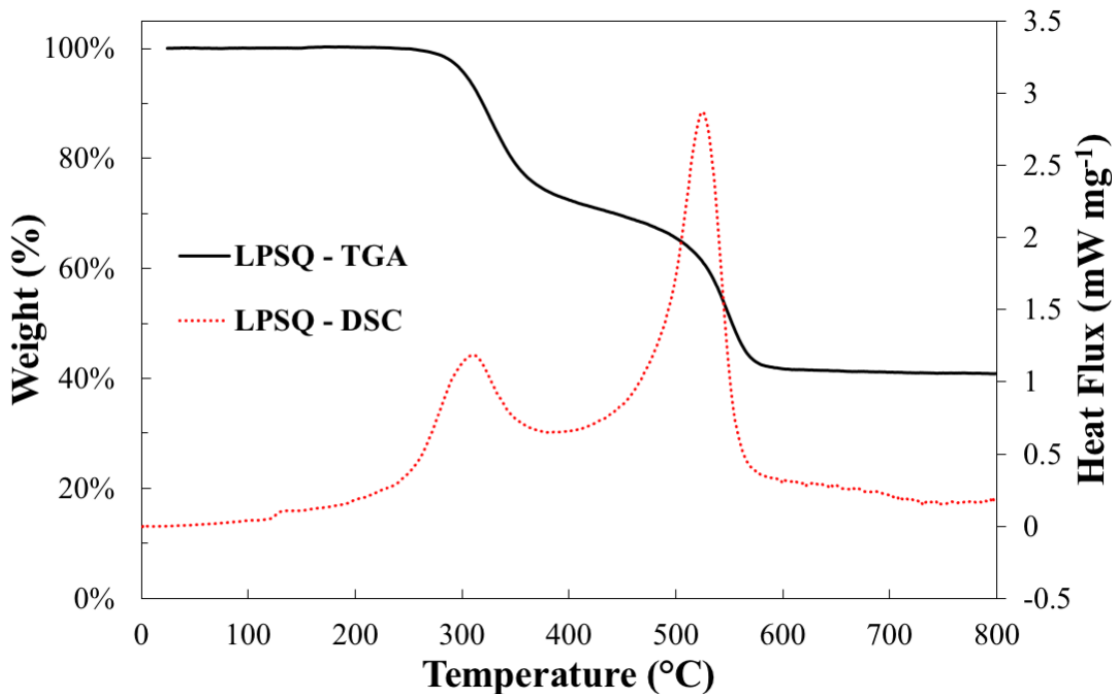


**Figure 6.2.** TGA/DSC of the LPSQ precursor.

Heat treatment and curing of the LPSQ precursor was first evaluated using TGA and DSC to find the reaction temperatures for the LPSQ and determine the precursors' inorganic content (Fig. 6.2). The DSC shows three peaks beginning with a small exothermic peak at 140°C which has been attributed to limited condensation of the LPSQ. A broad, exothermic peak found at 300°C establishes the temperature for more significant LPSQ crosslinking and removal of more volatile polar organic groups. The TGA shows that there is more than 20% mass loss from the LPSQ associated with this reaction as it forms a connected ceramic. Separately, LPSQ precursor was heat treated in a furnace for 4 hours at 300°C and showed a 78% yield, proving that the LPSQ has reacted and been crosslinked by the heat treatment. At temperatures above 500°C, calcination reduces the LPSQ to a pure inorganic material and 40.5% mass remains. Samples of PI sprayed with LPSQ were heat treated to 900°C and their resultant

inorganic content was used to calculate the LPSQ precursor added by AC-electrospraying and the amount of crosslinked ceramic after heat treatment. The LPSQ loading was found to be linear with time sprayed and the average loadings are listed in Table 6.1 for each sample tested. Coated samples will be differentiated by their heat treated loading.

**Table 6.1.**  
LPSQ areal loading by spray time.

Time Sprayed	LPSQ Loading (mg cm <sup>-2</sup> )	Heat Treated Loading (mg cm <sup>-2</sup> )
0.5 min.	0.071	0.055
1.0 min	0.141	0.110
2.0 min	0.282	0.220

FTIR analysis was used to examine the removal or reduction of active bonds to show that curing of the LPSQ took place (Fig. 6.2). The LPSQ samples show strong peaks at 1030 cm<sup>-1</sup> and 1130 cm<sup>-1</sup> attributed to asymmetric Si-O-Si stretching. The bimodal shape of the peaks is typical of siloxane groups in ladder structures [34, 45]. The untreated and 120°C LPSQ show peaks at 1640 cm<sup>-1</sup> and 1740 cm<sup>-1</sup> corresponding to C=C and C=O of acrylate groups as well as an Si-CH<sub>3</sub> group at 1300. The peaks are reduced in the 120°C sample but still have a significant presence. These peaks are not present or significantly reduced in the 300°C LPSQ, proving effective removal of the organic functional groups after heat treatment to form a ceramic coating for the PI separators.

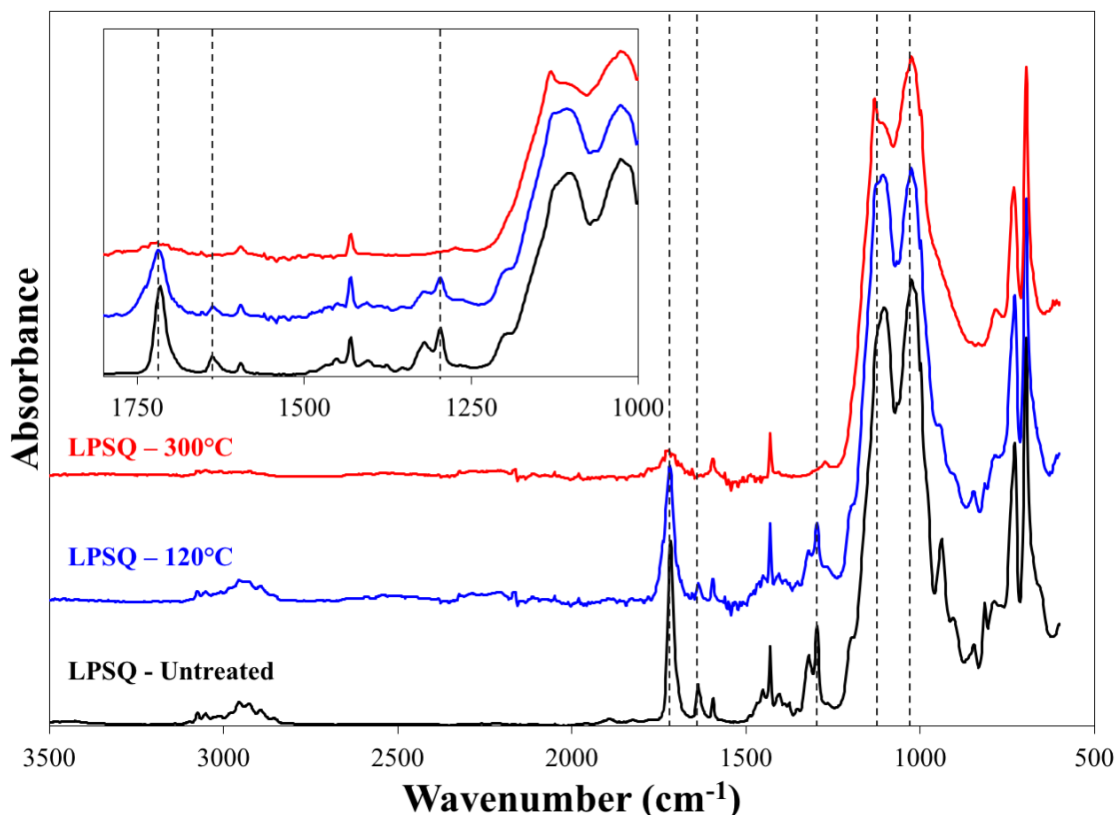


**Figure 6.3.** FTIR spectra of the LPSQ precursor at different stages of curing. The inset is a magnified look at peaks of interest.

Figure 6.4 shows the XRD of the LPSQ at different stages of heat treatment. For LPSQ, two peaks at about  $2\text{-Theta} = 7^\circ$  and  $20^\circ$  are expected, which are attributed to the ladder width (intramolecular chain-to-chain distance) and the ladder thickness of the LPSQ, respectively [46, 47]. While all the tested LPSQ fit this broad definition, the heat treated sample shows subtle changes that indicate some disruption to the ladder structure. The heat treated sample shows a shift in the location of the first peak (ladder width) from  $6.8^\circ$  to  $7.5^\circ$  as well as broadening of the peak. A similar shift and broadening are seen in the second peak at  $20^\circ$  compared to the dried and untreated LPSQ. The overall shift to higher  $2\text{-Theta}$  shows a condensing of the ladder structure in

both width and thickness as more volatile functional groups were removed during heat treatment. The broadening of the peaks suggests some loss of ordering from the original LPSQ, although the ladder structure still remains.

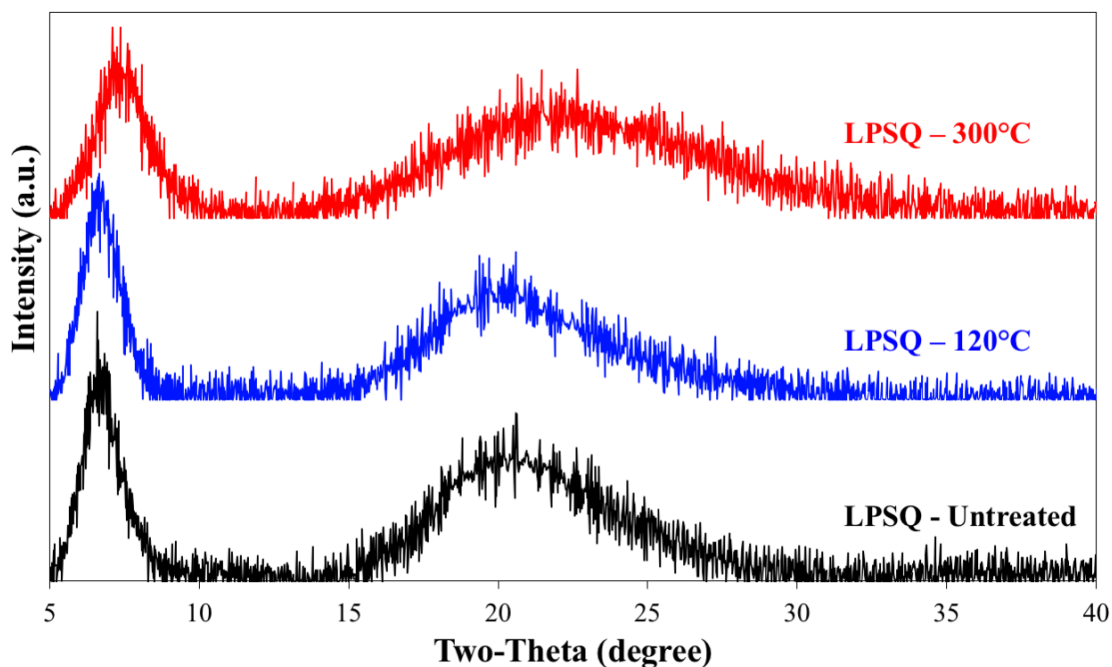


**Figure 6.4.** XRD of the LPSQ precursor after varied heat treatments.

The LPSQ was then tested for solubility in electrolyte to qualitatively show the effect of polar group removal and cross-linking (Fig. 6.5). 0.5 g of each sample was placed in 7g of electrolyte to fully submerge the LPSQ samples. Within 1 day, the untreated LPSQ had liquified and showed signs of incorporating into the electrolyte solution. There is no rigidity in the structure and the remaining LPSQ not dissolved into solution has a soft, gel-like quality even after removal from the electrolyte. The low temperature, 120°C heat treatment of LPSQ provided some stability, maintaining its structure, and only showed some signs of swelling in the solution. The LPSQ heat treated at 300°C displayed the highest stability in solution. The solubility steadily

improved with the increased curing and cross-linking seen from the TGA and FT-IR and demonstrated that the heat treatment of LPSQ is necessary for battery applications.

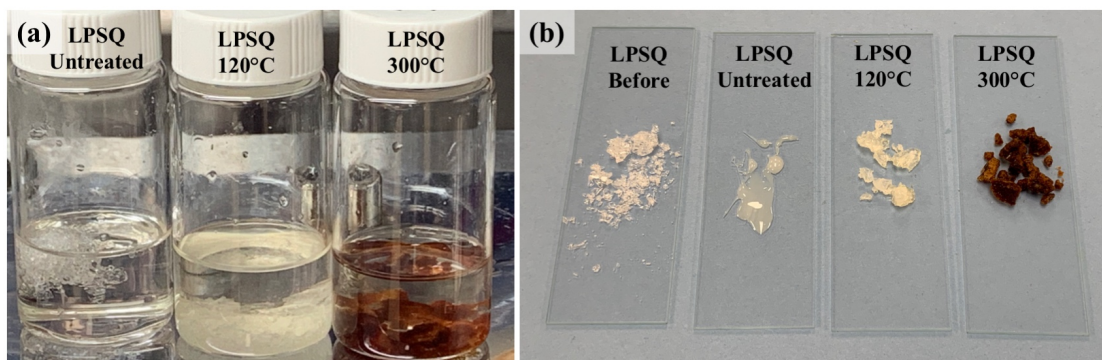


**Figure 6.5.** (a) Solubility testing of LPSQ after different levels of thermal treatment and (b) LPSQ samples after testing in electrolyte

LPSQ was electrospayed directly onto PI nanofiber sheets. The LPSQ solution is still wet as it reaches the fiber surface and forms a unique morphology as it coats the fibers. SEM of the coated surface shows that the LPSQ coats individual fibers and forms connective junctions of fibers with a ceramic webbing (Fig. 6.6). As seen in images 6.6a-c, the connective morphology of the LPSQ is present as the fibers are coated. Figures 6.6d-f show that the webbed junctions and continuous ceramic layer are maintained through heat treatment. Increased electrospaying duration increases accumulation of LPSQ amongst the fibers and occurrences of webbed junctions. The increased LPSQ loading also improves coverage across the fiber surface forming a more continuous PI/LPSQ layer. While there is more accumulation of ceramic, even at the highest loading shown here,  $0.22 \text{ mg/cm}^2$ , there is still open porosity for ion diffusion. The use of ACES with LPSQ onto a fiber framework adds ceramic into the natural pores of electrospun fiber layers and preserves them without clogging them, which is typical problem with packed nanoparticle or blade coating approaches. The PI fibers have a

smooth morphology and are free of defects such as beads (Fig. 6.6g). The fibers have a uniform fiber diameter of  $307 \text{ nm} \pm 73 \text{ nm}$ . The PI/LPSQ separators maintain a 25 to 30- $\mu\text{m}$  thickness that does not vary significantly with LPSQ coating. From cross-section imaging it can be seen that the ceramic addition forms an asymmetric separator, forming a dense layer that is approximately  $5 \mu\text{m}$  thick within the PI fiber framework (Fig 6.6h-i). The ceramic does not penetrate through the fiber mat and the bulk of the separator is a PI nanofiber mat.

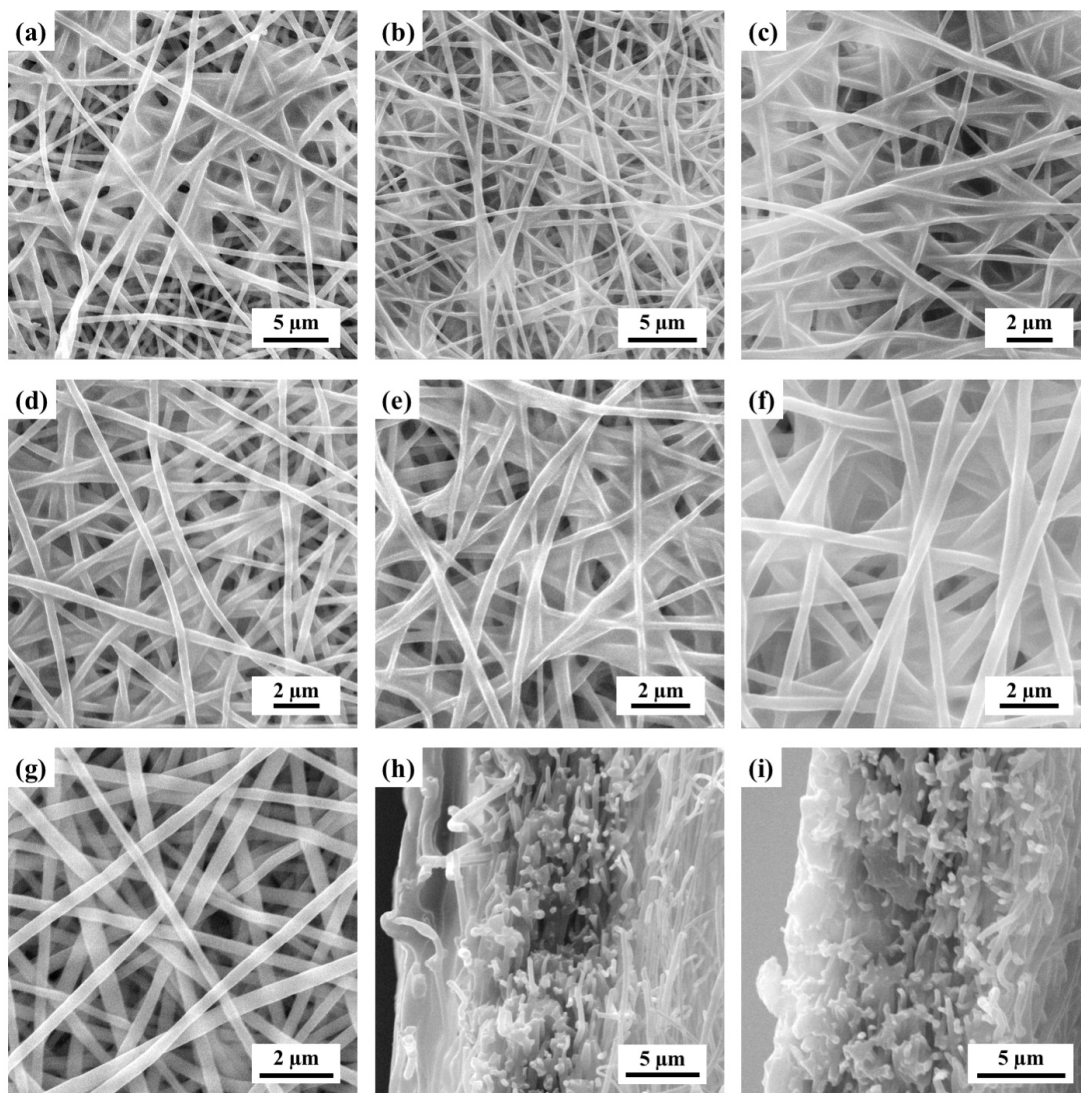


**Figure 6.6.** SEM imaging of PI/LPSQ separators. (a, b, c) PI/LPSQ samples after electro spray coating and before heat treatment of 0.055, 0.110, and 0.220 mg/cm<sup>2</sup> coatings, respectively. (d, e, f) PI/LPSQ samples after heat treatment of 0.055, 0.11, and 0.22 mg/cm<sup>2</sup> coatings, respectively. (g) PI fibers from reverse side of PI/LPSQ samples. (h) Cross-section of 0.11 mg/cm<sup>2</sup> electro sprayed sample and (i) 0.22 mg/cm<sup>2</sup> electro sprayed sample.

The LPSQ penetration into the separator and film formation affected the natural interfiber pore structure. Table 6.2 lists the porosity, mean pore size, and electrolyte uptake of the electrospun and spray coated separators. All three properties decreased with increasing LPSQ coating. Instead of stacking on top of the separator, the LPSQ coating was shown to fill in the top layers of the electrospun framework and reduce the nanofiber membrane's void space. This led to more than a 10% reduction in porosity and 100% reduction in electrolyte uptake. However, even at the highest LPSQ loading, the porosity and electrolyte uptake are significantly higher than Celgard 2400, with 41% porosity and 97% electrolyte uptake. Figure 6.7 shows the distribution of the uncoated PI versus the highest coating. The uncoated fibers have many pores in the 0.6 – 0.8  $\mu\text{m}$  range while the coated sample's largest pore size is around 0.4  $\mu\text{m}$ . Confirming what is seen by the SEM, the LPSQ drapes across the fibers and decreases the pore size, but preserves much of the natural porosity of the electrospun framework.

**Table 6.2.**

Porosity, mean pore size, and electrolyte uptake of PI fiber and ACES coated separators.

Sample	Porosity	Mean Pore Size	Electrolyte Uptake
PI Fiber	82.0%	0.470 $\mu\text{m}$	492%
0.055 $\text{mg}/\text{cm}^2$	79.9%	0.410 $\mu\text{m}$	414%
0.11 $\text{mg}/\text{cm}^2$	77.7%	0.347 $\mu\text{m}$	396%
0.22 $\text{mg}/\text{cm}^2$	69.4%	0.275 $\mu\text{m}$	382%

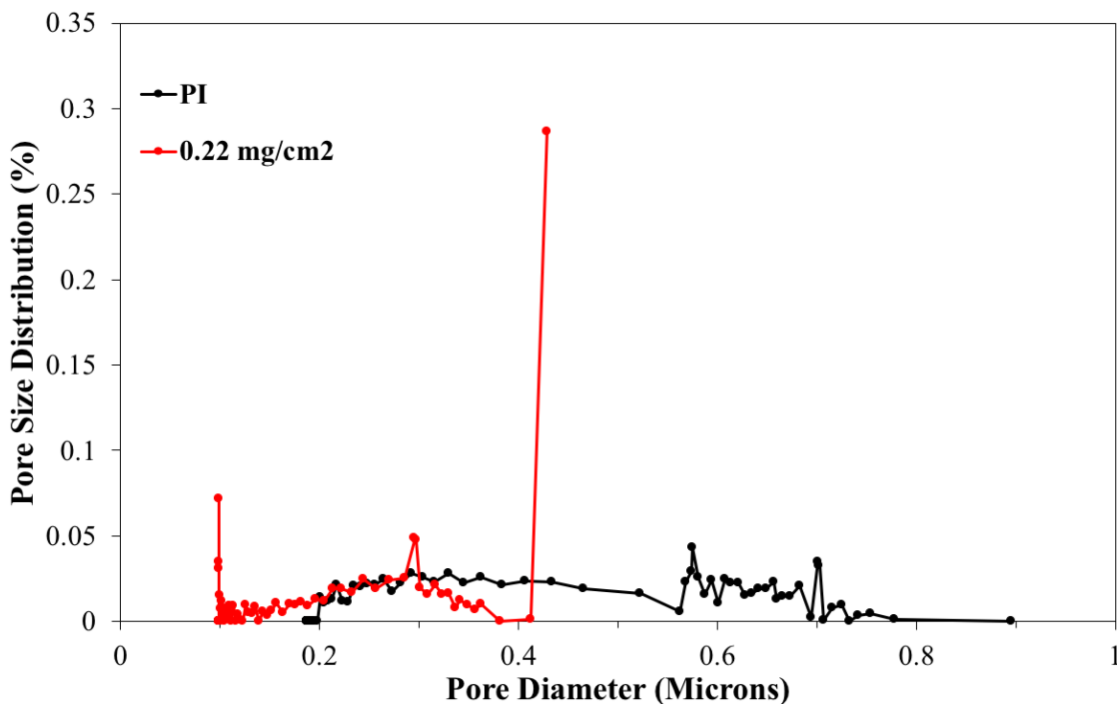


**Figure 6.7.** Pore distribution comparison of PI fibers and 0.22 mg/cm<sup>2</sup> LPSQ-coated fibers.

Thermal shrinkage is evaluated by taking 4-cm squares of the separator materials and placing them in a furnace at set temperatures for 1 hour. The areas of the samples are measured before and after the thermal aging and the area lost is plotted in Figure 6.8. Celgard was evaluated over a temperature range of 90°C to 170°C and showed significant shrinkage above 100°C. The majority of shrinkage was in the stretched, machine direction. There is no directionality in the shrinkage from the electrospun separators. The PI and LPSQ-coated separators were heat treated at 300°C and exhibit excellent thermal shrinkage properties, with no shrinkage at temperatures 300°C or lower. At 350°C, the PI and coated separators experience significant shrinkage. The 0.22 mg/cm<sup>2</sup> coating shows the least shrinkage with only 22% area lost, while all other separators lose at least 37%. At 400°C, the 0.22 mg/cm<sup>2</sup> coating performs best, but all of the separators show more than 50% shrinkage. The base fiber layer is controlling the

thermal shrinkage more than the coated ceramic. The addition of OPSZ to form PAN/PDC hybrid fibers in Chapter 5 offered much more thermal stability than the addition of an LPSQ-coating.

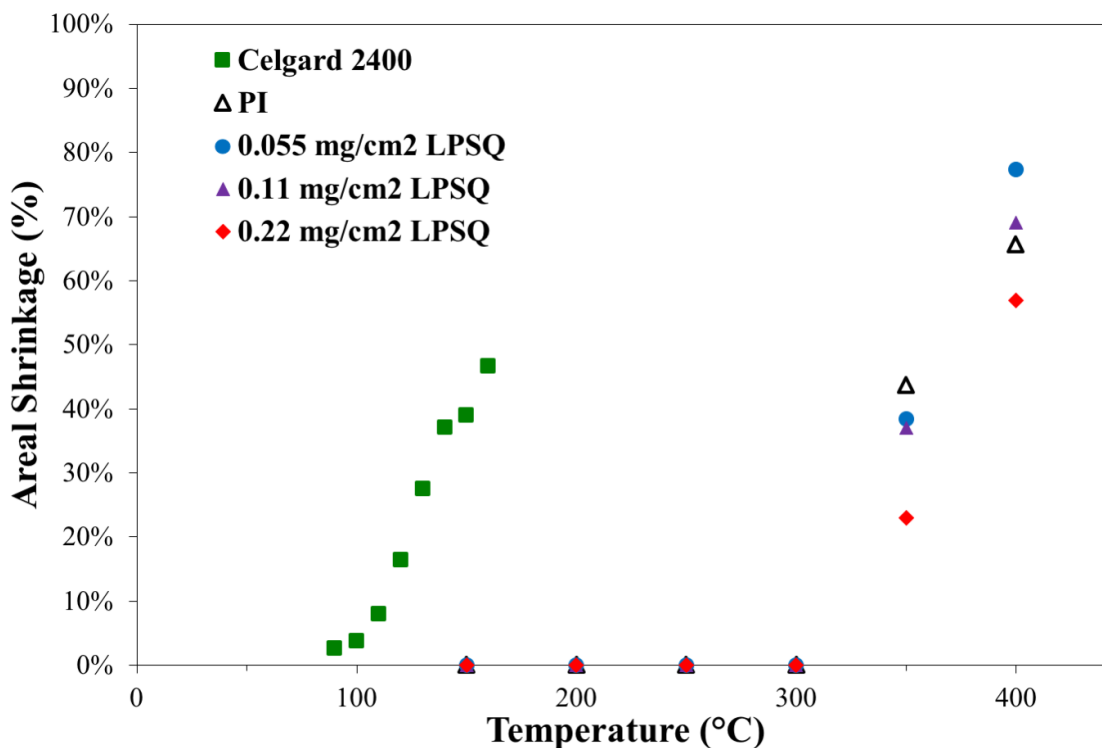


**Figure 6.8.** Thermal shrinkage was measured after holding materials at different temperatures for 1 hour. The area lost after 1 hour has been plotted for each separator type.

The flame resistance of the separators was tested with burning electrolyte. 4-cm squares of each material were placed in an aluminum pan with 20-ml of electrolyte. Figure 6.9 depicts the test and the effect on the separator samples. The PI sample shows significant bubbles and singeing from gas evolution by the electrolyte and significant area loss. As the LPSQ loading is increased both the bubbling and shrinkage decreased for the sample showing excellent flame resistance added by the ceramic coating. The shrinkage was 48.2%, 24.9%, 13.4%, and 2.5% shrinkage for PI and LPSQ loadings of 0.055, 0.11, and 0.22 mg/cm<sup>2</sup>, respectively. Increasing the amount of ceramic coating

the material improved the flame resistance of the separator. More importantly, the connected, webbed structure of the ceramic coating holds the entire surface together preventing both bubbles at the surface and loss of area to high heat or combustion. Celgard was tested separately and showed little flame resistance, shrinking by 96.4% during the test.

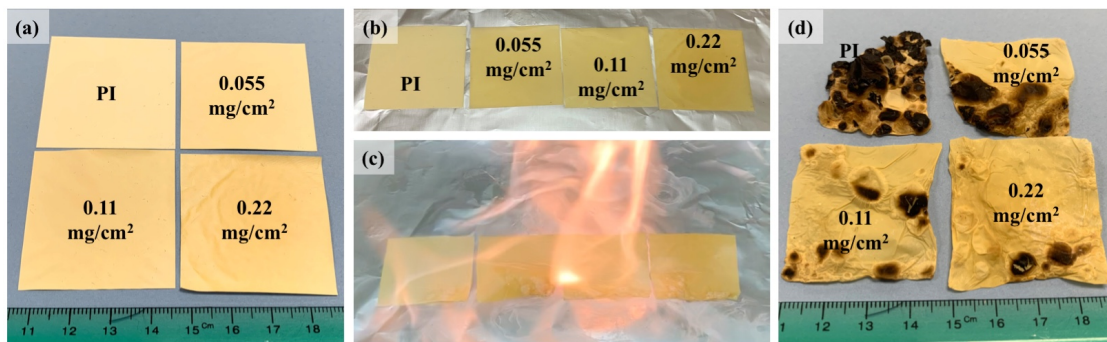


**Figure 6.9.** Flame testing: (a) Separator samples before flame testing. (b) Samples placed in tray and soaked with electrolyte. (c) The electrolyte is lit on fire. (d) Separator conditions post flame testing.

The separators were then evaluated for electrochemical performance. First, the 0.22 mg/cm<sup>2</sup> coated separators were tested by EIS to determine their ionic conductivity. The Nyquist plot in Figure 6.10 was generated from EIS results for the coated separator and Celgard reference and the inset is a zoomed image near the x-axis. The x-intercept of each plot represents the bulk resistance,  $R_b$ , in each cell attributed to the triple-stacked separators. The intercept was determined by a linear fit. This resistance value is then used to determine the ionic conductivity for each separator material. The coated separator demonstrated excellent ionic conductivity and achieved 3.16 mS/cm ionic conductivity – more than tripling Celgard 2400’s 0.95 mS/cm. The high ionic conductivity is due to a combination of the porous electrospun fiber network and the ceramic additions that coat many of the fibers. Ceramic materials improve ionic

conductivity by acting as Lewis acid-base centers, promoting salt dissociation that frees more Li-ions [48, 49]. This ionic conductivity is even higher than the 90:10 PI:OPSZ separators (2.39 mS/cm) demonstrated in the previous chapter. This could be due to LPSQ being more effective than OPSZ at improving ion conduction or that the PI/OPSZ separators had been calendered to a higher degree.

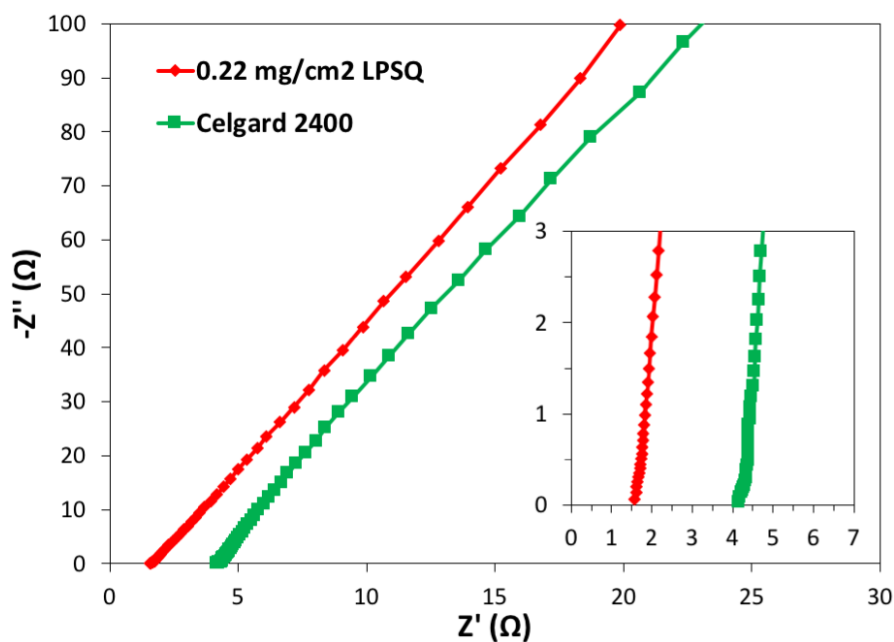


**Figure 6.10.** Nyquist plot from EIS of the SS-symmetrical cells with three layers of separators comparing the LPSQ-coated and Celgard separators.

The high ionic conductivity of the LPSQ-separators was apparent in rate capability testing. Figure 6.11 gives rate data for PI and ACES coated PI up to 4C discharge rate. The advantage of the LPSQ coating is seen at 0.1 C and is maintained at all tested current densities. At 4C, the discharge capacity improved with LPSQ loading and rose from 104 mAh/g for PI fibers to 122 mAh/g for 0.22 mg/cm<sup>2</sup> separators. The 4C rate retention was 55.0%, 55.7%, 60.3%, and 62.6% retention for PI, 0.055, 0.11, and 0.22 mg/cm<sup>2</sup> LPSQ separators, respectively. Despite the loss of porosity and

decreasing pore size, the higher loadings of LPSQ and the effect of having additional ceramic penetrate into the fiber framework provided faster ion transport. If the ceramic was only stacked on top of the fiber structure, as seen in blade coating, there is an increase in overall resistance and there is not an improvement in rate capability. The ACES coating is making it easier to transport through the fiber framework without making it thicker with a separate coated layer. The 0.11 mg/cm<sup>2</sup> coatings perform very similarly so there may be decreasing returns of additional ceramic or a point where the pore size becomes too small. All PI and coated separators recovered more than 95% of their initial capacity when they returned to 0.1C rate and showed excellent stability after high current densities.

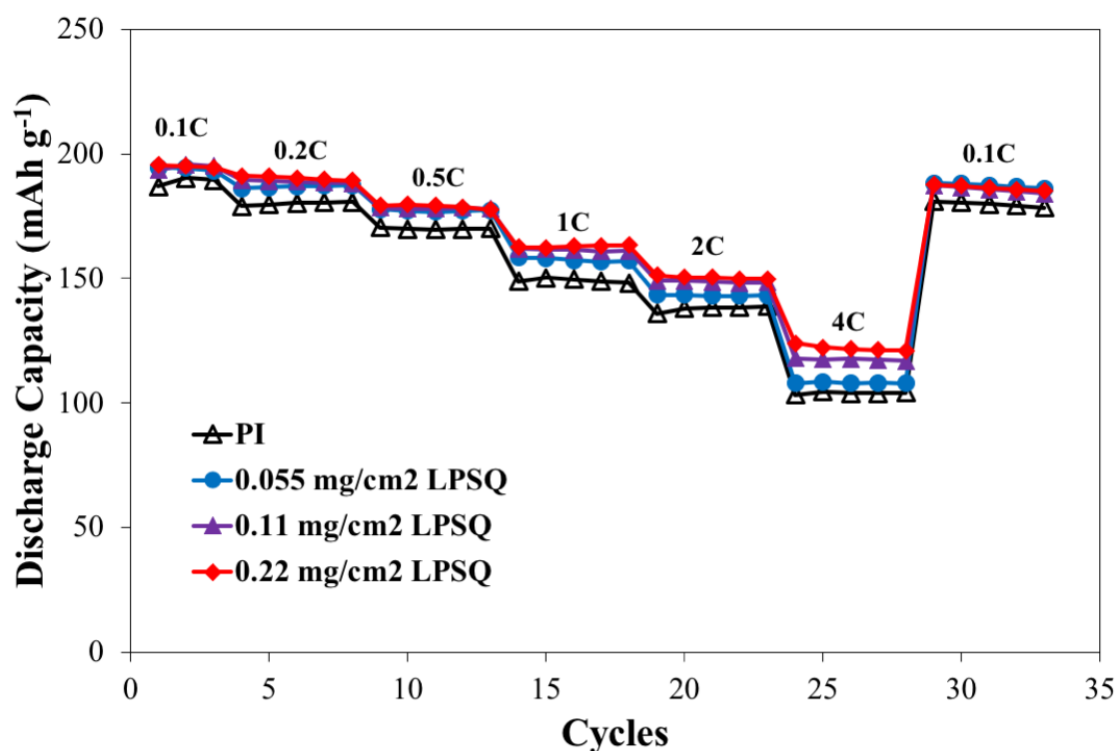


**Figure 6.11.** Results of rate capability tests for the NCM811/graphite full cells with various separator membranes. Discharge rates reach 4C while charge rates are limited to 1C in cell tests.

In addition to fast ion transport, the addition of LPSQ by ACES improved cycling capacity and stability. Figure 6.12 shows the results of 0.5C rate and 1C rate cycling of PI fiber, LPSQ-coated fiber, and Celgard 2400 separators. At both current densities, the Celgard performed the worst and then cycling improved with LPSQ loading. After cycling at 0.5C rate for 100 cycles, the capacities were 145, 150, 151, 159, and 162 mAh/g for Celgard, PI, 0.055, 0.11, and 0.22 mg/cm<sup>2</sup> separators, respectively. The coating improved the PI fibers' capacity retention, with PI fibers retaining 85.7% capacity and the 0.22 mg/cm<sup>2</sup> coatings retaining 88.5% capacity. The effect of the coating was even more significant at 1C cycling rate. A 1-hour charge would be a significant milestone for electric vehicles' viability for use on longer trips. The 0.22 mg/cm<sup>2</sup> separators showed the best performance through 250 cycles at 1C, with an excellent 140 mAh/g and 83% capacity retention. By comparison, Celgard had only 111 mAh/g capacity - 70% of their initial 1C capacity.

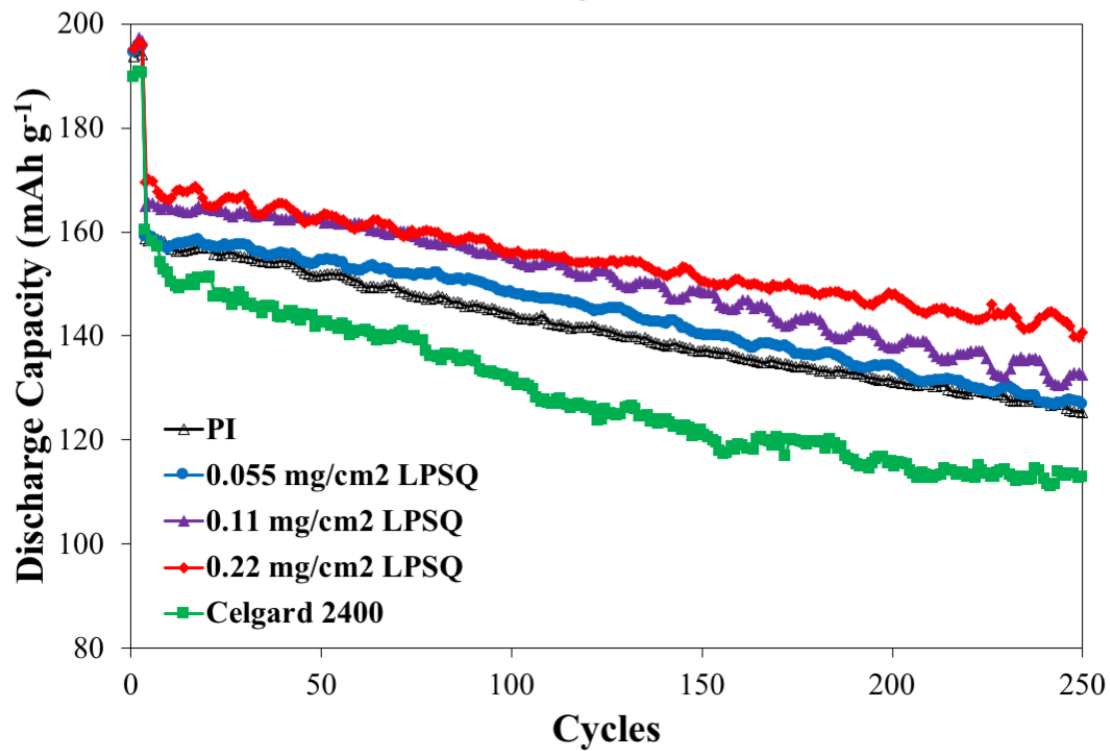
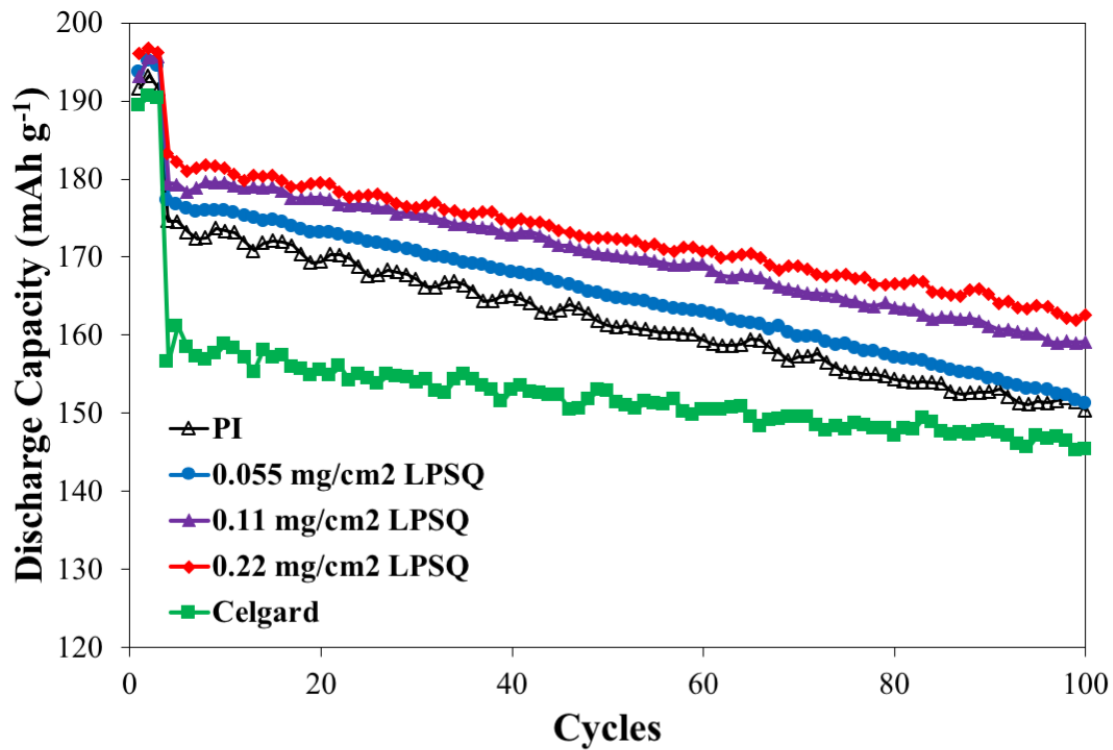


**Figure 6.12.** Cycling performance comparison of the PI, LPSQ-coated PI, and Celgard separators at (top) 0.5C and (bottom) 1C rates in NCM811/graphite full cells.

#### **6.4. Conclusions**

An asymmetric separator was formed using electrospun PI nanofibers with an AC-electrosprayed LPSQ coating. Separators were 25-30 microns thick with LPSQ penetrating ~5 microns into the spray coated side and not increasing the thickness of the original fiber membrane. The LPSQ addition was adhered to the fiber framework without binder and formed a unique morphology where LPSQ was draped over fibers and across pores with a webbed morphology that reduced the mean pore size and the porosity of the electrospun fiber framework but maintained the open pores of electrospun fiber mats. Heat treatment of the PI and LPSQ removed soluble functional groups, crosslinked the LPSQ, and improved the materials' thermal stability and flame resistance. While PI materials already showed robust thermal stability, the LPSQ coating significantly reduced shrinkage and separator singeing in an electrolyte fire for improved battery safety. The addition of ceramic into the fiber structure greatly enhanced the ionic conductivity and battery performance despite the reduction in pore size and porosity of the electrospun framework. 0.22 mg/cm<sup>2</sup> LPSQ coating on PI fibers improved the 4C discharge capacity from 104 mAh/g for PI fibers to 122 mAh/g in NMC811/graphite full cells. The ceramic addition improved cycling stability as well, with 0.22 mg/cm<sup>2</sup> coated separators retaining 83% capacity after 250 cycles at 1C rate, compared to 70.4% for Celgard 2400 and 78.9% for electrospun PI fibers. Air-controlled electrospayed LPSQ coatings on electrospun PI addresses safety concerns and performance needs for Li-ion batteries and their use in electric vehicles.

## 6.5. References

- [1] Smith, S. A., Park, J. H., Williams, B. P. & Joo, Y. L. Polymer/ceramic co-continuous nanofiber membranes via room-curable organopolysilazane for improved lithium-ion battery performance. *J Mater Sci* **52**, 3657–3669 (2016).
- [2] Scrosati, B. & Garche, J. Lithium batteries: Status, prospects and future. *Journal of Power Sources* **195**, 2419–2430 (2010).
- [3] Dunn, B., Kamath, H. & Tarascon, J.-M. Electrical energy storage for the grid: a battery of choices. *Science* **334**, 928–935 (2011).
- [4] Arora, P. & Zhang, Z. J. Battery Separators. *Chem. Rev.* **104**, 4419–4462 (2004).
- [5] Zhang, S. S. A review on the separators of liquid electrolyte Li-ion batteries. *Journal of Power Sources* **164**, 351–364 (2007).
- [6] Waqas, M., Ali, S., Feng, C., Chen, D., Han, J., & He, W. Recent Development in Separators for High-Temperature Lithium-Ion Batteries. *Small* **15**, 1901689 (2019).
- [7] Huang, X. Separator technologies for lithium-ion batteries. *J Solid State Electrochem* **15**, 649–662 (2010).
- [8] Orendorff, C. J., Lambert, T. N., Chavez, C. A., Bencomo, M. & Fenton, K. R. Polyester Separators for Lithium-Ion Cells: Improving Thermal Stability and Abuse Tolerance. *Adv. Energy Mater.* **3**, 314–320 (2012).
- [9] Feng, X., Ouyang, M., Liu, X., Lu, L., & He, X. Thermal runaway mechanism of lithium ion battery for electric vehicles: A review. *Energy Storage Materials* **10**, 246–267 (2018).
- [10] Wang, Q., Ping, P., Zhao, X., Chu, G., Sun, J., & Chen, C. Thermal runaway caused fire and explosion of lithium ion battery. *Journal of Power Sources* **208**, 210–224 (2012).
- [11] Park, J.-H., Cho, J.-H., Park, W., Ryoo, D., Yoon, S.-J., Kim, J. H., Jeong, Y. U., & Lee, S.-Y. Close-packed SiO<sub>2</sub>/poly(methyl methacrylate) binary nanoparticles-coated polyethylene separators for lithium-ion batteries. *Journal of Power Sources* **195**, 8306–8310 (2010).
- [12] Shi, C., Zhang, P., Chen, L., Yang, P. & Zhao, J. Effect of a thin ceramic-coating layer on thermal and electrochemical properties of polyethylene separator for lithium-ion batteries. *Journal of Power Sources* **270**, 547–553 (2014).
- [13] Zhu, X., Jiang, X., Ai, X., Yang, H. & Cao, Y. A Highly Thermostable Ceramic-Grafted Microporous Polyethylene Separator for Safer Lithium-Ion Batteries. *ACS Appl. Mater. Interfaces* **7**, 24119–24126 (2015).
- [14] Song, J., Ryou, M.-H., Son, B., Lee, J.-N., Lee, D. J., Lee, Y. M., Choi, J. W., & Park, J.-K. Co-polyimide-coated polyethylene separators for enhanced

- thermal stability of lithium ion batteries. *Electrochimica Acta* **85**, 524–530 (2012).
- [15] Lee, Y., Lee, H., Lee, T., Ryou, M.-H. & Lee, Y. M. Synergistic thermal stabilization of ceramic/co-polyimide coated polypropylene separators for lithium-ion batteries. *Journal of Power Sources* **294**, 537–544 (2015).
- [16] Shi, C., Dai, J., Shen, X., Peng, L., Li, C., Wang, X., Zhang, P., & Zhao, J. A high-temperature stable ceramic-coated separator prepared with polyimide binder/Al<sub>2</sub>O<sub>3</sub> particles for lithium-ion batteries. *Journal of Membrane Science* **517**, 91–99 (2016).
- [17] Shi, J., Xia, Y., Yuan, Z., Hu, H., Li, X., Zhang, H., & Liu, Z. Porous membrane with high curvature, three-dimensional heat-resistance skeleton: a new and practical separator candidate for high safety lithium ion battery. *Sci. Rep.* **5**, 3935–9 (2015).
- [18] Jung, J.-W., Lee, C.-L., Yu, S. & Kim, I.-D. Electrospun nanofibers as a platform for advanced secondary batteries: a comprehensive review. *J. Mater. Chem. A* **4**, 703–750 (2015).
- [19] Lee, H., Yanilmaz, M., Toprakci, O., Fu, K. & Zhang, X. A review of recent developments in membrane separators for rechargeable lithium-ion batteries. *Energy Environ. Sci.* **7**, 3857–3886 (2014).
- [20] Miao, Y.-E., Zhu, G.-N., Hou, H., Xia, Y.-Y. & Liu, T. Electrospun polyimide nanofiber-based nonwoven separators for lithium-ion batteries. *Journal of Power Sources* **226**, 82–86 (2013).
- [21] Jiang, W., Liu, Z., Kong, Q., Yao, J., Zhang, C., Han, P., & Cui, G. A high temperature operating nanofibrous polyimide separator in Li-ion battery. *Solid State Ionics* **232**, 44–48 (2013).
- [22] Wang, Q., Song, W.-L., Wang, L., Song, Y., Shi, Q., & Fan, L.-Z. Electrospun polyimide-based fiber membranes as polymer electrolytes for lithium-ion batteries. *Electrochimica Acta* **132**, 538–544 (2014).
- [23] Wu, D., Shi, C., Huang, S., Qiu, X., Wang, H., Zhan, Z., Zhang, P., Zhao, J., Sun, D., & Lin, L. Electrospun Nanofibers for Sandwiched Polyimide/Poly(vinylidene fluoride)/Polyimide Separators with the Thermal Shutdown Function. *Electrochimica Acta* **176**, 727–734 (2015).
- [24] Cao, L., An, P., Xu, Z. & Huang, J. Performance evaluation of electrospun polyimide non-woven separators for high power lithium-ion batteries. *Journal of Electroanalytical Chemistry* **767**, 34–39 (2016).
- [25] Lee, J., Lee, C.-L., Park, K. & Kim, I.-D. Synthesis of an Al<sub>2</sub>O<sub>3</sub>-coated polyimide nanofiber mat and its electrochemical characteristics as a separator for lithium ion batteries. *Journal of Power Sources* **248**, 1211–1217 (2014).
- [26] Sun, G., Dong, G., Kong, L., Yan, X., Tian, G., Qi, S., & Wu, D. Robust polyimide nanofibrous membrane with porous-layer-coated morphology by in

- situself-bonding and micro-crosslinking for lithium-ion battery separator. *Nanoscale* **10**, 22439–22447 (2018).
- [27] Zhong, G., Wang, Y., Wang, C., Wang, Z., Guo, S., Wang, L., Liang, X., & Xiang, H. An AlOOH-coated polyimide electrospun fibrous membrane as a high-safety lithium-ion battery separator. *Ionics* **25**, 2677–2684 (2019).
- [28] Baney, R. H., Itoh, M., Sakakibara, A. & Suzuki, T. Silsesquioxanes. *Chem. Rev.* **95**, 1409–1430 (1995).
- [29] Chinnam, P. R. & Wunder, S. L. Polyoctahedral Silsesquioxane-Nanoparticle Electrolytes for Lithium Batteries: POSS-Lithium Salts and POSS-PEGs. *Chem. Mater.* **23**, 5111–5121 (2011).
- [30] Lu, Q., Fu, J., Chen, L., Shang, D., Li, M., Xu, Y., Jia, R., Yuan, S., & Shi, L. Polymeric polyhedral oligomeric silsesquioxane ionic liquids based solid polymer electrolytes for lithium ion batteries. *Journal of Power Sources* **414**, 31–40 (2019).
- [31] Zhao, H., Deng, N., Yan, J., Kang, W., Ju, J., Wang, L., Li, Z., & Cheng, B. Effect of OctaphenylPolyhedral oligomeric silsesquioxane on the electrospun Poly-m-phenylene isophthalamid separators for lithium-ion batteries with high safety and excellent electrochemical performance. *Chemical Engineering Journal* **356**, 11–21 (2019).
- [32] Gui, X., Liu, L., Gao, S., Sun, L., Xu, K., & Chen, M. A novel silsesquioxanes modified electrospun composite fibrous separator by in-situ crosslinking method for lithium-ion batteries. *Materials Letters* **242**, 66–70 (2019).
- [33] Jeon, H., Roh, Y., Jin, D., Ryou, M.-R., Jeong, Y.-C., & Lee, Y. M. Crosslinkable polyhedral silsesquioxane-based ceramic-coated separators for Li-ion batteries. *Journal of Industrial and Engineering Chemistry* **71**, 277–283 (2019).
- [34] Choi, S.-S., Lee, A., Lee, H., Hyeon, Jeon, H., Baek, K., Choi, D., Hwang, S. Synthesis and characterization of UV-curable ladder-like polysilsesquioxane. *Journal of Polymer Science Part A: Polymer Chemistry* **49**, 5012–5018 (2011).
- [35] Zhang, L., Tian, G., Wang, X., Qi, S., Wu, Z., & Wu, D. Polyimide/ladder-like polysilsesquioxane hybrid films: Mechanical performance, microstructure and phase separation behaviors. *Composites Part B: Engineering* **56**, 808–814 (2014).
- [36] Fei, L., Yoo, S. H., Villamayor, R., Williams, B., Gong, S. Y., Park, S., Shin, K., & Joo, Y. L. Graphene Oxide Involved Air-Controlled Electro spray for Uniform, Fast, Instantly Dry, and Binder-Free Electrode Fabrication. *ACS Applied Materials & Interfaces* **9**, 9738–9746 (2017).
- [37] Lee, J., Ko, B., Kang, J., Chung, Y., Kim, Y., Halim, W., Lee J. H., & Joo, Y. L. Facile and scalable fabrication of highly loaded sulfur cathodes and lithium-

- sulfur pouch cells via air-controlled electrospray. *Materials Today Energy* **6**, 255–263 (2017).
- [38] Lee, J. H., Kang, J., Kim, S. W., Halim, W., Frey, M. W., & Joo, Y. L. Effective Suppression of the Polysulfide Shuttle Effect in Lithium–Sulfur Batteries by Implementing rGO–PEDOT:PSS-Coated Separators via Air-Controlled Electrospray. *ACS Omega* **3**, 16465–16471 (2018).
- [39] Halim, W., Lee, J. H., Park, S. M., Zhang, R., Sarkar, S., O’Neil, T., Chiang, E., & Joo, Y. L. Directly Deposited Binder-Free Sulfur Electrode Enabled by Air-Controlled Electrospray Process. *ACS Applied Energy Materials* **2**, 678–686 (2019).
- [40] Divvela, M. J., Zhang, R., Zhmayev, Y., Pinge, S., Lee, J. H., Kim, S. W., & Joo, Y. L. Control of formation of viscoelastic droplets and distribution of nano-inclusions in functional deposition for lithium–sulfur batteries. *Soft Matter* **15**, 6485–6494 (2019).
- [41] Vanherck, K., Koeckelberghs, G. & Vankelecom, I. F. J. Crosslinking polyimides for membrane applications: A review. *Progress in Polymer Science* **38**, 874–896 (2013).
- [42] Barsema, J., Klijnstra, S., Balster, J., van der Vegt, N., Koops, G., & Wessling, M. Intermediate polymer to carbon gas separation membranes based on Matrimid PI. *Journal of Membrane Science* **238**, 93–102 (2004).
- [43] Liu, H., Xu, J., Guo, B. & He, X. Preparation and performance of silica/polypropylene composite separator for lithium-ion batteries. *J. Mater. Sci.* **49**, 6961–6966 (2014).
- [44] Landesfeind, J., Hattendorff, J., Ehrl, A., Wall, W. A. & Gasteiger, H. A. Tortuosity Determination of Battery Electrodes and Separators by Impedance Spectroscopy. *J. Electrochem. Soc.* **163**, A1373–A1387 (2016).
- [45] Chang, S., Matsumoto, T., Matsumoto, H. & Unno, M. Synthesis and characterization of heptacyclic laddersiloxanes and ladder polysilsesquioxane. *Applied Organometallic Chemistry* **24**, 241–246 (2010).
- [46] Zhang, Z.-X., Hao, J., Xie, P., Zhang, X., Han, C., & Zhang, R. A Well-Defined Ladder Polyphenylsilsesquioxane (Ph-LPSQ) Synthesized via a New Three-Step Approach: Monomer Self-Organization–Lyophilization—Surface-Confining Polycondensation. *Chem. Mater.* **20**, 1322–1330 (2008).
- [47] Kim, Y., Choi, G.-M., Bae, J., Kim, Y. & Bae, B.-S. High-Performance and Simply-Synthesized Ladder-Like Structured Methacrylate Siloxane Hybrid Material for Flexible Hard Coating. *Polymers* **10**, 449–12 (2018).
- [48] Croce, F., Appetecchi, G. B., Persi, L. & Scrosati, B. Nanocomposite polymer electrolytes for lithium batteries. *Nature* **394**, 456–458 (1998).
- [49] Salem N., Abu-Lebdeh Y. (2012) Effect of Nanoparticles on Electrolytes and Electrode/Electrolyte Interface. In: Abu-Lebdeh Y., Davidson I. (eds)

Nanotechnology for Lithium-Ion Batteries. Nanostructure Science and Technology. Springer, Boston, MA.

## CHAPTER 7

### RECOMMENDATIONS FOR FUTURE WORK

This thesis has focused on developing new ways to form electrodes and separators for high performance energy storage application using electrospinning and electrospraying. Processes developed initially for one application have been retooled for other applications and this opens many new possibilities for future work. The focus of the projects presented here are to both combine existing work and add new layers to the processes we developed for continued energy storage improvement.

#### ***7.1. Preparation of silicon nanofibers with increased porosity and conductivity***

ACES, direct deposit RGO anodes, have shown to be an excellent system for a range of materials including now micron-size silicon. The prepared electrodes of micron-size silicon fibers in RGO sheets showed some stability cycling at high current density, as well as excellent rate capability. The combination of electrospinning silica and then using magnesium reduction with a salt heat scavenger yields many different possibilities to further improve on this design moving forward.

##### **7.1.1 Further study of carbons in silicon fibers**

We have shown preparation of silicon fibers with internal CNTs. These were preliminary results showing that by controlling the temperature during the magnesium reduction, we could have silicon fibers with conductive carbon forming a network internally. Initial slurry tests showed a strong silicon signature and that performance

was not hurt by CNT addition. The silicon/CNT fibers have not yet been tested in the ACES /GO system as Li-ion anodes, and that would be our first focus. Beyond initial rate capability testing there are several tracks to explore in this work, including the amount of carbon loading in the fibers and the choice of carbon additive. We have picked one initial loading of carbon to put in silicon fibers to test in our preliminary work, but the amount of carbon would affect the capacity and rate capability of the electrosprayed anodes. Additionally, while carbon nanotubes show excellent performance with silicon in fibers [1], the use of other carbon materials like graphene nanoribbons, or control of size and dispersion of the carbon within the silica matrix, could have improved results [2]. While previous works in this area showed strong effects in silicon nanofibers, the effects of conductive carbon should be far stronger in micron-size silicon particles, where charge transport is a larger issue.

### **7.1.2 Further study of fiber morphology**

Micron-sized silicon fibers showed high 1st coulombic efficiency and previously unseen cycling performance, but pulverization issues remain. Capacity retention is the most significant issue in our micron-silicon system. The pulverization issue was significantly mitigated by the layered RGO structure, but additional focus could be put on the design of the silicon fibers themselves. Currently, silicon expansion can occur outwards from the fiber, putting large stress at the outer edge of the fibers. This is an issue in nanofiber and nanoparticle materials as well. One way to reduce the stress on nanomaterials was to form them with hollow cores [3]. Preparation of hollow materials introduces free volume in the structure for expansion

to take place in two directions. This can more efficiently accommodate the strains of the alloying reaction and has shown a large improvement in cycle stability. One of the many advantages of electrospinning is the preparation of fibers with varied morphologies, including hollow fibers. While co-axial electrospinning is a more complicated approach, it can be used to form fibers with a core-shell structure. A shell layer of our silica solgel and a pure polymer core would create a hollow silica fiber after calcination. Using our magnesium reductions with salt preserves structure, making it possible to form hollow silicon fibers. This could improve the cycling stability without having to change from our micron size fibers and their high 1st coulombic efficiency.

## ***7.2 GO/metal oxide and graphene/metal oxide AC-electrosprayed films for high energy density supercapacitors***

The carbon/Mn<sub>3</sub>O<sub>4</sub> freestanding electrodes worked poorly in supercapacitor testing. A new approach with a different binder-free system may be more effective. Instead of forming freestanding hybrid fiber sheets, we can utilize our work with AC-electrospraying GO sheets and our work with electrospinning pure metal oxide fibers to form thin film, high energy density electrodes using a scalable, direct deposit method. GO sheets have shown significant interest for energy storage. More specifically, GO sheets can be reduced to RGO and can form layered structures that sandwich active material in between the RGO to provide protection and conductivity. The ACES/RGO system has shown to be the most scalable method to utilize these sheets, over other techniques like vacuum filtration [4]. In recent RGO work, it was

shown that using layered RGO sheets with  $Mn_3O_4$  particles could be used for supercapacitors [5]. The electrodes showed great capacity and cycle retention for over 60,000 cycles. Knowing that this binder-free approach does not suffer from the issues we saw with our freestanding fibers, we could apply some of what we learned to RGO layers to form high energy density supercapacitors. There are several alterations we could make to our work with micron-size silicon anodes to adapt to supercapacitor systems:

- [1] Use of graphene sheets in the suspension instead of GO
- [2] Use of the Joo group's highly loaded PVA:metal precursor technique to form metal oxide nanofibers, not limited to  $Mn_3O_4$
- [3] Both electrospinning and electrospraying can be done with water only, no toxic solvent used in the processing

Graphene sheets exhibit superior electrical conductivity to GO, an important consideration for supercapacitors needed for ultra-fast charge transport. Dispersions containing graphene could be an improvement to what has been accomplished with GO/RGO. The use of graphene may require the use of limited binder to have the same adhesion but the conductivity may still be improved and processing would be made simpler as it would not require the additional reduction of GO to RGO.

Secondly, we would focus on adding pure metal oxide fibers for high capacity. Similar to the success we saw with silicon fibers, we know that the layers will wrap and protect fiber morphology. Our group has had success forming metal oxide fibers by electrospinning using a highly loaded PVA:precursor method [6]. We had used this method previously to add pure ZnO fibers to Li-air electrodes, and they showed

excellent performance [7]. Using precursors such as manganese, nickel, and cobalt acetates to form metal oxide fibers could show a range of high performance materials for use in supercapacitors.

Perhaps the most important indication for success in this area is that both the use of ACES and PVA:precursor fiber electrospinning are highly scalable and environmentally friendly. Both methods produce materials from water-based solutions, avoiding toxic solvents, or any additional washing processes. Secondly, if gas-assisted electrospinning is used to form the fibers, both processes can form materials at industrial rates and with a great deal of control for size and shape of the materials prepared.

### ***7.3. Polyimide synthesis for improved strength of polyimide nanofiber separator***

Polyolefin microporous films have a distinct advantage in their high mechanical strength over most electrospun fibers. The PI fibers fabricated for this thesis typically reach 10-20 MPa of tensile strength compared to the >100 MPa achieved by Celgard. The high strength is necessary to survive the preparation of large-scale pouch cells and cylindrical cells that are used in electric vehicles.

Polyimides are well known for being mechanically strong, but how the material is prepared is important [8]. There are many examples of high strength electrospun PI nanofibers, but they were prepared differently (Table 7.1). The high strength examples are spun from the PI precursor molecule, polyamic acid (PAA). High MW PAA was prepared, electrospun, and then imidized after forming fibers. This process gives

excellent chain alignment and strength to the PI fibers. Further strength improvements can be achieved through blending several PAAs.

**Table 7.1**  
PI nanofiber materials strength comparison

Material	Tensile Strength	Young's Modulus
Hybrid: 90:10 P84:OPSZ [this work]	19.5 MPa	350 MPa
Celgard 2400 (25 $\mu$ m)	140 MPa	680 MPa
PI: BPDA+PDA, misaligned [9]	240 MPa	5800 MPa
PI: 6F-BAPP + BPDA [10]	308 MPa	2080 MPa
PI: BPDA + ODA + PDA, aligned [11]	1040 MPa	10000 MPa

This thesis has used P84 for electrospinning - a low MW, already imidized copolymer - due to the reactivity of OPSZ and PAA. With the development of ceramic coatings applied by ACES, the ceramic is removed from the spinning solution, and using PAA can be revisited. A strong focus can now be placed on optimizing the electrospun PI framework to improve the limiting mechanical properties of the PI/ceramic separators.

#### ***7.4. Non-woven separator prepared by papermaking method with air-controlled electrospayed coating with controlled pore size***

In chapter 4, a PAN/OPSZ coating was used to form a dense, tortuous layer over nanofibers as a way to prevent short-circuiting from an open pore structure. While helpful for electrospun nanofibers, the process could be used with other nonwoven materials with possibilities for energy storage such as those made by a wet-laid/paper-

making method [12-13]. In general, most conventional wet-laid nonwovens have native macroscaled porosity and nonuniform pore distributions that prevent their use as battery separators [14]. This has led to their use as mechanical supports for additional layers but those separators are too thick to be used in high energy density batteries. By using ACES, coatings could be applied to the nonwoven framework to decrease the pore size distribution without increasing the thickness to keep the separator thinner while limiting short-circuiting. The papermaking method also works as a roll-to-roll process and could feed directly into an electrospaying bank of needles for one process. Working with a more mechanically robust scaffold could be a replacement for the electrospun fibers to survive the high mechanical stresses of battery fabrication. This is an alternative method to gain the necessary strength for large scale manufacturing.

#### ***7.5. Continued improvement of polyimide nanofiber separator with ACES***

In this work, several different coatings were applied to separators using ACES. With both PAN/OPSZ and LPSQ coatings, only one side of each fiber separator was coated before application. These coatings decreased the pore size distribution but did not hinder the cell performance. With no observed limit to how much should be coated; it would be important to see the effect of increasing the coating applied. This could be done by coating both sides, a layered approach of alternating electrospinning with electrospayed coating, or a concurrent spin/spray setup. In the LPSQ AC-electrospaying preparations, LPSQ penetrated the fibers and formed ~5  $\mu\text{m}$  thick layers. For the 20- $\mu\text{m}$  thick separators this could mean 3 to 4 sprays would be needed during preparation to examine how having ceramic through the separator affects the

pore distribution and the Li-ion transport. The formation of a bonded ceramic network throughout would also have effects on the thermal stability and strength. While LPSQ has been the focus, exploration with spraying other cross-linking molecules could provide favorable properties for the spray-coated separators moving forward.

#### ***7.6. Multi-layered preparation by ACES/GAES for roll-to-roll battery fabrication***

The approach to battery materials is separated into the anode, separator, and cathode. Each component is prepared separately by its own fabrication and then the components are wound together in an additional step to form cells. There is an opportunity to simplify the entire procedure by building the layers together in one roll-to-roll process and could improve manufacturing efficiency as well as give excellent adhesion of the three layers. Anything that can be done to continue to drive down the costs of batteries will help to enable electrification whether it is through more EV sales or new energy storage installations for renewables.

The goal of preparing more layers at once has been approached in a few ways. The scientists at PARC have developed a co-extrusion printing technique (CoEx) that has been used to simultaneously extrude a lithium-ion cathode with a polymer separator [15]. Paired with CoEx's ability to prepare thick, complex interdigitated electrode films as well as being a drop-in replacement for conventional coating lines, CoEx could be a breakthrough for battery manufacturing. The goal is to produce a triple-stripe by including a graphite anode. In a straightforward approach, batteries could also be prepared through sequential addition of battery component "paints" [16]. The research group at Rice used a spray painting process to layer a carbon current collector, an LCO

cathode, a PVDF/PMMA/fumed SiO<sub>2</sub>, an LTO anode, and a copper conductive paint current collector. Batteries were painted on several different surface types including ceramics and plastic films and varied shapes. The simplicity of this process could also be applied to other energy storage devices.

These examples of multi-layered preparations have taken what are thought of as single-component steps and combined them to make the manufacturing simple and efficient. This thesis has focused on using electrospinning and electrospraying to reduce the processing steps for single components. The next step forward for proving the scalability and need for ACES and GAES at an industrial level would be to combine these electrosprayed films and separators into one combined, multi-layer battery. The nozzles could be placed in series to build the different layers and would offer excellent adhesion of the layers. There is no limit to the number of layers or types that could be used. Unlike the CoEx or spray painting processes, an ACES/GAES process prepares nanostructured materials and would offer performance improvements from each layer. In addition to performance improvements, this serialized fabrication could avoid the drawbacks of the mechanically weaker separators prepared by electrospinning. By using a direct deposit of separators to the electrodes, the winding step that requires high strength could be avoided entirely. Moving from preparation of single layers to a combined battery material will better showcase the improvements gained by ACES/GAES and prove the scalability and flexibility of the processes.

## 7.7. References

- [1] Shoorideh, G., Kim, Y. S. & Joo, Y. L. Facile, Water-Based, Direct-Deposit Fabrication of Hybrid Silicon Assemblies for Scalable and High-Performance Li-ion Battery Anodes. *Electrochimica Acta* (2016).
- [2] Kim, Y. S., Shoorideh, G., Zhmayev, Y., Lee, J., Li, Z., Patel, B., Chakrapani, J., Park, H., Lee, S., & Joo, Y.L. The critical contribution of unzipped graphene nanoribbons to scalable silicon-carbon fiber anodes in rechargeable Li-ion batteries. *Nano Energy* **16**, 446–457 (2015).
- [3] Yoo, J.-K., Kim, J., Jung, Y. S. & Kang, K. Scalable Fabrication of Silicon Nanotubes and their Application to Energy Storage. *Adv. Mater.* **24**, 5452–5456 (2012).
- [4] Fei, L., Yoo, S. H., Villamayor, R., Williams, B., Gong, S. Y., Park, S., Shin, K., & Joo, Y. L. Graphene Oxide Involved Air-Controlled Electro Spray for Uniform, Fast, Instantly Dry, and Binder-Free Electrode Fabrication. *ACS Appl. Mater. Interfaces* **9**, 9738–9746 (2017).
- [5] Xiong, T., Lee, W., Huang, X. & Xue, J. Mn<sub>3</sub>O<sub>4</sub>/Reduced graphene oxide based supercapacitor with ultra-long cyclic performance. *J. Mater. Chem. A* (2017). doi:10.1039/C7TA03319B
- [6] Hansen, N. S., Cho, D. & Joo, Y. L. Metal Nanofibers with Highly Tunable Electrical and Magnetic Properties via Highly Loaded Water-Based Electrospinning. *Small* **8**, 1510–1514 (2012).
- [7] Yin, J., Carlin, J., Kim, J., Li, Z., Park, J. H., Patel, B., Chakrapani, S., Lee, S., & Joo, Y. L. Synergy Between Metal Oxide Nanofibers and Graphene Nanoribbons for Rechargeable Lithium-Oxygen Battery Cathodes. *Adv. Energy Mater.* 1–8 (2014).
- [8] Ding, Y., Hou, H., Zhao, Y., Zhu, Z. & Fong, H. Electrospun polyimide nanofibers and their applications. *Progress in Polymer Science* **61**, 67–103 (2016).
- [9] Huang, C., Chen, S., Reneker, D. H., Lai, C. & Hou, H. High-Strength Mats from Electrospun Poly(p-Phenylene Biphenyltetracarboximide) Nanofibers. *Adv. Mater.* **18**, 668–671 (2006).
- [10] Cheng, C., Chen, J., Chen, F., Hu, P., Wu, X.-F., Reneker, D., & Hou, H. High-strength and high-toughness polyimide nanofibers: Synthesis and characterization. *J. Appl. Polym. Sci.* **32**, 1581-1586 (2010).
- [11] Yao, J., Pantano, M. F., Pugno, N. M., Bastiaansen, C. W. M. & Peijs, T. High-performance electrospun co-polyimide nanofibers. *Polymer* **76**, 105–112 (2015).

- [12] Zhang, J., Kong, Q., Liu, Z., Pang, S., Yue, L., Yao, J., Wang, X., & Cui, G. A highly safe and inflame retarding aramid lithium ion battery separator by a papermaking process. *Solid State Ionics* **245-246**, 49–55 (2013).
- [13] Zhang, H., Wang, X. & Liang, Y. Preparation and characterization of a Lithium-ion battery separator from cellulose nanofibers. *Heliyon* **1**, 1–16 (2015).
- [14] Deimede, V. & Elmasides, C. Separators for Lithium-Ion Batteries: A Review on the Production Processes and Recent Developments. *Energy Technology* **3**, 453–468 (2015).
- [15] Bourzac, K. Xerox PARC Materials Scientists Print Two Thirds of a Battery in 1 Go. *Scientific American* (2015).
- [16] Singh, N., Galande, C., Miranda, A., Mathkar, A., Gao, W., Reddy, A. L. M., Vlad, A., & Ajayan, P. M. Paintable Battery. *Scientific Reports* **2**, 1–5 (2012)